Gas-Phase Synthesis of Gold- and Silica-Coated Nanoparticles

A DISSERTATION
SUBMITTED TO THE FACULTY OF THE GRADUATE SCHOOL
OF THE UNIVERSITY OF MINNESOTA
BY

Adam Meyer Boies

IN PARTIAL FULFILLMENT OF THE REQUIREMENTS
FOR THE DEGREE OF
DOCTOR OF PHILOSOPHY

Steven L. Girshick

January, 2011

ACKNOWLEDGEMENTS

I would like to thank my advisor Professor Steven Girshick, who guided me in both the methods of research and the craft of organizing and presenting ideas. I am grateful for his patience and insightful discussions. The funding for my research came from the National Science Foundation under Award Number CBET-0730184, by the MRSEC Program of the NSF under Award Number DMR-0819885, Nitto Denko Technical Corporation and by the 3M Science and Technology Fellowship.

I would also like to thank several research collaborators who were instrumental in my academic development. In particular, I would like to acknowledge Professor Jeffrey Roberts (Purdue University) who actively provided feedback on my research throughout my tenure at the University of Minnesota even after his departure. Professor Joachim Heberlein provided helpful insights into plasma operation. Dr. Ozan Ugurlu (Characterization Facility, UMN) greatly assisted in characterization of samples within the TEM. I would like to thank the following graduate students for their assistance throughout the years: Pingyan Lei and Steven Calder, who collaborated to make many of these studies possible; Dr. Aaron Beaber and Dr. Lejun Qi, who gave me a great introduction to experimental methods within the laboratory; David Rowe and Rebecca Anthony for their thoughtful conversations; and Dr. Anil Bika, Dr. Luke Franklin and Dr. Jacob Swanson, who provided a welcome reprieve academic endeavors.

I am also particularly thankful for the collaborations with Professor David Kittelson and Professor Julian Marshal, whose work helped to give me a larger sense of how technology can be applied to meet world challenges. As a part of those studies I also appreciated the contributions of Dr. Winthrop Watts, Professor Elizabeth Wilson, Professor Steven Taff and Professor Tim Smith.

My thanks go out to the various departmental staff without whom the construction of my experiments would not be possible. Those staff include Bob Nelson, Robin Russell, Pat Nelson, Peter Zimmermann, Dale Lindbeck and Dave Hultman. I would also like to thank John Gardner for recruiting me to the University of Minnesota and helping with all of the academic paperwork once there.

I would thank my wife Abigail Boies who was loving and patient with all of the late nights and early mornings. Last, but not least, I would like to thank all my friends and family for their support and encouragement.

To my wife whose perseverance through adversity serves as constant inspiration

ABSTRACT

Composite nanoparticles consisting of separate core-shell materials are of interest for a variety of biomedical and industrial applications. By combining different materials at the nanoscale, particles can exhibit enhanced or multi-functional behavior such as plasmon resonance combined with superparamagnetism. Gas-phase nanoparticle synthesis processes are promising because they can continuously produce particles with high mass-yield rates. In this dissertation, new methods are investigated for producing gas-phase coatings of nanoparticles in an "assembly-line" fashion. Separate processes are developed to create coatings from silica and gold that can be used with a variety of core-particle chemistries. A photoinduced chemical vapor deposition (photo-CVD) method is used to produce silica coatings from tetraethyl orthosilicate (TEOS) on the surface of nanoparticles (diameter ~5-70 nm). Tandem differential mobility analysis (TDMA) of the process demonstrates that particle coatings can be produced with controllable thicknesses (~1-10 nm) by varying system parameters such as precursor flow rate. Electron microscopy and infrared spectroscopy confirm that the photo-CVD films uniformly coat the particles and that the coatings are silica. In order to describe the coating process a chemical mechanism is proposed that includes gas-phase, surface and photochemical reactions. A chemical kinetics model of the mechanism indicates that photo-CVD coating proceeds primarily through the photodecomposition of TEOS which removes ethyl groups, thus creating activated TEOS species. The activated TEOS then adsorbs onto the surface of the particle where a series of subsequent reactions remove the remaining ethyl groups to produce a silica film with an open site for further attachment. The model results show good agreement with the experimentally measured coating trends, where increased TEOS flow increases coating thickness and increased nitrogen flow decreases coating thickness.

Gold decoration of nanoparticles is accomplished by evaporation of solid gold in the presence of an aerosol flow. A hot-wire generation method is developed where gold particles are produced from a composite gold-platinum wire. Investigations of the hot-wire generator show that it can produce particles with a range of sizes and that more uniform, non-agglomerated particles are produced when using smaller diameter tubes where gas velocities across the wire are higher and recirculation zones are diminished. When gold is evaporated in the presence of silica nanoparticles, the silica aerosol is decorated by gold through either homogeneous gold nucleation and subsequent scavenging by the silica nanoparticles, or by heterogeneous nucleation on the silica surface in which the gold "balls up" due to the high surface tension of gold on silica. In both cases the resulting particles exhibit a plasmon absorbance resonance typical of gold nanoparticles ($\lambda \sim 550$ nm). Finally, the silica coating and gold decoration processes are combined with a thermal plasma technique for synthesizing iron-oxide to produce tri-layer nanoparticles.

TABLE OF CONTENTS

LIST OF TABLES

LIST OF FIGURES

NOMENCLATURE

Chapter 1

C – slip correction factor

d_p – particle diameter

e – elementary charge

Kn – Knudsen number

N – particle number concentration

q_c – clean air flow rate

V – voltage

Z_p – particle electric mobility

γ – number of elementary charges

Λ – DMA length parameter

λ – mean free path

μ – dynamic viscosity

Chapter 2

P_{sys} – system pressure

P_{vap} – vapor pressure

N – particle number concentration

N_∞ – total particle concentration

n_1 – concentration of individual primary particles

Q_c – carrier gas flow rate

Q_p – precursor volumetric flow rate

T – temperature

t – time

β – collision frequency function

κ_B – Boltzmann's constant

μ – dynamic viscosity

ρ – density

Chapter 3

A – Arrhenius pre-exponential factor

A – cross sectional area

A_s – surface area

a – sticking coefficient pre-exponential factor

a_i – internal surface area

b – sticking coefficient temperature exponent

c – sticking coefficient activation energy

d – collision cross section

d_p – particle diameter

E_i – Arrhenius activation energy

$h\upsilon$ – photon flux

i – reaction index

j – particle size class

k – species index

K_g – number of gas-phase species

K_{ci}, K_{pi} – equilibrium constant

k_f – forward reaction constant

k_r – reverse reaction constant

M_r – moment of size distribution

m – reduced mass

N – molecular concentration

N_{Avog} – Avogadro's number

P_{atm} – atmospheric pressure

q – rate of progress

$\dot{Q}_D$ – molecular destruction rate

R – universal gas constant

r – rate of deposition

S_r – size moment production term

$\dot{s}$ – molar production rate

T – temperature

u – axial velocity

v – stoichiometric coefficient

W – molecular weight

$[X]$ – molar concentration

Y – mass fraction

β – Arrhenius temperature exponent

β – collision frequency function

Γ – density of surface sites

γ – sticking coefficient

ΔS_i° – change in entropy

ΔH_i° – change in enthalpy

κ_B – Boltzmann constant

Θ – site fraction of surface species

$\dot{\omega}$ – production rate

ρ – density

ς – number of surface sites occupied

ϕ – reaction probability

χ – gas species

χ_{ps} – particle surface species

Chapter 4

D – diameter

d_p – particle diameter

e – elementary charge

Gr – Grashof number

g_i – electronic partition functions of ions

g_a – electronic partition function of atoms

g – gravitational acceleration

J – electron flux

L –length

N – particle number concentration

n_+ – fraction of ions

n_o – fraction of atoms

R – wire radius

Ra – Rayleigh number

T – temperature

U_i – ionization energy of atoms

U – bulk fluid velocity

α – ratio of ions to atoms

α – thermal diffusivity

β – thermal expansion coefficient

κ_B – Boltzmann constant

μ – dynamic viscosity

υ – kinematic viscosity

ρ – density

σ_g – geometric standard deviation

Φ – work function

Chapter 5

d_p – particle diameter

N – particle number concentration

P_{vap} – vapor pressure

T – temperature

β – collision frequency function

Chapter 1 - Introduction and Motivation

1.1 INTRODUCTION

Nano-scale materials and devices exhibit unique properties not seen at larger size ranges. Investigations of semiconductor materials such as silicon and cadmium selenide have led to the discoveries of new properties, including the quantum confinement of electrons that show promise in increasing solar cell efficiencies [1-3]. Studies of magnetic iron oxide materials have shown that superparamagnetic behavior is observed for nanosized materials (dimensions <10 nm), which have broad industrial and medical applications [4]. The increased surface area of nano-scale metal catalysts, such as silver and copper, has given rise to increased chemical reaction efficiencies that are of interest in creating next generation transportation fuels [5-7]. The production of devices at the nano-scale allows for new interactions of materials with biological tissue where sizes can be tuned to affect individual biological components such as DNA [8].

For nanoparticles to be useful in applications, it is critical that the particles retain their small sizes so that their unique properties are not lost. Also, many applications require that particles be functionalized to impart desired properties or control particle organization. Prevention of particle growth and particle functionalization can be accomplished by modifying the particle surfaces to impart a desired behavior. Surface modification of nanoparticles is critical in controlling many aspects of nanoparticle behavior because interactions of nanoparticles are often dominated by their surface properties due to their high surface area to volume ratio.

As investigators have recognized that particle surface modification is critical to the viability of nanoparticles, many have attempted to modify particle surfaces by coating nanoparticles to create core-shell structures. Most initial studies used wet-

chemistry methods to create particle surface coatings [9-12]. These investigations have shown that particle coatings can enhance the functionality of the nanoparticles. However for large scale production, wet-chemistry methods are undesirable because they are inherently batch processes that require the use and disposal of environmentally hazardous solvents. Nevertheless, wet-chemistry methods provide useful insight into the basic nature of core-shell nanostructures.

Gas-phase methods have also been used to create particle coatings. These production techniques have benefits over wet-chemistry methods for large scale particle production because they are continuous processes that do not require solvents. Several groups have investigated a variety of particle coating processes using heated flow tubes [13-19], flame synthesis [20, 21], spray pyrolysis [22], microwave plasma [23], and RF plasma [24, 25]. All of these methods create multi-layered aerosolized particles with relatively short production times without the use of solvents. While these methods allow for a higher throughput, they often have broader size distributions than wet-chemistry based methods [8].

Recent work by Zhang *et al.* and He *et al.* demonstrated another gas-phase method for creating multi-layered nanoparticles using photoinduced chemical vapor deposition (photo-CVD) to grow films on aerosolized particles [26, 27]. Their studies showed that the photo-CVD method can be used to reliably grow organic coatings on aerosolized particles of differing core sizes. The method uses vacuum ultra violet (VUV) light to radicalize an organic precursor in the presence of aerosolized particles. The activated precursor then reacts to form a CVD coating on the particle surface as the particle passes down a coating chamber. The organic particle coatings are generally uniform and can be tuned to differing thicknesses by varying key system parameters. While the photo-CVD method of coating nanoparticles has only been used to produce organic coatings of sodium chloride and aluminum particles, the method has potential for broader applications with different coating and core-particle chemistries.

While CVD methods are available to produce coatings from gas-phase precursors, not all materials have precursors with high vapor pressures that are commercially available or cost effective. In particular, precursors for precious and heavy metals are expensive and often hazardous [28]. As a result, other delivery methods have been proposed to produce gas-phase coatings and surface decoration from such materials. Nanoparticle surface decoration with gold and silver has been accomplished at low pressures ($\sim 10^{-3}$ Torr) by sputtering gold and silver targets in the presence of gas-phase particles [29]. The resulting particles have precious metals delivered to the surface primarily through agglomeration, which results in uneven coatings. Additional methods have been developed that rely on diffusion of materials within individual particles to self segregate and create composite structures [30]. While these methods have demonstrated the feasibility of creating surface decoration with precious metals, further work is warranted to develop methods that allow for the control of particle surface morphology.

1.2 MOTIVATION

As the ability to control the surface properties of nanoparticles has improved, researchers have begun to consider applications for engineered multi-functional particles. An area of particular interest for multi-component nanoparticles is their use for the imaging and treatment of cancerous tumors [31]. Magnetic nanoparticles, in particular magnetic iron oxide, can provide magnetic resonance imaging (MRI) contrast enhancement within cancerous cells and, if loaded in high enough concentrations, can be used to thermally ablate tumors due to the generation of heat through Brownian and Néel relaxation in an alternating magnetic field [4, 32]. Gold particles are effective delivery vehicles for tumor necrosis factor [33] as well as the labeling of cells [34]. Nanoparticles composed of hollow gold shells or thin layers of gold on the surfaces of electrically insulating cores, such as silica, can be tuned to absorb radiation from the visible to infrared

wavelengths [35-37]. A review of multifunctional particles composed of gold and iron oxide by Melancon *et al.* [38] discusses the current structures that have been synthesized (all wet-chemistry methods) as well as some of the barriers for use.

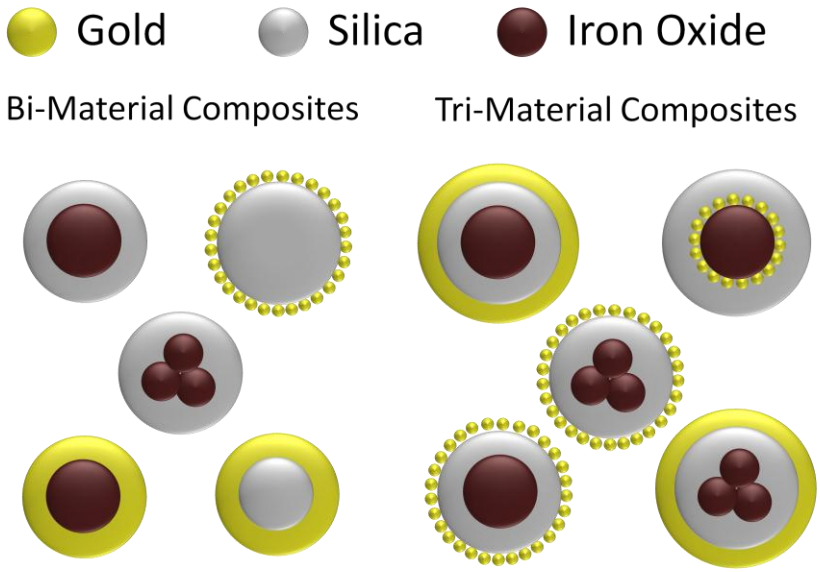

Figure 1.1: Idealized schematic of multifunctional nanoparticle composites for biological applications.

While many geometries and structures have been synthesized by wet-chemistry techniques, the advantages of gas-phase synthesis approaches warrant the exploration of aerosol methods to produce multi-component nanostructures. As shown in Figure 1.1, a variety of morphologies can be envisioned from combinations of iron oxide, silica and gold. The ultimate structure of the particles relies on the core-particle size and agglomeration rate, as well as the gas-phase delivery of material to the particle surface. In particular, coating morphology depends on whether coating materials are nucleated in the gas phase and then scavenged by the core particle, or grown on the surface as a result of physical or chemical vapor deposition.

The purpose of the present study is to investigate methods for the production of multi-layer composite nanoparticles, consisting primarily of iron

oxide, silica and gold. To produce composite nanoparticles, the study focuses on the development of decoupled gas-phase synthesis and coating approaches that can be connected to produce a variety of nanoparticle structures, as envisioned in Figure 1.1. One advantage of individual synthesis and coating modules is that new modules can be combined with existing ones to create different core-shell structures. This "assembly-line" approach to particle synthesis builds the nanoparticles from the core outward and does not rely on the thermodynamic properties of the materials to determine where each material is located within the particle. This study sets out to develop separate methods for producing core-shell structures with an ultimate aim of combining the systems to produce bi- and tri-layer nanoparticles. While iron oxide, silica and gold are the primary three materials of interest, other materials, such as silver and yttrium aluminum oxides, are used within the study to investigate the fundamental mechanisms of the individual coating processes. The central motivation for the study is to produce core-shell nanoparticles for biological applications as discussed above, but the production methods are general and other applications are discussed within each chapter. As the coating modules in this study vary from photo-CVD to thermal techniques, further background and motivation for the individual synthesis approaches are given.

1.3 Characterization Techniques

1.3.1 Tandem Differential Mobility Analyzer

The primary characterization device for the gas-phase coating processes discussed in this study is the tandem differential mobility analyzer (TDMA). The differential mobility analyzer (DMA) has long been studied as a method for characterization of aerosols [39-43]. DMAs classify particles by electrically attracting charged particles across a clean sheath flow in accordance with their

electric mobility, Z_p. The electric mobility is defined as the ratio of drift velocity to the magnitude of the applied electric field,

$$Z_p = \frac{\gamma e C}{3\pi\mu d_p}, \tag{1.1}$$

where γ is the number of elementary charges on the particle, d_p is the particle diameter, and μ is the fluid viscosity. The slip correction factor, C, determined by Allen and Raabe is given by the relation,

$$C = 1.0 + Kn(1.155 + 0.471\exp[-0.596/Kn]), \tag{1.2}$$

where the Knudsen number is $Kn = 2\lambda / d_p$ and λ is the mean free path of the gas [44]. Figure 1.2 shows a schematic of the DMA used in this study (TSI, Inc. model 3085). The charged particles entering the DMA must pass across the sheath flow to reach the monodisperse aerosol outlet. As shown by Knutson and Whitby, the particles pass both electrical and flow streamlines as they move down the tube where "the ratio of the number of streamlines crossed to the number of electric field lines crossed is always equal to the particle electric mobility" [40]. Their analysis derived the voltage required to attract particles of a given mobility,

$$V = \frac{q_c}{2\pi\Lambda Z_p}, \tag{1.3}$$

where q_c is the clean air flow rate, $\Lambda = L/\ln(b/a)$ and the dimensions L, b and a are shown in Figure 1.2.

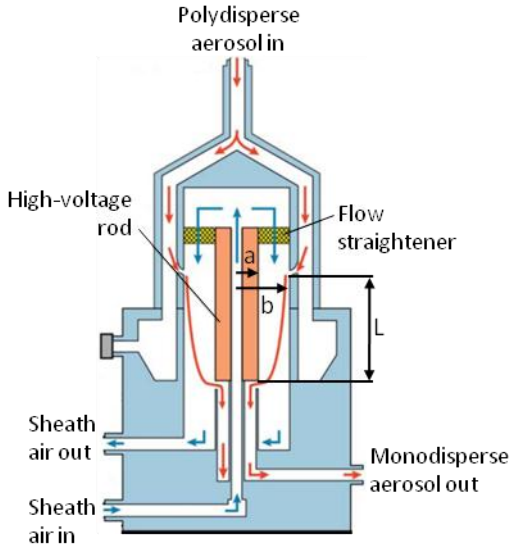

Figure 1.2: Schematic of TSI Model 3085 Nano DMA [45].

Results from Knutson and Whitby's single-DMA analysis are useful in determining the behavior of TDMAs. Kousaka *et al.* investigated two DMAs placed in series where the outlet of the first DMA was the inlet to the next. The first DMA was set to a constant voltage to select a discrete range of mobilities. The second DMA was used in conjunction with a condensation particle counter (CPC) to scan over a range of voltages in discrete increments to determine the particle mobility distribution. The results of the TDMA study showed that the concentration of the aerosol leaving the second DMA was exactly one third that of the concentration entering the first DMA when losses from Brownian diffusion were neglected [46]. More relevant to the present study is the classification of an aerosol that undergoes a size change between the two DMAs, which was first investigated by Rader and McMurry in 1986 [47]. Their study developed an analytical framework for determining the particle growth within a TDMA and proved experimentally that the method provides a reliable means for measuring changes in particle size down to 1% of the particle diameter.

In this study, both DMAs are operated with a 10:1 sheath to aerosol flow ratio. The voltage of the DMA-1 is held constant and the voltage of DMA-2 is scanned in discrete increments over a range of voltages. The concentration of the aerosol at the exit of DMA-2 is measured using an ultrafine condensation particle counter (UCPC, TSI, Inc. Model 3025A). In some cases a single DMA is used in series with a UCPC to scan over a range of particle mobilities in discrete increments, which is known as a discrete mobility particle sizer (DMPS). Both DMAs and the UCPC interface with a LabView (National Instruments) data acquisition board and are controlled by a personal computer.

The resulting particle counts, as measured by the UCPC, are corrected for particles losses to the tube walls, particle losses within the UCPC and the size dependent counting efficiency of the UCPC within the LabView software. The results of the LabView analysis give particle counts versus particle mobility for a given measurement. These results are comparable to a histogram in which the widths of the bins correspond to the DMA transfer function at each mobility. In order to determine the particle mobility distribution in terms of the number concentration of particles, N, the particle count data must be divided by the area of the transfer function at each mobility diameter. Further details for the conversion of raw counts to particle size distribution functions can be found in these references [39, 40]. In addition to correcting for the transfer function of the DMA, particles counts were also corrected for the charging efficiency of the Po-210 bipolar charger that was used to charge the aerosol [48]. Differences between distributions showing the raw particle counts corrected only for UCPC counting efficiency and wall losses, and the fully corrected particle mobility distribution are shown in Figure 1.3. The modes of the corrected particle mobility distributions shown in Figure 1.3b are lower than the modes of the raw count data, Figure 1.3a. This result highlights the effect of dividing by the charging efficiency and area of the transfer function, both of which are smaller (in terms of numerical magnitude) for smaller particles than for larger

particles. Additionally, Figure 1.3 highlights the need for correcting raw count data from the UCPC. All DMPS particle distribution data within this study were corrected during post processing. An implicit assumption for the conversion of DMPS data to a particle mobility distribution is that the particle concentration is constant across the width of the transfer function, which is typically valid for polydisperse aerosols. For TDMA data, the monodisperse nature of the aerosol means that strong concentration gradients can exist within the width of the transfer function, making the assumption invalid. Therefore the transformation from TDMA raw counts to a particle size distribution requires a more detailed conversion function not used within this study [49]. However as the TDMA data is primarily used to express differences in particle growth, the error of not correcting for the TDMA transfer function is minimal.

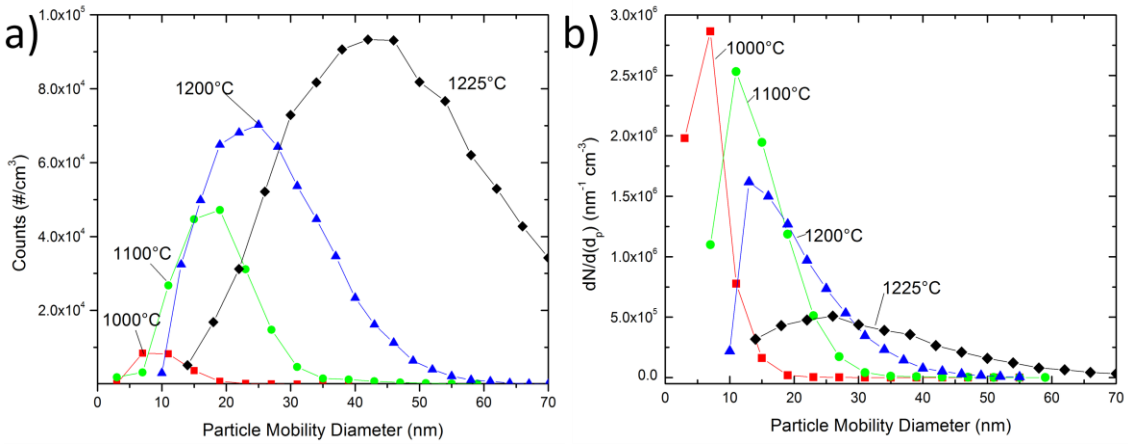

Figure 1.3: (a) DMPS measured counts corrected only for particle loss and UCPC counting efficiency and (b) particle mobility distribution determined by correcting for charging efficiency and by dividing by the transfer function of the DMA.

1.3.2 Chemical Characterization

The chemical composition of the nanoparticles and subsequent coatings is determined by Fourier transform infrared spectroscopy (FTIR). FTIR spectra from the Nicolet Series II Magna-IR System 750 provide information on the chemical bonds of the samples by passing infrared light with wave lengths from 2.5-20 μm

through the samples. Samples can either be analyzed in-situ by placing a mesh within the analysis cell of the FTIR and passing the aerosol flow through the mesh, or ex-situ by collecting samples and then analyzing them using diffuse reflectance infrared Fourier transform spectroscopy (DRIFTS). In either technique the samples absorb the infrared light by converting the photon energy to vibrational energy between covalently bound atoms. Since bonds vibrate only in discrete frequencies, specific wavelengths of light are absorbed that correspond to the natural frequencies of the bond. The FTIR instrument allows for a specimen's spectrum to be found by comparing the baseline transmitted light to the light transmitted through a specimen where specific wavelengths of light have been absorbed. The specimen's spectrum can then be compared to other pure specimens on record to determine which bonds are present.

1.3.3 PHYSICAL CHARACTERIZATION

For physical characterization and visualization of nanoparticle coatings, a transmission electron microscope (TEM) is used to provide high magnification images for particle analysis. The Tecnai T12 microscope used in this study has an operating voltage of 120kV with a LaB_6 filament as an electron source. The Tecnai T12 microscope allows for typical magnifications of 100-200 thousand times the original sample size. With such magnifications it is possible to resolve key features of the collected nanoparticles, including particle size, degree of agglomeration, coating thickness and morphology. Also, by using the diffraction mode of the T12, the crystalline nature of the particle and particle coating can be resolved.

Higher resolutions can be achieved with the Tecnai G^2 F30 microscope which provides imaging, diffraction and analytical techniques at high spatial resolution and detection efficiency. The F30 microscope allows for magnification in excess of 1 million times the original sample size. The electron emission source for the Tecnai G^2 F30 is a Shottky field emission gun with an operating voltage of the up to 300 kV.

The Tecnai G^2 F30 is also equipped with a silicon x-ray detector which detects photons released from the de-excitation of high-energy electrons in the sample that were initially excited by interaction with the TEM's electron beam. This technique, known as energy dispersive x-ray spectrometry (EDX), provides quantitative analysis of elements with atomic numbers from 5-92. Another technique available on the Tecnai G^2 F30 is electron energy loss spectroscopy (EELS), which like EDX gives information on the elemental makeup of the sample. EELS analysis determines the amount of the electron beam energy absorbed by the sample, which is unique for each element and is best used for lower atomic number samples (5-30). EELS provides higher resolution and is a faster sampling technique than EDX, but requires thinner samples and does not work on high atomic number elements [50].

While those characterization techniques discussed above are the primary ones used in this study, other characterization methods are discussed in detail within the individual chapters.

Chapter 2 - Photoinduced Chemical Vapor Deposition Particle Coating

2.1 Overview

As discussed in Chapter 1, nano-sized core-shell structures are of interest for a variety of applications. This study builds on the work of Zhang *et al.* and He *et al.* [26, 27] to produce inorganic films on nanoparticle surfaces. Like the organic coating process, a gaseous precursor is injected into a coating chamber where vacuum ultraviolet light (VUV) activates the precursor in the presence of aerosolized particles. The activated precursor then reacts to form a CVD coating on the particle surfaces as the particles pass down the coating chamber. The particle coatings are tested for chemical purity and coating morphology. The photo-CVD method of coating nanoparticles is investigated to determine whether it can be used for broadly to coat a variety of core materials.

Macroscopic photo-CVD film growth has received much study and is currently used to create many different thin films. An initial report by Kogelschatz *et al.* studied the theory of excimer discharge lamps and demonstrated the ability of the lamps to produce monochromatic VUV radiation capable of material processing [51]. Xenon excimer lamps were first used to create silica (SiO_2) coatings from silane (SiH_4) and nitrous oxide (N_2O) [52, 53]. Bergonzo *et al.* have shown that excimer lamps can be used to produce chemically pure coatings with fast film growth rates [52]. In an effort to simplify the number of precursors and limit use of the highly combustible silane, Takezoe *et al.* created silica films from a single precursor, tetraethyl orthosilicate, (TEOS $Si(OC_2H_5)_4$) [54]. Their group showed that VUV light is capable of creating silica films at room temperature[55]. Continued work has examined the properties of the silica films from the photo-CVD process including photoluminescence, electrical leakage, and smoothness [54, 56, 57].

The favorable characteristics of bulk silica make it a desirable coating material for particles at the nanometer scale. Silica coatings on nanoparticles have been shown to stabilize particles and prevent agglomeration in solution even at relatively high particle concentrations [58]. The high melting point of silica increases the thermal stability of coated particles and can prevent coated particles from sintering [59]. Also silica coatings can be used to stabilize particle photoluminescence with little shift in the excitation band of the coated particle [58, 60]. The silanol groups found at the surface of silica coatings also allow for the easy attachment of functionalizing ligands that are useful for a variety of biological applications [4, 61]. Silica acts as an effective electrical insulator which is of interest in creating multilayered films and nanoparticles that can be used in the semiconductor industry [56, 62]. Furthermore, silica is a cheap and abundant molecule that can be used to coat many particles at low cost [58].

In this chapter work is presented on the production of silica coatings on a variety of core particles. Initial studies are discussed that sought to determine an appropriate particle core to be used in the study of the photo-CVD coating process. Sodium chloride (NaCl), polystyrene latex (PSL), yttrium aluminum oxide perovskite (YAP) and silver (Ag) were all tested to determine whether they would be suitable core structures for silica coating. The yttrium aluminum oxide particles were of interest beyond fundamental studies as applications exist for yttrium aluminum oxides that photoluminesce, notably the cerium-doped yttrium aluminum oxide garnet (YAG) [63, 64]. Likewise, silica coated silver has potential applications for bacterial disinfection [65], labeling via plasmon resonance [66] and enhancement of Raman spectroscopy [67]. Further applications of the photo-CVD silica coating process were studied in the production of silica-coated magnetic iron oxide nanoparticles for applications such as enhanced magnetic resonance imaging [4] and thermal therapies [68]. The primary focus of this chapter is to investigate the key variables that control coating thickness and chemistry of films on the surface of

nanoparticles, as well as study the fundamental mechanisms involved in photo-CVD coating.

2.1.1 Photochemical Vapor Deposition Experimental Setup

A schematic of the typical configuration of the photo-CVD system is shown in Figure 2.1. The system consists of an aerosol source, precursor bubbler, coating chamber, and VUV excimer lamp. A pair of differential mobility analyzers (DMAs) and a condensation particle counter (CPC) are used for real time characterization. In combination the DMA and CPC are known as a discrete mobility particle sizer (DMPS). As shown, a polydisperse aerosol is introduced (1 slm) into DMA-1 where particles are size selected according to their electrical mobility. Concurrently, nitrogen gas is bubbled (0.03-1.1 slm) through a coating precursor, TEOS, where the precursor vapor is incorporated into the nitrogen flow stream. Assuming the exiting nitrogen/precursor mixture is at steady state, the flow rate of the precursor is determined according to the relation,

$$Q_p = Q_c \left(\frac{P_{vap}}{P_{sys} - P_{vap}} \right), \tag{2.1}$$

where P_{vap} and P_{sys} are the precursor vapor pressure and system pressure and Q_p and Q_c are the volumetric flow rates of the precursor and the carrier nitrogen. The vapor pressure of TEOS can be found using the Antoine equation,

$$\log_{10} P_{vap} = A - \left(\frac{B}{T + C} \right), \tag{2.2}$$

where P_{vap} is the vapor pressure in bar; T is the temperature in Kelvin; and A, B, and C are constants with the values 4.17, 1561.28, and -67.57 respectively [69].

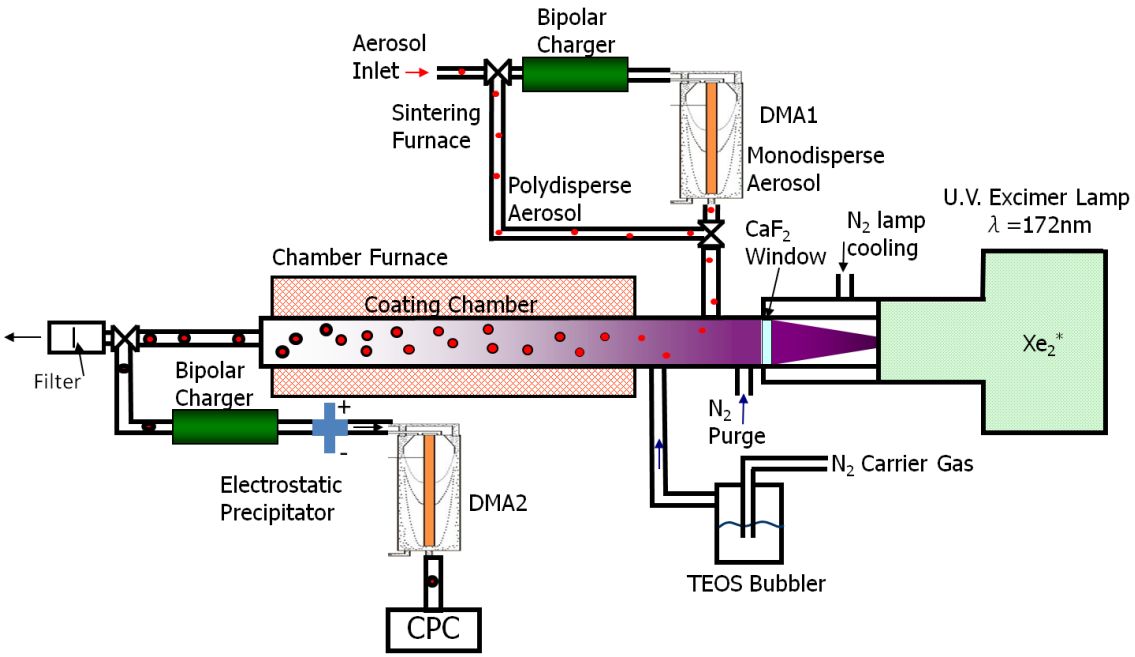

Figure 2.1: Schematic of photo-CVD coating reactor.

As the aerosol and precursor enter the chamber, they mix and are exposed to 172-nm radiation from a Xe* excimer source (USHIO model UER20H-172). The energy of the VUV photons, 7.2 eV, is greater than the binding energies of the C-O (3.8 eV) and C-H (4.2 eV) bonds within the precursor. When exposed to radiation, the precursor partially dissociates and then reacts on the particle surface, creating a CVD coating as particles flow down the chamber. The residence time of the aerosol-precursor mixture in the reaction chamber is primarily controlled by the flow of "purge" nitrogen (3-9 slm) introduced to the system in order to keep the VUV window clear of particles and to control the flow within the chamber. The coating chamber is encased in a tube furnace (Lindberg/Blue STF553463) that allows for temperature control of the chamber from ambient room temperature to 1100˚C. As the coated particles exit the photo-CVD chamber, they are either collected or characterized using tandem differential mobility analysis (TDMA), whereby the second DMA scans a range of particle mobilities and the CPC (TSI model 3025A)

counts the number of particles at each size. Particles are collected for characterization via impaction onto gold coated silicon wafers [70] and onto microscopy grids via electrostatic precipitation (at +3kV). An image of the entire experimental setup is shown in Figure 2.2. As seen, all tubing through which the aerosol passes is conductive, thus lowering the losses due to charge buildup on the tube walls.

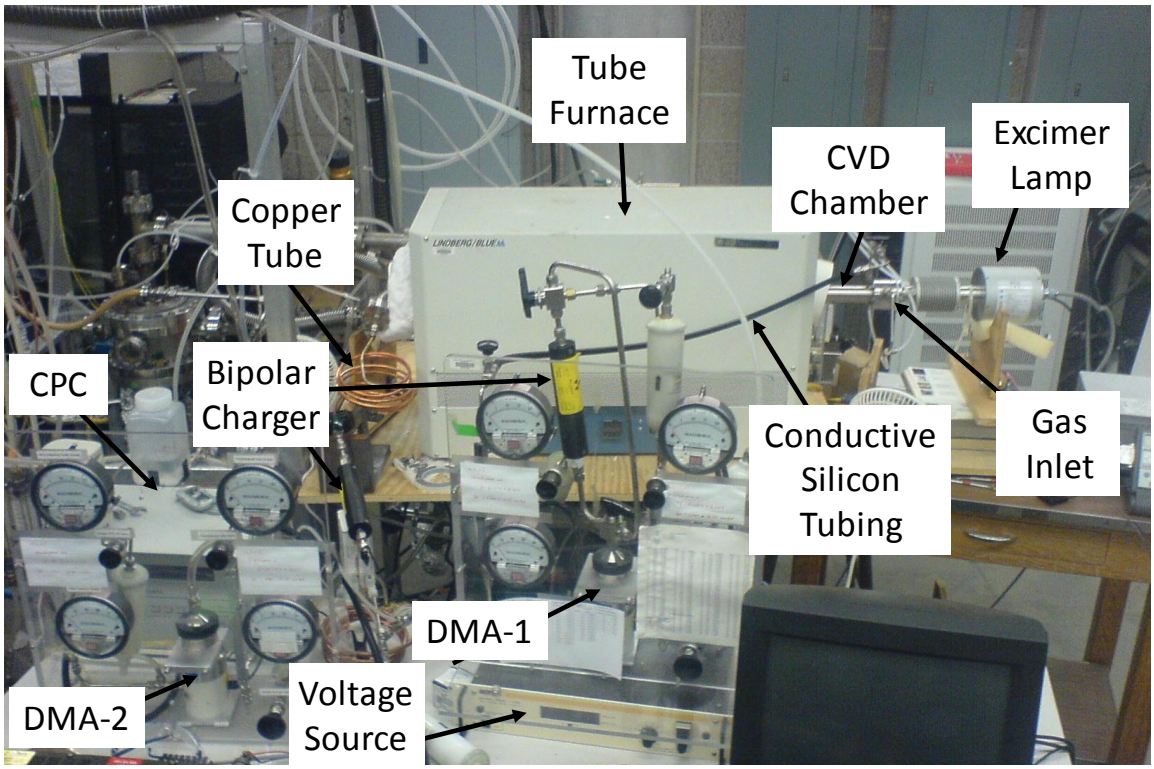

Figure 2.2: Photograph of photo-CVD experimental setup.

Throughout the experimental studies of the photo-CVD system, the radiation transmission through the window was tracked to ensure that the VUV intensity remained constant. Radiation transmission through the windows can be affected by particle fouling and light-induced degradation of the window after repeated use. As shown in Figure 2.3, a reduction in visible transmittance of the VUV window can be seen by inspection of the window. Radiation intensity measurements with each of

these windows showed that the transmitted intensities of 172-nm light through the silica (Figure 2.3b) and fouled calcium fluoride (Figure 2.3c) windows were 33% and 40%, respectively, of the intensity through a clean calcium fluoride window (Figure 2.3a). These results highlight the need to test the window transmission regularly, which was done for all studies. In most cases it was found that purge flow rates greater than 3 slm suppressed fouling of the windows with particles. After repeated testing, it became apparent that calcium fluoride windows resisted VUV induced degradation better than silica windows and were thus used for the majority of the studies within this chapter. All calcium fluoride windows had a 38-mm diameter and a 5-mm thickness, supplied by Koch Crystal Finishing, Inc. (Elyria, OH).

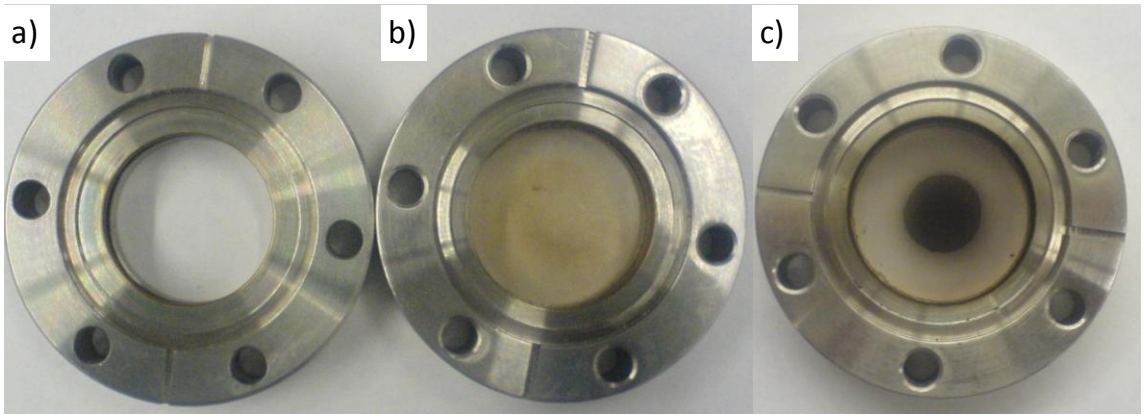

Figure 2.3: Images of different vacuum ultraviolet windows, consisting of (a) newly-installed calcium fluoride window, (b) silica window with VUV induced degradation, and (c) calcium fluoride window after significant particle deposition.

2.1.2 Particle Synthesis

Three methods were used to generate aerosols for the coating study, as shown in Figure 2.4. Nebulization, Figure 2.4a, aerosolizes particles suspended in a liquid by expanding a pressurized gas through an orifice to create a high-velocity, low-pressure region at the top of a capillary tube. The capillary tube draws the solution contained in the nebulizer up into the high-velocity flow which shears off

the liquid to create aerosolized droplets of the solution. Larger droplets are removed from the flow stream by means of impaction, leaving only droplets smaller than several microns in diameter in the aerosol. The aerosol is then passed through a desiccant dryer that removes the solvent from the droplets, leaving only the solid particles. Further details on nebulizers can be found in the following references [71, 72]

Inert-gas condensation, Figure 2.4b, forms nanoparticles by a process originally described by Scheibel and Porstendörfer, in which a solid precursor, *e.g.* silver, is melted in the presence of an inert carrier gas. The elevated temperature raises the vapor pressure of the precursor allowing it to evaporate into the carrier gas. As the flow passes out of the furnace, the temperature decreases, thus supersaturating the vapor and causing homogeneous particle nucleation. The particle nucleation results in a burst of a high concentration of small particles that quickly agglomerate to form clusters. The clusters are then prevented from further agglomeration by diluting the aerosol with additional nitrogen. The agglomerates are sintered as they pass through a second heated region, which encourages solid-state diffusion. A further discussion of inert-gas condensation is found in Section 2.5.

The third method of aerosol generation synthesizes particles by passing a liquid or gaseous precursor through a thermal plasma, Figure 2.4c. The elevated temperature of the plasma disassociates the precursor into its elemental components. As the monatomic vapors pass out of the plasma, they rapidly cool, which causes a supersaturation of the vapors and results in homogeneous nucleation of particles. A further discussion of plasma synthesis as it relates to the production of magnetic iron oxide nanoparticles is found in Section 2.6.

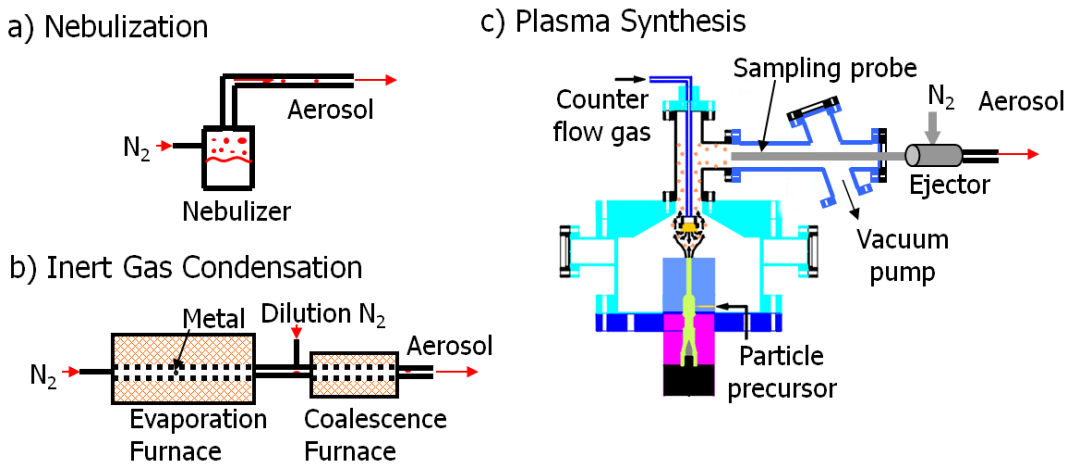

Figure 2.4: Nanoparticle generation mechanisms: (a) nebulization, (b) inert-gas condensation, and (c) plasma synthesis.

2.2 TEOS CHARACTERIZATION

In order for TEOS to be an effective precursor for silica coating of nanoparticles it must not homogeneously nucleate when exposed to VUV radiation. To determine the range of TEOS concentrations that does not result in homogeneous nucleation, TEOS was injected into the coating chamber along with VUV radiation and a nitrogen purge flow rate of 7.2 slm. The results, as shown in Figure 2.5 where N is the particle concentration (cm^{-3}) and d_p is the particle diameter (nm), indicate that no homogenous nucleation occurs at flow rates up to 1.8 sccm of TEOS. For lower nitrogen purge flow rates the likelihood of TEOS homogeneous nucleation increases due to higher residences times and TEOS concentration. When the nitrogen purge flow was 4.3 slm, nucleation began as low as 1 sccm of TEOS. TEOS homogeneous nucleation is further encouraged by the presence of oxygen in the system. Experiments using small flow rates of dry filtered air caused an increase in homogeneously nucleated TEOS particles, which were likely a result of oxygen participating in the photo-CVD reactions.

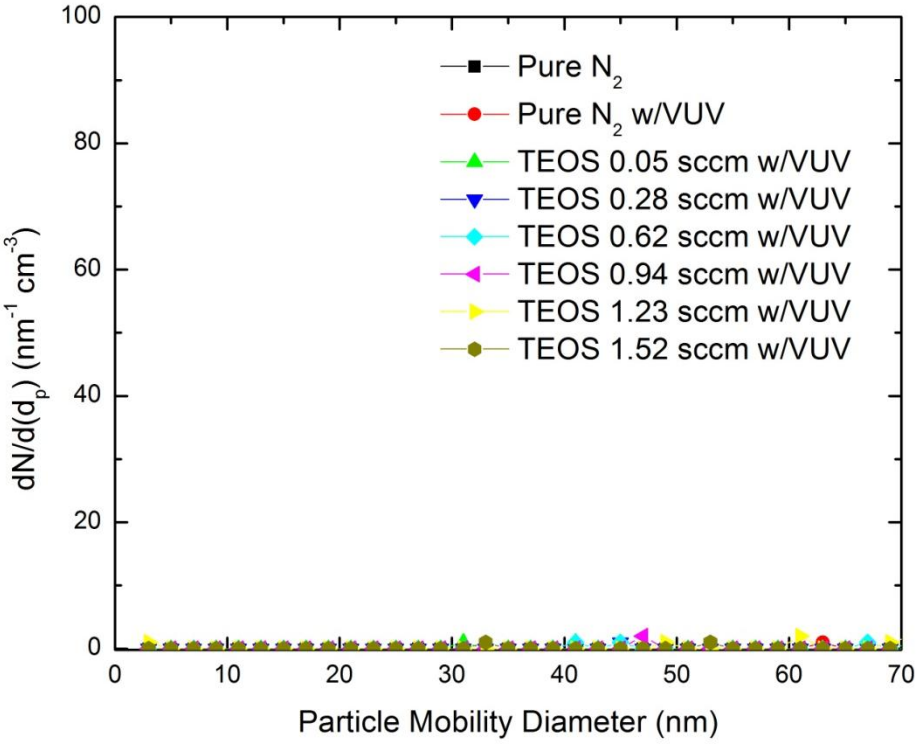

Figure 2.5: Particle size distribution of homogeneously nucleated TEOS particles with 7.2 slm nitrogen flow and varying flow rates of TEOS in the presence of VUV radiation.

To determine the chemical composition of the coatings formed from TEOS in the photo-initiated CVD process, a series of films were collected in the chamber on macroscopic substrates. Films were collected at four locations down the chamber on 80×80 stainless steel mesh per inch as shown in Figure 2.6a. Each mesh was immediately followed by a flow constrictor that forced the flow of TEOS through the mesh to a 0.5" diameter through the center of the mesh, concentrating the film on that region of the screen. The coatings were grown for 30 minutes with the lamp on and gas flow rates of 0.9 sccm and 7.2 slm for TEOS and nitrogen, respectively. FTIR analysis of the films, shown in Figure 2.6b, indicated that the films consisted largely of silica with few hydrocarbon contaminants. The signal intensity of the silica can be taken as an indication of the relative film thickness as films were grown on all

meshes for the same time and TEOS flow rates, and there are no significant peaks other than silica. The silica peak at 1100 cm^{-1} is relatively low at Position I, indicating that the TEOS vapor is not immediately activated by the VUV radiation and requires some time for exposure to create a thicker coating. The silica signal intensity continues to increase at Position II and is a maximum at Position III. The film collected out of view of the lamp, Position IV, had a much smaller signal than those collected upstream. The diminished response of Position IV may be an indication that the presence of radiation at the coating surface enhances the film deposition rate. However, because Position IV was the farthest downstream of the samples it is possible that a majority of the silica vapor may have condensed on the tube walls before reaching the sample.

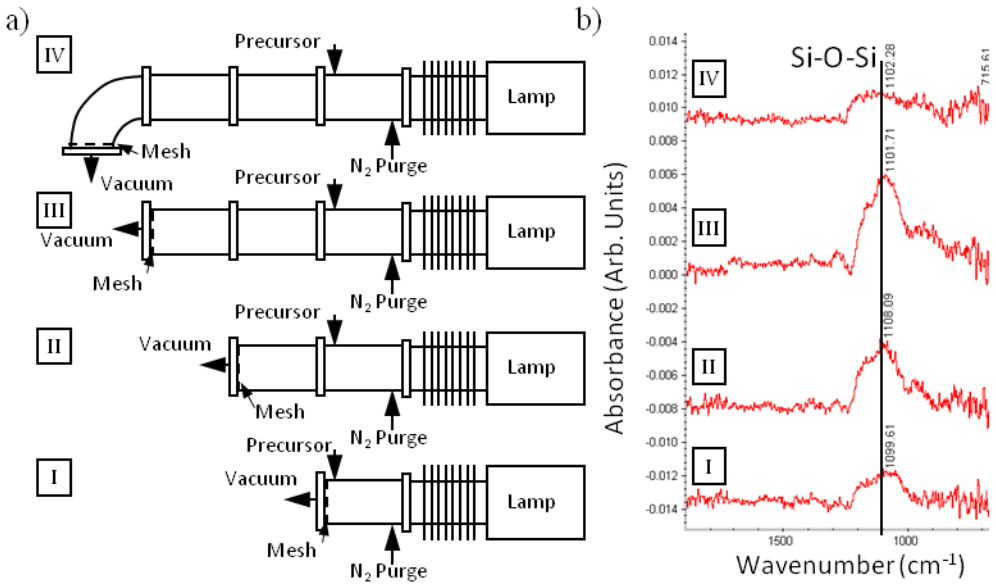

Figure 2.6: (a) Schematic of chamber configurations for film depositions. (b) FTIR absorbance spectrum of film samples collected at various locations within the chamber.

To further investigate the relationship between surface radiation and film growth, another experiment was performed that held the distance from the lamp to the mesh constant. As shown in Figure 2.7b, films were grown at equal distance

from the TEOS inlet on 80×80 stainless steel meshes. The sample collected in Configuration A was in view of the lamp and received radiation during coating while the film in Configuration B was located downstream of a 90° bend in the tube and received no radiation. FTIR spectra were taken of the two films as shown in Figure 2.7a. As with the previous result, the film grown in the presence of VUV radiation had a larger absorbance intensity for the Si-O-Si stretch than the film without radiation. While lower in intensity than the film grown in the presence of radiation, the significant absorbance of the silica film without surface radiation indicates it is possible that films can be deposited without direct photon interaction. However, as the signal intensity is nearly doubled for the film in which radiation is present at the surface, these results suggest that both interactions of radiation with the gas and at the surface are important. As no significant hydrocarbon peaks are seen in either spectrum, further study would be needed to definitively determine which film had fewer chemical impurities.

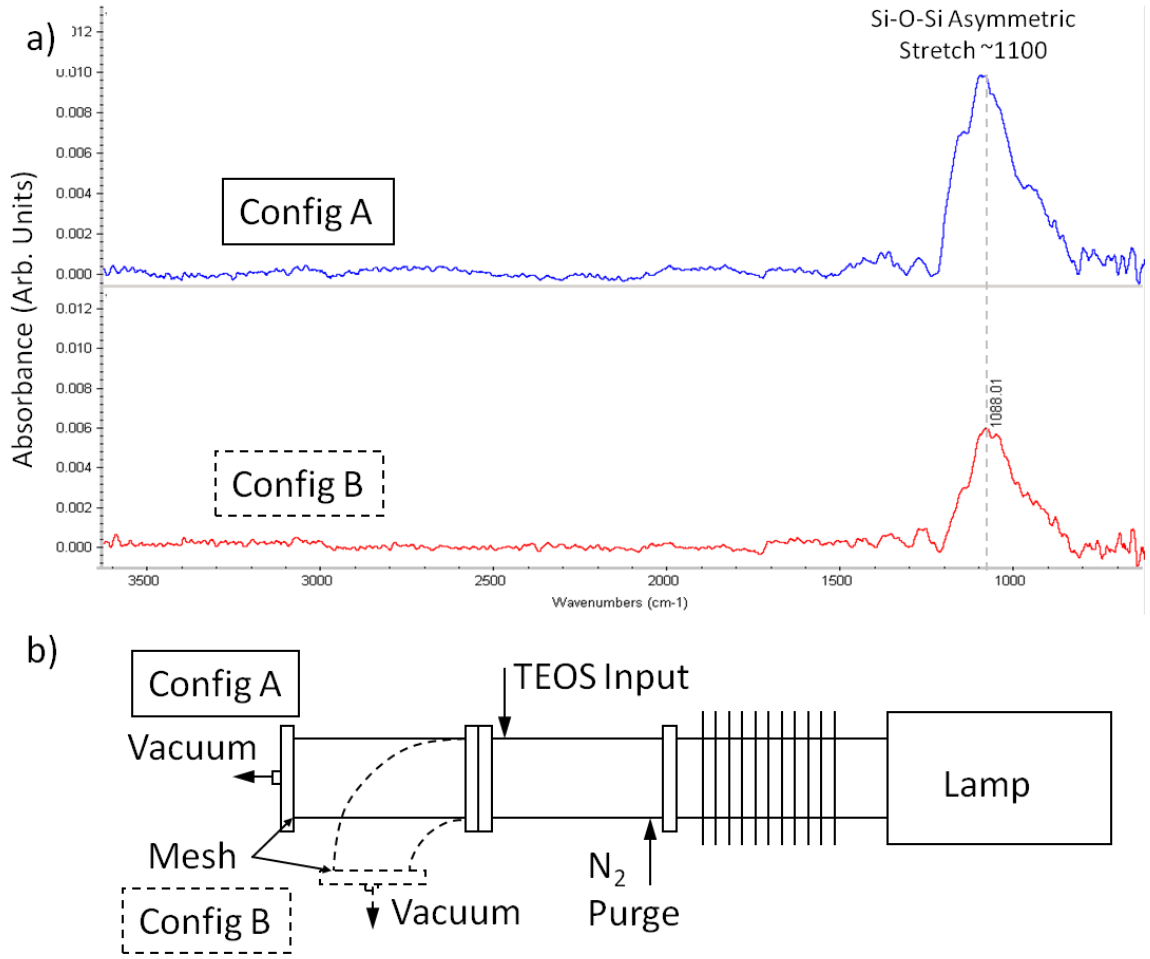

Figure 2.7: (a) FTIR absorbance spectrum of film samples collected with and without surface VUV radiation. (b) Schematic of chamber configurations for film depositions with and without surface VUV radiation.

2.3 Silica Coating of Sodium Chloride and Polystyrene Latex Particles

Initial studies of the silica CVD coating process used sodium chloride as test particles for coating study. Sodium chloride particles were chosen because they were easily aerosolized from aqueous solutions by using a nebulizer in series with a diffusion dryer. A 0.5 M sodium chloride solution was used, which was found by DMPS measurement to result in a distribution with the mode of the distribution at 50 nm. Next, to maximize the monodisperse concentration, 50-nm particles were

selected using DMA-1 and mixed with TEOS before being injected into the coating chamber. The resulting coating thickness of the particles was determined by scanning DMA-2 over a range of voltages, and thus particle mobility diameters, to determine the peak shift of the particles. As seen in Figure 2.8, a peak shift occurred when the TEOS was present and the lamp was on. For small TEOS flow rates there was little broadening of the distribution while at larger flow rates the distribution of the coated particles became broad and even unsteady for the 1.51sccm TEOS flow rate.

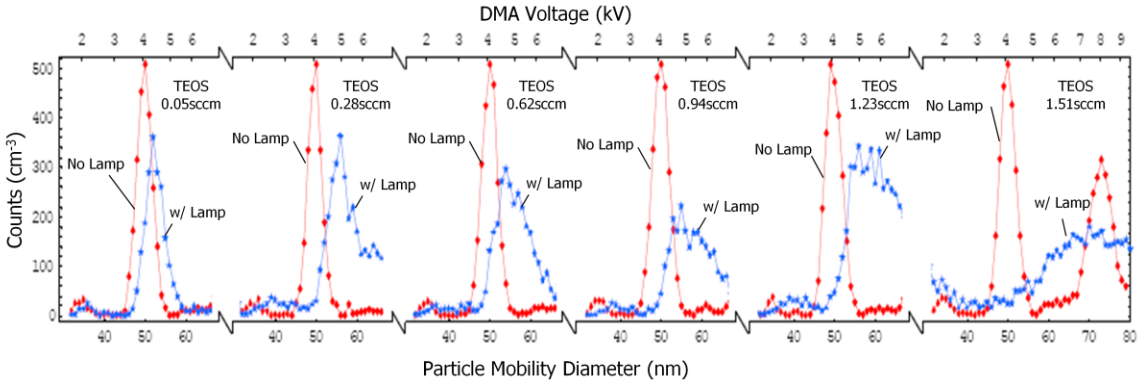

Figure 2.8: TDMA measurements of coated sodium chloride nanoparticles for varying TEOS flow rates.

A measure of average particle coating thickness was found by taking the difference in particle radius, as determined by Gaussian fits to each particle size distribution, between coated and uncoated particles. As shown in Figure 2.9, the coating thickness increased directly with TEOS flow rate from less than 1 nm to greater than 3 nm. Also, the variability of the coating thickness increased along with the TEOS flow rate where standard deviations of the Gaussian fit to the distributions went from 0.1 nm for 0.05 sccm of TEOS to 5.9 nm for the 1.23 sccm flow rate of TEOS.

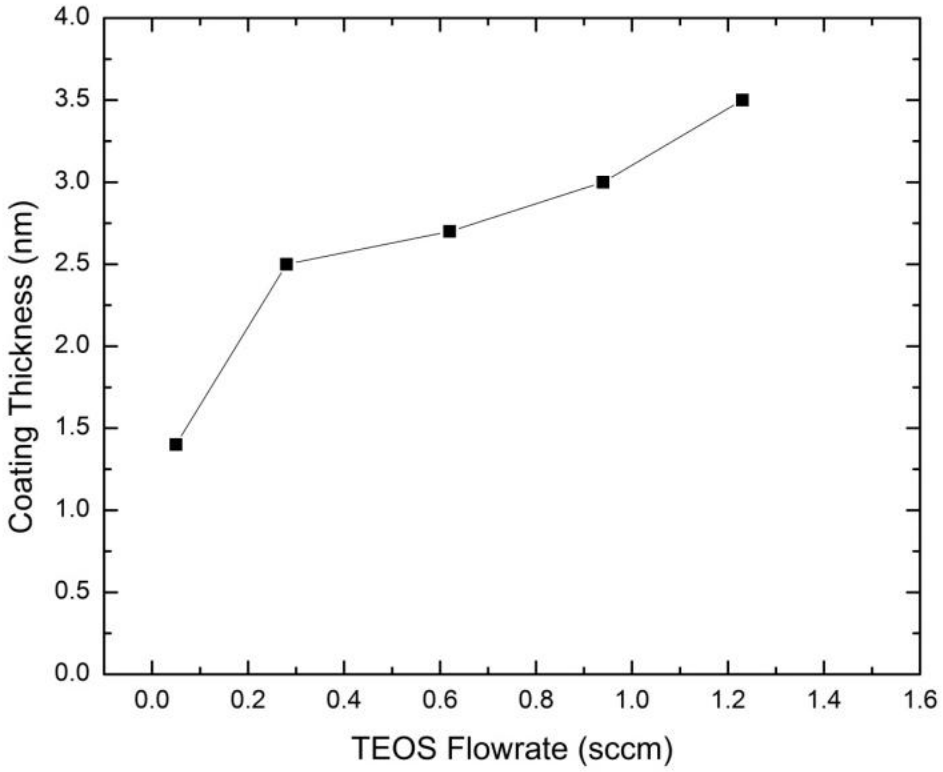

Figure 2.9: Coating thickness of sodium chloride particles for varying TEOS flow rates.

While the TDMA studies give an indication of the coating thickness, they do not give any measure of the chemical composition of the coating. In order to determine the bulk chemical structure at the surface of the particles, an FTIR analysis was performed on collections of particles both before and after coating. Each sample was collected on a 200×200 mesh placed at the exit of the chamber out of view of the lamp's radiation. The experiment was conducted with the lamp on and a nitrogen purge flow rate of 7.2 slm and TEOS flow rate of 0.62 sccm. Each sample was collected for 45 min, except for the coated sodium chloride which began to fully clog the screen after 25 min. As seen in Figure 2.10, the FTIR spectra from the sodium chloride particles with TEOS show that the characteristic Si-O-Si peaks are more significant than for the other samples. Also apparent in the sodium chloride

samples is the presence of water indicated by the O-H stretch at 3400-3500 cm^{-1}. The presence of water in the samples likely indicates that water remained after passing the nanoparticles through the diffusion dryer. The presence of hydrocarbons in the FTIR spectra (wavenumbers 1200-1600) with TEOS indicates that remnants of the hydrocarbon chains left over from the radicalized TEOS were also present in the sample. While FTIR is useful in providing information pertaining to the entire bulk sample it does not give detailed insight into chemical structures present on an individual particle surface.

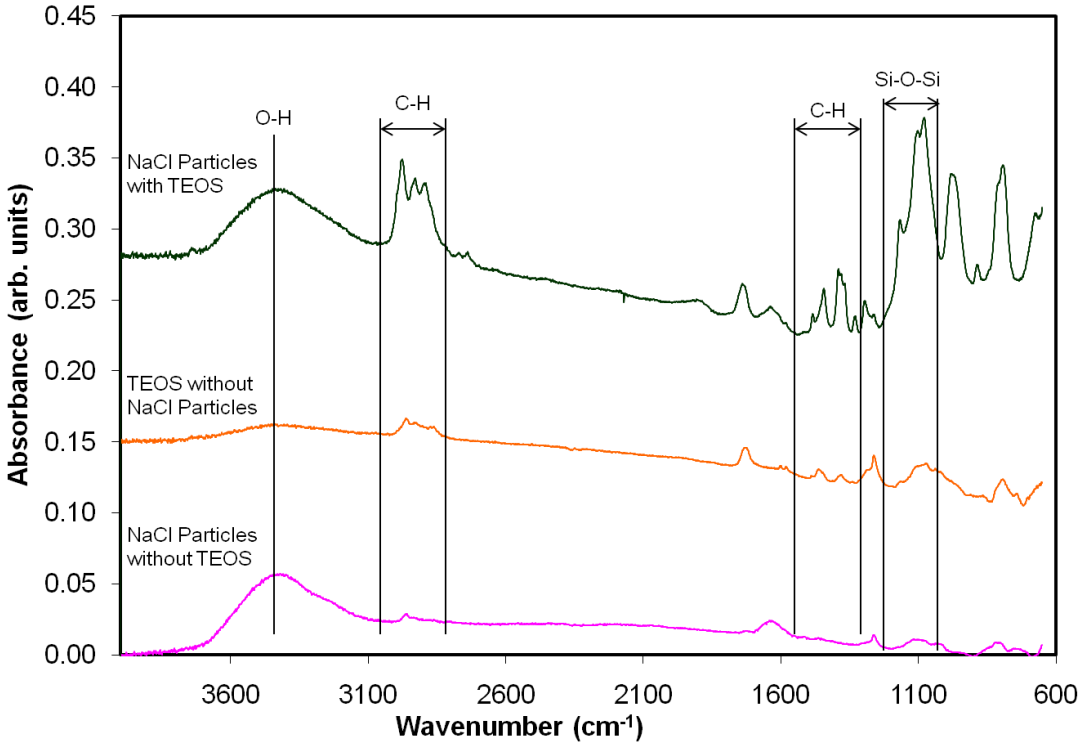

Figure 2.10: FTIR spectra of bare sodium chloride, sodium chloride with TEOS, and TEOS only collected on stainless steel meshes.

For more detailed probing of individual coated particles, TEM analysis with corresponding elemental analysis techniques such as EDX is required of the sodium chloride samples. However, TEM of sodium chloride particles is problematic due to

the propensity of sodium chloride to melt when exposed to an electron beam. Therefore further investigation of the coating phenomena requires use of other core nanoparticle materials.

To find particles that would provide better imaging capabilities, PSL was used as a core particle for coating. PSL particles have been shown by others to have highly reproducible particle sizes and are known to be stable within the TEM [43, 73, 74]. Also, PSL particles have known mobility characteristics, and are easily dispersed in solution and aerosolized without agglomeration [75]. Initial studies conducted with PSL particles characterized how particles behaved in the coating cell. Duke Scientific PSL particles with a diameter of 60±9 nm were mixed in an aqueous solution with Millipore filtered water at a ratio of 6-8 drops per liter. The solution was aerosolized in the same manner as the sodium chloride solution and was dried using a diffusion dryer. The aerosol size distribution was measured with a DMPS system for the particles passing through the system with and without VUV radiation. As seen in Figure 2.11, the measurement of particles without the lamp produced a weak mode in the size distribution near 60 nm. However when the lamp was on, the mode of the distribution shifted to ~25 nm and the concentration of particles increased by three orders of magnitude. Because no additional mass was added to the system, it is likely that the shift in size and concentration was caused by VUV disintegration of the PSL particles.

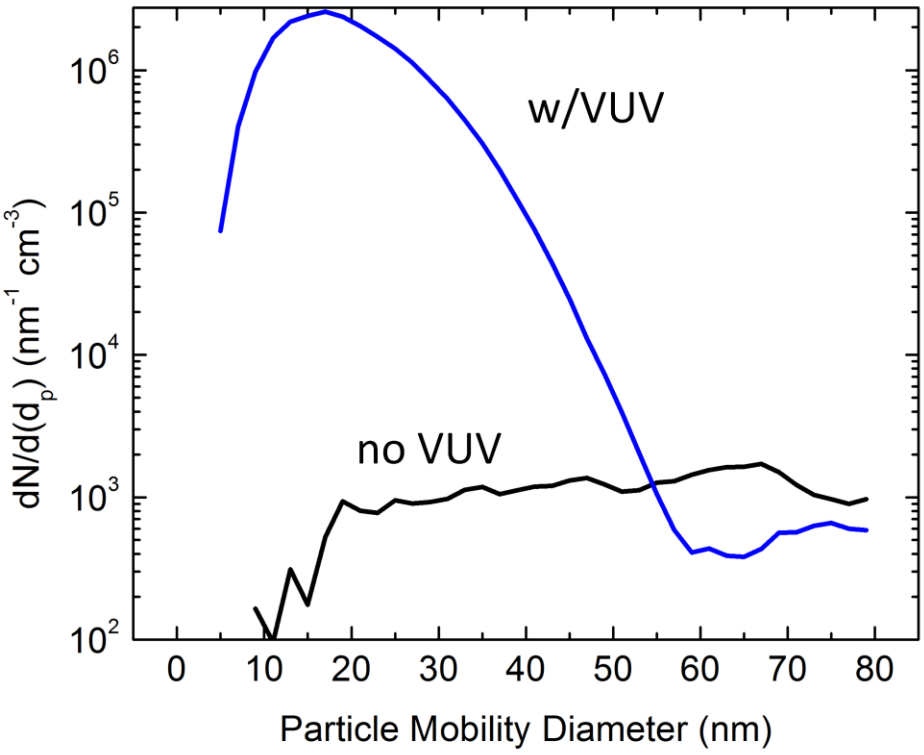

Figure 2.11: Particle mobility distribution of PSL particles with and without VUV radiation.

To confirm that the particles were being broken apart by the lamp's radiation, collections of particles were taken with and without VUV radiation. Particles were nebulized in the same manner as above and collected using an electrostatic precipitator after exiting the coating chamber. The particles were collected on lacey carbon TEM grids for 67 and 32 minutes for the lamp off and on, respectively. Each sample was then imaged using TEM and the results are shown in Figure 2.12. The particle sizes in each of the images correspond well to the DMPS results with smaller particles (<60 nm) present when the lamp was on. The images further confirm that 172-nm VUV radiation caused the PSL particles to be broken apart. The disintegration of PSL particles in the presence of VUV radiation excludes PSL particles as suitable substrates for fundamental coating studies.

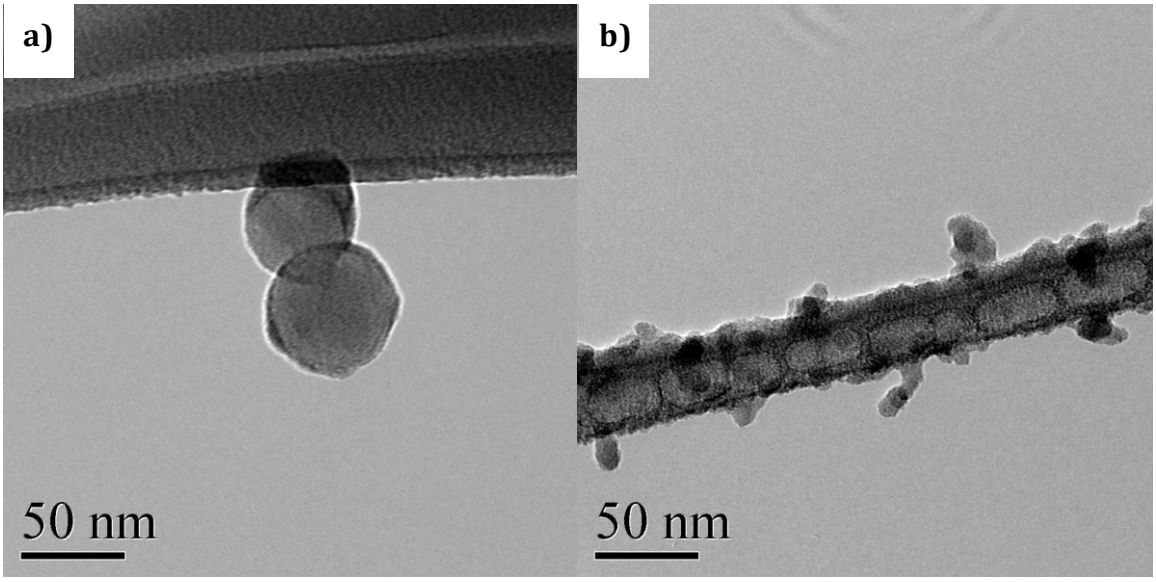

Figure 2.12: TEM images of PSL particles collected on lacey carbon grids (a) without VUV radiation and (b) with VUV radiation.

2.4 Silica Coating of Yttrium Aluminum Oxide Particles

For the study of coatings on yttrium aluminum oxide, YAP particles were selected for initial testing because they were commercially available at submicron sizes. Colloidal solutions were prepared using YAP powder (provided by Nitto Denko Technical Corporation, San Diego, CA) dispersed in methanol at 0.01 molarity and aerosolized in a manner similar to the sodium chloride and PSL nebulization. The methanol was removed from the aerosol by passing the aerosol through a diffusion dryer that contained molecular sieves. The sieves were selected with an effective pore size of 3Å which was large enough to remove methanol molecules from the flow stream [76]. The YAP aerosol was size selected at 35 nm, then mixed with TEOS at various flow rates and passed into chamber where VUV radiation initiated coating growth. The resulting size shifts were determined by TDMA measurements of particle diameter, as shown in Figure 2.13. The YAP particle diameter grows with TEOS flow rate, similar to sodium chloride particle growth in Figure 2.9. While the particle growth is similar for both sodium chloride and YAP

particles, the particle size distributions of coated YAP are significantly narrower at high TEOS flow rates and do not become unstable at 1.51 sccm.

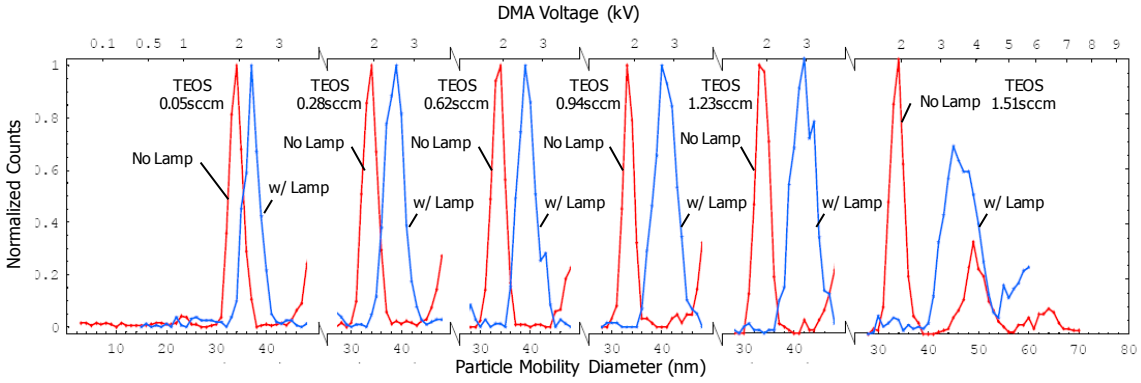

Figure 2.13: TDMA analysis of YAP particle diameter with varying TEOS flow rates.

The particle coating thickness versus TEOS flow rate was determined in the same manner as for NaCl particles. The coating thickness was measured for two different VUV radiation intensities, which were controlled by varying the lamp window transmissivity via the selection of window material. A thermopile radiation detector measured radiation intensities transmitted by a calcium fluoride and silica window. The transmitted intensity was found to be 7.5 mW cm^{-2} and 15 mW cm^{-2} for the silica and calcium fluoride windows, respectively. Measurements from the thermopile detector were not accurate enough to give absolute values of the intensity but were good indications of relative intensity. Therefore it can be concluded that the transmitted radiation intensity of the silica window was half that of the calcium fluoride window.

The coated YAP particle sizes were measured for systems with both the calcium fluoride and silica windows with a 7.2 slm nitrogen purge flow rate and a variety of TEOS flow rates. The resulting coating thicknesses for the two different radiation intensities are shown in Figure 2.14. The coatings produced using the calcium fluoride window were significantly thicker at higher TEOS flow rates than coatings that were produced using the silica window. At lower TEOS flow rates,

however, both coatings were nearly the same. This result indicates that the VUV intensity in the chamber was high enough with either window to dissociate all of the TEOS at lower flow rates, resulting in the same coating thickness. For higher TEOS flow rates the lower transmitted power of the silica window was insufficient in disassociating as much TEOS as the calcium fluoride window, resulting in thinner coatings.

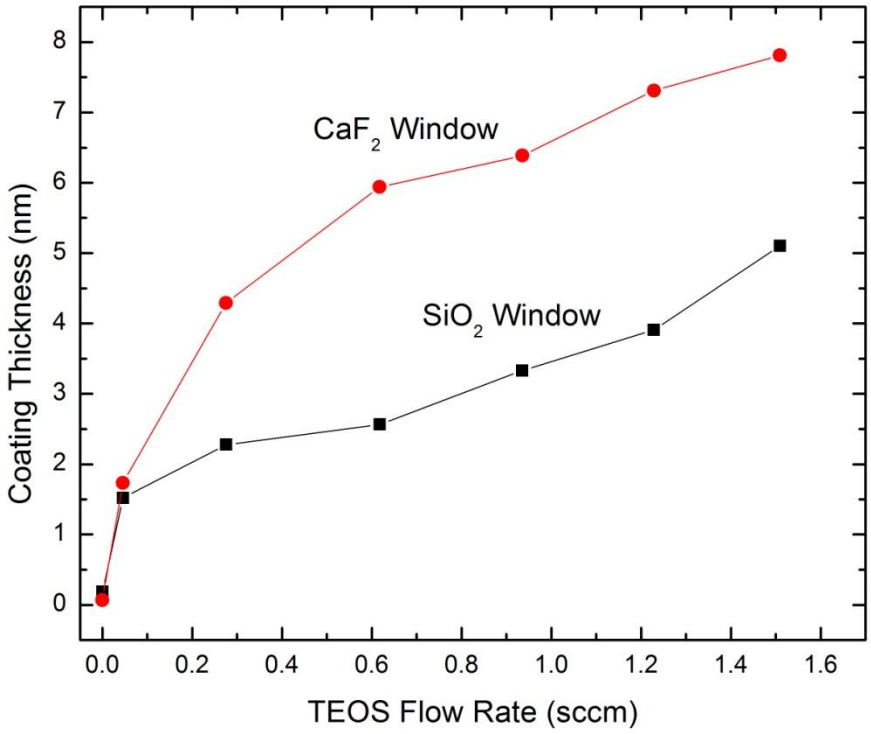

Figure 2.14: Coating thickness of YAP particles for varying TEOS flow rates and transmitted VUV power.

Images of YAP particles with and without coatings were obtained by TEM, as shown in Figure 2.15. The sample depicted in Figure 2.15b consisted of size-selected 40-nm particles that were coated with chamber conditions of 4.3 slm nitrogen flow, 0.9 sccm of TEOS and a CaF_2 window. The particles were gathered for 60 minutes onto a lacey carbon TEM grid via an electrostatic precipitator. The sample shown in Figure 2.15a was made by placing a droplet of the YAP solution on a TEM grid and

allowing the solvent to evaporate. As seen in Figure 2.15b, the particle coating appears to be in good agreement with the coating thickness reported for particles of similar size and flow rate in Figure 2.14. The particle coatings appear uniform around the particle, but neck into the lacy carbon grid at the point of contact to the grid. The necking of the coating may have been an indication of impurities in the film. Necking of the coatings is reduced by performing photo-CVD coatings at higher temperatures as discussed in Section 2.5.

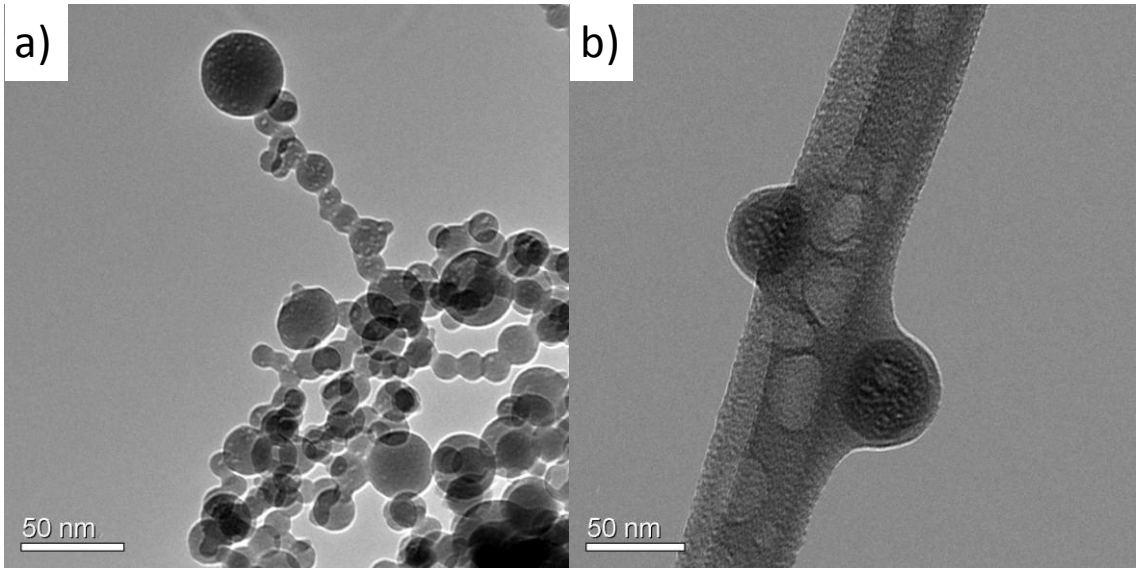

Figure 2.15: TEM image of (a) bare and (b) coated YAP particles.

While it was shown that aerosolized YAP particles could be achieved by nebulizing a YAP solution, the nebulization process had reproducibility drawbacks in terms of repeatable aerosol sizes and concentrations. Also, the ability to test small particles sizes (<30 nm) was limited as the residue after evaporation within the purest available water approached the same size as the particles when micron-sized water droplets were dried after nebulization. Ultimately, it was determined that in order to test the photo-CVD coating process over a range of sizes and concentrations, gas-phase synthesis processes would achieve more reproducible core particles.

2.5 Silica Coating of Silver Particles

Further study of the photo-CVD nanoparticle coating process was conducted using silver nanoparticles which have been shown to image well and are not disintegrated by VUV radiation [77, 78]. Silver nanoparticles were synthesized by inert-gas condensation where silver was evaporated in a tube furnace and then allowed to homogeneously nucleate [79]. In order to investigate the effect of furnace temperature within our system, a study was conducted holding all other parameters constant while furnace temperature was varied. The flow parameters were 2 slm of nitrogen through the tube furnace and 4.3 slm of post-production nitrogen dilution flow, which served to suppress further agglomeration. As shown in Figure 2.16, the increase in furnace temperature served to increase the mode and width of the distributions. The first silver particles were measured at ~800°C. Other parameters that were found to significantly affect the production size of particles from inert-gas condensation include the volumetric flow rate of both the inlet and purge gases, as well as the diameter of the tube within the tube furnace, which changes the velocity across the face of the evaporating metal.

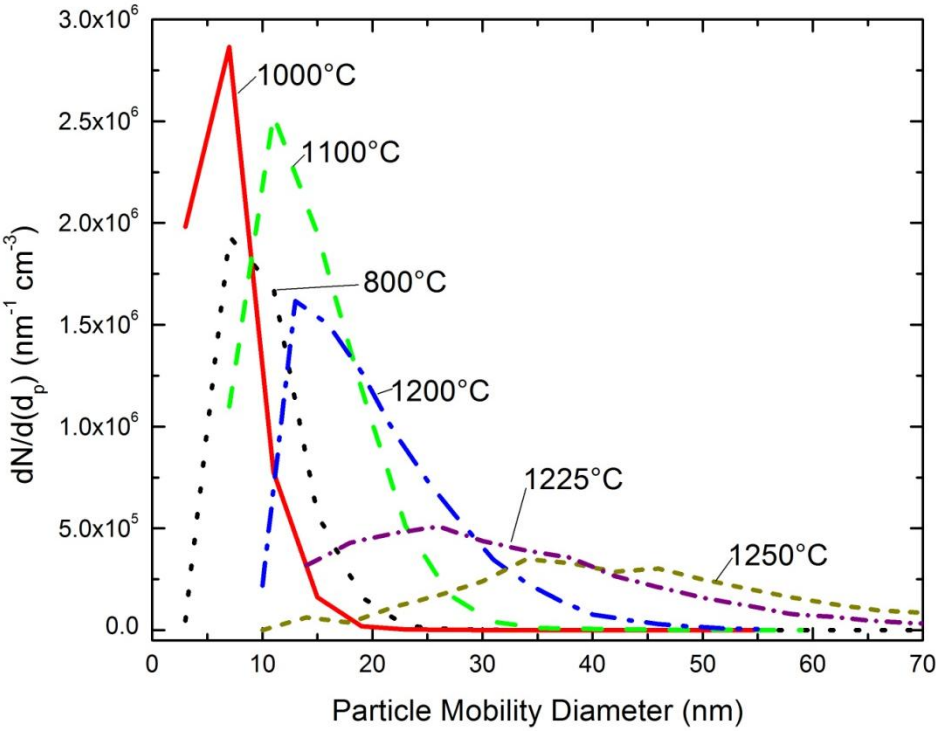

Figure 2.16: Particle mobility distribution for silver particles produced with different furnace temperatures.

In order to use TDMA as an analysis technique it was imperative that particles were produced in sufficient quantities such that the sample size of coated particles was large enough to represent the entire aerosol and could be accurately measured by the DMPS. An initial study sought to determine whether condensation of silver vapor could produce particle concentrations that were high enough for particle coating experiments. The furnace temperature was set at 1250˚C and the nitrogen flow rate was set to 2 slm. As shown in Figure 2.17, the resulting aerosol was characterized with a DMPS system and found to have a peak in the raw particle counts at 33 nm with total particle counts in excess of 10^5 cm^{-3} for the polydisperse distribution. When the particles were size selected at 33 nm with a DMA before entering the chamber, the particle counts at the peak were decreased by a factor of 2. The measured counts of particles delivered to the CPC were further decreased by

an order of magnitude when the aerosol was exposed to radiation from the VUV lamp and passed through another bi-polar charger. While the measured counts decreased when the aerosol was exposed to a second bi-polar charger and radiation, there was no actual decrease in particle concentration in the chamber. The drop in measured counts was due to a decrease in negatively charged particles by a redistribution of particle charge states by the second bi-polar charger and particle-photon interactions. Despite the measured counts of particles being drastically reduced by size selection and charge redistribution, the resulting sampled aerosol concentration was high enough (~5×10^3 counts cm^{-3}) to give a representative sample of the coating process.

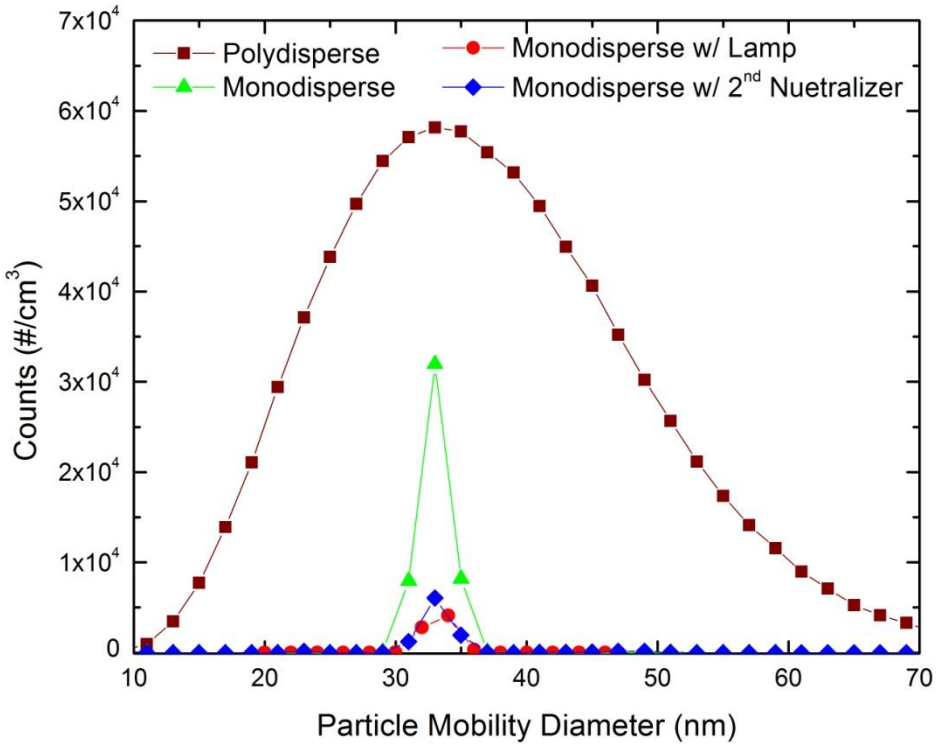

Figure 2.17: DMPS measurements of particle counts versus particle mobility diameter with various charging and size-selection effects.

While particle counts were sufficient, TEM analysis of the particle samples produced by the Scheibel and Porstendörfer method indicated that most particles

were agglomerates of smaller primary particles [79]. For fundamental study of the coating process individual spherical particles were desired for simplicity of geometry and smaller surface area per particle. Therefore a method was devised to sinter the agglomerated particles downstream of the particle nucleation point. Work by Ku and Maynard found that temperatures above 500˚C caused agglomerated silver particles in this size range to begin sintering [78]. To sinter the agglomerates a second tube furnace was added to the system along with a dilution nitrogen flow to suppress further agglomeration as shown in Figure 2.4b. Particles were produced with the first tube furnace at 1250˚C and particles were collected with and without the second tube furnace at 600˚C. The results of sintering can be seen in Figure 2.18 where the large agglomerates (Figure 2.18a), were reduced by dilution and sintering forming individual particles (Figure 2.18b). While the particles are largely sintered they have not completely coalesced into spheres. Higher temperatures of the second tube furnace (>700˚C) provide enough energy to fully coalesce the particles [78].

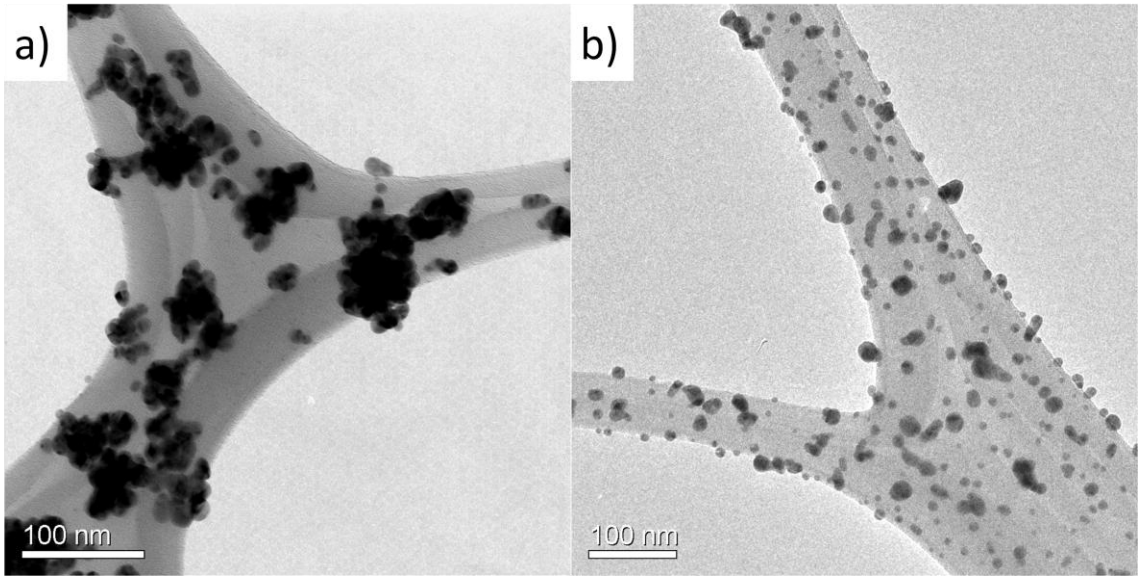

Figure 2.18: TEM images of agglomerated silver particles produced (a) without sintering and (b) coalesced particles produced with second tube furnace at 600˚C.

Figure 2.19a shows the normalized particle counts of coated and uncoated silver nanoparticles. The graph shows a series of eight DMA scans for the coated particles, normalized to the highest value measured for all eight scans. Figure 2.19b shows the corresponding TEM image of 35-nm size-selected particles that were coated with the following photo-CVD conditions: 1-slm aerosol flow, 0.5-sccm TEOS, 7-slm nitrogen purge flow, 400˚C chamber temperature, and $\sim 10^3$ cm^{-3} silver particle concentration. The particles were collected on lacey carbon TEM grids (Ted Pella 01890) over a 35 minute period. During the collection, eight TDMA measurements were made to determine the final diameter of the coated particles. As shown in Figure 2.19a, the coating size did not vary throughout the collection, indicating that all of the particles were coated with nearly uniform thickness. The TEM image of particles collected concurrently with the TDMA data indicates that the TDMA-measured 5-nm change in peak particle diameter, shown in Figure 2.19a, corresponds to the 2-3 nm coating thickness (change in radius) seen in Figure 2.19b. The particle coatings are nearly uniform, indicating that TDMA measurements, which assume spherical aerodynamic mobility diameter, are accurate measures of particle coating thickness. The silica coatings exhibit less necking at 400°C than coatings conducted at room temperatures as shown in Figure 2.15b.

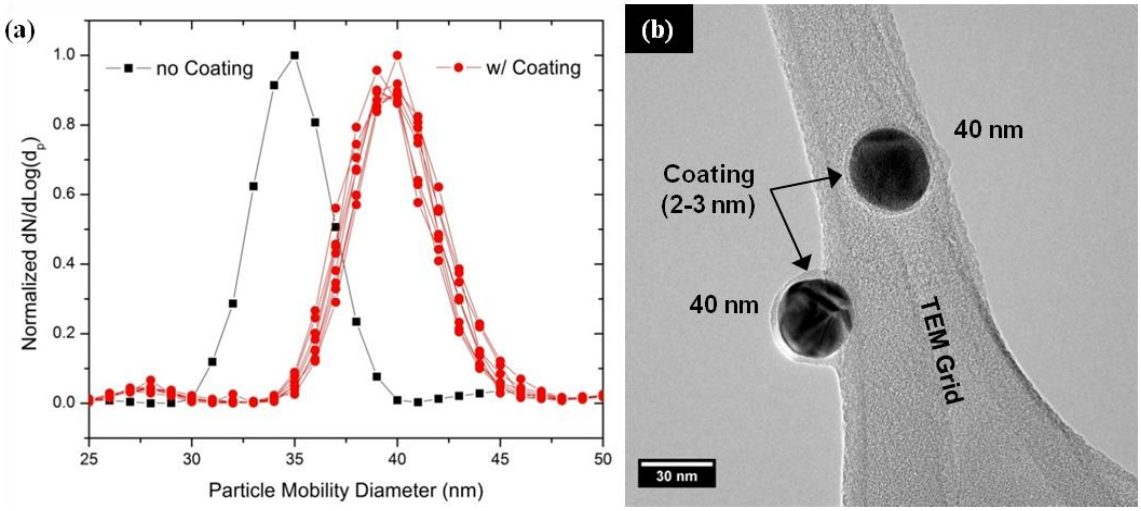

Figure 2.19: (a) TDMA-measured normalized particle counts versus particle mobility diameter, of silver particles with and without coating. (b) TEM image of coated silver particles collected concurrently with TDMA measurement.

In order to determine the effect of various system parameters on particle coatings, coating thicknesses were measured for a variety of system configurations. The two parameters that were found to influence particle coating thickness the most were the flow rate of TEOS and the flow rate of nitrogen purge gas. An experiment was conducted where size-selected 30-nm particles were coated at ambient temperature with three different nitrogen purge flow rates and a range of TEOS flow rates. All other conditions were held constant at the values listed above. The resulting coating thicknesses were measured as a difference in radius (defined as one-half the mobility diameter) between coated and uncoated particles, determined by the Gaussian fits to the TDMA particle size distribution. As shown in Figure 2.20, the coatings grew linearly with TEOS flow rate over the range of flows tested. The nitrogen purge flow rate also strongly influenced particle coating thickness. A change from 9.1 slm to 5.2 slm of nitrogen flow more than doubles the coating thickness for any given TEOS flow. Decreased flow rates of nitrogen purge gas increased coating thickness by increasing particle and precursor concentration as well as increasing residence time. While the decreased purge flow increased coating

thickness, it also increased the variance of the coating thickness distribution. The increase in the standard deviation of Gaussian fits to the size distributions varied from 3.4 to 8.4 nm for purge flow rates of 5.2 slm and 9.1 slm, respectively. These results demonstrate that by controlling critical photo-CVD parameters specific particle coating thicknesses can be obtained.

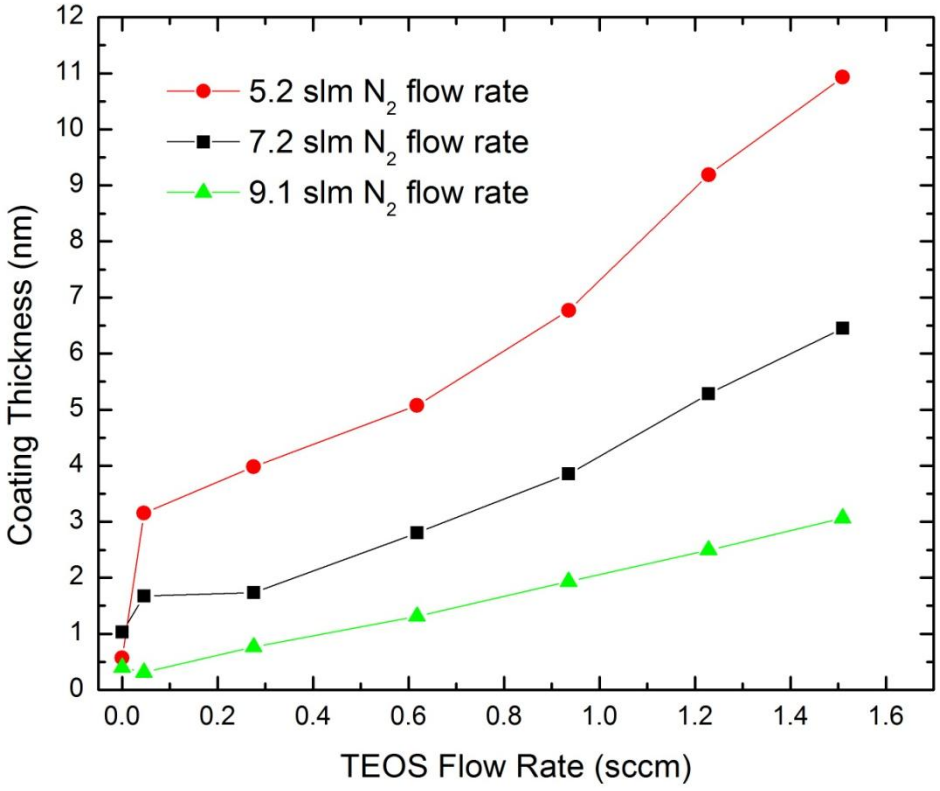

Figure 2.20. Coating thickness of silver particles for varying TEOS flow rates and with different purge nitrogen flow rates.

In order to determine the effect that particle size has on coating thickness, silver particles were size selected with three different particle mobilities that corresponded to 20-, 30-, and 40-nm particle mobility diameters. The particles were then coated using the photo-CVD process with operating conditions of 7.2-slm purge nitrogen flow, 3-slm tube furnace nitrogen flow, and tube furnace temperatures as stated above. The particle coating thickness was measured using the TDMA system

and plotted as a function of TEOS flow rate and particle size. As shown in Figure 2.21, the coating thickness increased nearly linearly over the range of TEOS flow rates measured for all initial particle sizes. Also, the initial particle size had no distinguishable effect on the resulting coating thickness. For particles in the continuum regime, $Kn<0.1$, theory predicts a $1/d_p$ dependence on the coating thickness for transport limited particle growth, *i.e.* condensation growth [80]. For the free molecule regime, $Kn>10$, there is no predicted dependence on particle size and for the transition regime, $0.1<Kn<10$, there is assumed to be a decrease in coating thickness with increased particle size, but less than $1/d_p$. The initial sizes of the particles indicated by Figure 2.21 are 20 nm, 30 nm, and 40 nm which correspond to Knudsen numbers of 6.5, 4.3, and 3.3, respectively. While all of the Knudsen numbers are within the transition regime, the particle coatings are expected to have a weak dependence on initial particle size. With the current resolution of instruments, no change in coating thickness was observed with different core particle sizes, which is contrary to previous work with photo-CVD produced organic coatings [26]. These results were repeatable for several different runs and served to indicate that the silica growth was not limited by transport but rather by reaction rates within the gas phase and at the particle surface. The rates of these reactions are considered in detail in Chapter 3.

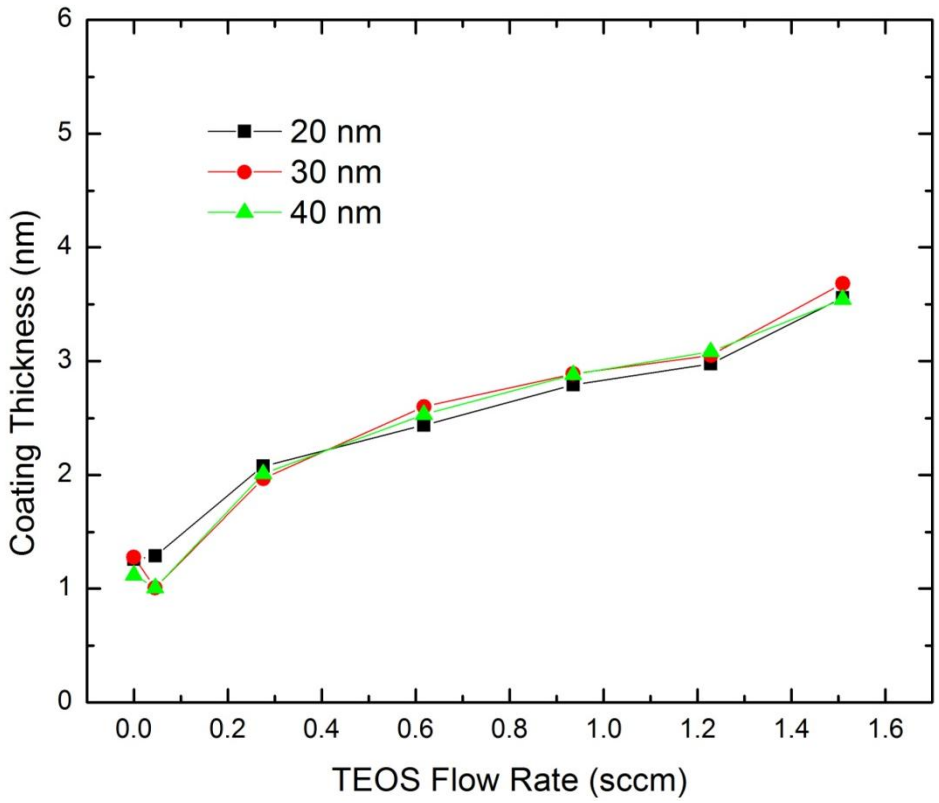

Figure 2.21: Coating thickness of silver particles for varying TEOS flow rates and initial particle sizes.

A study of differing aerosol and TEOS inlet positions sought to determine how spatial variations of the system could affect the resulting coating thickness. As inlet positions were moved from a location close to the lamp to farther down the chamber, both the residence time and radiation reaching the particles decreased. At each inlet position size-selected 30-nm particles were passed into the chamber with a nitrogen purge flow of 7.2 slm and varying flow rates of TEOS. A schematic of inlet positions and resulting coating thicknesses for variations in inlet positions and TEOS flow rates is shown in Figure 2.22. The coating thicknesses decreased dramatically as the inlet positions were moved down the tube and away from the excimer lamp. These results, alongside those from Figure 2.20, highlight the impact of residence time, which was 3.9 s, 3.6 s, 2.4 s for Position 1, 2, and 3, respectively

(note that the Position 1 curve in Figure 2.22 is the same as the 7.2 slm curve in Figure 2.20). The difference between the results of Figure 2.22 and Figure 2.20 is that the decreased residence time in Figure 2.20 coincides with a decrease in concentration of the precursor and particle concentrations, whereas in Figure 2.22, the concentrations remain constant.

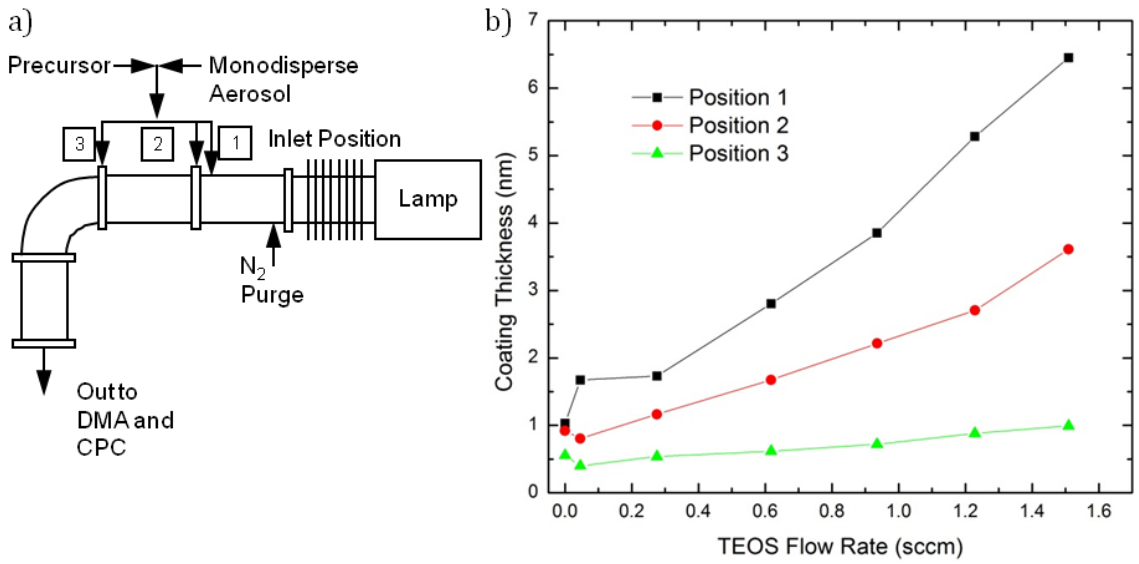

Figure 2.22: (a) Schematic of particle and TEOS coating chamber inlet positions. (b) Coating thickness of silver particles for varying TEOS flow rates and different particle and TEOS inlet positions.

To determine the role that reactions involving VUV radiation at the particle surface play in creating the coatings, the system was modified so that the TEOS and aerosol were injected into the chamber at different positions. The TEOS was introduced upstream of the aerosol and in view of the lamp. The aerosol inlet was placed 12.7 cm downstream of the TEOS inlet in two different configurations, as shown in Figure 2.23a. In configuration 1 the particles were injected in direct view of the lamp and thus exposed to radiation. In configuration 2, a 90˚ bend between the particle inlet and the lamp prevented radiation from reaching the particle surface. In both configurations, size-selected 30-nm particles were passed into the chamber at ambient temperature with 7.2 slm of nitrogen purge flow. Varying flow

rates of TEOS precursor were used and the coating thicknesses were measured using TDMA. As shown in Figure 2.23b, the coatings on the particles exposed to radiation were thicker than those that were not. However, the presence of a coating on the particles in configuration 2 indicates that gas-phase photochemical reactions alone are sufficient to produce films, but that by combining gas-phase and surface reactions, higher film growth rates are possible. Also, while films are grown without radiation at the surface, it does not mean that films grown with and without radiation have the same chemical purity. These results corroborate the thin film infrared experiments shown in Figure 2.7 where higher SiO_2 peaks were seen when radiation was present on the film surface.

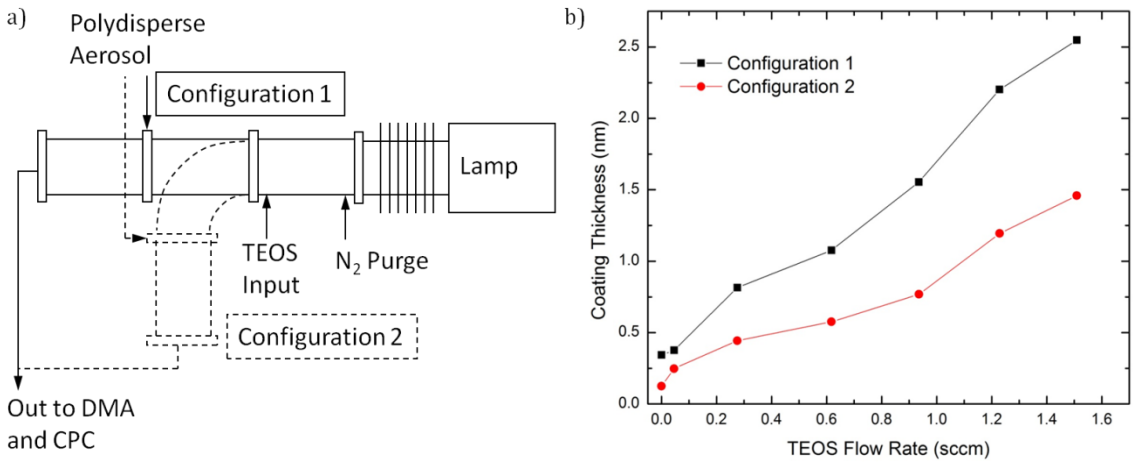

Figure 2.23: (a) Schematic of photo-CVD coating chamber configuration. (b) Coating thickness of silver particles for varying TEOS flow rates and different system configurations.

The coated silver particle thicknesses were measured for photo-CVD systems in which the radiation intensity was changed by inserting different transmission filters between the VUV excimer lamp and the chamber. In the experiment, the nitrogen purge flow was fixed at 7.2 slm of nitrogen, the CVD chamber temperature was held at 20°C, and the flow rate of TEOS was varied. The resulting coating thicknesses for the two different radiation intensities are shown in Figure 2.24. The

reduction in radiative flux caused by the 50% and 10% transmission filters significantly reduced the coating thicknesses at all TEOS flow rates when compared to the thicknesses produced without a filter. For the 10% transmission filter, the coating thickness actually decreased at high TEOS flow rates, possibly due to too high of a TEOS concentration in the chamber for the VUV radiation to properly decompose.

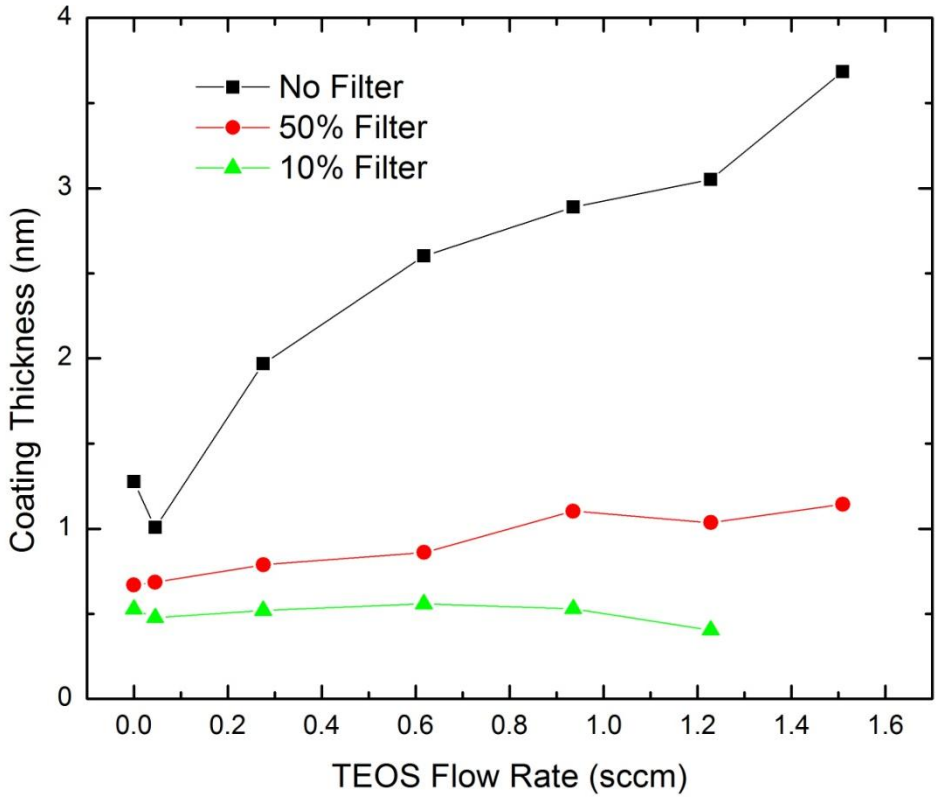

Figure 2.24: Coating thickness of silica-coated silver nanoparticles with varying powers of VUV radiation controlled by transmission filters.

FTIR spectroscopy was used to measure the chemical composition of coated particles produced by photo-CVD. Particle samples were produced by flowing polydisperse silver nanoparticles directly into the coating chamber without size selection at a flow rate of 3 slm. Concurrently, purge nitrogen (5.2 slm) and TEOS (1 sccm) flowed into the chamber and mixed with the aerosol in the presence of VUV

radiation. Upon exiting the chamber, the coated particles were collected via impaction onto gold-coated silicon wafers (100-nm Au film). The impaction was conducted by accelerating the aerosol through a 1-mm-diameter orifice placed 3 mm from the substrate, which resulted in subsonic flow delivering particles to the wafer. Coated particles were collected for 10 minutes on each substrate for chamber temperatures ranging from 20-700˚C. Spectra of the resulting particle films were then obtained using diffuse reflectance infrared Fourier transform spectroscopy (DRIFTS). Five spectra were taken for each film and then averaged to reduce variations due to spatial disparities in sample thickness.

Figure 2.25 shows the spectra of coated silver particles for differing coating chamber temperatures. While the spatial resolution of the DRIFTS is not fine enough to distinguish between the particles and the coatings, over the range of wavenumbers investigated vibrations of the silver bonds are not detectable. Therefore, the resulting spectra represent the chemical composition of the particle coatings and not the cores. As seen in Figure 2.25, the spectral signatures of silica at 1000-1200 cm^{-1} (Si-O-Si asymmetric stretching) and ~800 cm^{-1} (Si-O-Si symmetric stretching) are present in samples produced at all coating chamber temperatures. However, the amount of hydrocarbon impurities that remain from the organometallic precursor, indicated by the peak at ~1400 cm^{-1}, decreases with increased coating chamber temperature. While the intensity of the C-H peak decreases at higher temperature, the spectral signal in the range of 2900-3000 cm^{-1}, indicative of C-H, does not diminish and even slightly increases for certain elevated chamber temperatures. Additionally, other hydrocarbon impurities, seen at 1016 cm^{-1}, intensify as chamber temperature increases. Therefore while TEM images of coated particles (discussed later) indicate improved coatings at increased temperatures, infrared results show that hydrocarbon impurities remain.

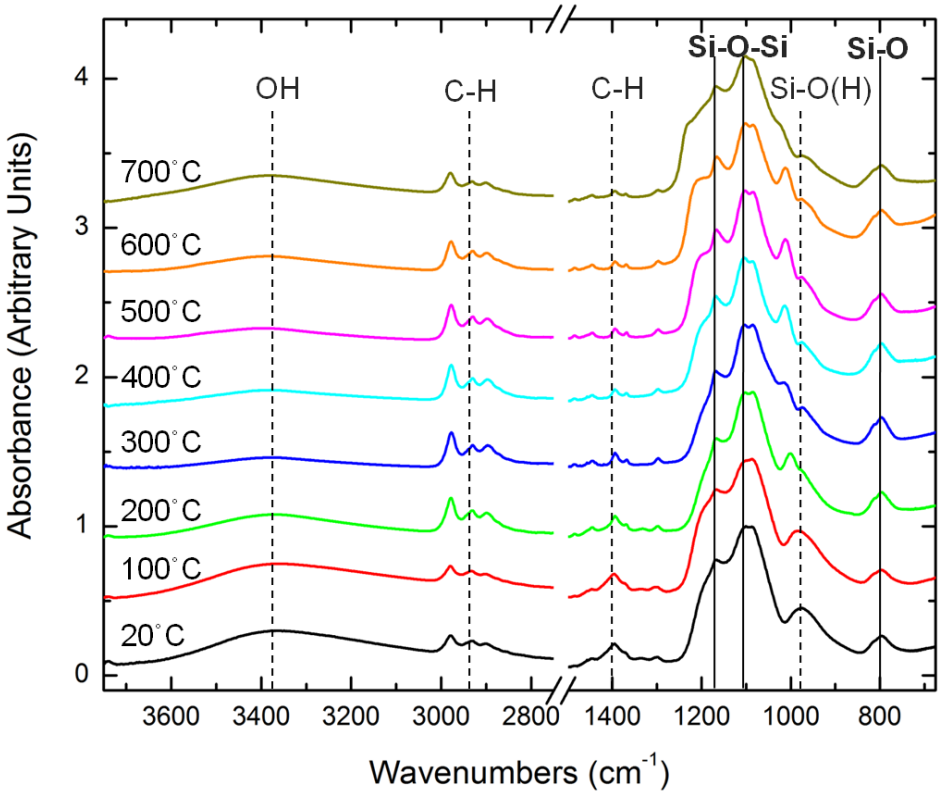

Figure 2.25. Normalized infrared spectra of coated polydisperse silver nanoparticles for varying chamber temperatures.

In order to reduce film impurities, oxygen was added to the system during the photo-CVD coating process. Samples were prepared at a fixed chamber temperature of 300˚C using the same nitrogen, particle, and precursor flow rates as used for samples shown in Figure 2.25. Varying flow rates of oxygen were added to the particle/precursor mixture just prior to entering the photo-CVD chamber and the resulting coated particles were collected via impaction as described above. As shown in Figure 2.26, the infrared spectra of the particles coated in the presence of oxygen differ substantially from the spectra of coated particles without oxygen. The particles coated with additional oxygen have significantly less C-H bond incorporated into the coating, as well as less intense signals of the contaminants found at 1400 cm^{-1}, 1200 cm^{-1}, 1016 cm^{-1}, and 975 cm^{-1}. In addition to reducing

hydrocarbon impurities, the presence of oxygen also improves the spectra in the region of the Si-O-Si peak by shifting the peak to a higher wavenumber, which is indicative of more structurally ideal silica [81]. As expected, the introduction of oxygen also increases the presence of OH (~3400 cm^{-1}). While the addition of 1 sccm of oxygen results in a higher-quality silica coating, further increases in oxygen flow does little to improve the quality of the coatings. Flow rates of oxygen in excess of 5.1 sccm resulted in significant TEOS self-nucleation as measured by TDMA. The results indicate that monatomic oxygen produced by VUV radiation may serve to enhance the radicalization of TEOS, as has been reported by others [82, 83].

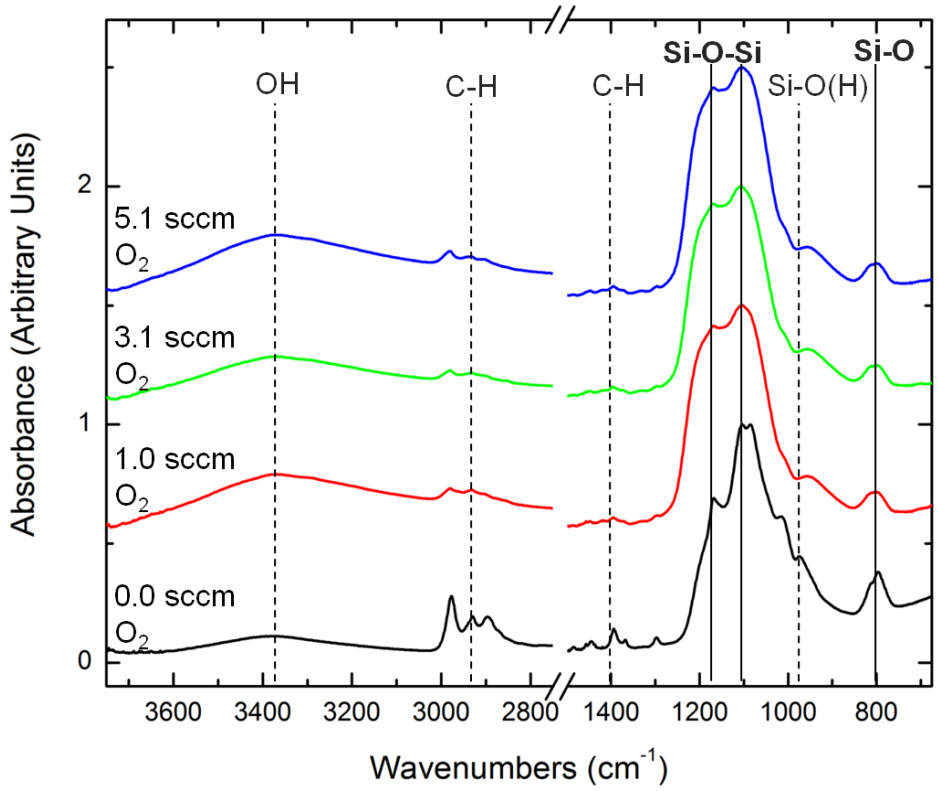

Figure 2.26. Infrared spectra of coated polydisperse silver nanoparticles with varying oxygen flow rates.

While infrared spectroscopy gives an indication of the quality of silica in the collected samples, it does not provide spatial information regarding where silica resides in relation to the silver particle. To confirm that the particle coatings seen in TEM are comprised of silicon and oxygen, EDX analysis of an individual particle was used to spatially determine the elemental composition of the particle core and shell. Monodisperse 30-nm particles were passed into the chamber at 1 slm along with 1 sccm of TEOS, 4.3 slm of purge nitrogen and no oxygen. Additionally, the particle coating chamber was held at 300˚C and the excimer lamp was on. As the particles exited the chamber, they were collected by electrostatic precipitation onto lacey carbon TEM grids for 10 minutes. As seen in Figure 2.27a and b, the STEM images depict a coated silver particle on a lacey carbon grid with a 30-nm core and a 10-nm coating. The line indicated by the red arrow is the scanned path of elemental information gathered by the EDX. As seen in the elemental spectrum in Figure 2.27c, the particle coating (0-10 nm and 40-50 nm) primarily consists of silicon and oxygen, while the core region of the particle (10-40 nm) is largely composed of silver. The reduced silicon and oxygen signal in the core region is a result of the coating in the foreground and background of the three dimensional particle, which is not apparent in the two dimensional image. The distinct boundary between the silver core and the silicon and oxygen shell indicates that little solid state diffusion occurs between the particle coating and the core. The background carbon present throughout the sample is a result of the lacey carbon grid on which the particle was collected. Because of the large carbon background signal, the level of carbon inclusion within the coating is not discernable. Unfortunately, no other commercial TEM grid coating materials exist that do not contain either silicon or carbon. Therefore, infrared spectroscopy measurements give a better indication of carbon impurities within the coatings.

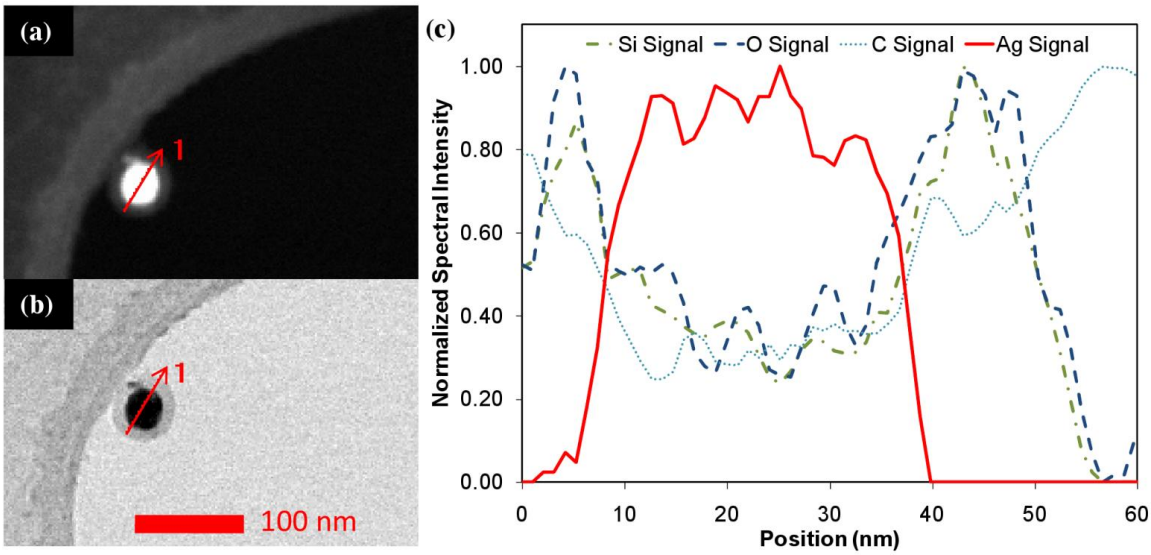

Figure 2.27: Coated silver nanoparticle on lacey carbon grid STEM (a) dark- and (b) bright-field images and (c) normalized EDX elemental line scan.

For each infrared collection depicted in Figure 2.25, particles were also collected on lacey carbon TEM grids via electrostatic precipitation. As shown in Figure 2.28, TEM images of the particles indicate that coating thickness varies in addition to infrared spectral intensity as the photo-CVD chamber temperature increases. As seen in Figure 2.28a, low coating chamber temperatures resulted in thinner particle coatings. Increased chamber temperatures near 400˚C, shown in Figure 2.28e, cause thicker coatings that are easily detectable by TEM. The thicker coatings prevent the particle cores from coming into contact with one another and thus retain the original structure of the silver nanoparticles despite the higher chamber temperatures. At chamber temperatures in excess of 500˚C, Figure 2.28f, the TEOS precursor begins to homogeneously nucleate, forming nanoparticle clusters inside the aerosol. These clusters agglomerate with the silver particles forming non-uniform films on the particles, as shown in Figure 2.28h. These results combined with the previous FTIR studies indicate that photo-CVD chamber temperatures from 300-400˚C form effective silica coatings that inhibit the

agglomeration of particle cores. It is important to note that this temperature is significantly below processing temperatures used for thermal CVD of TEOS on macroscopic substrates, which are typically above 700˚C [82].

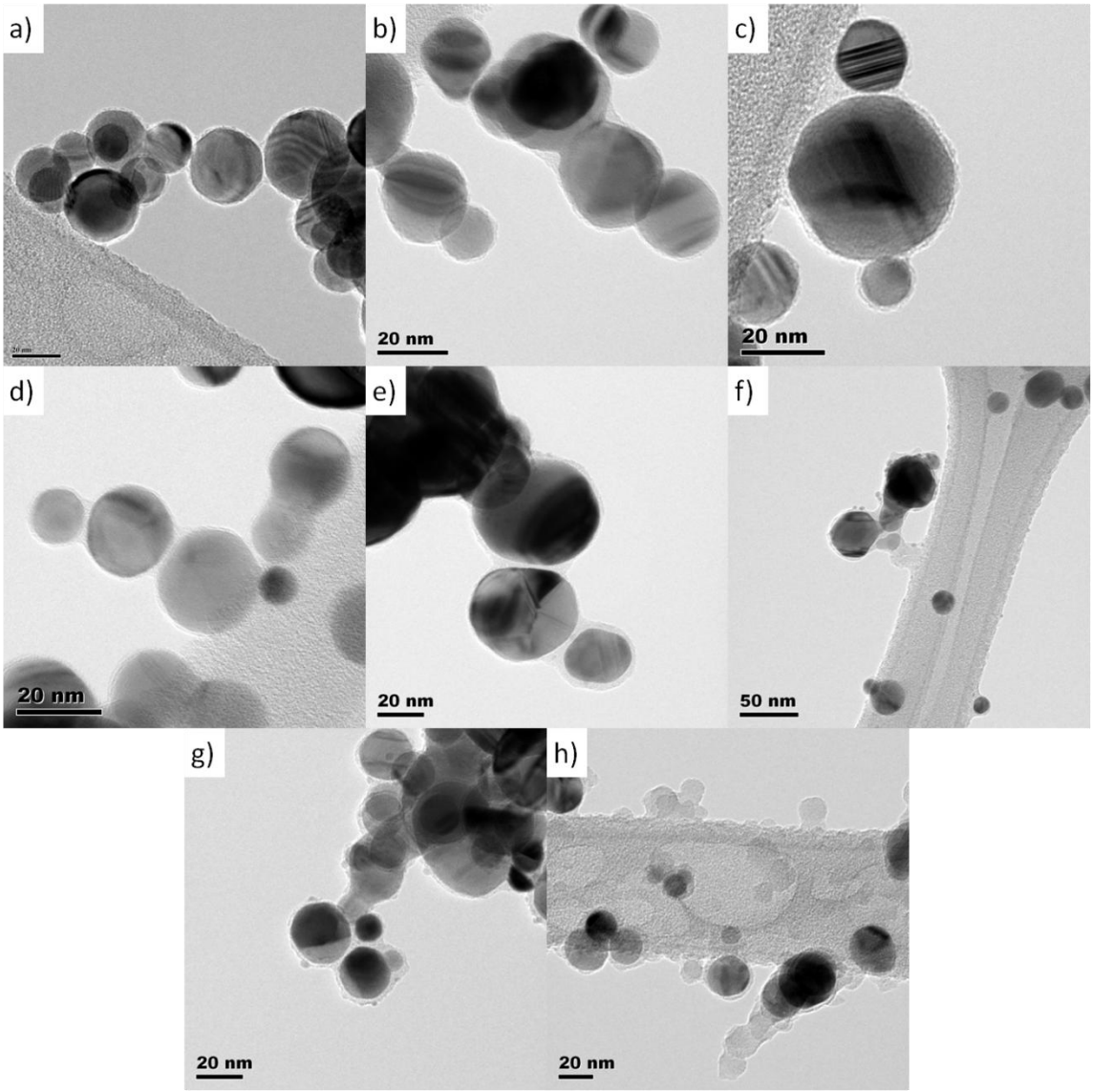

Figure 2.28: Polydisperse silver nanoparticles coated at (a) 20˚C, (b) 100˚C, (c) 200˚C, (d) 300˚C, (e) 400˚C, (f) 500˚C, (g) 600˚C, and (h) 700˚C at a concentration of 10^6 particles cm^{-3}.

In addition to resulting in different infrared spectra, particles coated at different temperatures and collected onto glass-fiber filters scattered radiation differently. Differences in sample colors were observed as particles were collected onto glass fiber filters for preliminary FTIR studies. Silver nanoparticles were coated under the same conditions as discussed previously for Figure 2.25 and Figure 2.28. As shown in Figure 2.29, the low-temperature coating experiments resulted in particles that appeared black or slightly brown. As the temperature of the coating chamber increased, the particles began to appear green. At the highest temperature, 700°C, the particles again appeared black or brown to the naked eye. These results were confirmed by several other experiments in which particles were collected with varying thicknesses of silica coating. In general, the results of these analyses indicated that while uncoated particles appeared black or brown, the presence of a silica coating resulted in a green appearance of the particles. An explanation for these results may be that by coating the particles with silica, the size and structure of the nanoparticles are preserved. Work by Mock *et al.* has shown that nano-sized silver materials exhibit unique plasmon resonances that can result in the scattering of green light for certain nanoparticle geometries [84]. While these results are generally of interest to the scientific community, they were not directly applicable to our current work and were thus not investigated further.

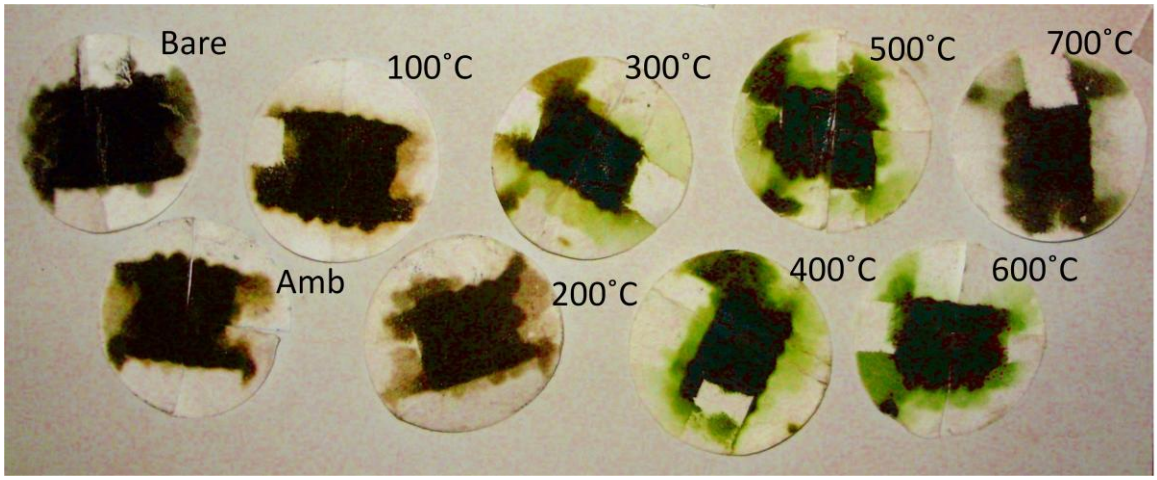

Figure 2.29: Photograph of silver nanoparticles collected on glass-fiber filters (~5 cm diameter) in which the particles were coated at varying chamber temperatures.

In order to determine the effect of particle coating on the dispersion of silver particles into aqueous solutions, ~1 mg of silver nanoparticles was collected onto glass-fiber filters for the same conditions as for Figure 2.29. The glass fiber filters were then placed in 50 mL of de-ionized water and sonicated for 7 minutes. As shown in Figure 2.30, the coated and uncoated nanoparticles resulted in drastically different dispersions. The uncoated silver nanoparticles, Figure 2.30a, remained hydrophobic as they did not disperse into the solution upon sonication and instead remained on the filter or in large agglomerates on the water surface or tube walls. The coated particles, in contrast, easily dispersed within the solution, creating solutions which adapted the color of the particles themselves. As seen in Figure 2.30b, the particles coated at ambient room temperature (~20°C) were able to be dispersed into solution despite the relatively thin coatings found on particles at such conditions (see Figure 2.28). The thicker-coated particles produced at 400°C retained their green color and were easily dispersed into the solution. It is not clear whether individual particles or small particle agglomerates were dispersed, but the dispersions remained stable for over two weeks without settling.

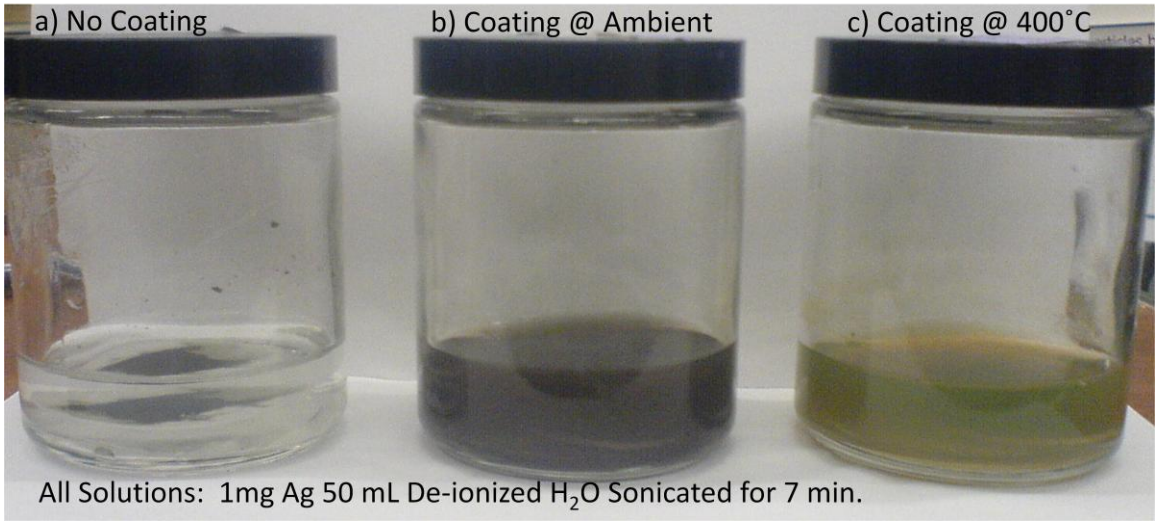

Figure 2.30: Image of dispersions of silver nanoparticles in aqueous solution for (a) uncoated particles and particles coated at (b) ambient room temperature and (c) 400°C.

To determine the effectiveness of coatings in suppressing agglomeration, a higher concentration of particles was coated, collected and imaged using TEM. Increased concentrations of particles were achieved by increasing the flow of aerosolized polydisperse silver particles to 7.0 slm and lowering the flow rate of purge nitrogen to 2.7 slm. Direct measurement of the concentration was not possible, because it exceeded the upper limit of the CPC (10^5 cm^{-3}). However, by diluting flows entering the CPC and accounting for the charging and selection efficiency of the DMAs, the particle concentration was estimated to be 10^7 cm^{-3}. The coating chamber temperature was controlled at 400˚C and the excimer lamp was on during processing of both coated and uncoated particles. The uncoated particles, seen in Figure 2.31a, passed through the heated chamber without the addition of the coating precursor and were collected on a lacey carbon TEM grid for 1 minute. Likewise the coated particles, seen in Figure 2.31b, were produced in the same manner with the addition of 0.5 sccm of TEOS. The uncoated particles appear agglomerated and the particle cores have sintered together, losing their original

spherical shape. In contrast, the silica shells of the coated particles provide a barrier to solid state diffusion of the particle cores, thus retaining the particles' original shape and size. The coatings on the particles shown in Figure 2.31b, also indicate that the photo-CVD technique is capable of producing uniform coatings at high particle concentrations.

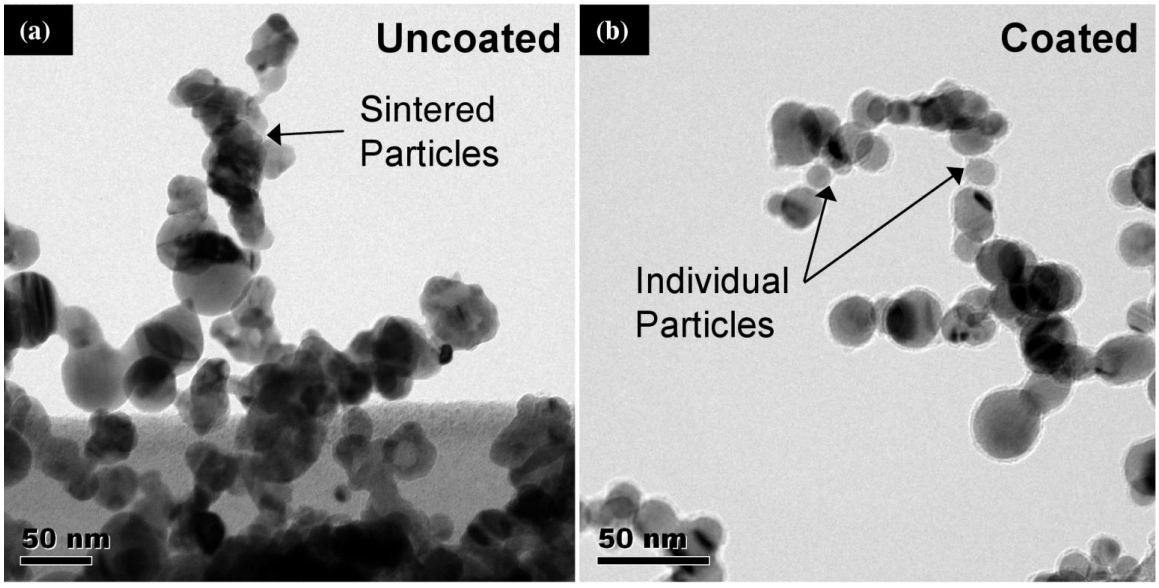

Figure 2.31: Polydisperse silver nanoparticles (a) uncoated and (b) coated at a concentration of 10^7 cm^{-3}.

An important factor in creating individually coated particles at high concentration is the rate of agglomeration for particles within the system. For systems with high agglomeration rates, *e.g.* high particle concentrations, the rate of agglomeration may be faster than the coating production rate. In these instances, the production of individually coated nanoparticles is impossible. The residence time within the photo-CVD system typically ranges from ~5-20 s, and is influenced by chamber volume and volumetric flow rates. In order to determine the concentration of individual particles that remain unagglomerated in a coagulating flow, an analytical study was performed using inputs typical to photo-CVD coating

conditions. As given by Friedlander [80], the rate of change in the concentration of individual primary particles, n_1, undergoing Brownian coagulation is given by the following relation for an initially monodisperse aerosol,

$$\frac{dn_1}{dt} = -\beta\, n_1\, N_\infty, \tag{2.3}$$

where t is time, K is the collision frequency function and N_∞ is the total concentration of all particles. Solving the differential equation for the ratio of the concentration of individual primary particles to the initial concentration of particles gives,

$$\frac{n_1(t)}{N_\infty(0)} = \left(1 + \frac{\beta\, N_\infty(0)\, t}{2}\right)^{-2}. \tag{2.4}$$

The collision frequency function for monodisperse spherical nanoparticles in the continuum regime is given by the relation [80],

$$\beta_{CR} = \frac{8\kappa_B T}{3\mu} \tag{2.5}$$

where κ_B is the Boltzmann's constant, T is temperature and μ is viscosity. The viscosity is a function of temperature and is given by, $\mu = \mu_o \times A/B \times (T/T_o)^{3/2}$, where $A = T_o + C$ and $B = T_o + C$. The values for the viscosity equation constants for a nitrogen gas are $C = 111$ K, T_o =300.55 K and $\mu_o = 1.781 \times 10^{-5}$ Pa s [85]. A simplified version of the collision frequency function for particles in the free molecule regime is given by [80],

$$\beta_{FM} = 4\sqrt{\frac{6\, d_p\, \kappa_B\, T}{\rho}}, \tag{2.6}$$

where d_p is the monodisperse particle diameter and ρ is the density of the particles, which for purposes of this analysis were set to $d_p = 30$ nm and ρ =10.49 g cm^{-3}.

As seen in Figure 2.32, the normalized concentration of individual particles at an initial concentration of 10^8 cm^{-3} decreases with time in both regimes. Within the continuum regime particles agglomerate faster than in the free-molecule regime under the given conditions. Increasing temperatures serve to increase the collision

rates in both regimes and thus reduce the concentration of individual particles at all times.

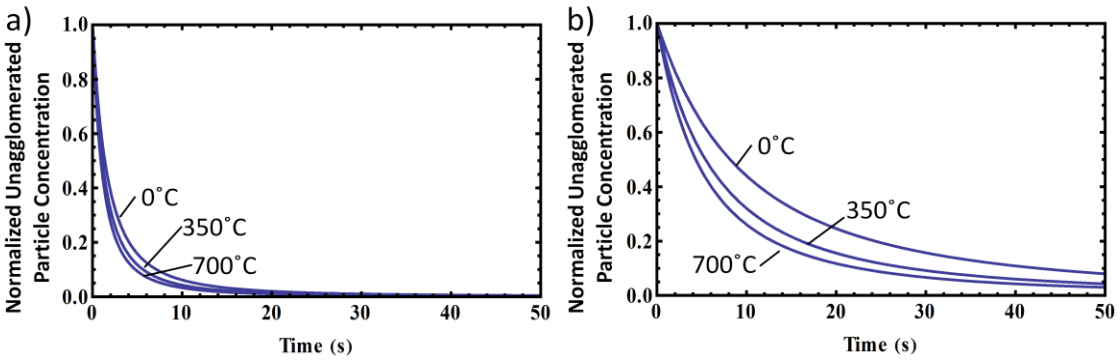

Figure 2.32: Unagglomerated primary particle concentration normalized to the initial particle concentration, 10^8 cm^{-3}, versus time for 30-nm particles undergoing Brownian coagulation at various temperatures in (a) the continuum regime and (b) free-molecule regime.

As shown in Figure 2.33, the initial particle concentration has a large effect on the reduction of the normalized unagglomerated primary particle concentration with time. In both regimes, increased initial particle concentration causes an increase in the agglomeration rates which is evident by inspection of Eqn. 2.4. The increased agglomeration rate leads to a decrease in the number of individual nanoparticles as time increases for both regimes. Under these conditions, the increase in particle concentration has a larger effect on the particles in the continuum regime than the free-molecule regime, as the decay is shown to be much faster for a given initial concentration in Figure 2.33a than Figure 2.33b. The nanoparticles coated in this study are typically in the transition regime as discussed previously and therefore fall somewhere between the two regimes shown in Figure 2.33. Despite the particles being in the transition regime within this study, the analysis depicted in Figure 2.33 is useful in determining the ultimate concentration that can be effectively coated within the photo-CVD system in its current design. For a coating chamber residence time of 5 s, a majority of particles in both the free-

molecule and continuum regime remain unagglomerated when the initial concentration is 10^7 cm^{-3}. These analytical results indicate that an initial concentration of 10^7 cm^{-3} can be effectively coated before significant agglomeration occurs, which agrees with experimental results shown in Figure 2.31. For initial particle concentrations on the order of 10^8 cm^{-3}, the number of unagglomerated particles at 5 s is less than 20% of the initial concentration in the continuum regime, indicating that particles in this regime would agglomerate before particles are effectively coated. For particles in the free-molecule regime (Figure 2.33b), over 60% of the individual particles remain after 5 s for an initial concentration of 10^8 cm^{-3}. The percentage of unagglomerated particles in the transition regime would be somewhere between the two regimes depicted in Figure 2.33, indicating that for an initial concentration of 10^8 cm^{-3}, 20-60% of the particles would remain unagglomerated after 5 s. The initial concentration of 10^8 cm^{-3}, therefore serves as an upper limit to the concentration of particles that can be individually coated under typical conditions within the photo-CVD process. These results show that decreased agglomeration rates occur for higher Knudsen number particles and signify that for all else equal, the agglomeration rates can be slightly suppressed by operating the chamber at lower pressures. The effect of pressure is small however when compared to the effects of temperature as shown in Figure 2.32. Higher concentrations of individual particles may be coated if attempts are made to decrease the collision frequency of the particles by modifying properties, such as the surface charge of the particles to a unipolar state so that electrostatic forces repel particles from each other.

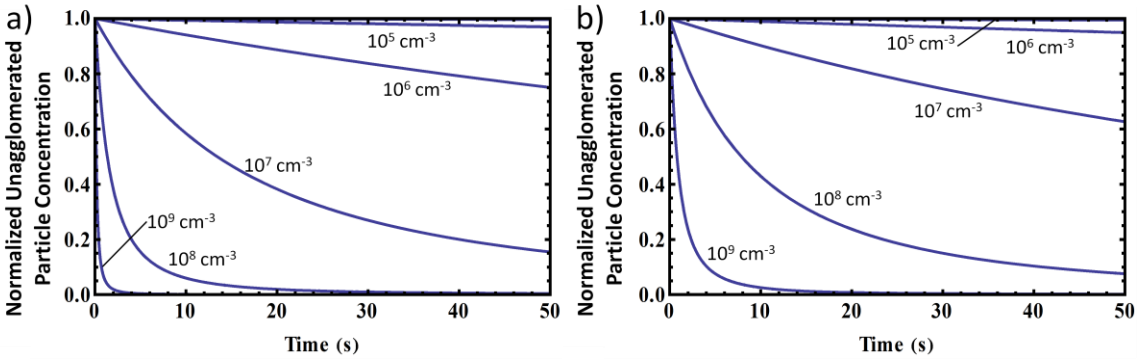

Figure 2.33: Unagglomerated primary particle concentration normalized to the initial particle concentration versus time for 30-nm particles undergoing Brownian coagulation at a set temperature of 20°C and varying initial particle concentrations in (a) the continuum regime and (b) free-molecule regime.

2.6 Silica Coating of Iron Oxide Particles

As discussed in Section 2.1.2, thermal plasmas can be used to produce nanoparticles by thermally decomposing a precursor and then allowing the precursor radicals to nucleate as they pass out of the plasma and begin to cool. Magnetic iron oxide nanoparticles were synthesized in a DC thermal plasma using ferrocene as a chemical precursor. While the direct synthesis of magnetic iron oxide nanoparticles is not the focus of this dissertation, the coating of magnetic iron oxide nanoparticles is of interest and thus experimental conditions are discussed as they relate to the coating process. The magnetic nanoparticles were produced by sublimating ferrocene (solid at room temperature) into an argon flow stream in a heated bed which is maintained at ~120°C and then injecting the ferrocene into the high-temperature zone of the plasma. The applied DC amperage is typically maintained at 250 A with a total power of 6-8 kW. Plasma gases are usually ~30 slm of argon flow and ~5 slm of helium flow, although these are varied. Other gases such as hydrogen have been introduced to determine their effect on the nanoparticle production. The pressure within the plasma chamber is typically maintained at 300 Torr (0.4 atm). Variables of interest within the plasma system that have been shown

to affect the magnetic properties and particle morphologies include oxygen flow rate and injection location, quench gas flow rates, precursor delivery rate and temperature profile downstream from the plasma. The high-temperature region that the gases and particles encounter downstream of the plasma is prolonged by the presence of a ceramic tube near the exit of the plasma jet. The axial location of the tube in relation to the plasma jet is a variable of interest. As shown in Figure 2.34a, the as-synthesized particles typically consist of agglomerates of primary particles with diameters less than 5 nm, which are produced at relatively high production rates (~10 mg hr^{-1}). Agglomeration of particles can be reduced by the addition of quenching flow. Experimental studies have shown that the crystal structure and thus the magnetic moment of the particles are strongly affected by system conditions, as shown in Figure 2.34. As is typical for particles less than 10 nm in diameter, the nanoparticles appear to be superparamagnetic, as indicated by the low coercivity for all curves in Figure 2.34b. As of this writing the maximum saturation magnetization that is regularly achieved for the iron oxide nanoparticles is ~30 emu g^{-1} and efforts are underway to increase this further.

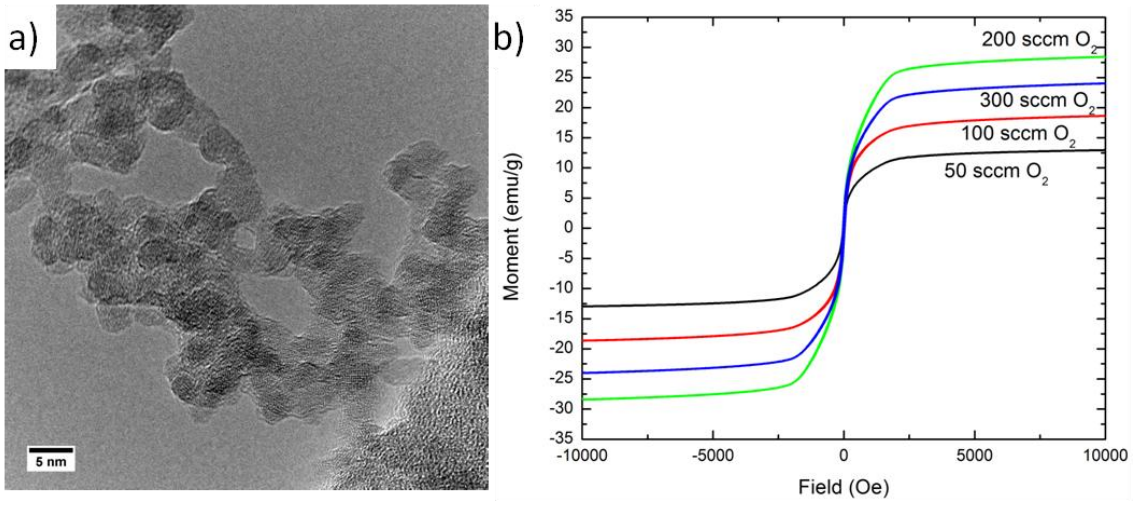

Figure 2.34: (a) TEM image of typical magnetic iron oxide nanoparticles produced in a DC thermal plasma and (b) magnetic hysteresis loops for different oxygen flow rates of iron oxide particles typical of the system.

The coating of iron oxide nanoparticles downstream of the plasma synthesis chamber presents several challenges. A challenge is the difference in pressures of the plasma system and the atmospheric pressure required to do online size measurement with the TDMA system. As shown in Figure 2.35, a venturi pump, *i.e.* ejector (Model: UV143H, Air-Vac Engineering, Seymour, CT), is used to extract aerosol flow from the low pressure plasma chamber and inject it into the higher pressure photo-CVD system. The use of a venturi pump results in a dilution of the aerosol flow of ~60:1 with the nitrogen gas that is typically used to achieve the extraction. This extraction results in a highly diluted flow with much lower mass concentrations than are possible without the venturi. It is possible to coat particles directly after the plasma synthesis process at lower pressures, but the coating cannot be monitored with TDMA equipment. Another challenge of coating particles directly after synthesis is that gases that may participate in photo-CVD reactions, such as hydrocarbons or oxygen, may be present which can affect the coating rate and chemistry.

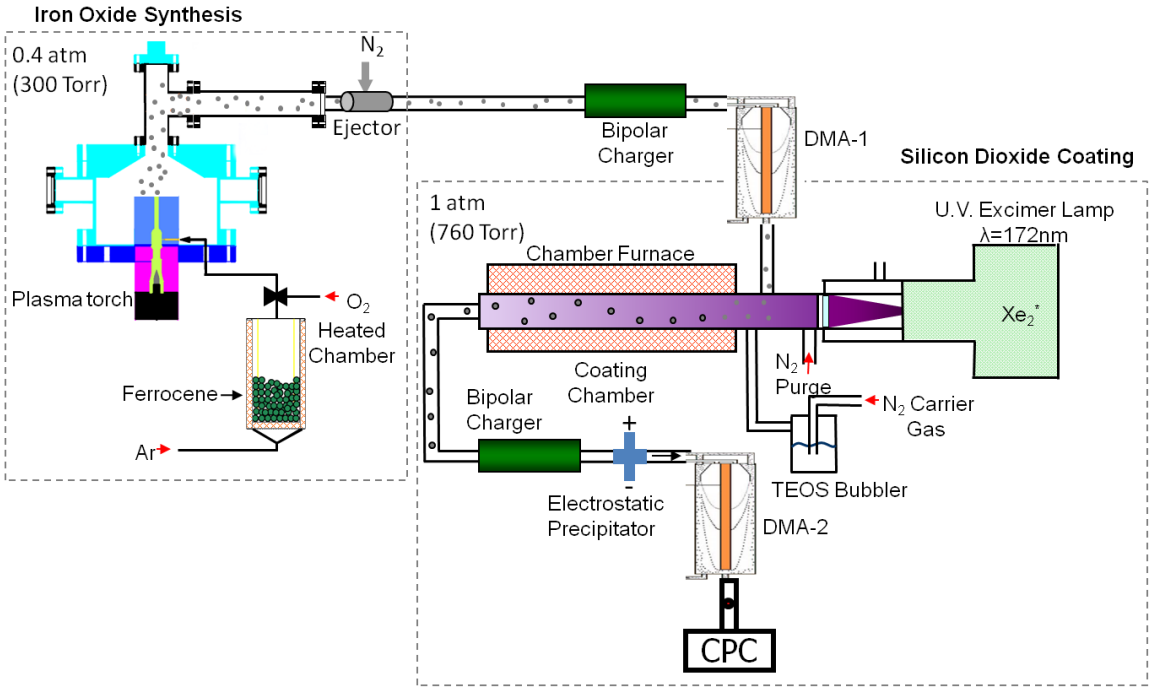

Figure 2.35: Experimental schematic of the photo-CVD coating of iron oxide nanoparticles produced via plasma synthesis.

Like the studies of the photo-CVD coating of silver particles, the coating of plasma-synthesized iron oxide particles was first investigated by TDMA analysis. Particles were ejected from the plasma chamber after synthesis and then size selected at the mode of the distribution, 20 nm, with DMA-1. The monodisperse aerosol flow out of DMA-1, 1 slm, was then injected into the photo-CVD chamber along with 7.2 slm nitrogen purge flow and varying flow rates of TEOS. No oxygen was deliberately added, as oxygen was already present in the aerosol flow as a result of being injected into the plasma during the synthesis of the magnetic iron oxide nanoparticles. The chamber temperature was maintained at 300°C, while VUV radiation served to initiate the coating process. As shown in Figure 2.36, TDMA analysis of coated particles indicated that particles were effectively coated with increasing coating thickness as the TEOS flow rate increased. Like the coating of

silver particles, the coated particles remained monodisperse with a slight increase in the standard deviation in particle size from 0.91 nm for size selected bare iron oxide nanoparticles (0 sccm of TEOS) to a standard deviation 1.79 nm for 1.23 sccm of TEOS. As shown in Figure 2.36b, the growth in coating thickness showed good agreement, in terms of overall coating thickness, with the coating thickness measured on silver nanoparticles under similar conditions shown in Figure 2.20. The increase in coating thickness was non-linear, which may have been the result of coating particle agglomerates rather than individual nanoparticles as was done for the silver experiments. Nevertheless, the similarity in the magnitude of growth and trends between Figure 2.36 and Figure 2.20 indicate that particle coatings can be achieved on a variety of core-particle chemistries with similar results.

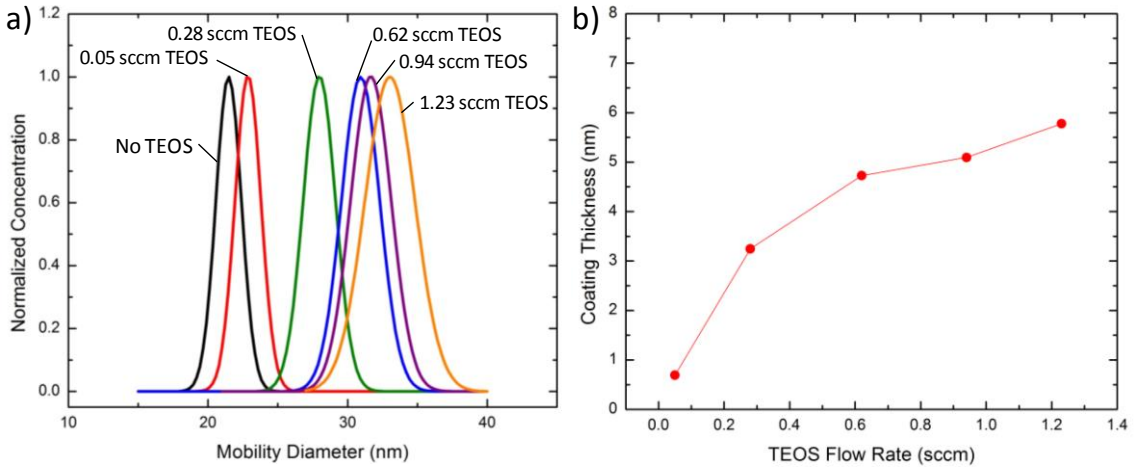

Figure 2.36: Normalized Gaussian distributions fit to TDMA data for the photo-CVD coating of magnetic iron oxide nanoparticles at different TEOS flow rates and (b) coating thickness versus TEOS flow rate.

In order collect sufficient particles for TEM analysis, coating experiments were conducted without the ejector where the aerosol chamber was operated at the same pressure as the coating chamber (~300 Torr). By injecting the iron oxide particles directly after synthesis into the photo-CVD chamber, the total concentration of the particles was much higher than if particles were diluted by the

ejector. Particles were collected at the exit of the coating chamber by electrostatic precipitation as discussed previously. An experimental run was conducted with similar flow and temperature conditions to Figure 2.36, where the nitrogen purge flow rate was 6.2 slm, the polydisperse aerosol flow rate was 1.5 slm, and the TEOS flow rate was 1.23 sccm. The photo-CVD chamber was maintained at 300°C and no additional oxygen gas was added. As shown in Figure 2.37a, many of the iron oxide nanoparticles were non-spherical. Despite their non-spherical structure the photo-CVD process appeared to coat both spherical and non-spherical particles alike. The high resolution image, Figure 2.37b, shows that the particle cores remain crystalline while the observed coating thickness at low pressures agrees well with the experimental results shown in Figure 2.36 for a TEOS flow rate of 1.23 sccm. The 3 Å lattice spacing corresponds to the (220) plane of γ-Fe_2O_3 and indicates that the particles examined consisted predominately of γ-Fe_2O_3 [86]. While these results were promising because γ-Fe_2O_3 is desirable due to its inherent high saturation magnetization, no attempt was made at doing a full statistical study of the core particles within the TEM. Further studies are required to better characterize the crystalline structure of the entire population of iron oxide particles. These results indicate that sub-atmospheric pressure coatings are possible directly after the plasma synthesis chamber. However, it is likely that the lower pressures and presence of different gases may affect coating thicknesses and that the results of Figure 2.36, may not be useful in guiding all sub-atmospheric experimental studies.

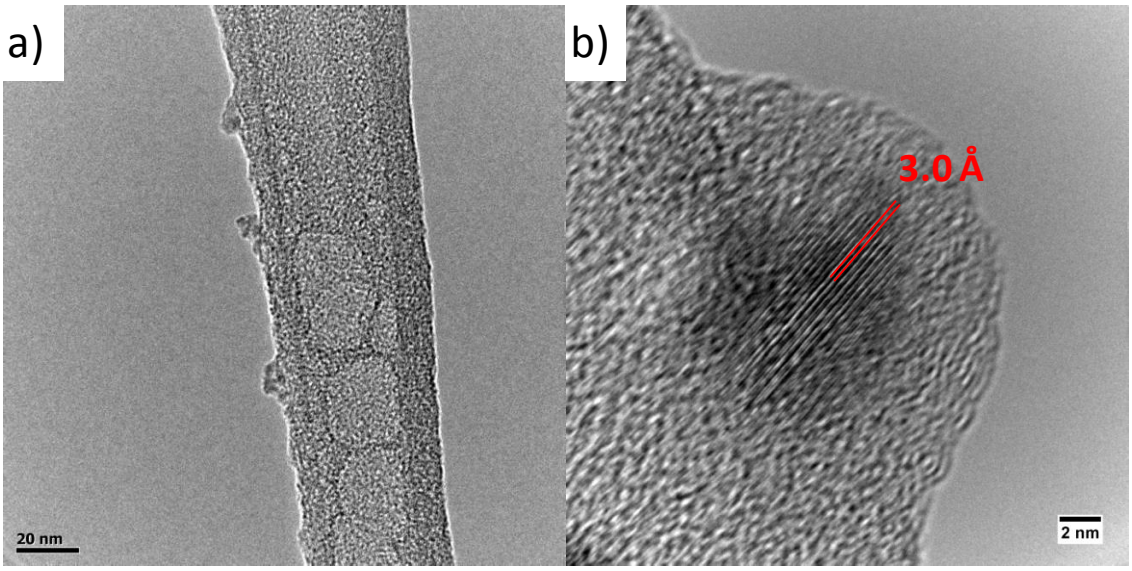

Figure 2.37: (a) Low and (b) high resolution TEM images of silica coated iron oxide nanoparticles.

While analysis of the core particle lattice fringes indicated that the cores consisted of iron oxide, an EDX line scan was conducted to determine the elemental composition throughout a coated particle. As shown in Figure 2.38, the coated iron oxide particles had a noticeable contrast difference between the core and shell structure within the dark- and bright-field STEM images, Figure 2.38a and b respectively. The elemental line scan indicates that the lighter-contrast region within the shell consisted primarily of silicon and oxygen. The higher contrast within the core indicates the presence of iron. For positions near the back of the particle, *i.e.* position greater than 12 nm, the iron, silicon and oxygen signals are dominated by the signal from the carbon grid to which the particle was attached. These results confirm that the particle coatings consist of silicon and oxygen, as was the case for the study of the silica coating of silver discussed previously in the chapter.

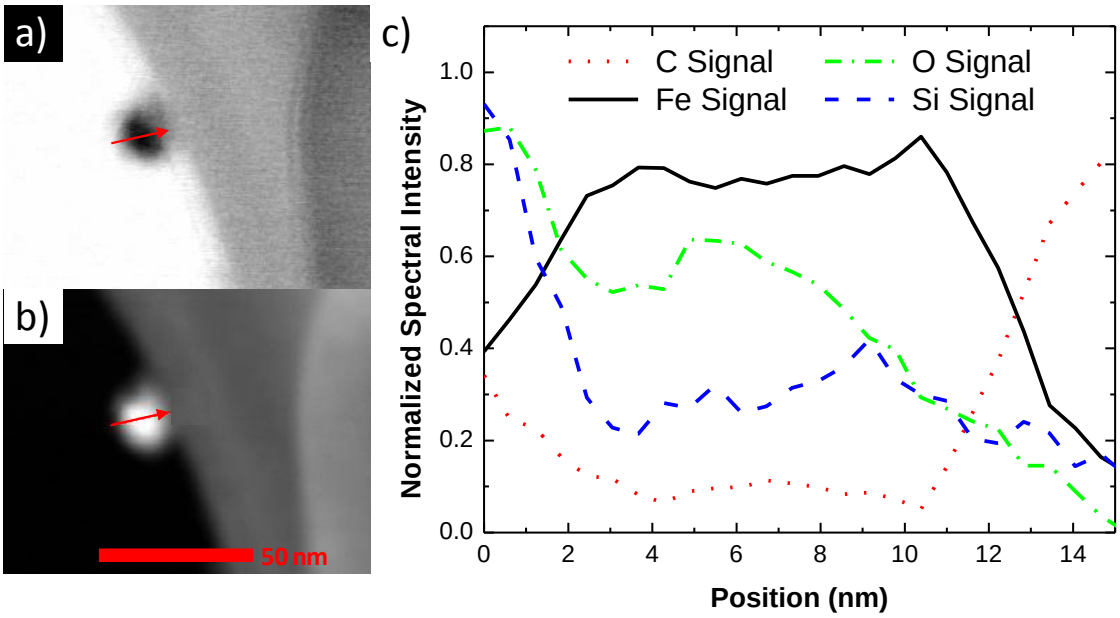

Figure 2.38: Silica coated iron oxide nanoparticle on lacey carbon grid STEM (a) dark- and (b) bright-field images and (c) normalized EDX elemental line scan.

2.7 SUMMARY

This study has shown that the photo-CVD process effectively produces coatings from a silicon oxide precursor on gas-phase nanoparticles. The chemical compound, TEOS, was shown to be an effective precursor for the production of silica coatings and regimes were identified where homogeneous nucleation of the precursor was not present. Sodium chloride and PSL particles were found not to be suitable candidates for a coating study of the photo-CVD process as sodium chloride particles melted under a TEM electron beam and PSL particles were disintegrated by the VUV lamp. YAP particles were successfully coated and characterized using the photo-CVD process. Results indicated that YAP could be used to study fundamental mechanisms of the coating process, but its use was abandoned as the production of reproducible solutions for nebulization was problematic.

Studies have determined that silver particles are well suited for fundamental coating studies because of the ease of production and characterization. Using silver

particles we have determined the relation between coating thickness and key system parameters such as precursor flow rate, bulk gas flow rate, particle size, and VUV radiation intensity. From infrared spectrometry and elemental analysis it was confirmed that the quality of the silica coatings depends on the coating-chamber temperature and is improved by the presence of oxygen within the coating chamber. Experimental studies indicate that both gas and surface reactions are important in the coating process and that growth may be limited by reactions rather than by diffusion of gas-phase species to the particle surface. The photo-CVD coating technique was shown to produce silica coatings that provide an effective barrier to particle core agglomeration, and to provide uniform coatings at particle concentrations at least as high as 10^7 cm^{-3}. Analytical analysis indicates that 10^8 cm^{-3} is an upper limit to the concentration of particles that can be individually coated in the photo-CVD chamber due to the increased agglomeration rates of aerosols with higher initial concentrations. Methods such as unipolar charging could be employed to suppress agglomeration at higher concentrations, but were not studied here.

Studies of the photo-CVD coating of plasma-synthesized magnetic iron oxide particles indicated that particles can be coated directly after plasma synthesis. Challenges exist in the coupling of the photo-CVD coating process with the plasma chamber. Using an ejector, particles were sampled from the low-pressure plasma chamber and injected into the photo-CVD coating chamber where TDMA analysis indicates that iron oxide particles are coated in a similar manner as silver particles. Experiments have also shown that the photo-CVD chamber can be operated at pressures equivalent to the plasma synthesis chamber (300 Torr). While operating the chamber at lower pressures limits the ability to monitor the growth by TDMA, both TEM and EDX analysis have shown that iron oxide nanoparticles can be coated at low pressures and that the particles are successfully coated with silica even when non-spherical geometries exist. Further work is needed to determine the effect of the silica coating on the magnetization of the particles.

Chapter 3 - Chemical Kinetics Model of Photo-CVD System

3.1 Overview

As discussed in Chapter 2, the synthesis of core-shell nanoparticles has received much interest in recent years as the production of such structures can enhance properties such as thermal stability [87], plasmon resonance [88], catalytic activity [89] and surface functionalization [90] among others. There are currently a wide variety of techniques available to produce composite particle structures including gas- [91], liquid- [92] and solid-phase [93] synthesis. While all approaches have inherent advantages, the production of composite nanoparticles by gas-phase methods allows for particles to be produced at high throughputs, in inert or non-reacting environments with little or no surface impurities. Photochemical vapor deposition (photo-CVD) is a gas-phase approach that allows for the production of a variety of core-shell compositions including organic [26] and inorganic coatings [94] of nanoparticles. While the approach has been shown to work experimentally, a fundamental understanding of the chemical mechanisms involved in the coating process does not yet exist.

Silica coatings are particularly important at both the macro- and nano-scale because of silica's thermal stability [95], high electrical resistivity [62] and surface that is easily functionalized through ligand attachment [96]. Several research groups have examined chemical mechanisms involved in the thermal decomposition of tetraethyl orthosilicate (TEOS) onto macroscopic surfaces for purposes of producing films relevant to the semiconductor industry [82, 97-99]. Coltrin *et al.* specifically examined the decomposition of TEOS to produce silica films on a series of wafers placed perpendicular to a reacting flow stream. While the approach highlighted the production of silica for a specific geometry, it provided a general mechanism that

relied on experimental [98] and theoretical [100] studies of the TEOS-silica system. The Coltrin *et al.* mechanism included four gas-phase reactions and eight surface reactions, none of which included oxygen (monatomic, diatomic or ozone) as a separate reactant in any form. The primary gas-phase reaction involved in the production process was reported as the beta-hydride elimination of ethylene, which is the least endothermic gas-phase reaction (~10 kcal/mol) for TEOS [101]. The primary surface reactions responsible for film growth were found to be the adsorption of the TEOS radical, triethoxysilanol [$Si(OH)(OC_2H_5)_3$], onto the surface and then subsequent removal of the remaining ethyl groups. Modeled growth rates from Coltrin *et al.* provide adequate agreement with molecular beam experiments and CVD experiments performed by Kalidindi and Desu [102]. Their study concludes that at lower temperatures the gas-phase TEOS reaction is the rate-limiting reaction while at higher temperatures the ethyl removal at the surface is rate limiting [82].

Work by Romet *et al.* focused on the production of silica from TEOS by examining ozone related reactions [97]. Their mechanism contained many reactions, including the gas-phase reactions of TEOS with monatomic oxygen as well as ozone. In all they developed a mechanism with 33 gas-phase reactions, which included TEOS decomposition reactions as well as oligomer formation. The reaction of TEOS with monatomic oxygen, an important reaction in this study, was estimated from experimental work by Sanogo and Zachariah [98]. Like Coltrin *et al.* they found that the gas-phase decomposition of TEOS to form triethoxysilanol was the dominant reaction when ozone was used as a precursor. Additionally, they showed that under certain conditions it was possible to form oligomers, which can grow large enough to be detected as particles, which has been observed within our experimental setup under certain conditions. The surface reactions of Romet *et al.* included a simplified mechanism whereby the remaining ethyl groups on adsorbed triethoxysilanol were removed in a single step to form another receptor site for further growth. This assumption caused the total mechanism to be gas-phase-

reaction limited in all cases. The Romet *et al.* mechanism accurately predicts the growth of films at low temperatures, but begins to deviate at high temperatures. The mechanism predicts growth rates accurately at pressures up to 500 Torr but begins to deviate at higher pressures due to the formation of oligomers [97].

While previously developed mechanisms accurately describe the production of thin films from thermal decomposition or reaction with monatomic oxygen, they do not include photochemical reactions. The purpose of this study is to develop a chemical mechanism that includes photochemical reactions to model the growth of silica films on nanoparticle surfaces as described in Chapter 2. The previous TEOS mechanisms serve as a starting point for this study's chemical mechanism. While to our knowledge no group has examined the chemical mechanisms involved with photo-CVD, others have experimentally investigated the production of thin films with TEOS on macroscopic substrates by photo-CVD [56, 83]. These analyses did not explicitly examine the reaction kinetics but the research identifies important reaction parameters by experimentally investigating the chemical structure of films produced by modifying different system parameters such as precursor and purge gas flow rates, as well as additional reacting gases such as oxygen. In addition to adding the photo-induced reactions to the chemical mechanism, the present study introduces nanoparticles as the surface sites for CVD growth.

3.2 MODELING

3.2.1 MODEL THEORY

In this study a chemical kinetics model was developed within the framework of a commercially available kinetics software package, CHEMKIN-PRO (Reaction Design, San Diego, CA) to numerically solve the series of differential equations that represent the chemical mechanism within the photo-CVD system. The existing software platform allowed for the direct implementation of gas-phase, gas-surface and surface reactions. To model reactions that occur on nanoparticle surfaces and

by nanoparticle and gaseous precursor collisions, an additional software package, Particle Tracking Module, is used to model the behavior of these interactions. The Particle Tracking Module uses the method of moments to describe the properties of a size distribution of particles in terms of their average characteristics [103]. The method of moments increases the calculating efficiency of particle models when compared to other methods of solving the aerosol general dynamics equation. Variations of this method are used by many in numerical simulations and are accurate, so long as the aerosol has a well-behaved monomodal distribution [80, 104, 105]. The Particle Tracking Module is based on the work of Frenklach and Harris which approximates the general dynamics equation to account for particle nucleation, coagulation, and particle growth [106]. The method makes no assumption about the particle size distribution or the collision coefficient, but instead gains numerical efficiency by approximating the infinite sum that arises in the moments of particle distributions with one that is more readily solved. A detailed derivation of the model can be seen in Frenklach and Harris and the CHEMKIN theory manual shows how it is implemented within the code [82, 106].

The theory for the entire CHEMKIN-PRO modeling platform is contained within the CHEMKIN Theory Manual [103]. The following discussion highlights those aspects of the model that pertain directly to modeling the photo-CVD coating of nanoparticles.

Gas-phase reactions are modeled using Arrhenius parameters for each specific reaction within mechanism. The production rate for the k^{th} species is determined by the following relation,

$$\dot{\omega}_k = \sum_{i=1}^{I} v_{ki} q_i \quad (k = 1, \dots, K) \tag{3.1}$$

where v is the stoichiometric coefficient for the i^{th} reaction. The rate of progress, q, is given by the law of mass action from the difference in the forward and reverse reaction rates according to,

$$q_i = k_{fi} \prod_{k=1}^{K} [X_k]^{v'_{ki}} - k_{ri} \prod_{k=1}^{K} [X_k]^{v''_{ki}} \quad (3.2)$$

where $[X]$ is the molar concentration and v' and v'' are the stoichiometric coefficients for the reactants and products respectively. For each reaction, the Arrhenius coefficients for the forward reaction constant are calculated according to the equation,

$$k_{fi} = A_i T^{\beta_i} \exp\left(\frac{-E_i}{RT}\right) \quad (3.3)$$

where T is the temperature and R is the universal gas constant. The pre-exponential factor A, the temperature exponent β and the activation energy E_i were provided as inputs into the model. The reverse reaction constant, k_r, was calculated from the forward reaction constant and the equilibrium constant, K_c, according to the relation,

$$k_{ri} = \frac{k_{fi}}{K_{ci}} \quad (3.4)$$

where the equilibrium constant is more easily described in terms of non-dimensional pressure units by

$$K_{ci} = K_{pi} \left(\frac{P_{atm}}{RT}\right)^{\sum_{k=1}^{K} v_{ki}} \quad (3.5)$$

in which P_{atm} is the atmospheric pressure (or comparable reference pressure of data set). The equilibrium constant based on pressure units can then be determined from fundamental thermodynamic data of each species according to the relation

$$K_{pi} = \exp\left(\frac{\Delta S_i^\circ}{R} - \frac{\Delta H_i^\circ}{RT}\right) \quad (3.6)$$

where ΔS_i° and ΔH_i° refer to the change in entropy and enthalpy, respectively that occurs from entirely passing from reactants to products at standard pressure [103]. For each reversible reaction within the model the reverse reaction rate constant is calculated from the forward rate constant and the equilibrium constant based on user-input thermodynamic data for each species contained within the mechanism. All thermodynamic data came from the NASA Glenn Research Center with a reference state of 298.15 K and 1 bar [107].

Surface reactions are modeled in a similar manner as the gas-phase reactions, whereby the surface production rate [mole cm^{-2} sec^{-1}] for the k^{th} species, regardless of phase, is determined by the following relation,

$$\dot{s}_k = \sum_{i=1}^{I} \nu_{ki} q_i \quad (k = 1, \dots, K) \tag{3.7}$$

where q is the net reaction rate of the reactions involving surface species. Similar relations to Eqns. 3.2-3.6 are used in determining the net surface production for a given species on a macroscopic substrate. Surfaces within the model are tracked according to surface site density in which a site location can be occupied by different surface species compatible with that site. The number of surface sites occupied by an individual species is tracked according to its site fraction, Z_k. The molar concentration on the surface is then determined by

$$[X_k] = Z_k \Gamma / \varsigma_k \tag{3.8}$$

where Γ is the density of sites [moles cm^{-2}] and ς is the number of surface sites occupied by species k (ς =1 for all species in this study).

In order to simulate reactions between gas-phase precursors and the particle surface, the model uses the surface reaction solver for macroscopic surfaces to determine reactions that occur on the particle. The resulting change in particle size, surface area, mass, etc. are tracked with the Particle Tracking Module by incorporating the changes into the appropriate moments. For gas-particle reactions the model determines the reaction rates between gas-phase species and particles by assuming that all interactions are in the free-molecule regime. The frequency function of reacting collisions is given by the relation,

$$\beta_{\chi,j} = \gamma \times \sqrt{\frac{\pi \kappa_B}{2 m_o}} \times \sqrt{T} \times (d_\chi + d_j)^2 \times \prod (\Theta_{\chi(s)})^{\nu_{\chi(s)}}, \tag{3.9}$$

where γ is the sticking coefficient, κ_B is the Boltzmann constant, m is the reduced mass, d is the collision cross section, and χ and j are the gas species and particle size class respectively. The dimensionless term $\Theta_{\chi(S)}$ is the site fraction of surface

species $\chi(s)$, and $v_{\chi(s)}$ is the stoichiometric coefficient of the surface reactants. The typical CHEMKIN-PRO model rate of progress solver uses a sticking coefficient, γ, for both TEOS and sub-TEOS species by using the STICK subroutine within CHEMKIN-PRO. Using the STICK routine, stick parameters are input for each gas-particle reaction in order to calculate the sticking coefficient according to the following relation,

$$\gamma_i = a_i T^{b_i} \exp\left(\frac{-c_i}{RT}\right) \tag{3.10}$$

where *a, b* and *c* are the input parameters. Because the sticking coefficient is a probability, its value lies between 0 and 1 and thus any values greater than 1 are replaced with unity. The rate constant for an adsorption reaction, *i*, is given by,

$$k_{fi} = \frac{\gamma}{\pi} \times \sqrt{\frac{\pi \kappa_B}{2m_o}} \times \frac{\prod(\chi(s))^{\nu_x(s)}}{\Gamma^{\sum \nu_x(s)}}. \tag{3.11}$$

Therefore the rate of deposition, r_{is}, in terms of [mole cm^{-2} s^{-1}] for an adsorbing species, $\chi(s)$, is

$$r_{is} = k_{fi}[\chi] \prod[\chi(s)]^{\nu_x(s)}. \tag{3.12}$$

Gas-phase coagulation is omitted as experimental studies discussed in Chapter 2 have shown no indication of significant particle agglomeration when concentrations are less than 10^8 cm^{-3}. Nucleation of the gas-phase reactants is modeled by including oligomerization reactions which give an indication whether particles are likely to homogenously nucleate from TEOS.

The simulation uses a plug-flow reactor routine as the basis for modeling the photo-CVD reaction chamber whereby the gas-phase composition is assumed to be kinetically limited. As a result, the transport of species is assumed to be infinitely fast at each axial location of the gas. All gas and aerosol properties are assumed to be well-mixed on the cross-flow plane, that is, no mass or energy transfer in the transverse direction. Additionally, the gas velocity is assumed to be large enough so that diffusion fluxes in the flow direction are insignificant and therefore axial

diffusion is neglected [103]. Therefore, the transport equation governing the gas-phase species balance for a plug-flow system is given by

$$\rho u A \frac{dY_k}{dx} + Y_k \sum_{m=1}^{M} a_{i,m} \sum_{k=1}^{K_g} \dot{s}_{k,m} W_k = W_k \left(\sum_{m=1}^{M} \dot{s}_{k,m} a_{i,m} + \dot{\omega}_k A \right) \quad (3.13)$$

where Y_k is the mass fraction of species k, $\dot{\omega}$ is its molar rate of production by homogeneous gas reactions, ρ is density, u is the axial velocity of the gas, K_g is the number of species, W_k is the molecular weight and $\dot{s}_{k,m}$ is the molar production rate of species k by all surface reactions. The transport equation in the plug-flow reactor for species on particle surfaces, χ_{ps}, is given by,

$$u \times \frac{d\Theta_{ps}}{dx} + \Theta_{ps} \times \frac{du}{dx} = \frac{\sigma_{ps} \times \dot{s}_{ps}}{\Gamma} + \frac{1}{A_s} \times \sum_{nuc} \left[\left(\Theta_{nuc,ps} - \Theta_{ps} \right) \times \left(\frac{dA_s}{dt} \right)_{nuc} \right] \quad (3.14)$$

where Θ_{ps} is the site fraction of surface species. As stated previously, nucleating reactions are neglected and therefore the transport equation for bulk species can be simplified to be

$$u \times \frac{d\Theta_{ps}}{dx} + \Theta_{ps} \times \frac{du}{dx} = \frac{\sigma_{ps} \times \dot{s}_{ps}}{\Gamma}. \quad (3.15)$$

Finally the change in the moment of the size distribution, M_r, as a result of diffusion is given by the following relation

$$u \times \frac{dM_r}{dx} + M_r \times \frac{du}{dx} = S_r, \quad (3.16)$$

where S_r is the production term for the r-th particle size moment produced by surface reactions.

As of this writing no other known studies have modeled gas-photon and particle-photon reactions within the CHEMKIN environment. To determine how photochemical reactions are best modeled within CHEMKIN, the study first investigated the photodecomposition of O_2. The basics of a photochemical reaction, as discussed by Wayne [108], for a simple O_2 decomposition reaction is described by the following relation,

$$O_2 + h\nu \rightarrow 2O \quad (3.17)$$

where $h\nu$ denotes the flux of photons, which in this study have 7.2 eV per photon (corresponds to 172 nm wavelength). The reaction rate between the photons and the O_2 depends on the absorption of the photons by oxygen as they pass through the volume. Using the Beer-Lambert law to describe the decay of light as it passes through a medium, the rate of photon absorption can be found for the assumption that all light not transmitted is absorbed, *i.e.* that no light is scattered. As a result, the number of photons absorbed across a given volume with width x [cm] is described by

$$h\nu_a = h\nu_i(1 - e^{-\sigma N_{O_2} x}) \tag{3.18}$$

where $h\nu_a$ and $h\nu_i$ are the absorbed and incident photons, respectively with units of [photons cm^{-2} s^{-1}]. The exponential factors σ and N are the gas-absorption cross section [cm^2] and gas number density [cm^{-3}], whereby $N_{O_2} = [O_2]N_{Avog}$. For cases in which x is small relative to the overall length of the system, higher order terms can be omitted in the power series expansion of $e^{-\sigma N x}$. The resulting equation for absorbed photons is then given by the linear relation,

$$h\nu_a = h\nu_i \sigma N_{O_2} x. \tag{3.19}$$

The rate of O_2 molecular destruction can be related to the number of absorbed photons by the relation,

$$\dot{Q}_D = -\frac{d[O_2]}{dt} = \frac{\phi}{N_{avg}} \frac{d(h\nu_a)}{dx} \tag{3.20}$$

where $\dot{Q}_D$ is the destruction rate and ϕ the probability that an absorbed photon will cause a dissociating reaction. By solving for the derivative in Eqn. 3.20 when combined with Eqn. 3.19, the resulting destruction rate is given by

$$\dot{Q}_D = \phi \frac{d(h\nu_i \sigma N_{O_2} x)}{dx} = \frac{\phi}{N_{avg}} \left(h\nu_i \sigma N_{O_2} + h\nu_i \frac{d(N_{O_2})}{dx} \sigma x + \frac{d(h\nu_i)}{dx} \sigma N_{O_2} x \right). \tag{3.21}$$

Note that a unit analysis, using units compatible with the model, indicates that $\dot{Q}_D$ has units of [mole cm^{-3} s^{-1}], which corresponds to the right hand side of Eqn. 3.21, where ϕ is the reactions per absorbed photon (a number from 0 to 1), N_{avg} has

units of [molecules mole^{-1}], σ has units of [cm^2 s^{-1}] and N_{O_2} has units of [molecules cm^{-3}]. The representation of the gradients of N_{O_2} and $h\nu_i$ with respect to x, denoted by the terms $\frac{d(N_{O_2})}{dx}$ and $\frac{d(h\nu_i)}{dx}$, are explored in the model and are discussed further in the results sections of this chapter.

3.2.2 Model Structure

As stated previously, CHEMKIN-PRO does not contain the ability to address photo-chemical reactions within its existing framework. As a result, a subroutine is called for each photo-chemical reaction in order to determine the correct reaction rate and track the flux of photons at each point down the perfectly stirred reactor. As shown in the flowchart depicted in Figure 3.1, the model has information input about the overall reaction mechanism, consisting of Arrhenius reaction parameters for reactions that do not involve photons. All gas, surface and photochemical reactions are specified within the input files, but the photochemical reactions are provided by a user defined rate of reaction by specifying the term USRPROG after the reaction definition (for further details about the user defined rates of progress command USRPROG, see the CHEMKIN-PRO Applications Programming Interface Manual [109]). By specifying the USRPROG command, the model takes in specified rates of reactions from the CKUPROG routine which is modified to calculate the correct rates of progress for photochemical reactions under different modeling conditions. For each position step, the series of coupled differential equations that represent the chemical mechanism is solved using the CHEMKIN-PRO numerical solver. As the photon flux varies as a function of position, the current position of the solver is needed to determine the correct rate of progress for the photochemical reactions. The position for each iteration step is recorded using the PLGEOM routine [109], which is activated by declaring a user-defined geometry for the tube cross section within the graphical interface of the CHEMKIN-PRO modeling environment. The PLGEOM routine is modified to maintain the geometry of the plug-flow reactor,

but also record the axial location of each iteration to a separate file. The CKUPROG routine then reads in the axial location at each calculation step and determines the rate of progress for each photochemical reaction. Examples of the PLGEOM and CKUPROG routines are given in Appendix A.

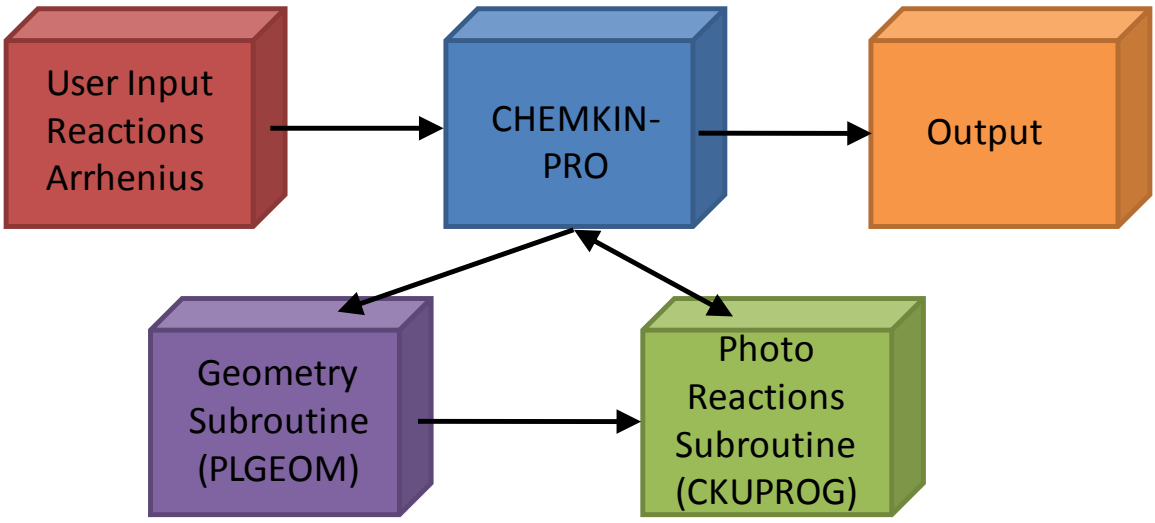

Figure 3.1: Flow chart of model information for purposes of simulating photo-CVD reactions.

3.2.3 Model Inputs

The kinetics model simulates the photo-CVD coating of particles with silica using TEOS as a precursor for conditions that match the experimental study discussed in Chapter 2. The experimental schematic shown in Figure 3.2a depicts the conditions that the model simulates, where a pre-synthesized aerosol enters with TEOS and purge flow near an ultraviolet lamp and then flows down a cylindrical chamber, away from the lamp, as particle growth occurs due to CVD reactions. While a variety of experimental configurations were investigated, this model simulates the conditions that were used experimentally when producing Figure 2.20. Therefore the chamber is modeled as a tube with an inner diameter of 3.4 cm and a length of 122 cm. The lamp emits VUV photons with a power of 50 mW

cm^{-2} across a 7.07 cm^2 area which corresponds to a photon flux of 3.4×10^{16} photons s^{-1} cm^{-2}. Flow rates of nitrogen purge gas, TEOS and oxygen are varied to match experimental conditions. The reactor is maintained at 400°C and atmospheric pressure within the model and the energy equations are not solved to increase calculation efficiency. The photo-CVD reactor is modeled within the CHEMKIN-PRO environment by a series of components, as shown in Figure 3.2b. The components within the model are (from left to right) the fully mixed inlet, where the bulk flow rate of the system and mole fractions of the flow are defined along with the aerosol parameters (referred to as condensed-phase media) such as the initial concentration and particle diameter; the perfectly-stirred reactor (PFR), where conditions such as system temperature and chamber geometry are specified; and reactor products, which serves as an outlet for the entire system. Unless otherwise noted, the core particles included in the inlet into the system are defined as silica particles with a concentration of 10^7 cm^{-3} and an initial particle size of 30 nm.

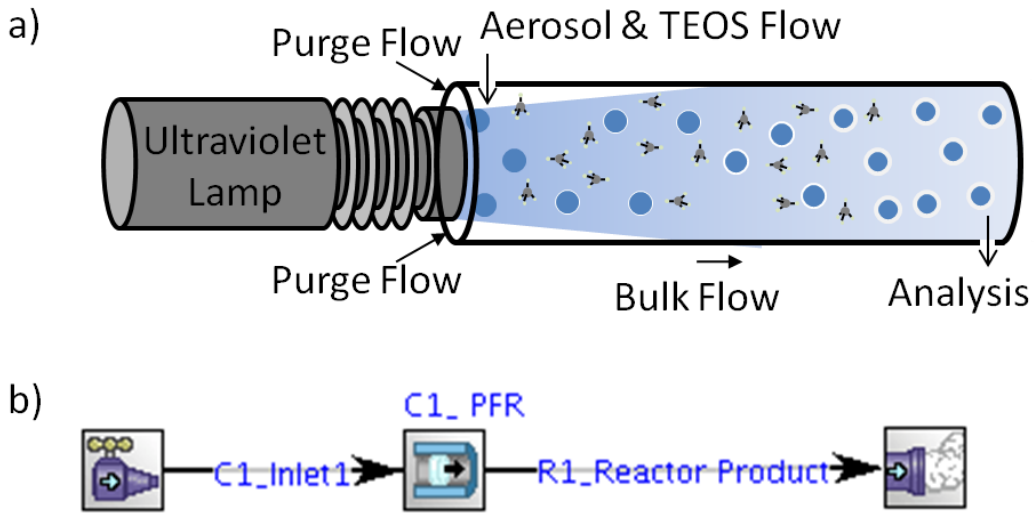

Figure 3.2: (a) Experimental schematic of nanoparticle silica coating by photo-CVD with TEOS as a precursor. (b) Schematic of CHEMKIN representation of photo-CVD system.

Inputs to the plug-flow reactor model are presented as a series of gas-phase, surface, and thermochemical data in accordance with CHEMKIN-PRO input requirements [110], examples of which can be found in Appendix A. The complete chemical mechanisms for both gas-phase and surface reactions are given by Table 1 and Table 2, respectively. The dominant reaction mechanism is shown schematically in Figure 3.3a. As shown in Figure 3.3b, the same notation is employed for surface species as proposed by Coltrin *et al.* [82] where G refers to glass bonds (Si-O-Si) with the particle surface and E refers to a surface ethoxy group. The model also includes a nucleation reaction which is not shown in Table 1 (shown in Appendix A). The nucleation reaction is required for the Particle Tracking Module to run effectively, but the reaction rate is set to zero so that no nucleation occurs. Both the gas-phase and surface mechanisms include TEOS reactions from Coltrin *et al.* [82], TEOS and oxygen reaction from Romet *et al.* [97] and photochemical reactions distinct to this study. The photochemical reactions only include species that had mass within the mechanism input files and therefore the photons are not included within the reaction but rather within the Arrhenius coefficients. The reaction dynamics of the photochemical reactions are fit to Arrhenius coefficients for a hypothetical scenario in which the photon flux remains constant for all axial locations (note that this rate is overridden when the USRPROG is included). As an example, when the photon flux is held constant for the oxygen decomposition reaction as shown in Eqn. 3.17 and the change in oxygen concentration is assumed to be negligible over each differential element, then the rate of progress for the reaction is given by the relation

$$q = \phi h\nu\sigma \frac{N_{O_2}}{N_{avg}}. \tag{3.22}$$

By comparison of Eqn. 3.22 with Eqn. 3.3, the resulting Arrhenius parameters are found, $A = \phi h\nu\sigma$, β=0 and E =0. For all photochemical reactions considered within this study ϕ=1 because of the high energy associated with radiation at 172 nm

wavelength [108]. The radiation absorption cross section of diatomic oxygen is σ=6×10^{-19} cm^2 [111]. The absorption cross sections for other species are not well known and were used as variable parameters within the model.

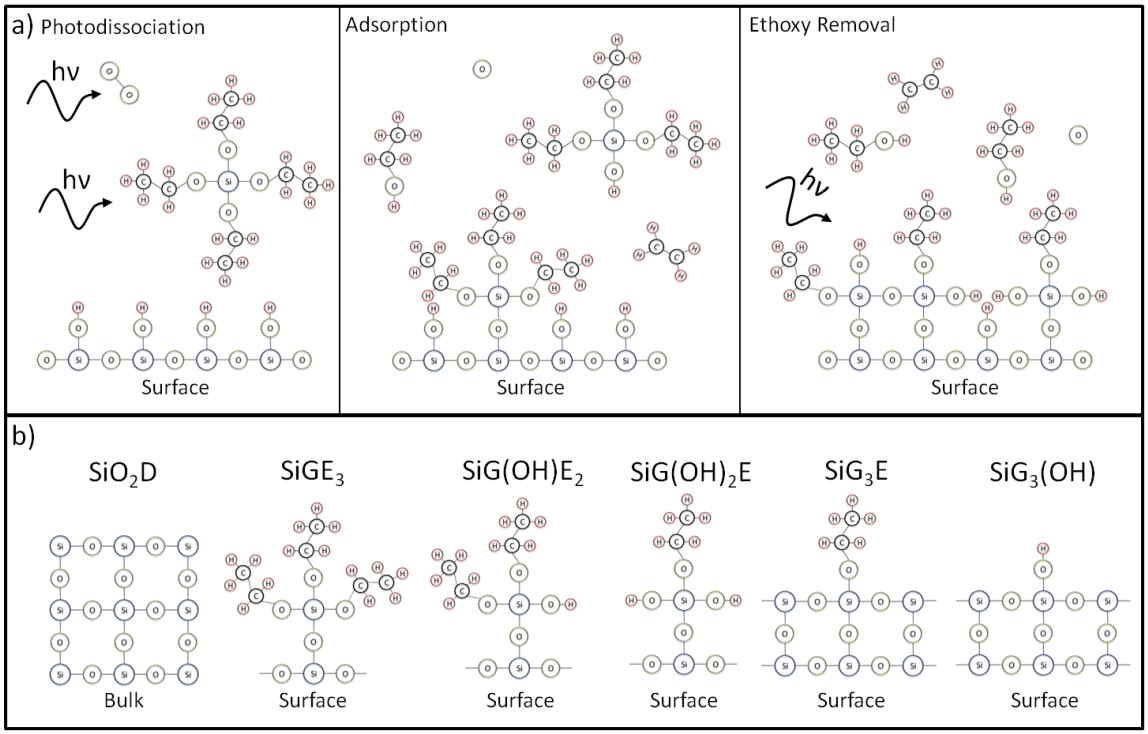

Figure 3.3: (a) Schematic representation of dominant reaction mechanism and (b) depiction of bulk and surface species.

The model differential equation solver parameters are held constant for all runs. The geometric step size is determined by an optimization method within the code but is not allowed to exceed 1 cm to ensure that the differential elements are small. Additionally, the maximum number of iterations per axial position is increased from the default of 4 to 100, the absolute tolerance is set to 10^{-9} and the system is set to "Force Non-negative Solution" which allows for small negative numbers that arise due to numerical rounding error to be set to zero.

Table 3.1: Gas-phase reactions included in the photo-CVD chemical mechanism [82, 97]. (Dominant reactions are in bold.)

		A (mol, cm & s)	b	E_A (cal/mol)	Ref.
G1	**O_2 + hv => 2O**	2.04E-02	0	0	-
G2	**$Si(OC_2H_5)_4$ + hv => $Si(OH)(OC_2H_5)_3$ + C_2H_4**	2.04E-02	0	0	-
G3	$Si(OH)(OC_2H_5)_3$ + hv => $Si(OH)_2(OC_2H_5)_2$ + C_2H_4	2.04E-02	0	0	-
G4	**$Si(OC_2H_5)_4$ => $Si(OH)(OC_2H_5)_3$ + C_2H_4**	4.90E+13	0	61460	Coltrin et al.
G5	$Si(OC_2H_5)_4$ + H_2O = $Si(OH)(OC_2H_5)_3$ + C_2H_5OH	1.00E+11	0	25000	Coltrin et al.
G6	$Si(OH)(OC_2H_5)_3$ + $Si(OC_2H_5)_4$ = $O(Si(OC_2H_5)_3)_2$ + C_2H_5OH	1.00E+11	0	30000	Coltrin et al.
G7	**$Si(OC_2H_5)_4$ + O = $Si(OH)(OC_2H_5)_3$ + CH_3CHO**	2.04E+13	0	10800	Romet et al.
G8	$Si(OC_2H_5)_4$ + O_3 = $Si(OH)(OC_2H_5)_3$ + CH_3CHO + O_2	8.64E+08	0	29100	Romet et al.
G9	$Si(OH)(OC_2H_5)_3$ + O = $Si(OH)_2(OC_2H_5)_2$ + CH_3CHO	2.04E+13	0	10800	Romet et al.
G10	$Si(OH)(OC_2H_5)_3$ + O_3 = $Si(OH)_2(OC_2H_5)_2$ + CH_3CHO + O_2	8.64E+08	0	29100	Romet et al.
G11	CH_3CHO + O = CH_3CO + OH	1.10E+13	0	9610	Romet et al.
G12	CH_3CHO + OH = CH_3CO + H_2O	1.00E+13	0	0	Romet et al.
G13	CH_3CO + O = CH_3 + CO_2	9.60E+12	0	0	Romet et al.
G14	CH_3CO + OH = CH_3 + CO + OH	3.00E+13	0	0	Romet et al.
G15	CH_3 + O = CH_2O + H	8.00E+13	0	0	Romet et al.
G16	CH_3 + OH = CH_3O + H	5.74E+12	-0.2	58300	Romet et al.
G17	CH_2O + O = HCO + OH	1.82E+13	0	12900	Romet et al.
G18	CH_2O + OH = HCO + H_2O	3.43E+09	1.2	1880	Romet et al.
G19	HCO + HCO = CH_2O + CO	1.82E+13	0	0	Romet et al.
G20	CH_3O + O = CH_2O + OH	6.00E+12	0	0	Romet et al.
G21	CH_3O + OH = CH_2O + H_2O	1.80E+13	0	0	Romet et al.
G22	HCO + O = CO + OH	3.00E+13	0	0	Romet et al.
G23	HCO + OH = CO + H_2O	3.00E+13	0	0	Romet et al.
G24	HCO + O = CO_2 + H	1.00E+13	0	0	Romet et al.
G25	O_3 + CO = CO_2 + O_2	6.02E+02	0	0	Romet et al.
G26	2$Si(OH)(OC_2H_5)_3$ = Oligomer + H_2O	1.00E+10	0	0	Romet et al.
G27	Oligomer + O = Oligo(OH) + CH_3CHO	1.00E+10	0	0	Romet et al.
G28	Oligomer + O_3 = Oligo(OH) + CH_3CHO + O_2	8.64E+08	0	29100	Romet et al.
G29	Oligo(OH) + $Si(OH)(OC_2H_5)_3$ = Oligomer + H_2O	1.00E+10	0	0	Romet et al.

Table 3.1 Continued

		A (mol, cm & s)	b	E_A (cal/mol)	Ref.
G30	$2Oligo(OH) = Oligomer + H_2O$	1.00E+10	0	0	Romet et al.
G31	$Oligo(OH) + O = Oligo(OH)_2 + CH_3CHO$	2.04E+13	0	10800	Romet et al.
G32	$Oligo(OH) + O_3 = Oligo(OH)_2 + CH_3CHO + O_2$	8.64E+08	0	29100	Romet et al.
G33	$Si(OH)(OC_2H_5)_3 + Oligo(OH)_2 = Oligo(OH) + H_2O$	1.00E+10	0	0	Romet et al.
G34	$Oligo(OH) + Oligo(OH)_2 = Oligo(OH) + H_2O$	1.00E+10	0	0	Romet et al.
G35	$Si(OH)(OC_2H_5)_3 + Si(OH)_2(OC_2H_5)_2 = Oligo(OH) + H_2O$	1.00E+10	0	0	Romet et al.
G36	$Si(OH)_2(OC_2H_5)_2 + Oligo(OH)_2 = Oligo(OH) + H_2O$	1.00E+10	0	0	Romet et al.
G37	$2Si(OH)_2(OC_2H_5)_2 = Oligo(OH)_2 + H_2O$	1.00E+10	0	0	Romet et al.
G38	$Si(OH)_2(OC_2H_5)_2 + Oligo(OH)_2 = Oligo(OH)_2 + H_2O$	1.00E+10	0	0	Romet et al.
G39	$Oligo(OH)_2 + Oligo(OH)_2 = Oligo(OH)_2 + H_2O$	1.00E+10	0	0	Romet et al.

Table 3.2: Surface reactions included in the photo-CVD chemical mechanism [82, 97]. (Dominant reactions are in bold.)

		A (mol, cm & s)	b	E_A (cal/mol)	Ref.
S1	**$SiG_3E + hv => SiG_3(OH) + C_2H_4$**	1.74E+01	0	0	-
S2	$SiG(OH)E_2 + hv => SiG(OH)_2E + C_2H_4$	1.74E+01	0	0	-
S3	$SiGE_3 + hv => SiG(OH)E_2 + C_2H_4$	1.74E+01	0	0	-
S4	$SiG(OH)_2E + hv => SiG_3(OH) + C_2H_5OH$	1.74E+01	0	0	-
S5	$SiG(OH)E_2 + hv => SiG_3E + C_2H_5OH$	1.74E+01	0	0	-
S6	$SiG(OH)_2E + hv => SiG_3E+H_2O$	1.74E+01	0	0	-
S7[a]	$Si(OC_2H_5)_4 + SiG_3(OH) => SiO_2(D) + SiGE_3 + C_2H_5OH$	8.75E+03	0	43830	Coltrin et al.
S8	$SiG_3E => SiG_3(OH) + C_2H_4$	1.70E+12	0	47000	Coltrin et al.
S9	$SiG(OH)E_2 => SiG(OH)_2E + C_2H_4$	3.40E+12	0	47000	Coltrin et al.
S10	$SiGE_3 => SiG(OH)E_2 + C_2H_4$	5.10E+12	0	47000	Coltrin et al.
S11	$SiG(OH)_2E => SiG_3(OH) + C_2H_5OH$	2.00E+12	0	44000	Coltrin et al.
S12	$SiG(OH)E_2 => SiG_3E + C_2H_5OH$	2.00E+12	0	44000	Coltrin et al.
S13	$SiG(OH)_2E => SiG_3E+H_2O$	2.00E+12	0	44000	Coltrin et al.
S14[a]	**$Si(OH)(OC_2H_5)_3 + SiG_3(OH) => SiO_2(D) + SiGE_3 + H2O$**	2.00E+01	0	12000	Coltrin et al.
S15	$SiG(OC_2H_5)_3 + 18O_3 => SiO_2(D) + 6CO_2 + 8H_2O + 18O_2$	1.00E+12	0	0	Romet et al.
S16	$Si(OH)_2(OC_2H_5)_2 + 12O_3 => SiO_2(D) + 4CO_2 + 6H_2O + 12O_2$	1.00E+12	0	0	Romet et al.
S17	$SiGE_3 + 18O => SiG_3(OH) + 6CO_2 + 7H_2O$	1.00E+17	0	0	Romet et al.
S18	$SiG(OH)E_2 + 12O => SiG_3(OH) + 4CO_2 + 5H_2O$	1.00E+17	0	0	Romet et al.

[a] Coefficients are sticking parameters rather than Arrhenius parameters

3.3 RESULTS AND DISCUSSION

The chemical mechanism detailed above was used to determine the dominant reactions within the system, the concentrations of gas- and surface-phase species, and rate of particle growth for different system parameters. As the model was developed, several different configurations were tested to determine how numerical outputs compared to experimental findings. The results of these studies are discussed below.

3.3.1 VERIFICATION OF PHOTOCHEMICAL REACTION KINETICS

In order to verify that the CHEMKIN-PRO photochemical reaction kinetics produced accurate results, a simplified mechanism corresponding to Eqn. 3.17 was tested so that the modeled results could be compared to analytical and other numerical models. The first analysis compared analytical results from the use of the simplified version of the Beer-Lambert law (Eqn. 3.19) with the full expression (Eqn. 3.18) for a plug-flow reactor in a hypothetical analysis in which the level of oxygen did not vary, *i.e.* the oxygen was not dissociated. The oxygen molecular density was held at 1.4×10^{15} molecules cm^{-3}, which corresponds to a 1 sccm flow rate of oxygen with a nitrogen flow rate of 7.7 slm, flow rates typical of the photo-CVD system. The initial photon flux was 3.4×10^{16} photons $cm^{-2}\,s^{-1}$, also typical of the experimental system. As shown in Figure 3.4, the modified Beer-Lambert law slightly overestimates the number of absorbed photons across the entire reactor with a maximum percent error of 5%. In the CHEMKIN-PRO analysis, the differential element size is set to be a maximum of 1 cm which corresponds to an error of less than 0.05% (Figure 3.4b) and is thus a good simplifying assumption.

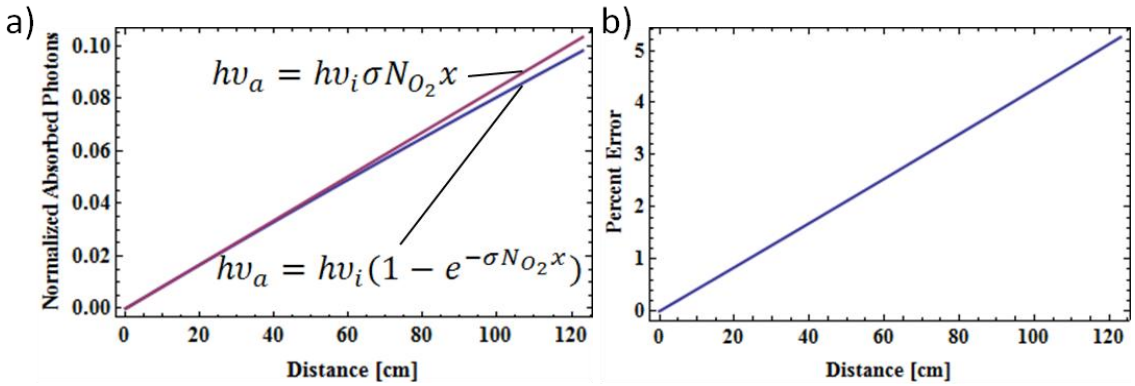

Figure 3.4: (a) The absorbed photon flux, normalized by the initial photon flux, versus axial location for a non-reacting oxygen gas using the Beer-Lambert law and an absorption approximation. (b) The percent error of the approximate Beer-Lambert law relative to actual law.

In order to determine the effect of the variation in oxygen concentration on the number of absorbed photons, an analytical solution was solved for the plug-flow system depicted in Figure 3.5. The concentration of O_2 was modeled as either fixed regardless of absorbed photons or the concentrations of O_2 was assumed to decrease for each O_2-photon reaction. The solution to the differential equation where oxygen is being dissociated (and no longer absorbing) upon absorption of a photon is as follows,

$$N_{O_2}(x) = \frac{u_o \, N_{O_2,i}}{(u + h\nu_i \sigma x)}. \tag{3.23}$$

The bulk velocity, u_o, was set to a typical value for the experimental system, 32 cm s^{-1}. As shown in Figure 3.6a, the results of the two analyses indicate that the assumption of non-reacting gas slightly overestimates the number of absorbed photons. The reason fewer photons are absorbed for the reacting oxygen model as compared to the non-reacting case is that as the oxygen concentration decreases, the absorbed photons dissociate diatomic oxygen leaving less absorbing species. The percent error is still small over the entire plug-flow tube, as shown in Figure

3.6b, and is less than 0.1% for the first 1 cm which is the maximum step size within the CHEMKIN-PRO model.

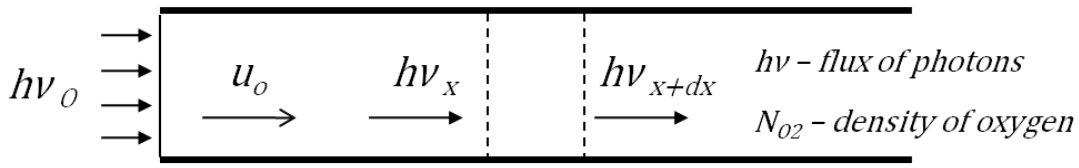

$$u_o \frac{dN_{O_2}}{dx} + \dot{Q}_d = 0$$

$$\dot{Q}_D = \frac{\phi}{N_{avg}} h\nu_i \sigma N_{O_2} \quad or$$

$$\dot{Q}_D = \frac{\phi}{N_{avg}} \left(h\nu_i \sigma N_{O_2} + h\nu_i \sigma x \frac{d(N_{O_2})}{dx} \right)$$

Figure 3.5: Schematic and analytical analysis of the photodecomposition of oxygen in a plug-flow reactor.

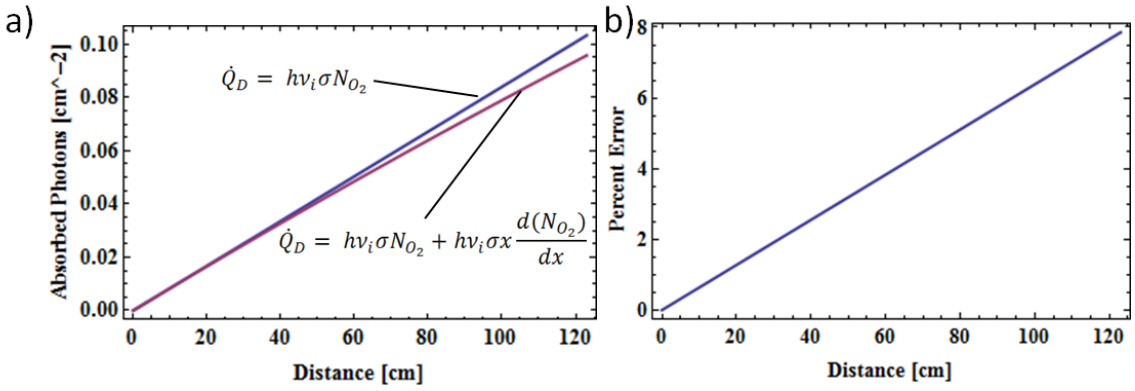

Figure 3.6: (a) The absorbed photon flux normalized by the initial photon flux versus axial location for a reacting and non-reacting oxygen gas using the simplified Beer-Lambert law. (b) The percent error of the non-reacting gas relative to a reacting one.

In order to compare the results involving photochemical reactions from the CHEMKIN-PRO simulation to results that could be obtained analytically, a simplified mechanism corresponding to Eqn. 3.17 was modeled analytically and numerically in

a discretized model as well as within CHEMKIN-PRO. The analytical and numerical discretized models were calculated in Mathematica, a mathematical and modeling environment developed by Wolfram Research, Inc.. The analytical results were compared to the CHEMKIN-PRO solution of the oxygen decomposition mechanism discussed above. The solution was determined for conditions that correspond to a 1-sccm flow rate of oxygen with a nitrogen flow rate of 7.7 slm and constant photon flux corresponding to 3.4×10^{16} photons $cm^{-2}\,s^{-1}$ (350 mW across a 3.4 cm diameter chamber with 7.2 eV $photon^{-1}$). The changing mole fractions of diatomic and monatomic oxygen as a result of photochemical reactions modeled in CHEMKIN-PRO and Mathematica are shown in Figure 3.7. The results indicate that there is good agreement between the analytical and model outputs with a maximum error of less than 0.05%. As expected, the decrease in diatomic oxygen leads to an increase in the mole fraction of monatomic oxygen. These results show that the photochemical mechanism employed within the CHEMKIN-PRO model accurately represents oxygen photodecomposition.

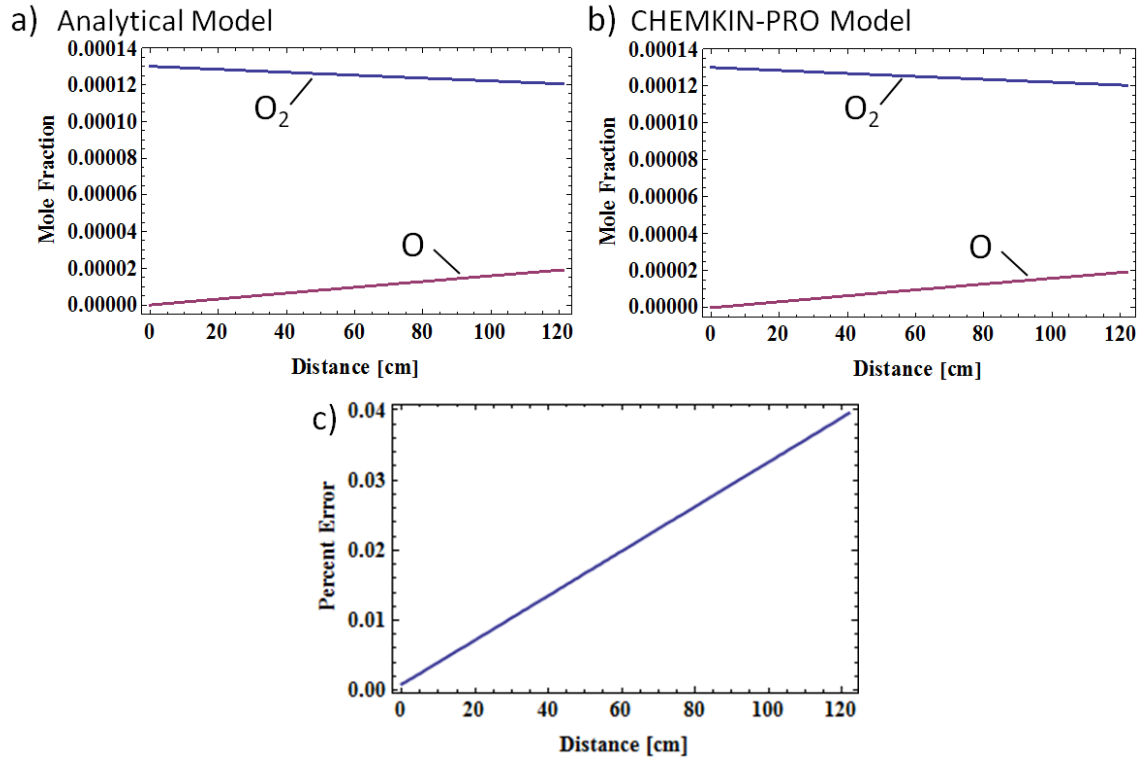

Figure 3.7: (a) Analytical and (b) CHEMKIN-PRO modeled mole fraction of diatomic and monatomic oxygen resulting from photochemical reactions and (c) the percent error between the analytically and numerically modeled solutions.

3.3.2 Photochemical Decomposition of Oxygen with Subsequent TEOS Reactions

The silica photo-CVD coating process was modeled for conditions that match those typical of the experimental study discussed in Chapter 2. To determine whether the dissociation of oxygen is the dominant photochemical reaction, the chemical mechanism includes only the photodecomposition of O_2 denoted by G1 in Table 1 (reactions G2, G3 and S1-S6 are not included), as well as all of Coltrin *et al.* and Romet *et al.*'s gas-phase and surface reactions. The inlet conditions for the system consist of 1 sccm of O_2, 7.7 slm of N_2, 1 sccm of TEOS and an inlet particle concentration of 10^7 cm^{-3} with an initial particle volume fraction of 1.4×10^{-10} cm^3 cm^{-3}, which corresponds to 30-nm diameter particles. The model is a steady-state

flow simulation with a constant photon flux of 3.4×10^{16} photons cm^{-2} s^{-1}. The model outputs the chemical species present in the gas phase and on the particle surfaces as a function of axial distance. As shown in Figure 3.8a, the photodecomposition of O_2 results in a decrease in the O_2 mole fraction as axial distance increases. The decomposition of O_2 forms O, but the mole fraction of O remains low as the highly reactive O quickly combines with TEOS, $Si(OC_2H_5)_4$, through reaction G7, resulting in triethoxysilanol, $Si(OH)(OC_2H_5)_3$. The production of oligomers (G26-G39) is monitored throughout the run and none are formed, indicating that the production of homogenously nucleated TEOS radicals at these conditions is unlikely. The surface-site concentration of species on the nanoparticles, shown in Figure 3.8b, indicates that as axial distance increases, the SiG_3OH groups decrease as the fraction of $SiGE_3$ increases primarily through reaction S14. By comparing the average particle diameter (*i.e.* number-mean diameter) as shown in Figure 3.8c with Figure 3.8b, it is apparent that the surface reactions lead to an increase in particle diameter of 0.4 nm. However as the particle surface saturates with ethoxy groups there are no sites available for attachment of subsequent $Si(OH)(OC_2H_5)_3$, thus halting the surface growth. The growth of films by thermal CVD on macroscopic surfaces has been experimentally shown to depend on the relative concentration of OH on the surface [99]. However from the experimental studies discussed in Chapter 2, it is apparent that the growth of silica is not limited by ethoxy groups to the extent this mechanism predicts and that instead the model's surface reaction rates are too slow in terms of the ethoxy conversion to glass bonds (reactions S8-S13). The contributions of oxygen reactions S17 and S18 at the surface are minimal as the majority of O reacts in the gas-phase leaving little react at the surface.

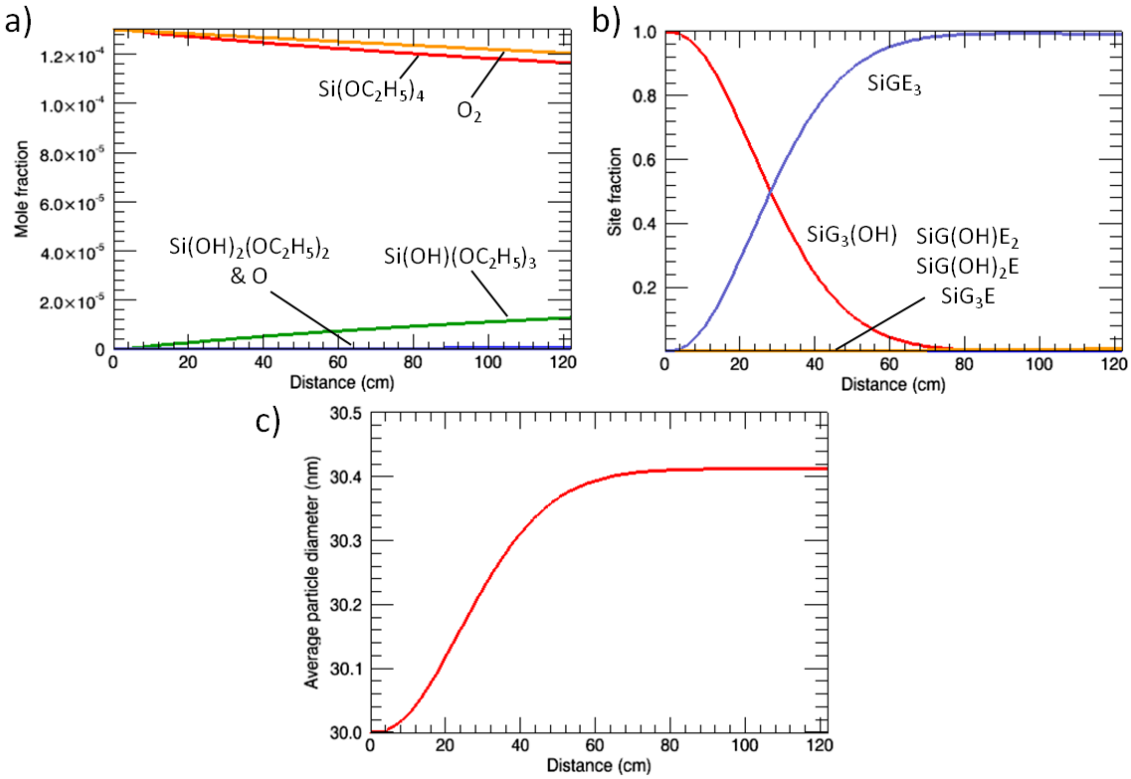

Figure 3.8: (a) Gas-phase mole fraction, (b) surface-site fraction and (c) average particle diameter as a function of axial distance in a plug-flow reactor where only oxygen reacts photochemically and the flux of photons is constant.

In order to determine whether a modification of Coltrin *et al.*'s reaction coefficients for the conversion of ethoxy groups to glass bonds may increase the particle growth rate, the pre-exponential factor, A, of reactions S8-S13 was increased from 10^{12} s^{-1} to 10^{15} s^{-1}. This is a similar method that was employed by Romet *et al.* to ensure that the surface reactions were not the limiting reactions [97]. All other inputs were held consistent to those used to produce Figure 3.8. While this increase in the pre-exponential factor was primarily done as a test of the model, a possible physical justification for this increase is that nano-scale effects may enhance the conversion process as bonds on the surface of high curvature structures such as nanoparticles are not as stable as those on macroscopic

substrates. As shown in Figure 3.9a, the increase in the surface reaction rates does not affect the molecular concentration of the gas-phase species. However as shown in Figure 3.9b, the increase in the conversion of ethoxy groups to glass bonds results in a markedly different surface-site concentration profile. While the concentration of available $SiG_3(OH)$ sites decrease with distance, there remains a significant concentration of the active sites at all axial locations. As a result, the average particle diameter, shown in Figure 3.9c, increases along the entire distance, resulting in a linear increase with distance. While the increase in surface reactions leads to an increase in particle diameter, the 1-nm change in diameter is less than the experimental results where under similar conditions the total change in diameter is ~8 nm. However given the uncertainty in the rate parameters and absorption cross sections, the difference of less than an order of magnitude between the experimental and model results represents good agreement.

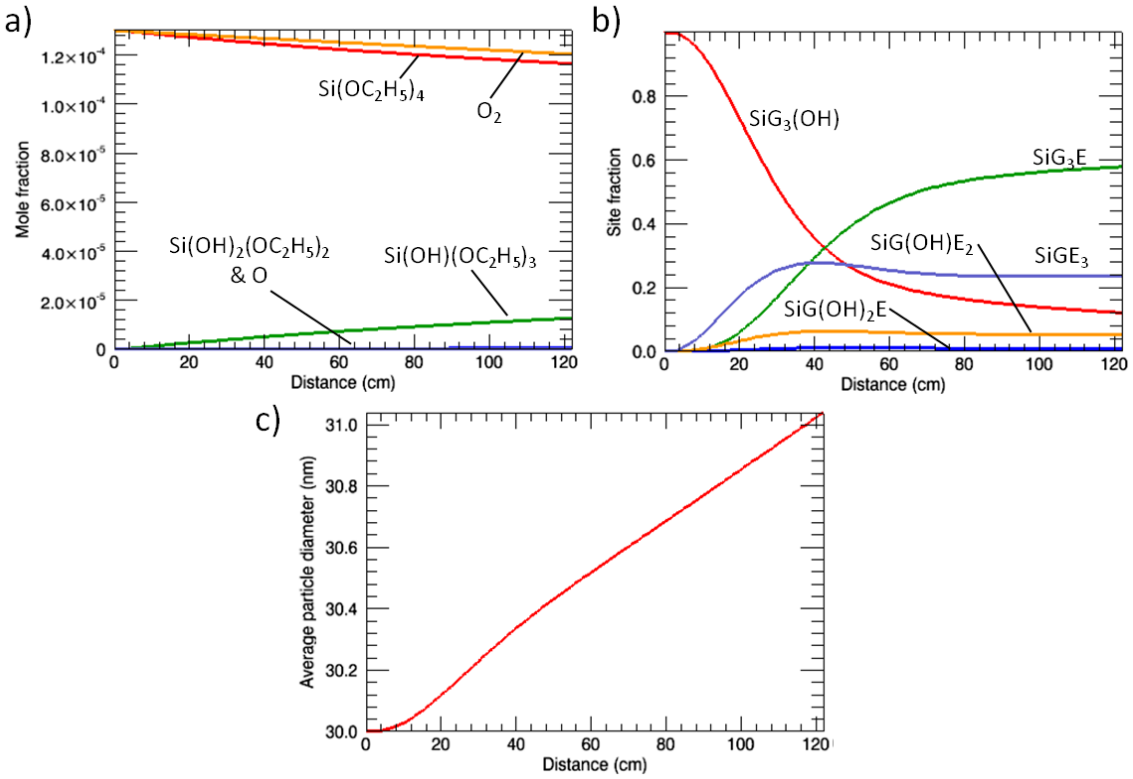

Figure 3.9: (a) Gas-phase mole fraction, (b) surface-site fraction and (c) average particle diameter as a function of axial distance in a plug-flow reactor where only oxygen reacts photochemically with a constant photon flux and particles have an enhanced ethoxy removal surface mechanism.

3.3.3 Oxygen and TEOS Photochemical Reactions with Constant Radiation

In order to determine the modeled effect of photochemical reactions with TEOS and the nanoparticle surface, a chemical mechanism was included that has the surface reactions S1-S6 and gas-phase reactions G1-G3 with the same conditions modeled in Figure 3.8 and Figure 3.9. The resulting gas-phase mole fraction, shown in Figure 3.10c, indicates that reactions G2 and G3 lead to an increase in the concentration of $Si(OH)(OC_2H_5)_3$, and $Si(OH)_2(OC_2H_5)_2$. The production of TEOS radicals increases the concentration of gas-phase species that are available for particle adsorption. As noted previously, the value of the radiative absorption cross section for TEOS is not known and therefore the value for oxygen is used as an

initial estimate, $\sigma_{TEOS} = \sigma_{subTEOS} = 6 \times 10^{-19}\text{cm}^2$, which represents a lower bound. The particle surface site fractions, Figure 3.10b, indicates that the inclusion of photochemical reactions on the particle surface increases the conversion of ethoxy groups to glass bonds with a hydroxyl termination. The abundance of gas-phase activated TEOS species and available surface sites leads to an increase in the growth rate of the particles, as the average particle diameter, shown in Figure 3.10, increases by more than 4 nm over the entire distance. The non-linear behavior in the growth of the average particle diameter indicates that the growth rate increases with axial distance, as the number of activated TEOS species increases.

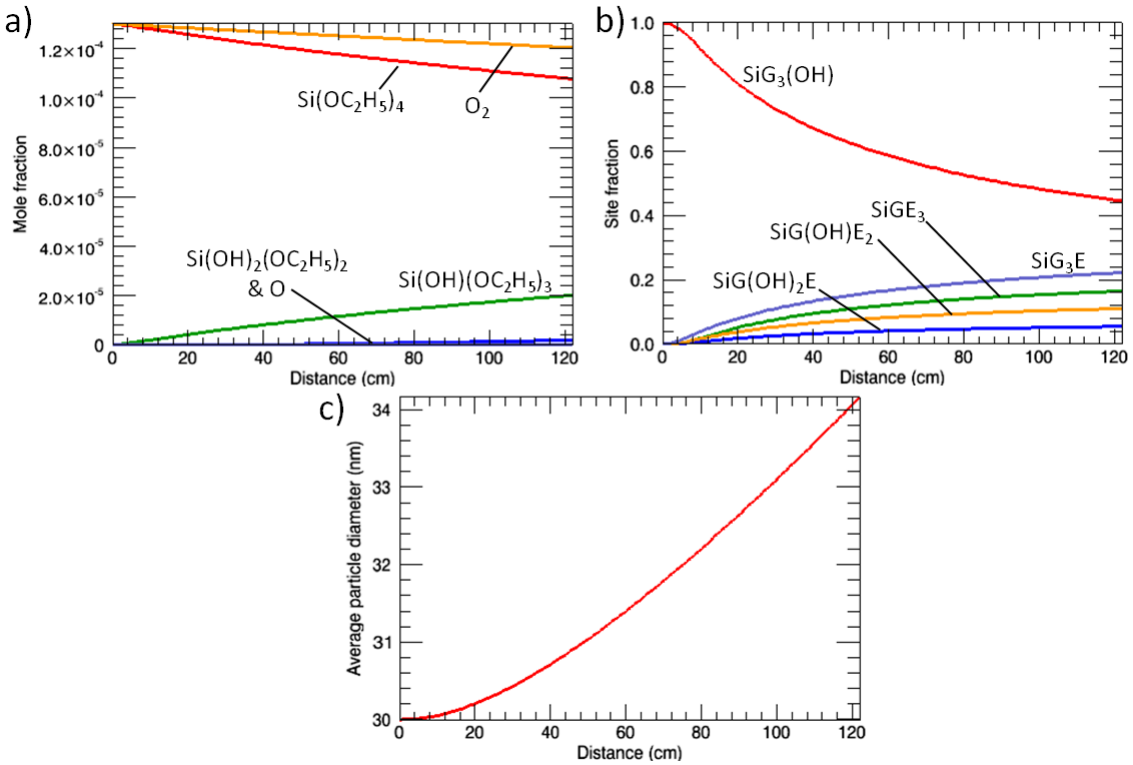

Figure 3.10: (a) Gas-phase mole fraction, (b) surface-site fraction and (c) average particle diameter as a function of axial distance in a plug-flow reactor with a kinetic mechanism that includes photochemical reactions of TEOS, oxygen and particle surface species with a constant photon flux.

In order to determine how the modeled particle growth varies with different inlet flow conditions, simulations were conducted for various TEOS, oxygen and nitrogen flow rates that correspond to experimental studies discussed in Chapter 2. As shown in Figure 3.11, the resulting particle coating thickness at the end of the coating chamber is shown versus TEOS and nitrogen flow rates for modeled and experimental results. The coating thickness increases for both the experimental and modeled results as the TEOS flow rate increases and nitrogen flow rate decreases. While oxygen was not deliberately added in the experimental study, the experiment was performed at atmospheric pressure without evacuation of the chamber prior to operation and it is likely that oxygen was present (~100 ppm). The modeled growth in coating thickness without oxygen present, Figure 3.11b, appears to grow in proportion to increasing TEOS flow, but overall the modeled coatings are thinner than in the experimental study. By increasing the oxygen flow rate into the model to 1 sccm and 2 sccm, Figure 3.11c and Figure 3.11d respectively, there is an increase in the overall thickness, which plateaus above 0.6 sccm of TEOS. The 1-sccm and 2-sccm oxygen flow rates result in an oxygen concentration of ~100 and 200 ppm, respectively within the model, comparable to the amount of residual oxygen estimated to be in the experimental system. These results indicate that while TEOS photo-dissociates at these conditions, the photodecomposition of oxygen still plays an important role in the process. There is agreement in the trends of increased coating thickness with precursor flow rate and decreased nitrogen flow rate, despite unknowns for various input parameters, such as the absorption cross section of TEOS.

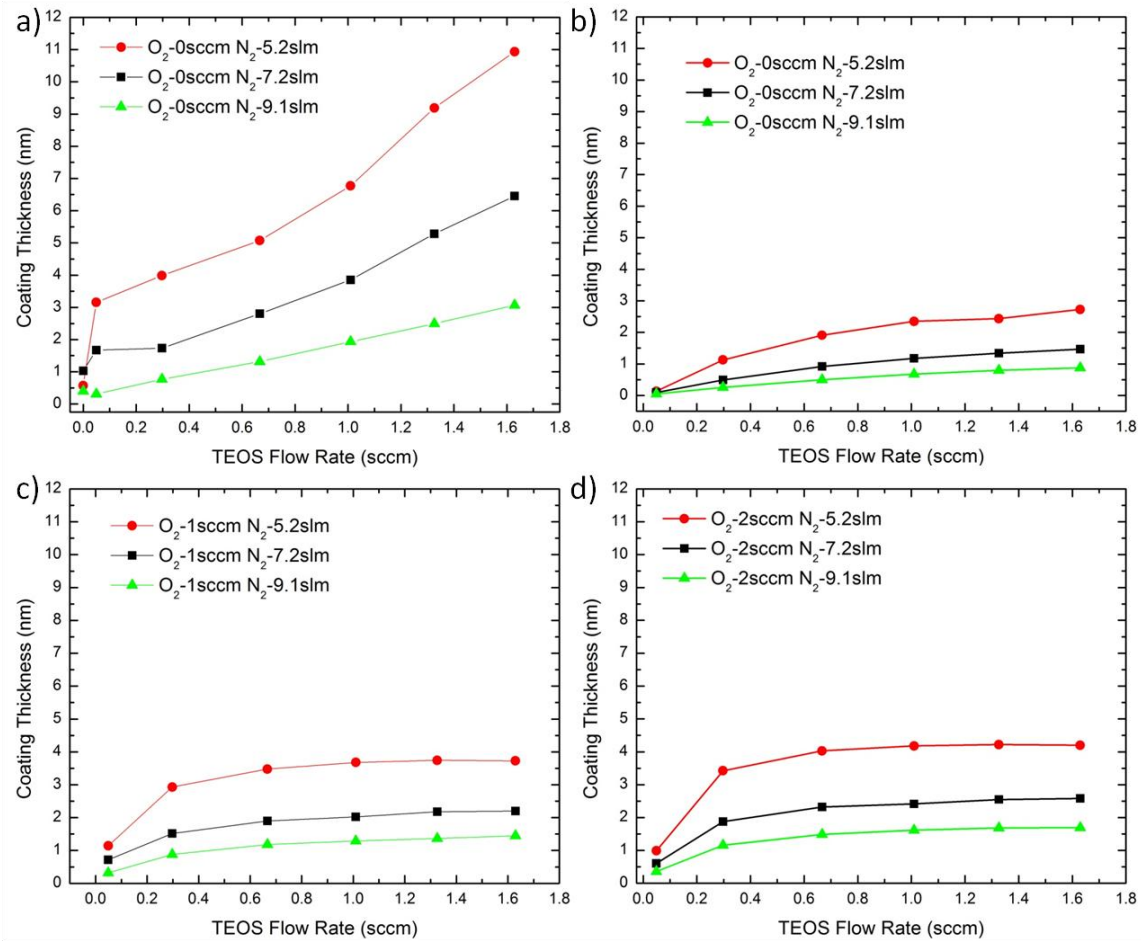

Figure 3.11: (a) Experimental coating thickness, and modeled coating thickness with (b) 0 sccm, (c) 1 sccm and (d) 2 sccm oxygen flow rate as a function of TEOS and nitrogen flow rates. The modeled kinetic mechanism included photochemical reactions of TEOS, oxygen and particle surface species with a constant photon flux.

The effect of radiation absorption cross section on coating thickness was studied by increasing the TEOS and triethoxysilanol absorption by an order of magnitude ($\sigma_{TEOS} = \sigma_{subTEOS} = 6 \times 10^{-18}\text{cm}^2$). While no published values are available for the radiation absorption cross section of TEOS, values of similar gases are available for similar VUV wavelengths, such as trimethyl silane [$SiH(CH_3)_3$, σ=8×10^{-18} cm^2 at 172 nm wavelength], allyltrichlorosilane [$SiCl_3CH_2CHCH_2$, σ=2×10^{-17} cm^2 at 191 nm wavelength] and silane [SiH_4, σ=4×10^{-18} cm^2 at 160 nm

wavelength] [111]. The results of a module run where all conditions other than the absorption cross section were held constant to the values used previously (Figure 3.11) are shown in Figure 3.12. The increase in TEOS absorption cross section serves to increase the modeled coating thickness of particles when oxygen is not present, Figure 3.12b. However, the addition of oxygen, Figure 3.12c and d, does not increase the coating thickness as shown in Figure 3.11. These results indicate that with the larger radiation absorption cross section, the direct photodecomposition of TEOS becomes the dominant gas-phase reaction rather than a TEOS and oxygen reaction. These results conflict somewhat with the experimental findings of Chapter 2 where it was shown that the presence of oxygen aides in the production of silica at the nanoparticle surfaces by reducing the hydrocarbons present within the coating, as shown by FTIR analysis. Further increases in the radiation absorption cross section of TEOS and triethoxysilanol make little difference in the coating thickness, as the growth is limited by surface reactions.

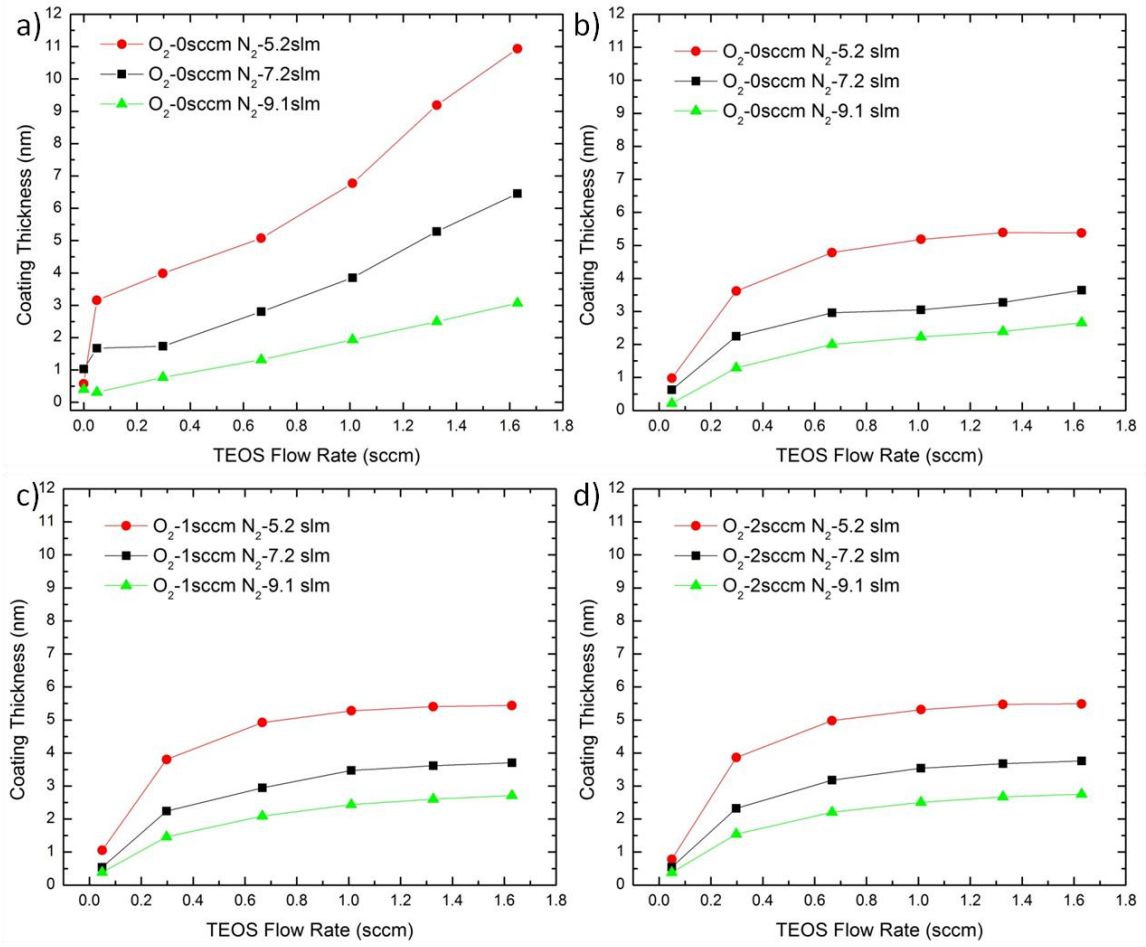

Figure 3.12: (a) Experimental coating thickness, and modeled coating thickness with (b) 0 sccm, (c) 1 sccm and (d) 2 sccm oxygen flow rate as a function of TEOS and nitrogen flow rates. The modeled kinetic mechanism included photochemical reactions of TEOS, oxygen and particle surface species with a constant photon flux and an increased absorption cross section of TEOS and triethoxysilanol of $\sigma_{TEOS} = \sigma_{subTEOS} = 6 \times 10^{-18}\text{cm}^2$.

3.3.4 Oxygen and TEOS Photochemical Reactions with Variable Radiation

In order to test the effect that the variation in the radiation flux has on coating growth, the model was modified to account for the axial variation in radiation flux. While the previous model runs were all conducted with a constant photon flux, representing a maximum within the system, in the experiments discussed in Chapter 2 the photons were not perfectly collimated and were

absorbed as they passed down the chamber. Therefore the model was modified to have a position dependent flux value that corresponds to a diffuse light source, representing the minimum flux profile within the system. The diffuse source is represented using the relation, $h\nu = h\nu_i \frac{{x_i}^2}{(x_i+x)^2}$, where $h\nu_i$=3.4×10^{16} photons s^{-1} cm^{-2} and x_i= 1 cm. For diffuse radiation the decrease in flux is dominated by reduction due to spreading of the radiation, rather than the absorption of photons by gas-phase species for typical concentrations found in the experimental studies conducted in Chapter 2. As shown in Figure 3.13, for an extreme case where both the concentration of absorbing species and absorption cross section of those species are increased by an order of magnitude over values typical in the photo-CVD system, the profile of radiation from a diffuse source is still less than a collimated source with absorbing species.

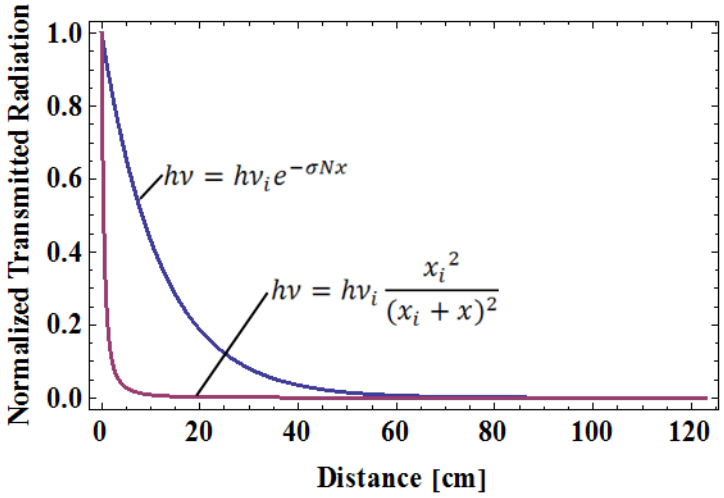

Figure 3.13: Transmitted radiative flux from (a) a collimated source with absorbing gas species at a concentration of 10^{16} molecules cm^{-3} and an absorption cross section of 6×10^{-16} cm^2, and (b) radiation from a diffuse source where x_i= 1 cm.

The photo-CVD coating process was modeled for a single run that corresponds to the model conditions used to produce Figure 3.10. As shown in Figure 3.14a, the diffuse source model results in much less TEOS and oxygen

photodecomposition. This in turn leads to a higher fraction of hydroxyl terminated species on the particle surface, as shown in Figure 3.14b. Despite the available sites for attachment the lack of TEOS radicals decreases the growth rate and results in a 1-nm growth over the entire reactor, much less than the 4-nm growth in the constant radiation results shown in Figure 3.10. The growth throughout the entire reactor occurs more linearly indicating that the silica growth rate is nearly constant throughout the reactor.

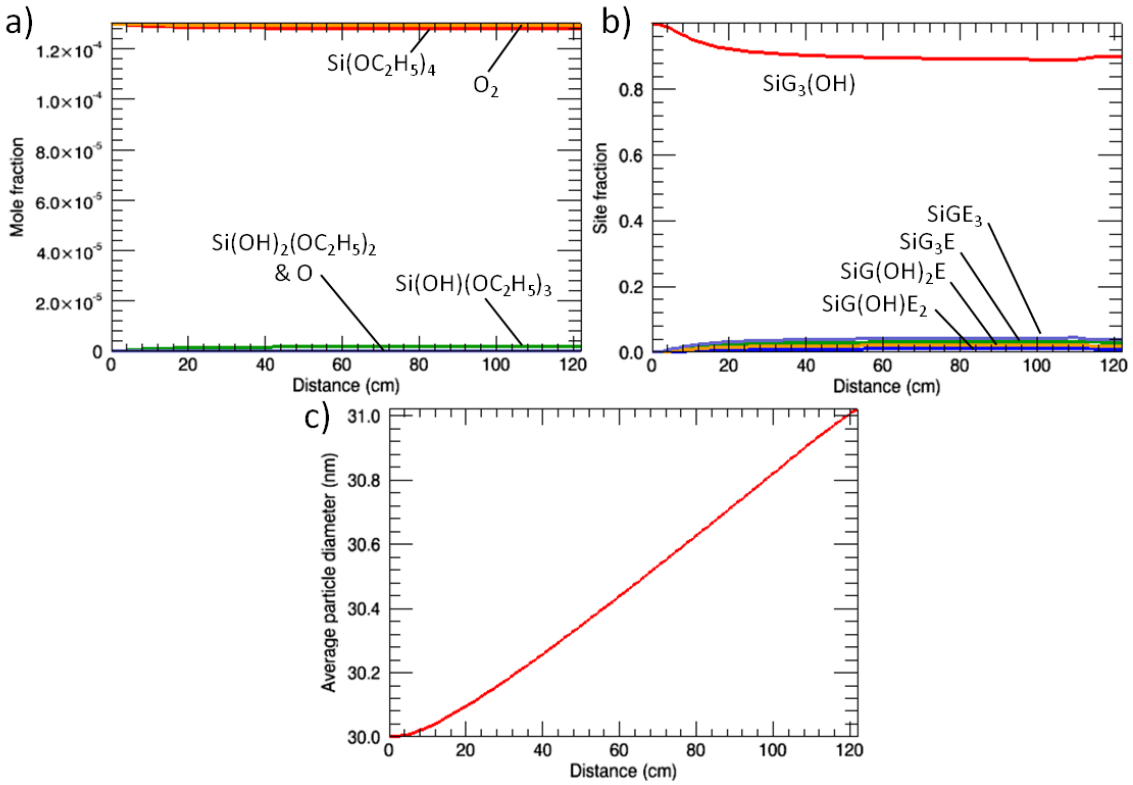

Figure 3.14: (a) Gas-phase mole fraction, (b) surface-site fraction and (c) average particle diameter as a function of axial distance in a plug-flow reactor with a kinetic mechanism that includes photochemical reactions of TEOS, oxygen and particle surface species with a photon flux that corresponds to a diffuse source.

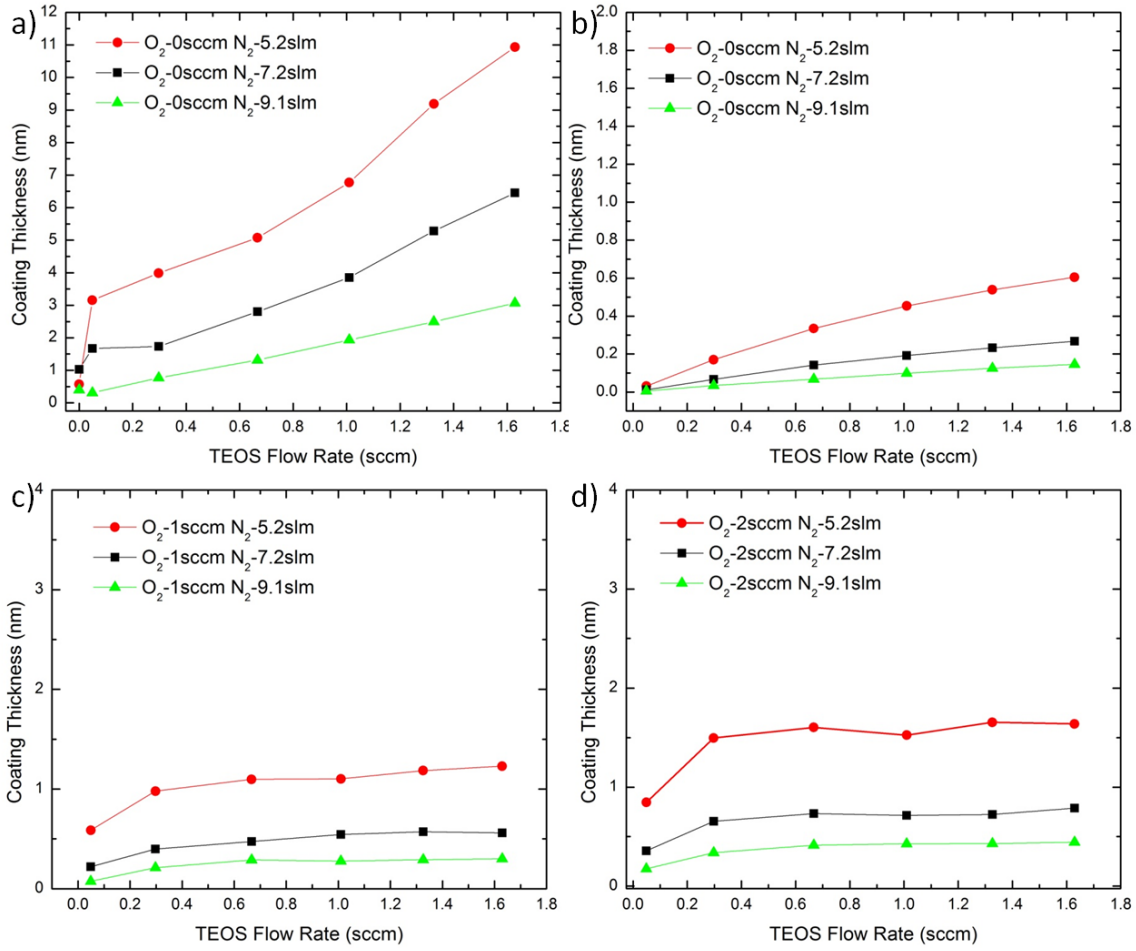

Figure 3.15: (a) Experimental coating thickness, and modeled coating thickness with (b) 0 sccm, (c) 1 sccm and (d) 2 sccm oxygen flow rates as a function of TEOS and nitrogen flow rates. The modeled kinetic mechanism included photochemical reactions of TEOS, oxygen and particle surface species with a photon flux representative of a diffuse source.

As done previously, the mechanism that includes a variable photon flux was also examined to determine how variations in precursor and nitrogen flow rates affect the overall coating thickness of the particles at the end of the plug-flow reactor. As shown in Figure 3.14, the modeled coating thickness has the same general trends as experimental and previous modeled results; increased TEOS flow and decreased nitrogen flow results in an increased coating thickness. The growth

as a function of TEOS flow rate is more linear for the diffuse source model without oxygen, Figure 3.15b, than for runs in which oxygen is included, Figure 3.15c & d. Like previous studies the modeled coating thickness with oxygen included quickly plateaus as the TEOS flow rate increase. All of these results indicate that with a diffuse radiation source, the modeled coating thicknesses are significantly thinner than for constant radiation.

As a final study, the model mechanism was modified to include radiation intensity akin to a diffuse source, and have an increased TEOS and triethoxysilanol radiation absorption cross section ($\sigma_{TEOS} = \sigma_{subTEOS} = 6 \times 10^{-18}\text{cm}^2$). The results of this analysis are shown in Figure 3.16. As in Figure 3.12, the increase in absorption cross section results in an increase in the modeled coating thickness when oxygen is not present within the system. The overall modeled coating thickness is not significantly affected by the addition of oxygen as the photodecomposition of TEOS is the primary gas-phase reaction. The modeled coating thickness appears to grow more linearly with TEOS flow rate for the case in which oxygen is not present then when oxygen is present. The overall magnitude of the growth is still within an order of magnitude of the experimental results and the growth trends appear to have good agreement with modeled variations in inputs.

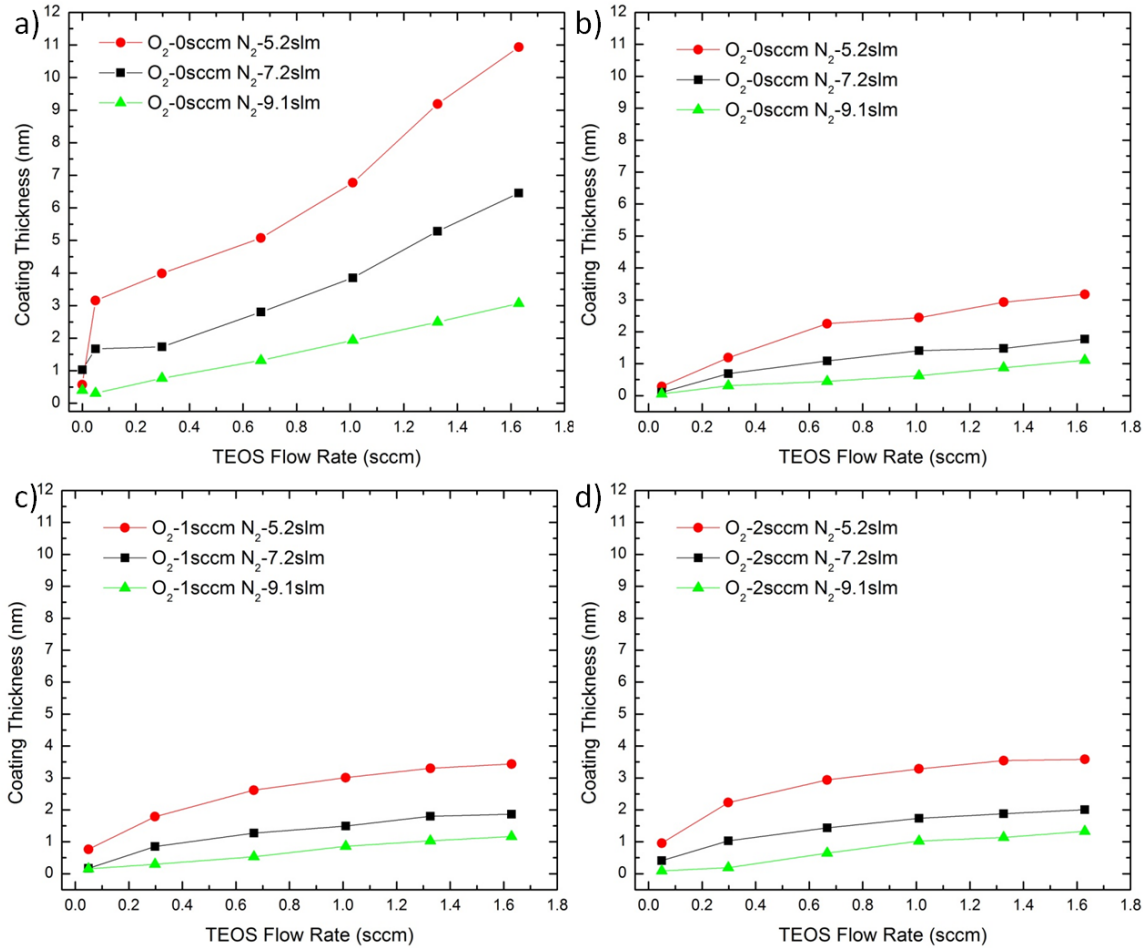

Figure 3.16: (a) Experimental coating thickness, and modeled coating thickness with (b) 0 sccm, (c) 1 sccm and (d) 2 sccm oxygen flow rates as a function of TEOS and nitrogen flow rates. The modeled kinetic mechanism included photochemical reactions of TEOS, oxygen and particle surface species with a photon flux representative of a diffuse source and an increased absorption cross section of TEOS and triethoxysilanol of $\sigma_{TEOS} = \sigma_{subTEOS} = 6 \times 10^{-18}\text{cm}^2$.

3.4 SUMMARY

Gas-phase coating of nanoparticles by photo-CVD was shown in Chapter 2 to be an effective way to produce silica coatings with controllable thickness for a variety of different particle cores. While the experimental studies were able to elucidate some of the underlying phenomena occurring during the photo-CVD

process, a chemical kinetics model was developed in order to better describe the photochemical reactions occurring during the production of silica coatings on nanoparticles. This study's kinetic mechanism for the production of silica from TEOS built largely upon the previous work of Romet *et al.* [97] and Coltrin *et al.* [82] that examined silica thin film growth from thermal decomposition of TEOS with and without oxygen, respectively. In addition to thermal reactions, photochemical reactions are included within the chemical mechanism. To solve the photochemical reactions the differential equation solver, CHEMKIN-PRO, had to be modified to read in a user-developed subroutine which calculated the rate of progress for the photochemical reactions. The CHEMKIN-PRO modeled composition of gas-phase species was compared to an analytically derived gas-phase composition for the photochemical reaction of oxygen within a perfectly stirred reactor. The model agrees well with the analytical results indicating that photodecomposition can be modeled well within CHEMKIN-PRO.

In addition to gas-phase reactions, the model includes condensed phase species suspended within the gas, *i.e.* aerosolized nanoparticles. The nanoparticles are modeled as silica cores within a perfectly-stirred reactor and their growth is tracked by a method of moments approach. The kinetic mechanism includes the photodecomposition of diatomic oxygen and subsequent reaction of TEOS with monatomic oxygen which is followed by thermal gas and surface reactions discussed previously. Modeled results indicate that a chemical mechanism that includes only oxygen photodecomposition results in too little particle growth because of the slow generation of the TEOS radical, triethoxysilanol, and the slow removal of surface ethoxy groups to produce glass bonds. Monitoring of the oligomer forming reactions from TEOS and TEOS radicals indicates that no oligomers are formed, which agreed well with experimental studies in which homogenous nucleation was not present under similar conditions.

The radiation absorption cross section of TEOS and TEOS radicals is an unknown parameter within the system, as no experimental studies have been conducted for TEOS to determine its cross section. As the absorption cross section of TEOS and triethoxysilanol is increased, the photodecomposition of TEOS began to dominate the gas-phase reactions, thus causing the introduction of oxygen to have little effect. The inclusion of a radiation flux subroutine that models the flux from a diffuse light source, results in thinner coatings as less radiation at points farther from the radiation source slows the decomposition of TEOS and surface reactions. Overall the model shows agreement with experimental results in that coating thickness increases with increasing TEOS flow and decreasing nitrogen flow. The modeled growth trends of coating thickness as a function of TEOS flow rates match experimental results best in the cases of variable radiation without oxygen present. In almost all cases the modeled results are within an order of magnitude of the experimental results, which represents good agreement given the uncertainties of reaction rates.

While this model is the first known chemical mechanism containing photochemical reactions and growth on nanoparticles surfaces modeled within CHEMKIN-PRO, further work remains. Future work would include a variable-photon model that directly accounts for absorbed photons. Validation of the modeled gas-phase products could be confirmed with on-line FTIR and mass spectrometry measurements at the exit of the photo-CVD chamber. Additionally, testing of a wide variety of parameters should be done within the model to give insight into nanoparticle coatings conducted in different regimes, such as low pressures, different temperatures or different initial particle diameters. The chemical mechanism could be further expanded to include the possible increased reaction rates of charged particles with charged gas-phase and surface species.

Chapter 4 - Hot-Wire Synthesis of Gold Nanoparticles

4.1 Overview

Gold nanoparticles are one of the oldest forms of nanotechnology with the first known publication examining the use of gold colloids for medical purposes by Francisci Antonii [112]. Since that time gold colloids and more generally gold nanoparticles have been widely used because of their unique properties. These properties arise from quantum effects that occur when gold has dimensions on the nanometer scale [113]. Currently gold nanoparticles are used for a variety of industrial and commercial applications, such as gas sensors [114], visual displays [115], catalysis [116] and electronic devices [117, 118]. As in Antonii's day, gold nanoparticles are still being investigated for a variety of medical purposes, which offer some of the most promising applications of gold nanomaterials. To date gold nanoparticles have been used in the treatment of cancerous tumors by photo-thermal ablation [119], imaging [120], drug delivery for hypothermia [121] and hyperthermia [122].

Most applications take advantage of gold nanoparticles' distinctive behavior, such as plasmon resonance and catalytic effects which occur when the particles are smaller than about 10 nm in diameter. These effects are dependent on the size, shape and surface chemistry of the particles [123]. While most researchers produce nanoparticles by wet-chemistry methods [124-126] the use of solvents to prepare gold solutions can lead to contamination within the particles and unwanted surface chemistry due to impurities in the solvents. Gas-phase nanoparticle production offers a distinct advantage over wet-chemistry synthesis techniques by allowing particles to be produced in environments where the surrounding gas is either inert or non-reacting, such as helium or nitrogen. The most common technique for the production of gas-phase metal nanoparticles is inert-gas condensation [79], in

which a metal is evaporated or sublimated into a passing inert-gas flow stream at elevated temperature. Upon cooling, the metal vapor supersaturates and homogeneously nucleates, causing a burst of particles which rapidly agglomerate. While this facile process readily produces metal particles it requires a high temperature tube furnace, additional dilution to suppress agglomeration, and a sintering furnace to coalesce the agglomerates if spherical metal nanoparticles are desired [94, 127]. Also, if the carrier gas reacts at high temperature or the surface chemistry of the particle is important, superior results can be achieved when the surrounding gas is not heated to the high temperatures required to evaporate the metal [128].

Another gas-phase method for the production of metal nanoparticles is spark generation, where particles are produced from the electrode material by sublimation [129-131]. Spark generation of nanoparticles is most commonly achieved by repeatedly discharging a current between two electrodes composed of a metal of interest. The discharge serves to evaporate the electrode material as a result of high local temperatures at the electrode surface. The gas-phase metal is then carried away from the electrode by a gas cross flow which cools the metal, resulting in particle nucleation. Byeon *et al*. have effectively used spark generation to produce gold agglomerates with a geometric mean diameter of 49 nm at a total concentration of ~8×10^{6} cm^{-3} [132]. Particles of different sizes were achieved by varying the flow rate, discharge frequency and electrode gap. The composition of the gas cross flow can affect the gas breakdown characteristics. As a result ultra-high purity gases are often used to control the breakdown, which has the added benefit of limiting impurities that may arise from highly reactive monatomic species such as oxygen and nitrogen radicals that are produced by the arc [130, 132].

An alternative approach is hot-wire nanoparticle synthesis. Hot-wire synthesis is analogous to inert-gas condensation and spark generation in that metal vapor is evaporated into a gas flow. However in hot-wire nanoparticle synthesis only the metal, *i.e.* the wire, is heated, by electrical resistance, and the bulk gas flow

remains relatively cool and is not ionized. In hot-wire synthesis the metal vapor is supersaturated almost immediately upon leaving the wire surface, similar to spark generation, and thus quickly nucleates homogenously to form nanoparticles. Hot-wire production is unique in that the carrier gas does not have a large effect on the properties of the particles produced, which is not the case for spark generation, in which the electrical breakdown characteristics of the gas are critical in controlling particle production. Previous studies have shown that hot wires can produce nanoparticles with nearly any electrically conductive material that has a vapor pressure higher than 5×10^{-3} Pa at its melting point [133]. As Peineke *et al.* state, for materials such as gold that do not have sufficiently high vapor pressures at their melting points ($\sim2\times10^{-3}$ Pa at T_{melt}), the wire melts and thus breaks the electrical circuit before significant quantities of nanoparticles are produced. Although pure gold wires break when used as evaporation sources, a previous study showed that gold particles can be produced by a hot-wire method using composite wires and high purity gases in ultra-high vacuum systems [134]. While such methods are promising, no study has yet shown whether hot-wire methods can produce gold nanoparticles of small sizes (< 10 nm) with industrial-grade gases at atmospheric pressure.

This chapter investigates the hot-wire production of gold nanoparticles at atmospheric pressure and room temperature in a nitrogen flow. The effects of key system parameters are reported as they affect particle size, morphology, and concentration. A computational fluid dynamics model is developed to determine the temperature and velocity profiles within the hot-wire generator. The results of the model are compared to an analytical analysis that examines the transition from a forced flow to buoyancy driven flow within the hot-wire generator for different geometries.

4.2 Experimental Setup

The investigation of hot-wire production of gold nanoparticles was conducted by injecting nitrogen (99% purity) into an ISO-100 stainless-steel vacuum cross with inner tube dimensions of 98 mm. As shown in Figure 4.1, variation of the effective diameter of the system was achieved by mounting an alumina tube with a 20-mm inner diameter and 2.5-mm wall thickness between flanges (20 cm long) in which gas entered and exited. A further reduction in diameter was achieved by the addition of a boron nitride nozzle within the alumina tube, which served to constrict the area of the flow as it passed over the hot wire. The nozzle had a 3-mm throat diameter and 75-mm length, with an approximate entry and exit angle of 45˚. The O-rings on each of the four cross flanges as well as the O-rings connecting the alumina tube to flanges were composed of Viton and were monitored to ensure that the temperatures of the rings were kept below 300˚C, in turn ensuring that particles were not produced from the O-rings themselves. Pressure within the system was monitored by a Pirani gauge and was maintained at 101±2 kPa.

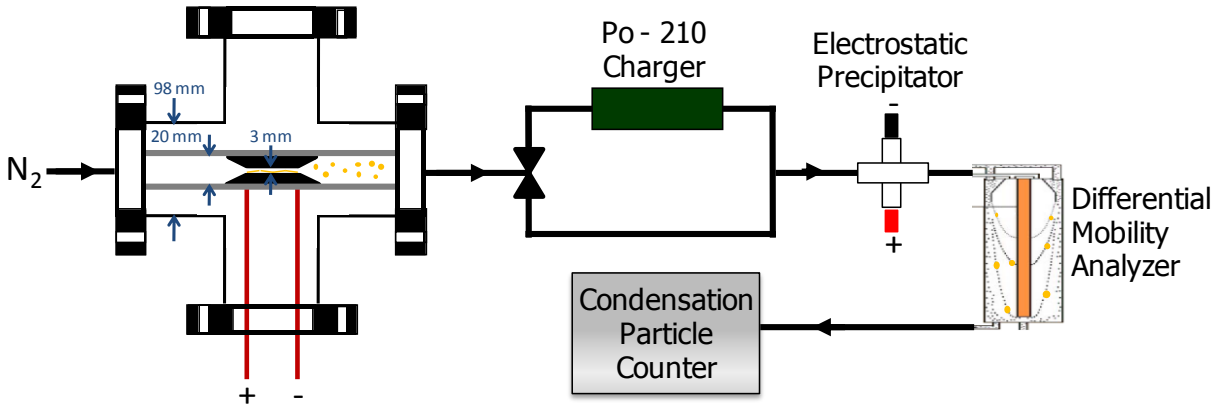

Figure 4.1: Schematic of hot-wire gold nanoparticle synthesis experimental apparatus.

Wires composed of gold-coated tungsten, gold-coated molybdenum and gold-coated platinum (~0.5 mm diameter) were tested for their suitability in producing gold nanoparticles. Each of the wire's ends was wrapped with additional gold wire (0.5 mm diameter) leaving a 20-mm center portion of gold-coated-tungsten wire exposed within the crossing nitrogen flow to produce nanoparticles. A DC voltage was applied across the wire using a Sorensen DCS 12-250E power supply, with maximum power of 3 kW. The wire connecting the voltage source to the hot wire had a minimum diameter of 2.6 mm (10 gauge) to ensure that most of the power dissipation occurred across the 20-mm central section of the hot wire.

Upon exiting the hot-wire apparatus the generated aerosol was either charged by a Po-210 bi-polar charger or passed directly into a TSI model 3085 differential mobility analyzer (DMA) with an applied DC voltage provided by a Bertan 205B power supply, which classified the particles according to their electrical mobility. Particle counts were monitored using a TSI 3025A condensation particle counter (CPC) with a 3-nm lower-detection limit and accompanying discrete mobility particle sizer LabView software. Particle size distribution functions were determined by correcting the discrete count data for CPC counting efficiency, DMA efficiency, tube penetration efficiency and charging efficiency [48] and dividing by the DMA transfer function at each particle mobility. Particles were collected onto transmission electron microscopy (TEM) grids via electrostatic precipitation (ESP) with an applied field of 3 kV across a 2.3 cm gap. The DMA measurements of the particle size distribution were performed with no voltage applied to the ESP, in which case the particles were unaffected by the ESP and passed freely to the DMA. Particles were imaged using a FEI Tecnai G^2 F30 TEM. The F30 microscope was also used for scanning TEM (STEM) and to perform energy dispersive x-ray (EDX) analysis. Additional composition analysis was conducted using x-ray photoemission spectroscopy (XPS) with a Surface Science SSX-100.

4.3 Experimental Results and Discussion

Initial attempts to produce gold nanoparticles in the gas phase sought to modify the typical physical vapor deposition configuration by injecting a cross flow into an evaporation chamber and thus cooling the evaporated gold vapor, causing the nucleation of nanoparticles. The typical gold physical vapor deposition process uses high-melting-temperature metal boats which are connected to electrodes. A voltage source is then applied to the electrodes causing current to pass through the boats and thus inducing resistive heating. A gold slug or powder is placed in the boats and resistively heated to cause sublimation of the gold solid. An image of a modified physical vapor deposition configuration is shown in Figure 4.2a, where the electrode began to emit visible radiation when high currents were applied. Upon operation of the modified evaporator at atmospheric pressure, large numbers of aerosolized particles were detected without the presence of gold slugs in the boats. Investigation of the metal evaporation boats after heating at atmospheric pressure in a nitrogen environment indicated that the boats showed signs of oxidation, Figure 4.2b. The apparent oxidation occurred for evaporation boats composed of molybdenum, tungsten and tantalum. The propensity of the boats to oxidize at atmospheric pressure made them unsuitable for producing gold nanoparticles in an oxygen containing environment.

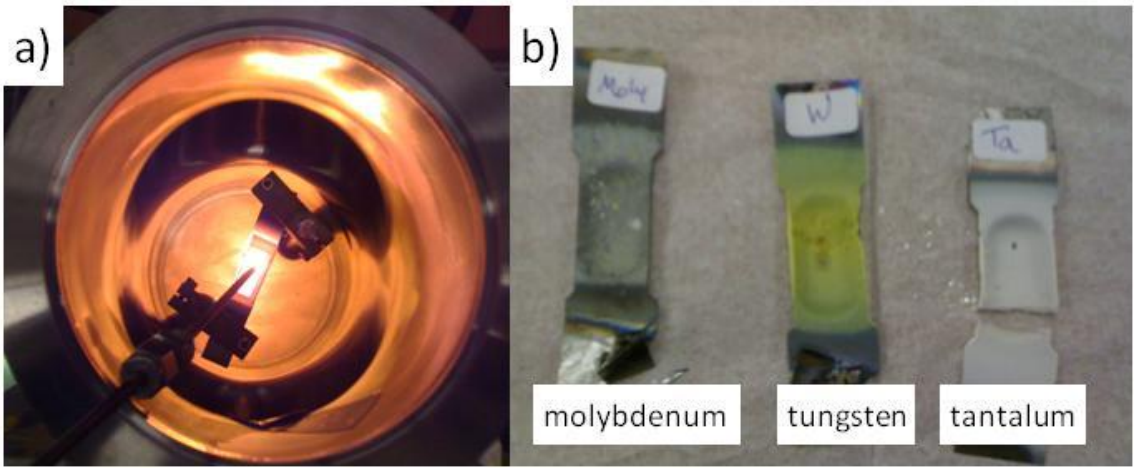

Figure 4.2: (a) Image of physical vapor deposition evaporator using heating elements to evaporate a gold slug and (b) image of heating elements composed of different materials after slug evaporation at atmospheric pressure in the presence of air.

Next, attempts were made to use gold-coated tungsten as the hot wire. Tungsten's high melting temperature relative to gold makes it an effective core material provided the oxidation of tungsten is suppressed by the outer gold shell. A variety of core and shell diameters were tested and particles were readily produced by this method, shown in Figure 4.3a. However, upon examination of the elemental composition of the particles by EDX, Figure 4.3b, it was found that a majority of the particles were composed of tungsten oxide. Inspection of the hot wires after use indicated that the high contact angle of gold on the tungsten surface exposed large portions of the tungsten surface to oxidation. Similar results were found using gold-coated molybdenum wire. Thus both tungsten and molybdenum core wires were found to be unsuitable for the production of gold nanoparticles at atmospheric pressure.

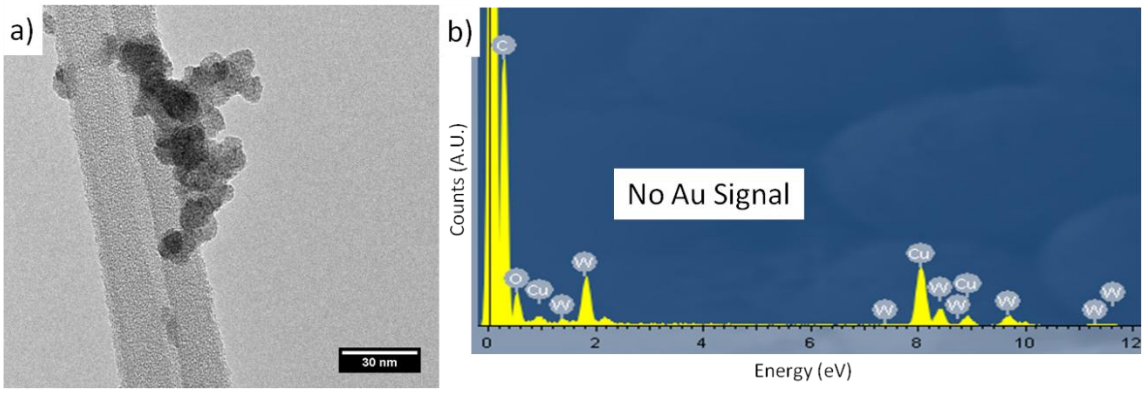

Figure 4.3: (a) TEM image of particles collected from hot-wire evaporator using a gold coated tungsten wire and (b) EDX signal from the analysis of the particles.

To produce gold nanoparticles by a hot-wire method we sought to use a high-melting-point material for the core wire that could be resistively heated by the electrical current until the thin outer coating of gold melted, thereby generating gold vapor that would be entrained in the passing nitrogen flow stream. Since gold has a relatively high electrical conductivity (~1.2×10^7 S m^{-1} at 1000 K) the sizing of the core-shell diameter is crucial in ensuring that most of the current passes through the core wire and not the gold shell. For thick gold coatings the melting of the gold causes a break in the shell, forcing all of the current through the core wire, which in turn causes a rapid heating and melting of the core wire. In the experiments reported here, we maintained the electrical resistance per unit length of the core wire to be half that of the gold shell, or $R_{core} \leq \frac{1}{2}R_{shell} = \frac{1}{2}\rho_{shell}A_{shell}{}^{-1}$, where R, ρ and A are resistance per unit length, resistivity and cross-sectional area respectively.

In order to eliminate the oxidation of the core wire at high temperatures, platinum was chosen for the core material. Platinum's melting point (1758°C), while lower than the melting points of tungsten and molybdenum, is still much higher than that of gold (1064°C) at atmospheric pressure. As shown in Figure 4.4, the vapor pressure of platinum also remains several orders of magnitude lower than

gold across a range of temperatures [135]. The platinum core also resists oxidation and is stable in oxygen atmospheres at temperatures beyond its melting point. Nanoparticles were synthesized using a hot wire with a core platinum diameter of 0.404 mm and a gold shell of 3 μm that was produced by electroplating by an outside company (Professional Plating Inc., Minneapolis, MN).

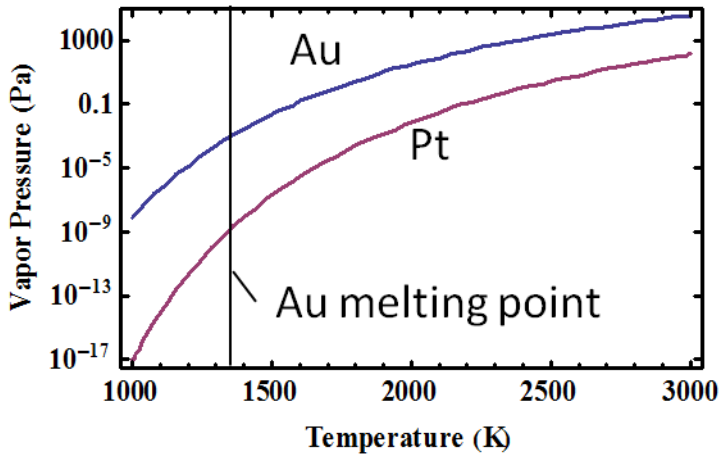

Figure 4.4: Plot of gold (Au) and platinum (Pt) vapor pressure as a function of temperature [135].

As shown in Figure 4.5, particles produced using the gold-coated platinum wire in the 98-mm stainless-steel cross with 2 slm of nitrogen flow had a wide distribution of sizes with a total concentration, integrated over the size distribution, of ~9×10^7 particles cm^{-3} (the peaks in the particle mobility distributions were less than 10^7 $nm^{-1}cm^{-3}$). Particle production was first measured at 8.1 W power delivered to the hot wire. Increasing the power increased the mean particle size and decreased the geometric standard deviation of the distributions to σ_g=1.81 for the 12-W curve when fit with a log-normal distribution. The particle distributions did not exhibit a smooth log-normal curve, which may be due to flow recirculation zones within the cross. Because of the large flow area it is likely that most of the flow remains unheated except in close proximity to the wire, and that gold enters

the main part of the flow stream as nanoparticles that nucleated very close to the wire surface.

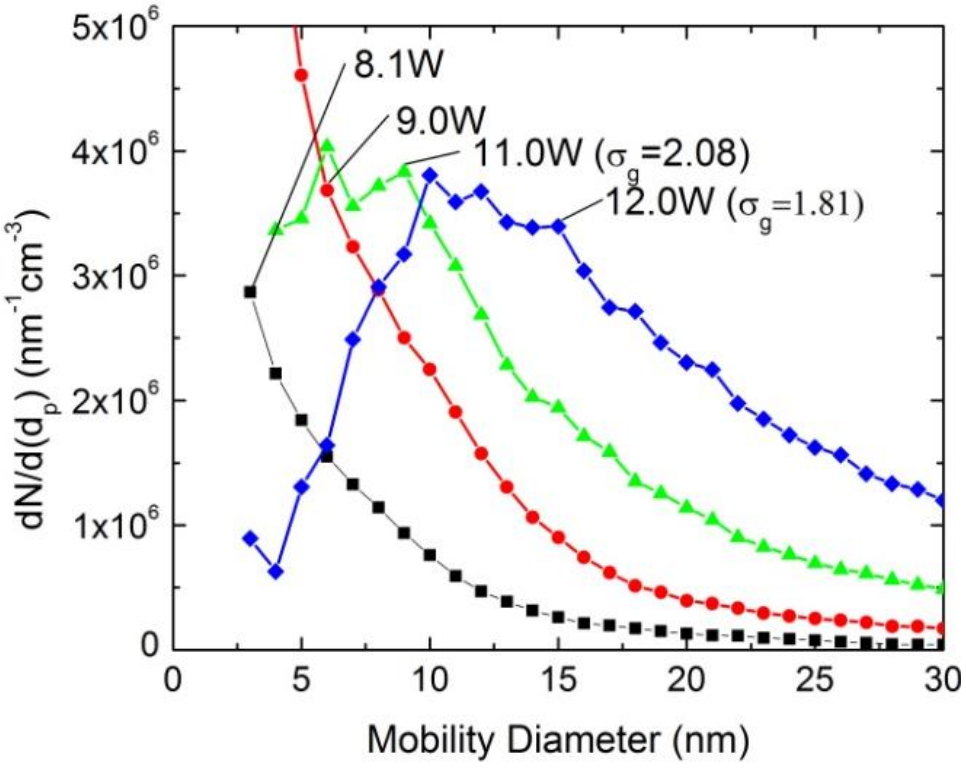

Figure 4.5: Particle size distributions of gold nanoparticles produced at varying wire powers in a 98-mm chamber with 2 slm of nitrogen flow.

As shown in Figure 4.6, TEM images of particles collected using electrostatic precipitation for five minutes (as was done for all TEM collections) for the 9-W and 12-W experiments had a wide distribution of particle sizes and morphologies. The irregular shape of many of the particles produced at 12 W, seen in Figure 4.6a, suggests that these particles are composed of partially sintered primary particles. The multiple crystal orientations seen in the high resolution image, Figure 4.6b, may also indicate that the particles are composed of multiple, separately-nucleated gold nanocrystals, although it is also possible to grow polycrystalline particles by vapor deposition due to twinning. Even at 9 W, the TEM images, Figure 4.6c and d, indicate that there is a wide distribution of particle sizes and that multiple crystalline planes

are present, despite their more spherical shapes. Analysis of the lattice spacings of the high-resolution images (Figure 4.6b and d) correspond to the (111) and (002) faces of gold, which have documented spacings of 2.36 Å and 2.04 Å, respectively [86].

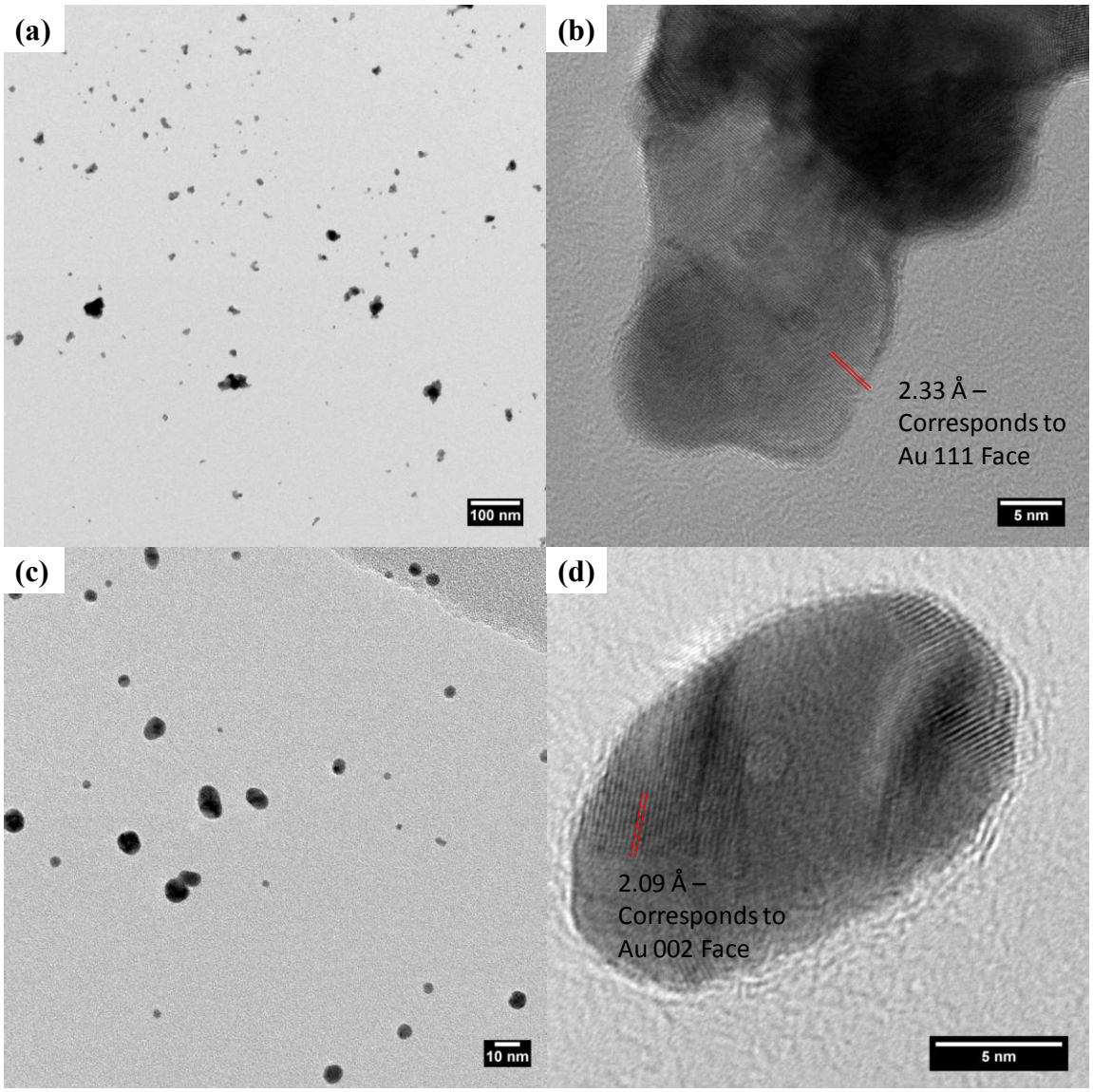

Figure 4.6: TEM images of gold particles produced from gold-coated platinum wire in 98-mm chamber for wire powers of 12 W (a & b) and 9 W (c & d).

In order to produce smaller particles with smaller geometric standard deviations, the nitrogen flow, still maintained at a flow rate of 2 slm, was directed through a tube diameter of 20 mm and a nozzle with a throat diameter of 3 mm, increasing the gas velocity across the wire. As shown in Figure 4.7, the resulting particle mobility distributions are smoother than in Figure 4.5, and have smaller geometric standard deviations, with a maximum of $\sigma_g = 1.61$ and $\sigma_g = 1.46$ for the cases of 20-mm and 3-mm diameters, respectively. The geometric standard deviation for a self-preserving size distribution of completely spherical particles (fractal dimension of 3) is $\sigma_g = 1.46$ [136], which indicates that the 3-mm diameter nozzle produces particles that follow the same temperature profile and recirculation is avoided. Additionally, the smaller tube diameters increased the peak of the mobility distribution by nearly an order of magnitude for the case of the 3 mm nozzle compared to the case of the 98-mm-diameter tube, and by a factor of three between the 3-mm and 20-mm cases. The total concentration of particles produced in the 3-mm nozzle is roughly double the 20-mm tube, $\sim 2\times10^8$ cm^{-3} versus $\sim 9\times10^7$ cm^{-3}, respectively. The increased velocity of the nitrogen flow for the smaller tube diameters increases the convective cooling of the hot wire and thus increases the minimum power required to maintain a wire temperature that is high enough to produce particles. Therefore the power required for the onset of particle production was increased from 8.1 W with the 98-mm tube to 9.9 W with the 20-mm tube, to 15.4 W with the 3-mm nozzle. The 3-mm nozzle, which is the minimum achievable nozzle diameter with the current setup, gives the highest concentration and narrowest size distribution with a mode in the distribution less than ~10 nm.

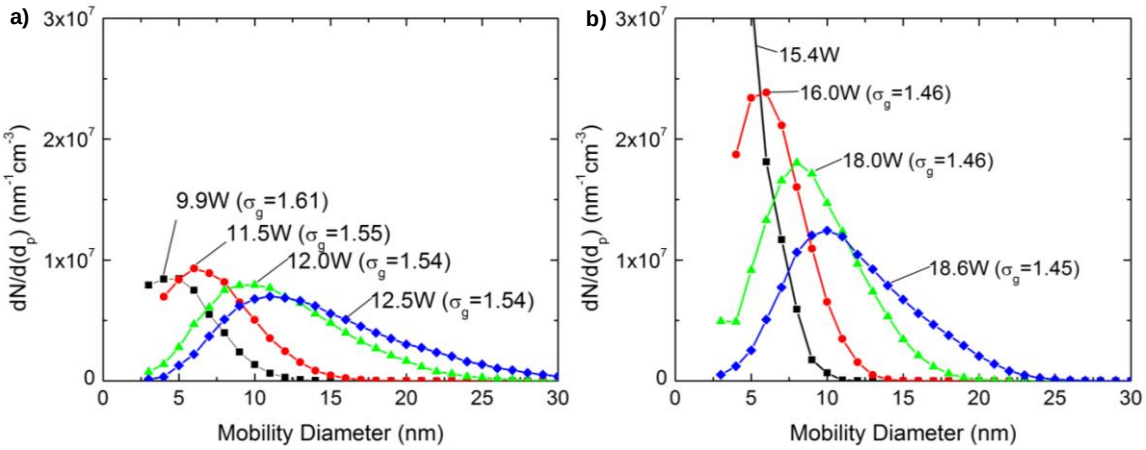

Figure 4.7: Particle size distributions of gold nanoparticles produced at varying wire powers in (a) a 20-mm tube and (b) a 3-mm nozzle with 2 slm of nitrogen flow.

As seen in Figure 4.8, TEM images of particles produced in the 20-mm tube show that increased power increases the size of the particles, which corresponds to the results shown in Figure 4.7. It is likely that for the 12.5-W synthesis (Figure 4.8a and b) the particles consist of partially-sintered primary particles as evidenced by their non-spherical shape. For the 9.9-W synthesis, Figure 4.8c and d show particles are spherical, with less disparity in size indicating that the particles are likely individually-nucleated primary particles rather than agglomerates. As in Figure 4.6d, the lattice spacings of the high-resolution images, Figure 4.8b and d, correspond to the (002) face of gold (2.04 Å).

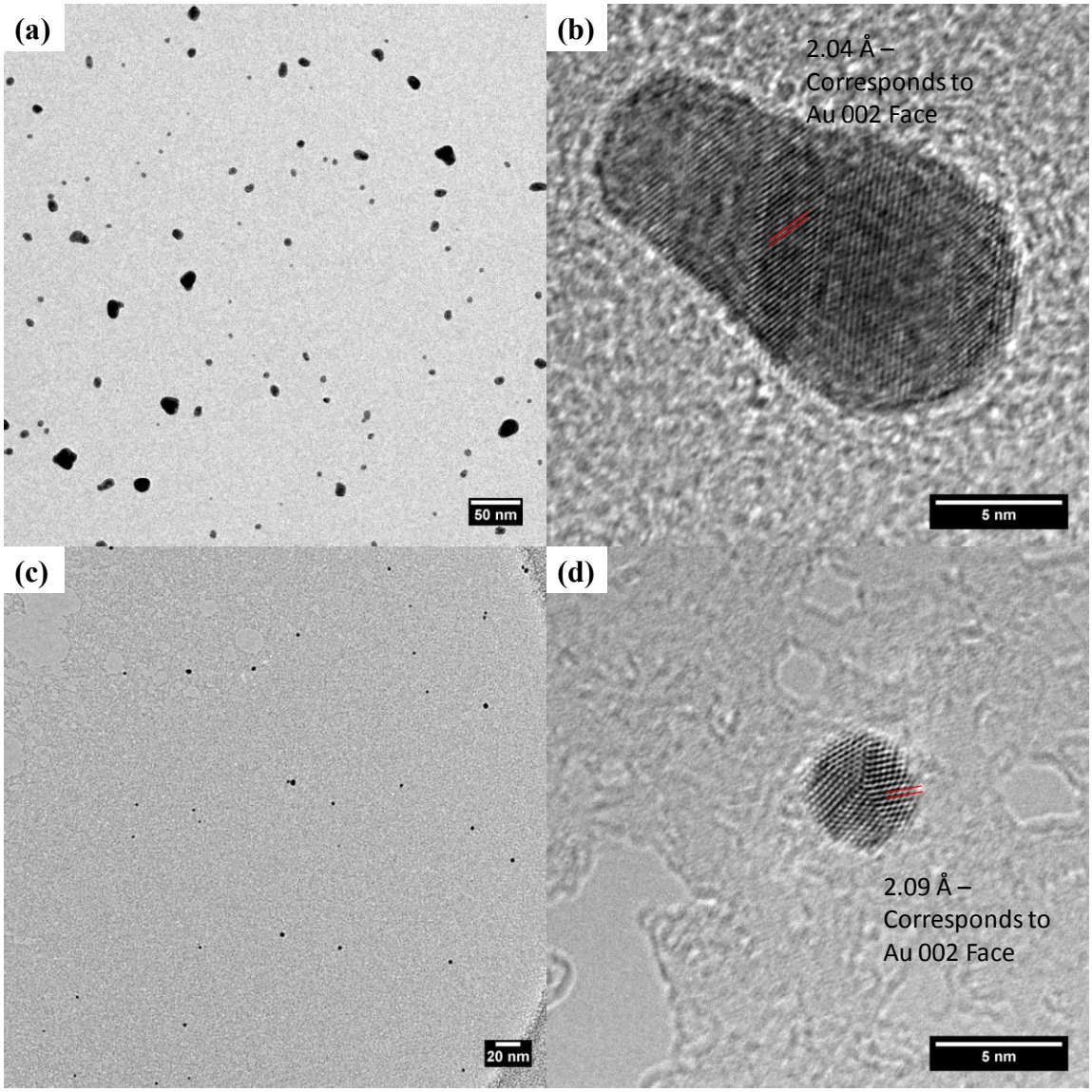

Figure 4.8: TEM images of gold particles produced from gold-coated platinum wire in 20-mm tube for 12.5 W (a & b) and 9.9 W (c & d).

As shown in Figure 4.9, the particles produced using the 3-mm nozzle are close to spherical for both the 18.6-W and 15.4-W syntheses. The increased velocity through the 3-mm nozzle serves to produce spherical particles while also lowering the standard deviation and mean particle size shown in Figure 4.7. The particles produced in the 3-mm nozzle appear to be single crystals without multiple

crystalline orientations for the majority of the particles analyzed. The particles appear to have more uniform size, see Figure 4.9a, than the particles produced with the larger tubes which agrees well with mobility size distributions shown in Figure 4.7. The small sizes of these particles coupled with their crystalline structure indicate that the 3-mm nozzle is effective in producing high concentrations of close-to-spherical and unagglomerated gold nanoparticles. As with the previous collections the lattice spacings of the high-resolution images of particles in Figures Figure 4.9b and d correspond to the gold (002) (2.04 Å) and (111) (2.35 Å) faces, respectively.

While the variation of the tube diameter changes the velocity of the gas it does not change the overall volumetric flow rate of gas through the system. To test the effect of volumetric nitrogen flow rate on the mobility size distribution of the gold nanoparticles, mobility distributions were measured for different gas flow rates passed over the hot wire in the 3-mm nozzle at atmospheric pressure. As shown in Figure 4.10, increasing the volumetric flow rate serves to decrease the mean particle mobility size. These results are in agreement with reports of silver nanoparticle production [133], but are more pronounced likely because in our study the voltage was held constant for all of the runs whereas Peineke *et al.* intentionally varied their applied voltage for the different runs to maintain a constant hot wire color (this was not feasible with our setup as the wire was not visible).

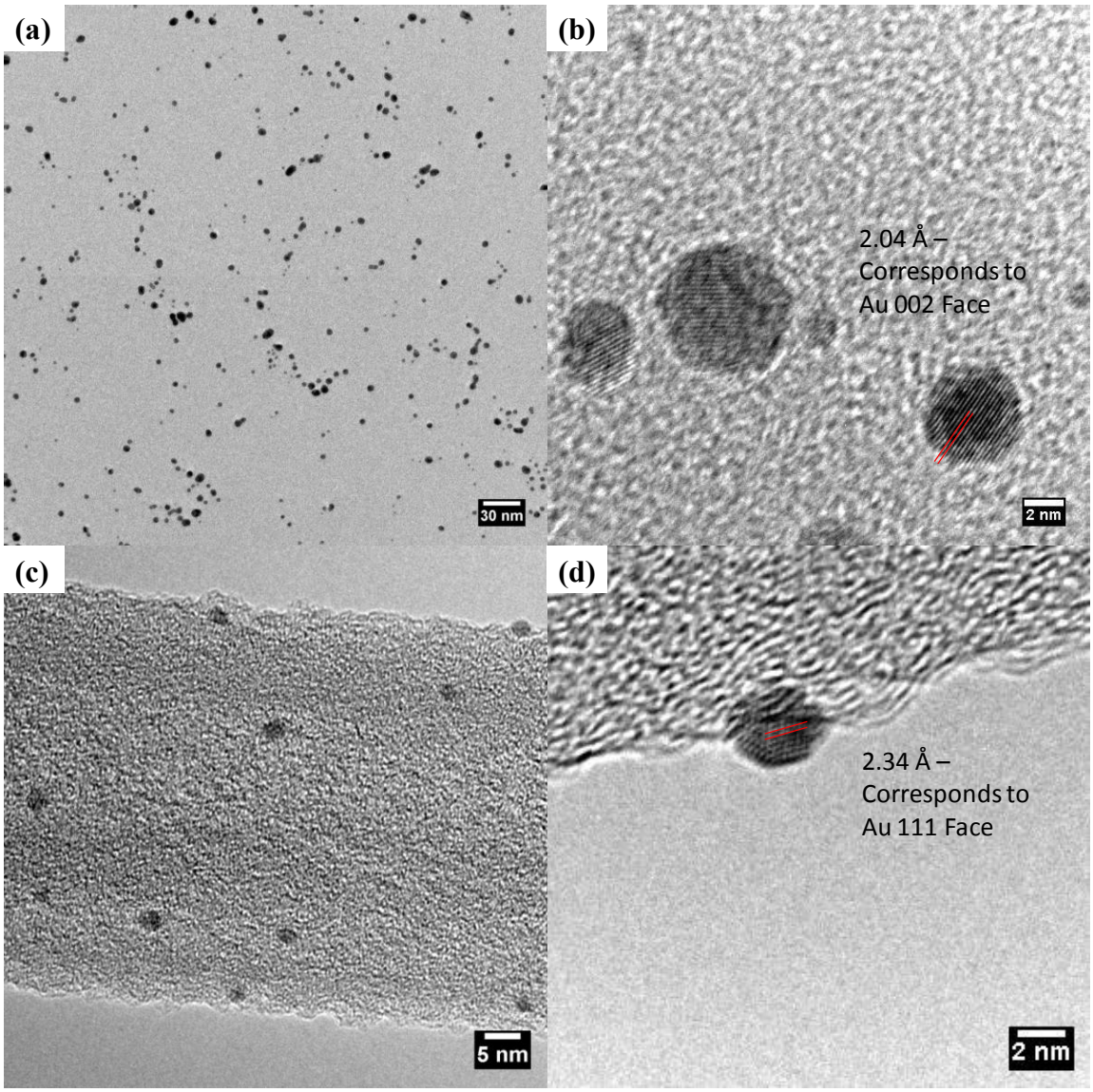

Figure 4.9: TEM images of gold particles produced from gold-coated platinum wire in 3-mm nozzle for 18.6 W (a & b) and 15.4 W (c & d).

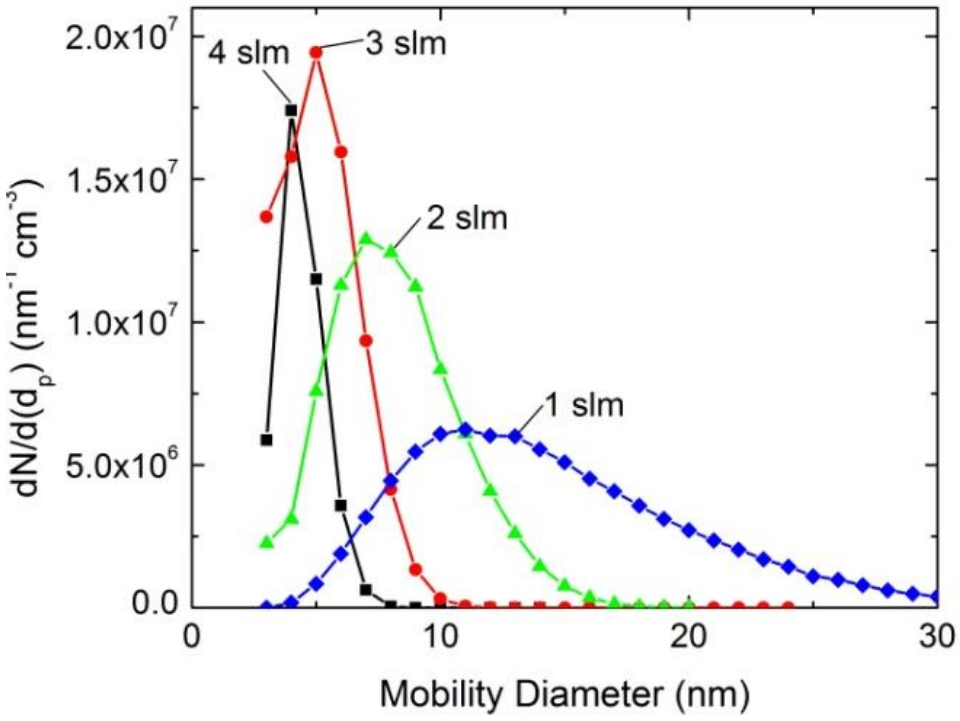

Figure 4.10: Particle size distributions of gold nanoparticles produced by a hot-wire generator in a 3-mm nozzle with varying nitrogen flow rates and a constant applied voltage of 1.5 V. (As a result of differing convective cooling rates of the wire the total power varied from 16.5 W for the 1-slm flow to 18 W for the 4-slm flow.)

Because the particles produced in this study result from evaporation of the gold outer layer of a gold-platinum composite wire, one potential issue is whether any impurities, platinum or otherwise, are contained within the particles. To investigate this, large particles were produced using the 20-mm tube with an applied power of 17.6 W in a nitrogen flow of 1.7 slm. The particles were collected on a lacey carbon grid and imaged using STEM, and their composition was analyzed using EDX. The resulting bright- and dark-field images, shown in Figure 4.11a and b, indicate that the particles consisted of large, partially-sintered agglomerates of primary particles. While these particles were larger than our optimal nanoparticles, single crystalline spheres < 10 nm, their size allowed for sufficient signal to be obtained from EDX analysis. As seen in Figure 4.11c, the EDX analysis indicates that

the particles are composed solely of gold with no detectable platinum contamination. The peaks of copper and carbon are due to the underlying grid, a lacey-carbon grid on a copper mesh, and do not indicate impurities.

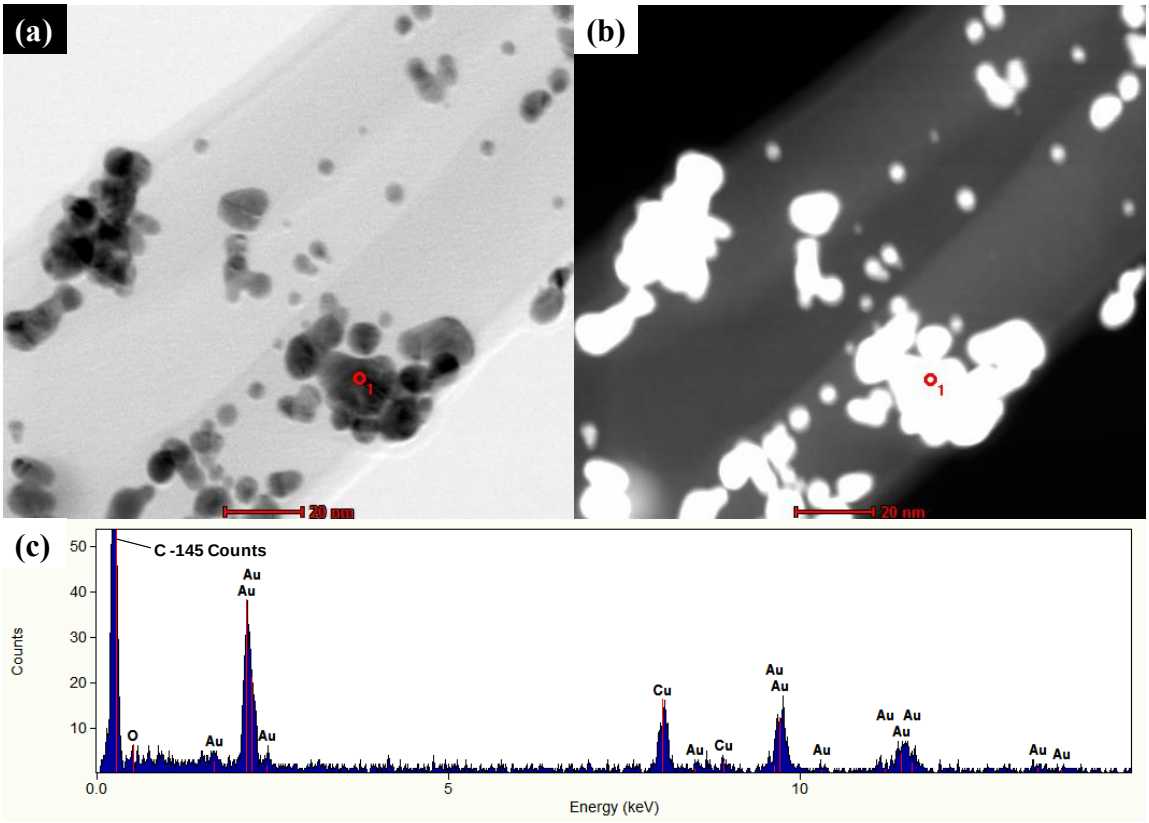

Figure 4.11: Bright- (a) and dark-field (b) STEM images of gold nanoparticles produced by hot-wire evaporation in a 20-mm nozzle with 1.7 slm nitrogen flow and 17.6W applied power. EDX (c) of nanoparticles indicating that particles consist of Au with few impurities. (The particles are collected on a copper mesh with lacey carbon grid).

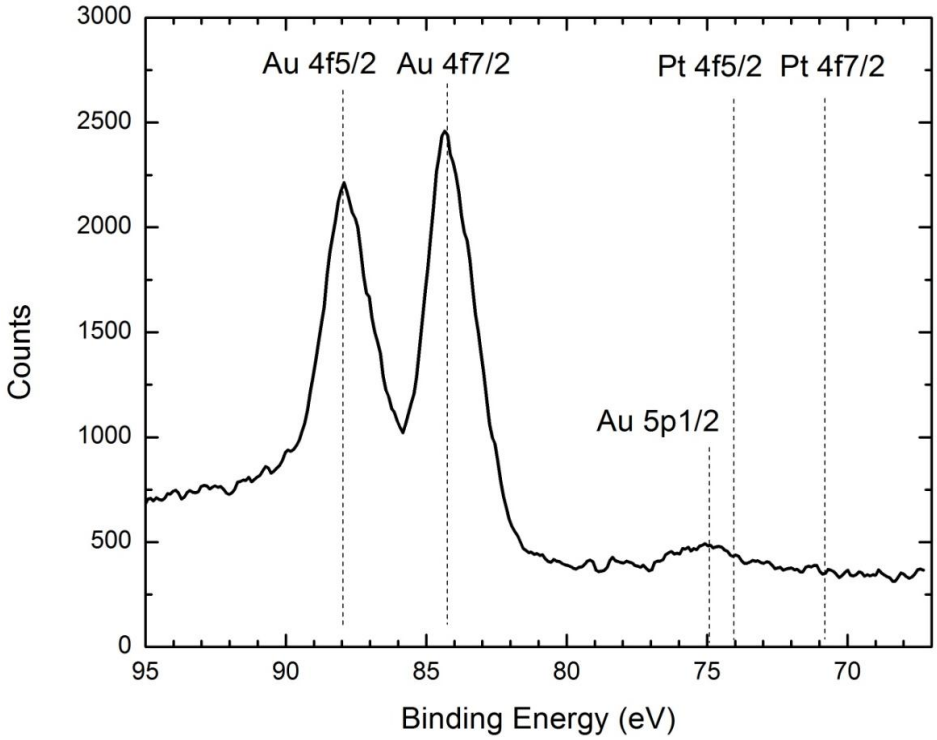

Figure 4.12: High-resolution x-ray photoelectron spectrum of gold nanoparticles highlighting the $4f_{5/2}$, $4f_{7/2}$ and $5p_{1/2}$ signature regions of the gold (~ 87.7, 84.0 and 75.0 eV, respectively) and the $4f_{5/2}$, $4f_{7/2}$ regions of the platinum (~74.3 and 71.1 eV, respectively) [137].

To further test the particle composition, nanoparticles were synthesized from the hot-wire generator operating at 18 W with 2 slm nitrogen flow. The particles were collected on a glass-fiber filter placed in line with the flow stream for 12 minutes, at which point particles were visible on the filter surface. The bulk characteristics of particles collected on the glass-fiber filter were then analyzed using XPS. The resulting spectrum was corrected for charging, as the particles were on a non-conductive filter, by comparing the established location of the C 1s peak (~285.3 eV) to its location in the survey spectrum (287.6 eV), corresponding to a shift of 2.3 eV [137]. This shift was confirmed by analysis of other known peaks present in the filter, namely for Si and O. As indicated in the high-resolution spectrum shown in Figure 4.12, the particles produced by the hot-wire generator

exhibited a strong gold signal at both the $4f_{5/2}$ and $4f_{7/2}$ Au spectral lines as well as a weaker signal at $5p_{1/2}$. There was no signal from the particles in the platinum doublet location of $4f_{5/2}$ and $4f_{7/2}$, indicating that the concentration of platinum was below the 0.1% detection limit of the XPS. These results confirm that the platinum core of the hot wire does not evaporate at the powers required to produce gold nanoparticles, and thus does not contribute impurities to the particles.

The "as-generated" charge distribution of particles is of particular interest for aerosol applications because the charge state can affect aerosol dynamics such as nucleation, agglomeration and wall loss, as well as measurements such as the electrical mobility within a DMA and transferred charge within an electrometer. The charge distribution of particles from a hot-wire generator is dictated by the number of ions and electrons leaving the surface of the wire along with the gold atoms. Theoretical work by Peineke and Schmidt-Ott [138] has shown that positive particle charges arise from the emission of ions from the wire surface as dictated by the Saha-Langmuir equation [139],

$$\alpha = \frac{n_+}{n_o} = \frac{g_i}{g_a} \exp\left(-\frac{e(U_i - \Phi)}{\kappa_B T}\right), \tag{4.1}$$

where n_+ and n_o are the fraction of ions and atoms leaving the surface, α is the ratio of ions to atoms, g_i and g_a are the electronic partition functions of the ions and atoms. U_i is the ionization energy of atoms on the surface of the wire, Φ is the work function of the substrate material, e is the elementary charge, κ_B is the Boltzmann constant and T is the temperature of the wire. As shown by Peineke and Schmidt-Ott, it is possible to calculate the ratio of ions to atoms leaving the surface for different substrate, *i.e.* wire, materials and atoms at the surface. While the composite wire used in this study began as a 99.9% pure platinum wire, the electrochemical coating of gold on the surface of the wire may have increased the impurities in the wire, which were not quantified. Therefore in addition to examining the ratio of ions to atoms leaving the wire for gold and platinum, it is necessary to consider other

common impurities such as lithium, sodium, potassium, magnesium, and calcium. As shown in Table 4.1, the ratios of ions to neutral atoms are small for gold and platinum when calculated at the respective substrate melting points. However, for various wire impurities the ratio of ions to atoms is much higher, with more ions than atoms being generated for those materials that have lower ionization energies than the work functions of gold and platinum, *e.g.* sodium and potassium. Therefore it is likely that even a small amount of impurity can account for the majority of positive gold-particle charging. While the number of positively charged ions increases as the wire substrate temperature increases so too does the number of electrons leaving the surface. The flux of electrons from the surface is governed by the Richardson equation,

$$J = A\,T^2 \exp\left(-\frac{\Phi}{\kappa_B\,T}\right) \tag{4.2}$$

where A is a constant. As shown by Peineke and Schmidt-Ott [138] the overall charge state is dominated by the emission of electrons at high temperatures, eventually resulting in more negatively charged particles than positive ones.

Table 4.1: Surface ionization energies and the ratio of ions to atoms leaving the hot-wire surface for gold and platinum wire substrates at their respective melting temperatures.

			Substrates			
			Au (Φ=5.31 eV)		Pt (Φ=5.64 eV)	
		U_i (eV)	U_i-Φ (eV)	α	U_i-Φ (eV)	α
Surface Atoms	Au	9.22	3.92	8.80×10^{-16}	3.59	7.01×10^{-10}
	Pt	9.00	3.69	1.88×10^{-14}	3.36	7.60×10^{-9}
	Li	5.39	0.08	0.250	-0.25	2.07
	Na	5.14	-0.17	2.19	-0.50	8.58
	K	4.34	-0.97	2.26×10^{3}	-1.30	810
	Mg	7.64	2.33	3.33×10^{-9}	2.00	2.31×10^{-5}
	Ca	6.11	0.80	1.94×10^{-3}	0.47	0.138

We investigated the charge state of "as-generated" gold particles produced by the hot-wire generator with the 3-mm-diameter nozzle and 1.5 slm of nitrogen flow. To accomplish this, we measured the mobility distributions of both positively- and negatively-charged particles by using a DMA in series with a CPC, without first passing the aerosol through a charger or neutralizer. We also measured the mobility distributions of all particles, charged and uncharged, by passing particles produced under the same conditions through a bi-polar Po-210 charger, and then correcting for the known size-dependent charging efficiency [48]. As in the previous experiments, all particles were assumed to be singly charged.

As shown in Figure 4.13, the portion of charged particles is < 10% for all applied powers. For the 14.0 W experiment, Figure 4.13a, the portion of negatively-charged particles is only 20% that of the positive particles, indicating that ion attachment is the dominant charging mechanism. As the applied power increases to 14.3 and 16.8 W, Figure 4.13b and c respectively, the overall fraction of charged particles increases as does the ratio of negative to positive particles. The increase in negatively-charged particles is consistent with theory and the findings of similar studies conducted of silver and palladium particle charging from hot-wire generators [133]. While the positive charges are a result of ion impurities, it is important to note that these impurities correspond to only a few atoms within a nanoparticle and do not represent a significant amount of contamination. One difference between the work of Peineke and the present study is the relative proximity and the temperature of the nozzle wall, which is closer and reaches higher temperatures, respectively, in our experimental setup. These differences may play a role in the emission of ions and electrons from the nozzle surface in addition to the wire surface. Further particle charging may be possible by changing the bias voltage of the hot wire relative to the rest of the chamber. This was not attempted for this study.

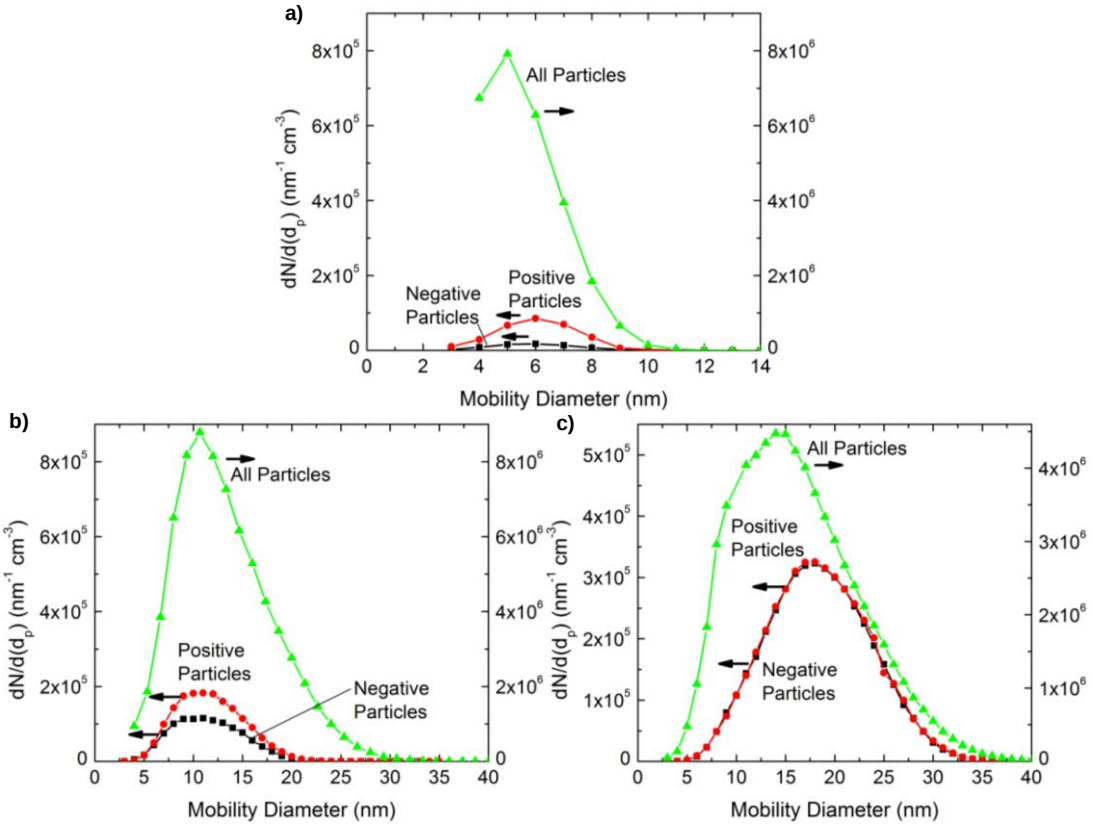

Figure 4.13: Particle size distributions of positive and negative singly-charged gold nanoparticles produced by hot-wire generator at (a) 14 W, (b) 14.3 W and (c) 16.8 W in a 3-mm nozzle with 1.5 slm of nitrogen flow.

4.4 Model Results and Discussion

In addition to experimental studies, a computational fluid dynamics (CFD) model was developed to give a better understanding of the temperature and velocity profiles within the hot-wire nanoparticle generator. The discretized CFD model was developed within Fluent (a commercially available computational fluid dynamics platform by ANSYS, Inc.). The model includes meshes for each of the different tube geometries discussed in the experimental section, a 3-mm nozzle, 20-mm tube and 98-mm tube. The model solves both the conservation of energy and momentum equations for a compressible fluid. A standard k-ε 2-equation model is

used to solve for the turbulent conditions with the following constants, C_{μ}-=0.09, $C_{1\epsilon}$=1.44, $C_{2\epsilon}$=1.92, σ_k=1.0, σ_ϵ=1.3 [140]. A standard laminar flow model is also included for comparison. No viscous heating or radiant heat transfer is included. The model is single phase with only gas-phase nitrogen present in the flow. Nitrogen is modeled as an ideal gas with density varying accordingly. The specific heat of nitrogen varies with temperature according to a piecewise linear function. The thermal conductivity and viscosity are constant at 0.0242 W $m^{-1}K^{-1}$, and 1.663×10^{-5} kg $m^{-1}s^{-1}$, respectively. The boundary conditions of the system include a constant face velocity at the inlet corresponding to a flow rate of 2 slm, a no-slip boundary condition at the walls, an axisymmetric condition at the center of the tube, and a constant pressure outlet that is maintained at atmospheric pressure. The incoming gas has a temperature of 20°C and all other surfaces act as insulating walls. The model uses a body force weighted pressure solution method where the effect of gravity is included in the direction perpendicular to the flow. The momentum, turbulent kinetic energy, turbulent dissipation rate and energy equations are all solved with the first-order upwind method. The residuals for convergence are 10^{-3} for the continuity, x-velocity, r-velocity, k and epsilon, and the energy residual was set at 10^{-5}.

As shown in Figure 4.14, the hot-wire generator with the 3-mm nozzle was modeled with a wire surface at a constant temperature of 1,338 K (1,065°C, the melting temperature of gold which is the minimum required temperature to produce particles [133]). Models with a constant power boundary condition that corresponds to the experimental powers discussed previously result in unrealistically high wire temperatures that are the result of the single-phase model in which the latent heat of evaporation is not accounted for when gold vapor leaves the solid surface (an endothermic process), nor is it accounted for downstream in when the particles nucleate (an exothermic process). As a result the model cannot be used to determine absolute values, but rather is useful to indicate temperature

and velocity trends. The temperature profile with the constant wire temperature, Figure 4.14a, indicates that a strong temperature gradient exists near the wire surface and that 0.5 mm away from the wire surface the gas temperature is less than 500 K. The velocity vectors in Figure 4.14b show that the flow is laminar with no recirculation and a maximum velocity of ~10 m/s. These results give evidence to support the theory that as the gold vapor leaves the wire surface it is quickly entrained by the nitrogen cross flow. The gold then likely nucleates as it is supersaturated in the much lower gas temperatures. The formation of particles in the laminar flow stream prevents turbulent driven agglomeration.

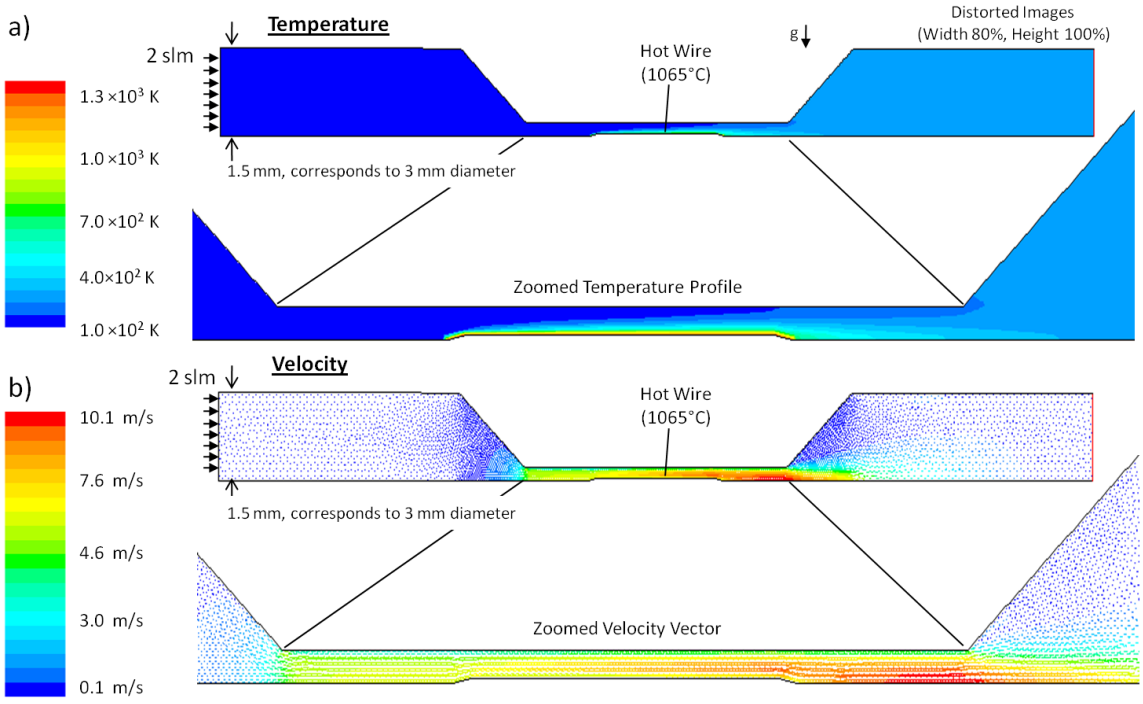

Figure 4.14: Computational fluid dynamics model results for the (a) temperature profile and (b) velocity vectors within a hot-wire generator with 2 slm of nitrogen flow and a wire temperature of 1065°C within a 3-mm converging-diverging nozzle.

The CFD model was also ran with a geometry that modeled the hot-wire generator with the 20-mm tube and a constant wire surface temperature of 1,338 K. As shown Figure 4.15a, the 20-mm model also indicates that a high temperature

gradient exists near the wire surface. However as the flow has a lower velocity across the face of the wire in the 20-mm tube, buoyancy effects begin to affect the flow. The temperature profile begins to become non-symmetric about the wire. The velocity vectors, shown in Figure 4.15b, still indicate that the flow is mostly laminar with a maximum velocity of 0.18 m/s. Close inspection of the velocity vectors indicates that there are slight radial components in the velocity vectors, which may indicate the beginning of buoyant driven flow. As noted previously the particles produced in these tubes consist of larger agglomerates which may be due to the longer residence time of gold after leaving the wire surface.

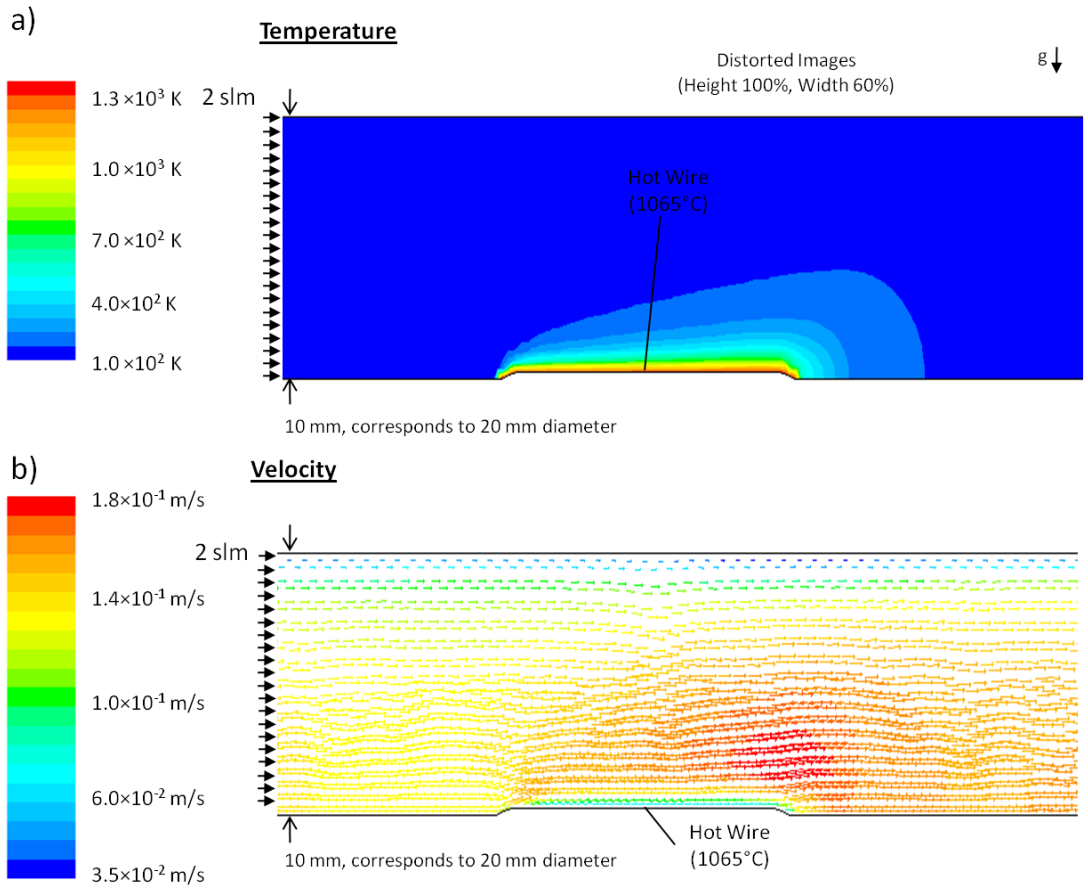

Figure 4.15: Computational fluid dynamics model results for the (a) temperature and (b) velocity profile within a hot-wire generator with 2 slm of nitrogen flow and a wire temperature of 1065°C within a 20-mm tube diameter.

As shown in Figure 4.16a, the modeled temperature profile in the 98-mm tube indicates that a high temperature gradient exists at the wire surface. As shown in Figure 4.16b, the modeled velocity is significantly lower than the previous simulations with a maximum at 0.02 m s^{-1}. Inspection of the velocity vectors indicates that recirculation regions within the flow develop despite the low forced-flow rates. The recirculation regions result from buoyancy forces that begin to dominate within the system as the forced flow decreases, a consequence of increasing the tube diameter. Recirculation regions within the flow may lead to the increased agglomeration and broad size distribution that are shown in Figure 4.6.

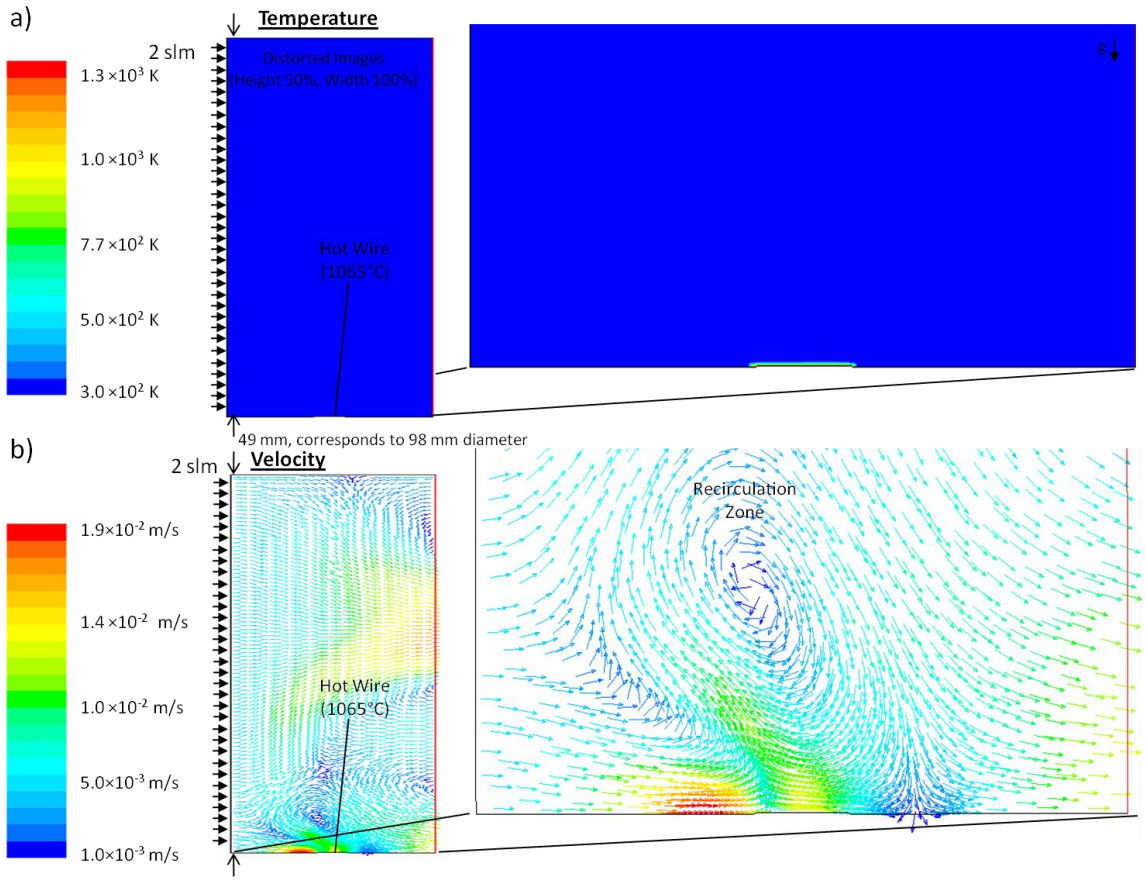

Figure 4.16: Computational fluid dynamics model results for the (a) temperature and (b) velocity profile within a hot-wire generator with 2 slm of nitrogen flow and a wire temperature of 1065°C within a 98-mm chamber.

In order to further investigate the relative contributions of forced and buoyant flows for the hot-wire generator an analytical framework was developed to determine which flow dominated at differing geometries. The transition between forced and buoyancy driven flows has been the focus of much research and the analysis below largely follows the work of Mills [141]. An important parameter for buoyancy driven flows is the Grashof number ($Gr = \frac{g\beta\Delta TL^3}{v^2}$), where g is the gravitational acceleration, β is the thermal expansion coefficient ($\beta = 1/T$ for ideal gasses), ΔT is the difference in fluid temperature within the system, L is a representative length scale and v is the kinematic viscosity. For an analysis of flow between two concentric cylinders the length scale of interest for the Grashof number is half the difference between the two cylinders, $L = (D - d)/2$ where D is the inner diameter of the outer cylinder and d is the outer diameter of the inner cylinder. For forced flow an analogous term to the Grashof number is the Reynolds number, $Re = \frac{UD}{v}$, where U is the bulk fluid velocity within the system and D is a representative length scale (D is the inner diameter of the outer tube). In order to determine whether a flow is dominated by buoyancy or forced flow, the ratio of the Grashof number to the square of the Reynolds number gives an indication of the dominant flow within the system,

$$\frac{Gr}{Re^2} = \frac{g\beta\Delta TL^3}{U^2D^2}. \tag{4.3}$$

When Gr/Re^2 is less than 1, forced flow dominates and conversely when Gr/Re^2 is greater than 1, buoyancy effects dominate. A transition region occurs when Gr/Re^2 is $\sim$1 where both forces are important. In buoyancy driven flows, an important parameter in determining whether the buoyant flow is laminar or turbulent is the Rayleigh number which is defined as,

$$Ra_L = \frac{g\beta\Delta TL^3\rho}{\mu\alpha} \tag{4.4}$$

where ρ is the density of the fluid, μ is the dynamic viscosity and α is the thermal diffusivity. For the specialized case in which the system consists of horizontal concentric cylinders a correction factor has been developed where the Rayleigh number is defined as,

$$Ra_{cyl} = \frac{\left(\ln\left[\frac{D}{d}\right]\right)^4}{L(d^{-3/5}+D^{-3/5})^5} Ra_L. \quad (4.5)$$

Laminar flows are typical for $Ra < 10^8$ whereas transitional and turbulent flows are found within the regions $10^8 < Ra < 10^{10}$ and $Ra > 10^{10}$, respectively.

To determine the respective dominance of differing flow regimes in each of the tube geometries discussed previously, an analytical framework was developed that corresponds to the idealized flow shown in Figure 4.17. In the analytical model nitrogen, constant flow rate of 2 slm, flows into the region between the two concentric cylinders in which the inner cylinder has a constant wall temperature of 1338 K, which corresponds to the melting point of gold. Other values for the analysis included, g=980 cm s^{-2}, ΔT=1750 K, β=10^{-3} K^{-1}, μ=3.9×10^{-10} g cm^{-1} s^{-1}, v=1.2 cm s^{-1}, ρ= 3.4×10^{-4} g cm^{-3} and α=1.7×10^{-4}. All of the values were taken for nitrogen at 1000 K and at 1 bar including the calculation of velocity.

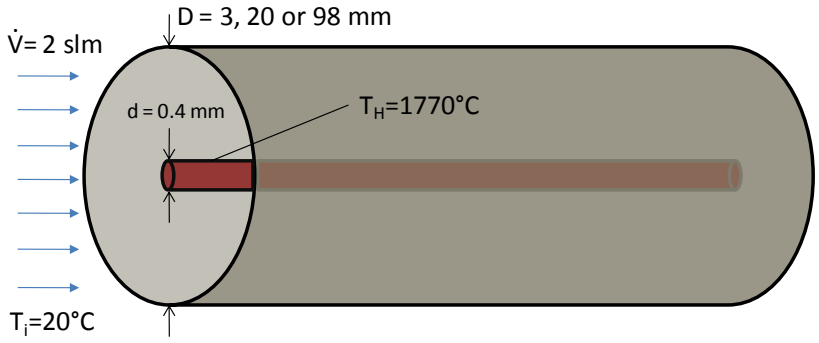

Figure 4.17: Schematic of hot-wire generator for purposes of analytical analysis.

As shown in Table 4.2, the ratio, Gr/Re^2, is 1.2×10^{-5} for the hot-wire generator with a 3-mm nozzle, indicating that forced flow dominates the system. At 20 mm, the ratio, Gr/Re^2, is 0.17 which is close to unity and indicates that both

buoyant and forced flows are critical. As the diameter of the tube increases to 98 mm, so too does Gr/Re^2, 4.8×10^2, indicating that buoyancy flows are dominant. These results indicate that the flow within the hot-wire generator is increasingly dominated by buoyancy effects as the tube diameter increases for a set volumetric flow. For the flows in which the buoyant forces are important, the Rayleigh number indicates whether the buoyant flow is turbulent or laminar flow. The Rayleigh numbers for the 20-mm and 98-mm cases are 4.6×10^8 and 3.0×10^{10}, respectively, which signify that the buoyant flows are transitional and turbulent, respectively. These results corroborate the experimental and modeled findings that show that the larger diameter chamber causes increased particle agglomeration and non-uniform growth which are likely a result of recirculation regions within the flow due to buoyant forces. By decreasing the effective diameter of the nozzle, the forced flow dominates which results in laminar flow through the hot-wire generator.

Table 4.2: Analytically determined parameters describing the nature of the mixed, buoyant and forced flow within the hot-wire generator.

	Diameter		
	3 mm	20 mm	98 mm
L (cm)	0.15	1.00	4.90
U (cm/s)	1726.7	38.9	1.6
Gr	2.5	7.6×10^2	8.9×10^4
Re_D	448.1	67.2	13.7
Gr/Re^2	1.2×10^{-5}	1.7×10^{-1}	4.8×10^2
Ra_{cyl}	1.8×10^6	4.6×10^8	3.0×10^{10}

4.5 SUMMARY

This chapter demonstrates that gold nanoparticle production is possible using a hot-wire generator at atmospheric pressure without wire oxidation or significant impurities when a composite gold-platinum wire is used. Care must be taken in designing the relative diameters of the platinum core and gold shell so that most of the current passes through the platinum core and melting of the gold shell

does not significantly affect the total wire conductivity. The size and concentration of gold particles produced from the hot wire are largely affected by the generator system parameters of applied power, tube diameter, and gas flow rate. By increasing the flow rate and decreasing the tube size the geometric standard deviation of the particle size distribution is decreased. The use of a 3-mm-diameter nozzle and sufficiently high applied powers results in a high concentration of nanoparticles less than 10 nm. The measured charge state of the particles as produced using the 3-mm nozzle is similar to previous findings using a hot-wire generator, where an increasing fraction of the particles is charged at higher powers as a result of thermionic emission by the generator. As with methods such as spark discharge and evaporation-condensation particle production, there is an upper limit to the number of particles that can be produced with hot-wire generators before the characteristic time for particle-particle collisions is on the same order as the residence time of the system, thus resulting in formation of agglomerates. Additional measures, such as applying a bias voltage to the system, may result in the production of a high fraction of unipolar charged particles, which would suppress coagulation, allowing for the production of higher concentrations while maintaining individual unagglomerated particles.

CFD modeling of the fluid flow gives insight into the velocity and temperature profiles within the hot-wire generator. The results of the model indicate high temperature gradients exist near the wire surface that likely serve to quickly cool the gas-phase gold vapor upon leaving the wire. As the tube geometry varies from smaller to larger diameters, the modeled velocity within the hot-wire generator decreases and begins to show recirculation zones. An analytical analysis of the system based on the ratio of inertial to buoyant forces corroborated the modeled results, indicating that at small diameters the flow is dominated by inertial forces and at large diameters becomes dominated by buoyant forces. The transition from a forced flow to a buoyant-dominated flow also coincides with a transition to

turbulence in the buoyant flow. The prediction of the turbulent flow from the analytical analysis supports the CFD model results and gives insight into the particles produced at large tube diameters which were shown to be non-spherical as a result of agglomeration. The presence of the nozzle within the hot-wire generator reduces the impact of buoyant forces, thus eliminating the recirculation zones and reducing particle agglomeration.

Chapter 5 - Nanoparticle Surface Decoration with Gold

5.1 Overview

Gold-decorated nanoparticles are of interest due to their unique plasmon resonance [142] and catalytic effects [143]. The catalytic effects have applications in various industrial products such as fuel cell production [144, 145] and chemical synthesis by hydrocarbon oxidation [146, 147]. Researchers are considering gold-decorated nanoparticles because of their plasmon resonance effects for biological applications including drug delivery[121], thermal therapies [119] and cancer diagnostics [148]. A recent study by Gaiduk *et al.*, highlights the use of gold nanoparticles in imaging single molecules for biological applications [149].

Currently most gold nanoparticles and nanoparticle coatings are synthesized using wet-chemistry techniques that require the use of solvents containing inherent impurities that can affect the surface of the nanoparticles. A review by Daniel and Astruc [113] discusses methods of synthesizing and controlling solution-phase nanoparticles with gold surfaces and demonstrates the complexities of controlling gold growth in a solution. The preeminent gold coating process used currently is one developed by the Halas group [36, 150] whereby silica particles are prepared by a wet-chemistry technique and then gold nanoparticles are attached to the surface. The gold particle surface acts as a nucleation site for successive attachment of gold until a gold shell is completed. As the gold islands on the particle surface grow and begin form a continuous film, the absorption spectrum of the particles shifts from the visible to the infrared region due to changes in surface plasmon resonance in accordance with Mie theory [36]. Wet-chemistry synthesis processes of this sort typically require multiple solution steps, take hours or days to complete, and are batch processes.

An alternative to wet-chemistry batch synthesis is the continuous production of gold-decorated silica nanoparticles by a gas-phase method. The synthesis can be conducted in an inert or non-reacting gaseous environment with low impurities, thus avoiding the inherent impurities of synthesis when using liquid solvents. Also, because the gas-phase synthesis is a continuous process in which gas-phase precursors are reacted within a flow stream, the overall production of nanoparticles occurs within seconds rather than hours. Several methods exist for the production of nanoparticles within the gas phase including flame synthesis [151], inert-gas condensation [79, 94], plasma synthesis [152], hot-wire generation [133], spark discharge [131], and chemical vapor synthesis [153]. Chemical vapor synthesis is an attractive method for producing nanoparticles from precursors with sufficiently high vapor pressures which can be delivered to a hot-wall reactor and thermally decomposed in the presence of an inert or non-reacting gas such as nitrogen. Hot-wire generators are an effective, low-cost way of producing gas-phase nanoparticles from solid, electrically-conductive materials such as metals. As discussed in Chapter 2, the photo-CVD production of coatings is a controllable way to produce films, so long as precursors are available with high vapor pressures.

This chapter includes a discussion on the creation of gold-decorated silica and iron oxide nanoparticles by a gas-phase production method. The silica nanoparticles were produced by chemical vapor synthesis whereby tetraethylorthosilicate (TEOS, $Si(OC_2H_5)_4$) was decomposed in a tube furnace within a nitrogen environment. The silica nanoparticles were subsequently decorated with gold produced from two different evaporation methods, hot-wire and tube-furnace evaporation, downstream of the silica nanoparticle synthesis. Studies were also conducted that investigate the surface decoration of plasma synthesized iron oxide nanoparticles with gold by evaporative techniques. Initial studies are also discussed regarding the gold coating of silica particles by photo-CVD from an organometallic gold precursor, dimethyl-gold-hexafluoroacetylacetonate ($Me_2Au(hfac)$,

$AuO_2F_6C_7H_7$). Finally the combination of multiple synthesis and coating techniques is shown to be capable of producing tri-layer nanoparticles, consisting of an iron oxide core with a silica shell and gold surface decoration. For each study the particle morphologies were investigated by varying critical system parameters and the fundamental mechanisms behind the two different evaporation methods were explored.

5.2 Decoration of Silica Nanoparticles with Gold

5.2.1 Experimental Procedure

The gold-decorated silica synthesis method is shown schematically in Figure 5.1. In the typical setup, TEOS is evaporated into a flow stream by bubbling nitrogen (~26 sccm) through a liquid TEOS bubbler (results in ~0.06 sccm) which is then mixed with oxygen (1 slm) and additional nitrogen (2 slm) before it enters the decomposition furnace (900°C). The furnace dissociates the TEOS, which then homogeneously nucleates to form silica nanoparticles in the gas-phase. Due to their high concentration, the silica nanoparticles quickly begin to agglomerate upon leaving the furnace. The agglomeration is suppressed by the addition of a nitrogen dilution flow (~2 slm). The agglomerated particles are then sintered to form fully-coalesced, spherical particles by being passed through a second tube furnace (800-1400°C). The typical residence time the process is approximately 6 s. All tubing has an inner diameter of 3.75 mm except for the tubes within the furnaces which has an inner diameter of 10.4 mm in the decomposition furnace and 20 mm in the sintering furnace.

Gold decoration occurs by passing the silica particles through one of two different gold evaporation chambers. In Path A, the aerosol passes through a tube furnace (1200-1500°C) whereby the entire aerosol is heated before it passes over a gold slug which evaporates, introducing gold vapor into the aerosol. Upon cooling, the vapor heterogeneously nucleates on the surface of the nanoparticles, thus

creating gold decoration. The particles are then either directly collected or characterized in-situ.

In Path B the aerosol passes over a hot-wire evaporator where a gold-coated platinum wire is heated by electrical resistance to introduce gold into the aerosol. The diameter of the tube is decreased in the region surrounding the gold-coated wire to 3 mm, as discussed in Chapter 4. In the hot-wire evaporator the gold is heated directly and the aerosol remained cooler than the surface temperature of the wire, thus resulting in a different delivery method of the gold to the particle surface which is discussed later. Once the gold is introduced to the aerosol, the particles are then either passed through an agglomeration chamber, which increases the residence time (~30 s) to allow for further agglomeration, or directly collected and/or characterized in-situ.

The in-situ characterization techniques used for the aerosol synthesis process were particle mobility measurement by differential mobility analyzers (DMAs) and in-situ infrared spectroscopy. The DMA coupled with an ultrafine condensation particle counter (CPC) were configured as a discrete mobility particle sizer (DMPS) by adding them in series at the end of the process to measure the mobility diameter of the synthesized particles. Additionally, a tandem differential mobility analysis (TDMA) setup was used to study coating mechanisms by adding a DMA after the silica synthesis to select a monodisperse stream of silica particles for subsequent gold decoration. In-situ infrared spectroscopy was performed by collecting the nanoparticles in flight on a stainless steel mesh within the analysis cell of a Fourier transform infrared (FTIR) spectrometer. The particles were collected for ex-situ characterization by electrostatic precipitation at +3 kV onto lacey carbon microscopy grids. A transmission electron microscope (TEM) was used to image particles and perform energy dispersive x-ray (EDX) analysis.

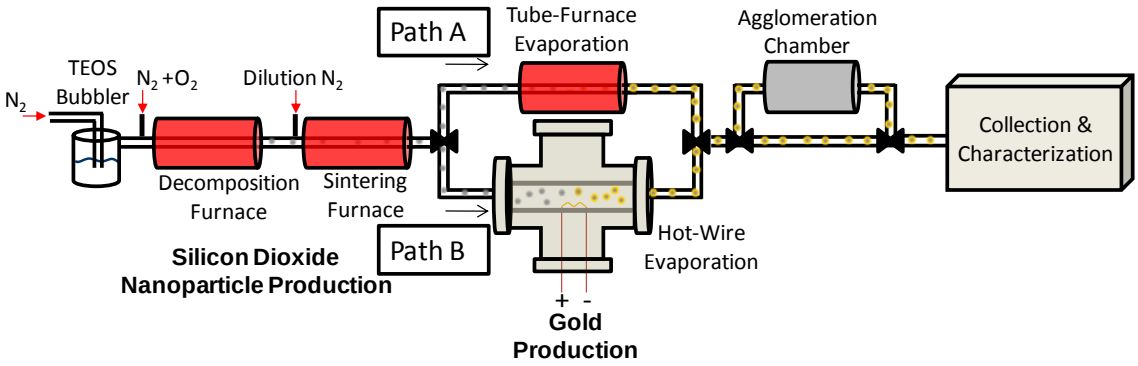

Figure 5.1: Schematic of gold-decorated silica particle production with hot-wire (Path A) and tube-furnace (Path B) evaporative techniques.

5.2.2 Experimental Results

Silica nanoparticles were synthesized using 0.06 sccm of TEOS, 2 slm of nitrogen and 1 slm of oxygen in a tube furnace at 900°C. The particles were diluted with an additional 2 slm of nitrogen and sintered at varying temperatures. As seen in Figure 5.2a the particle concentration increased with increasing sintering temperature up to 1200°C, indicating that in addition to sintering, the furnace caused unreacted TEOS to nucleate, producing more particles. Above 1200°C the increase in temperature did not increase the total concentration of particles, indicating that all of the TEOS had been decomposed and only sintering occurred. For particles sintered at 1500°C, there was actually a slight loss in particle concentration when compared to sintering at 1400°C, which is likely a result of increased losses to the tube walls at increased temperatures. Therefore, the optimal particle production was found to occur from 1200-1400°C where all of the TEOS was decomposed but losses to the wall were not substantial. As seen in Figure 5.2b, a TEM image of particles produced at a sintering temperature of 1400°C shows that the particles were spherical and mostly unagglomerated. Figure 2c shows the effect of adding oxygen when producing silica nanoparticles by comparing the infrared spectra of particles produced with oxygen to those produced without. In each case, the particles were produced with the aforementioned conditions and collected on a

stainless steel mesh in the FTIR cell for 45 minutes. As shown, the particles produced with oxygen exhibit a much more intense peak at the Si-O-Si stretching region, 800 cm^{-1}, and at the Si-OH stretching region ~940 cm^{-1}. Additionally, the presence of oxygen shifts the peak from the Si-O-Si asymmetric stretch, 1000-1200 cm^{-1}, toward higher wavenumbers, an indication of more structurally ideal silica [81]. As these results indicate, the silica particles are best produced with a sintering temperature from 1200-1400°C and with 1 slm of oxygen. All of the following results in this study use this production method unless otherwise noted.

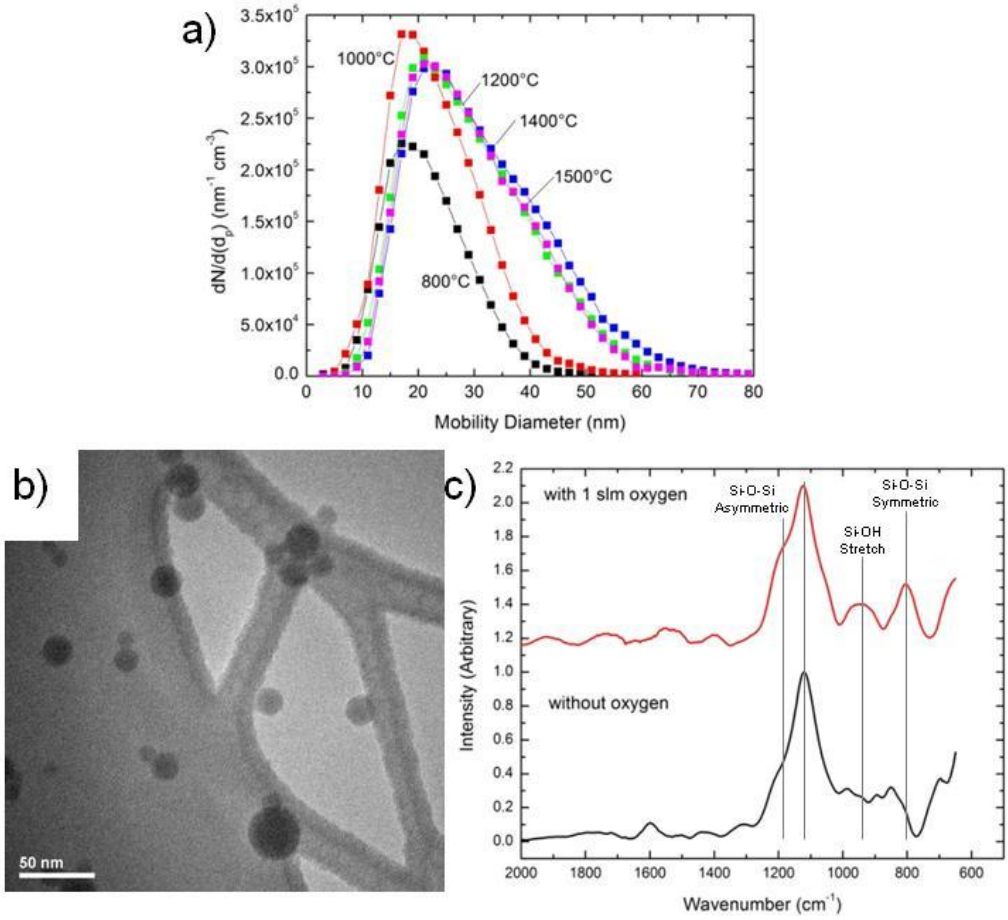

Figure 5.2: (a) DMPS measurements of silica nanoparticles produced from the thermal decomposition of TEOS at 900°C and subsequent sintering at varying temperatures. (b) TEM image of silica nanoparticles sintered at 1400°C. (c) FTIR spectra of silica particles produced with and without oxygen.

Gold decoration of the silica nanoparticles was first investigated by passing the silica aerosol through Path A, whereby the entire aerosol was heated and then passed over a gold evaporation slug. By heating the entire aerosol gold-decorated particles were produced, Figure 5.3. For lower temperatures, as shown in Figure 5.3a, almost all of the gold decorated the silica surface and little gold appeared independently on the lacey carbon grid. As the furnace temperature increased, so too did the amount of gold vapor entering the aerosol stream, resulting in an increase in the gold nanoparticles independent of the silica particles observed on the lacey carbon shown in Figure 5.3a and b. A likely explanation for this behavior is that at lower vapor concentrations the gold preferentially nucleated on the silica particle surface, however as the vapor pressure of the gold increased so too did the propensity for gold to homogenously nucleate. The homogeneous nucleation of gold results in increasing numbers of independent gold particles. In all cases the gold appeared to "ball up" on the surface of the silica nanoparticles, which was likely due to the difference in surface energies between silica and gold. At temperatures near the melting point of gold, ~1063°C, the contact angle of gold on a pure silica surface is 140° [154]. Because the silica particles were hot when the gold condensed on their surfaces, the gold atoms possess enough energy that they arrange in the manner that lowers the collective surface energy of the gold and thus result in gold decoration rather than a thin film.

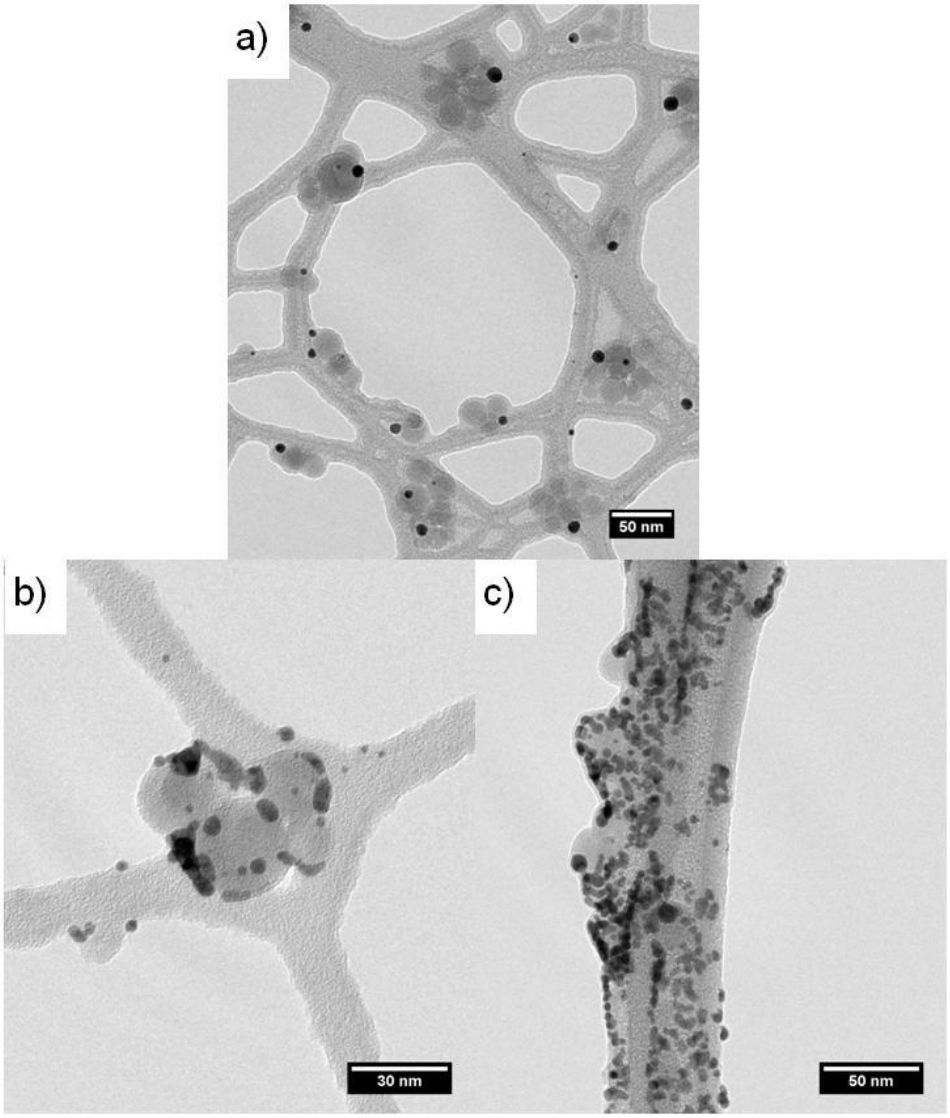

Figure 5.3: TEM images of gold decorated silica particles collected at the varying evaporation furnace temperatures of (a) 1300°C, (b) 1350°C and (c) 1425°C.

To investigate the effect of heating just the gold rather than the entire aerosol, silica particles were passed through the hot-wire evaporator along Path B as indicated in Figure 5.1. As shown in Figure 5.4, the amount of gold decoration on the silica particle surface increased when the power applied to the gold-coated wire was increased. The increased gold evaporation from the hot wire, due to the

increase in wire surface temperature at higher powers, also resulted in more gold being collected independent of the silica particles, a similar result as found in Path A. In all cases, gold decorated the particle surface rather than forming a continuous film. Unlike when the aerosol was purposely heated to evaporate gold, along Path A, the aerosol was only heated indirectly as it came into contact with the gold-coated hot wire. Therefore, as gold vapor left the surface of the wire, gold homogenously nucleated. Upon nucleation, the gold particles were then hypothesized to be scavenged by the larger silica nanoparticles.

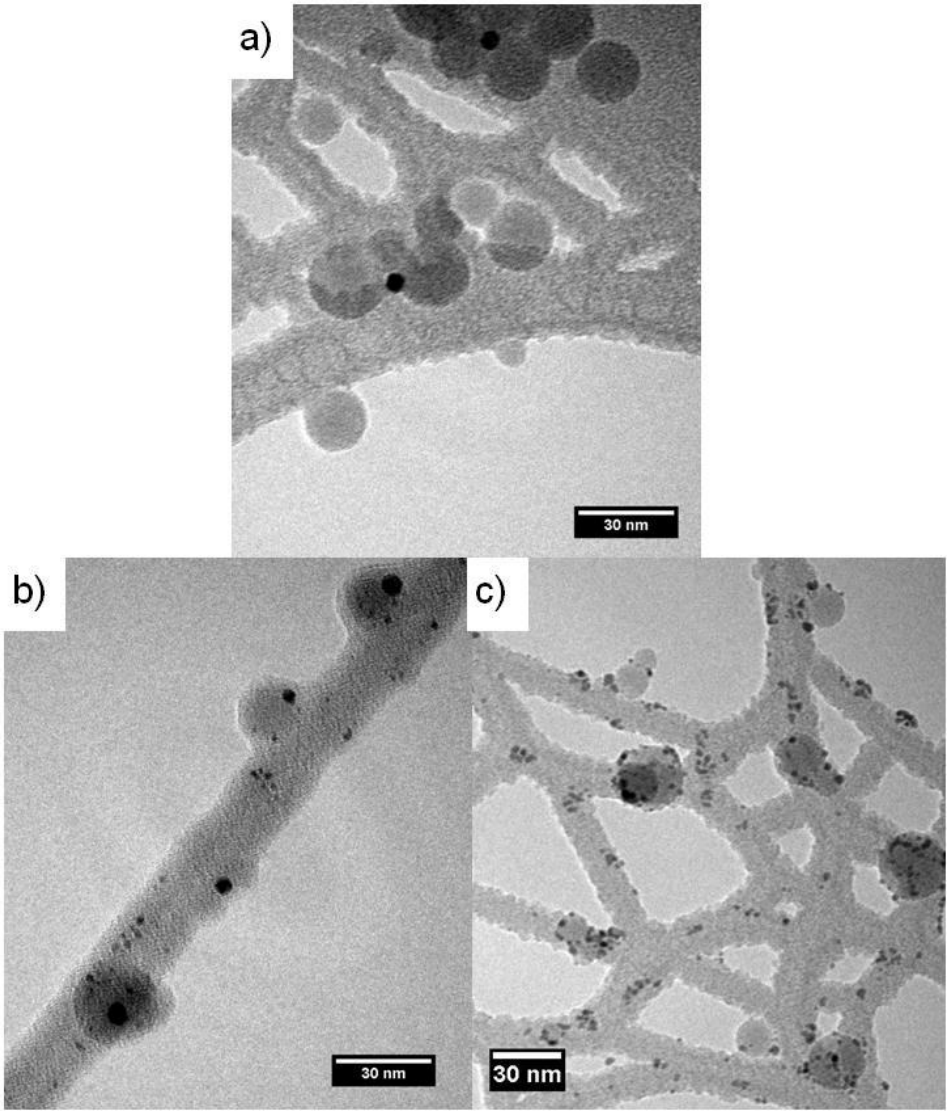

Figure 5.4: TEM images of Au decorated silica particles at varying hot-wire voltages (a) 19.5 W, (b) 20.8 W and (c) 23.8 W.

In order to confirm that the gold particles nucleated homogenously and were then scavenged by the silica particles, a series of TDMA studies were conducted where silica was size selected at 30 nm prior to entering the hot-wire evaporator. Upon size selection with the first DMA, the concentration of the aerosol was reduced. The resulting aerosol flow passed through the hot-wire evaporator at a flow rate of 1 slm. By on-line analysis and subsequent TEM study, it was confirmed

that particle decoration only occurred in the hot-wire evaporator when a smaller particle mode developed, as shown in Figure 5.5a. When the aerosol was analyzed immediately after leaving the hot-wire evaporator, the silica mode shifted to a larger size but there remained a significant difference between the smaller gold particle mode and the larger silica particle mode. The TDMA of the directly collected nanoparticles is confirmed in Figure 5.5b where it is apparent that while some gold lies on the silica particle surface, a large number of gold particles remained unattached to the silica particles. When the silica particles and nucleated gold were instead passed through the agglomeration chamber, the TDMA results, Figure 5.5a, show that the shift in the silica mode was greater with the agglomeration chamber. Additionally with the increased residence time, the gold particles agglomerate resulting in an increased lower mode. The gold and silica particles have a greater collision frequency function ($\beta_{3nm,30nm} \approx 10^{-8}$ cm^3 s^{-1}) due to their difference in size than do silica-silica or gold-gold particle collisions ($\beta_{3nm,3nm} \approx \beta_{30nm,30nm} \approx 10^{-9}$ cm^3 s^{-1}) [80]. As a result more gold was found on the silica particle surface and fewer individual gold particles were present when the particles were allowed to agglomerate, as shown in the TEM image seen in Figure 5.5c.

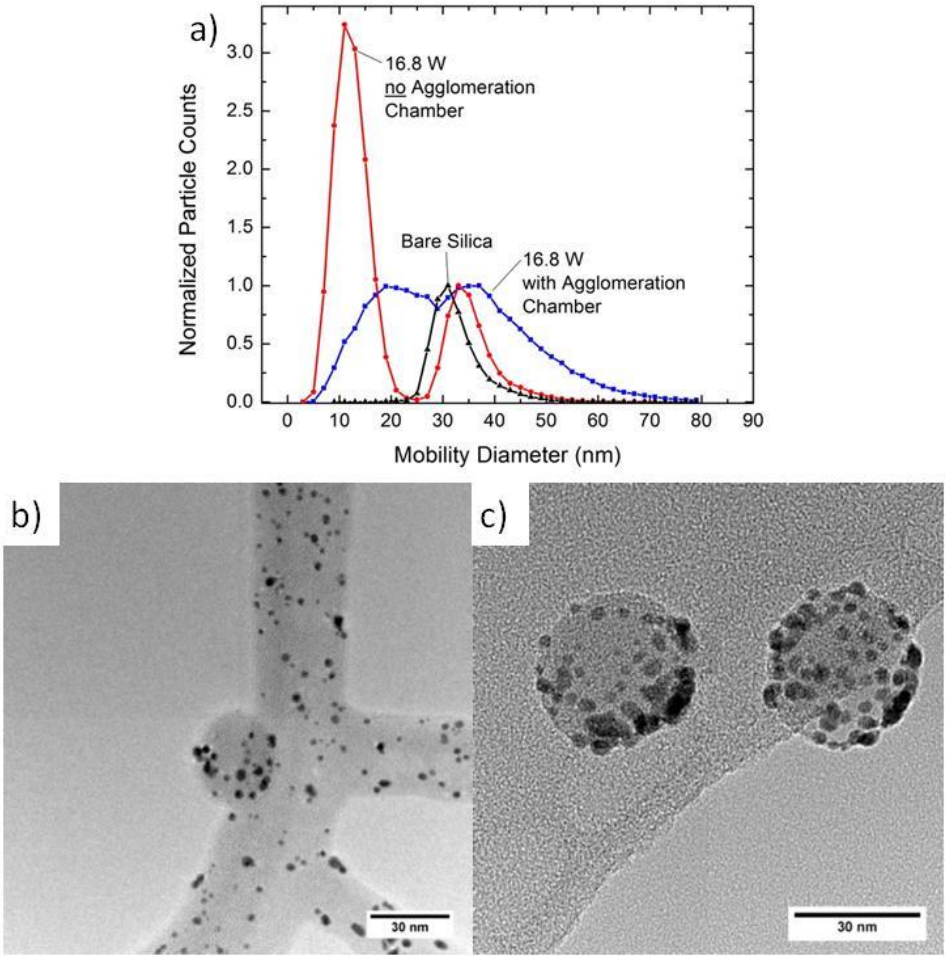

Figure 5.5: (a) TDMA particle size distribution of bare and gold-decorated silica nanoparticles produced via a hot-wire generator with and without being passed through an agglomeration chamber. (The plot is normalized to the bare silica particle peak.) Corresponding TEM images of gold-decorated silica nanoparticles produced by a hot-wire generator (b) without and (c) with an agglomeration chamber.

Further densification of gold on the silica nanoparticle surface was found to be possible by increasing the number of gold particles produced by the hot-wire evaporator. Increased gold particle production can be accomplished by increasing the power of the hot-wire evaporator or by increasing the gas velocity across the wire surface, which serves to produce a higher concentration of smaller particles

[155]. By increasing the aerosol flow rate from 1 slm (Figure 5.5) to 5 slm and increasing the hot-wire power to 27 W, more gold particles were produced. The gold-decorated silica particles were then passed through the agglomeration chamber and size selected at 15 nm before being collected on a lacey carbon TEM grid. As shown in Figure 5.6, the TEM image of the gold-decorated silica nanoparticle shows that it has a high density of gold on its surface. Despite the high surface density of gold, the surface remains decorated rather than coated by a thin contiguous film. While size selecting the particles after the production eliminates the number of gold particles independent from the silica particle surface, it also reduces the overall particle yield.

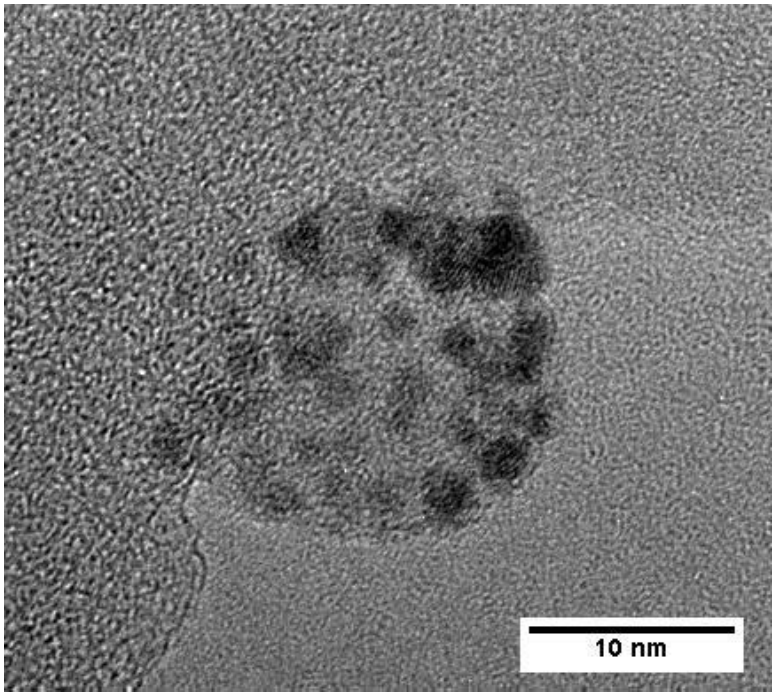

Figure 5.6: TEM image of densified gold-decorated silica nanoparticle produced by hot-wire gold evaporation coupled with increased system residence and online particle size selection.

In order to confirm that higher contrast areas seen in the TEM images represent gold on the silica particle surface, EDX analysis was conducted on a gold-decorated silica particle. The composite particles were produced by the hot-wire evaporator at a power of 12 W with the flow rates and temperatures as used to produce Figure 5.5b, but with a polydisperse aerosol rather than a size-selected monodisperse aerosol. The resulting particles were not passed through the agglomeration chamber. As seen in Figure 5.7a, a silica particle was imaged using scanning transmission electron microscopy (STEM) and shows a silica particle with gold decoration (high-contrast regions). When EDX was performed on the same particle, the element analysis (Figure 5.7b) showed that the core particle consists primarily of oxygen and silicon in roughly a 2 to 1 ratio as is expected in silica. The elemental analysis shows that the gold signal peaked in two spots which correspond to the locations of high contrast seen in the STEM image. It should be noted that no traces of platinum were detected with the elemental analysis, indicating that only the gold coating on the wire was evaporating and not the inner platinum core.

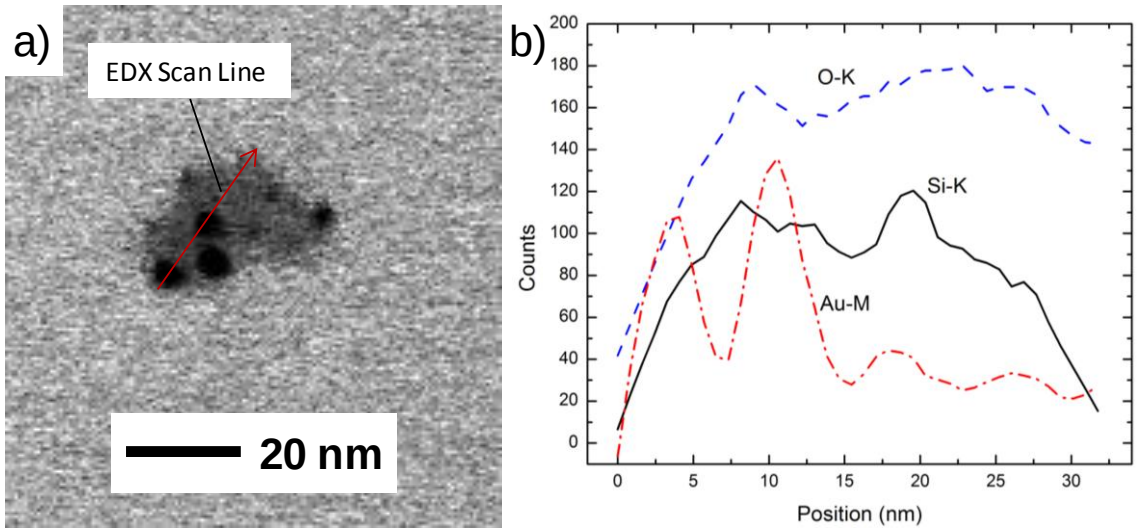

Figure 5.7: (a) Bright-field STEM image and (b) EDX elemental line scan of a gold-decorated silica nanoparticle.

Many studies have investigated the radiation absorption properties of gold nanoparticles due to the unique plasmon resonance that occurs in nano-sized gold particles and films [36, 113]. The absorption characteristics of the gold-decorated silica nanoparticles produced in this study were measured by collecting the synthesized nanoparticles on glass-fiber filters for 15 minutes from both production methods. The collected particles were then analyzed directly without dispersion by placing the filter within an integration cell, and the absorption spectra were collected using a UV-NIR spectrometer (Ocean Optics Model USB4000). The results, as shown in Figure 5.8, appear similar for the particles produced in both evaporation methods. Both methods resulted in particles that absorb in the 500-550 nm wavelength region, which is typical of gold nanoparticles [156]. As the tube furnace temperature or hot-wire power was increased, the amount of absorption increased while the peak absorption location did not shift. These results confirm that the nanoparticles were decorated with gold rather than coated with a thin film which would serve to shift the peak in the absorbance toward the infrared region [156]. It should be noted that there was no difference seen in the particles that were synthesized using the agglomeration chamber to those synthesized without the chamber.

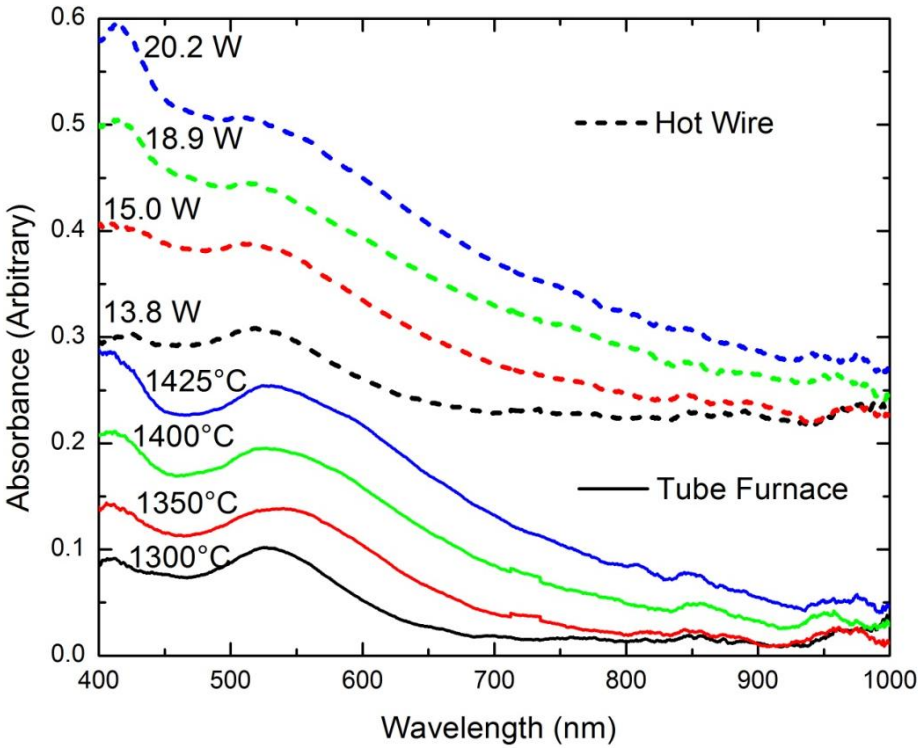

Figure 5.8: UV-NIR spectrum of gold-decorated silica nanoparticles produced at varying hot-wire powers and tube-furnace temperatures.

Many of the potential applications for gold-decorated silica particles require the particles to be stable at high temperatures. Therefore, the particles were examined using a heated TEM stage to determine whether the gold becomes mobile or leaves the silica particle surface. Gold-decorated silica particles were prepared using the tube-furnace evaporator at 1350°C. The particles were collected on lacey-carbon TEM grids and imaged while being heated. As shown in Figure 5.9, the original grids contained mostly gold-decorated silica particles with few stand-alone gold nanoparticles. As the particles were heated, the gold remained stable on the particle surface at temperatures below 900°C. As the temperature increased above 957°C, the gold began to reorient on the silica particle surface forming gold agglomerates as seen in the enlarged images of Figure 5.9c. Also while the grid temperatures remain below the melting point of bulk gold, it is apparent that the

vapor pressure is high enough that gold begins to evaporate. As shown in Figure 5.9b, the gold decoration is reduced on several of the particles, but no increase in size is seen on the remaining gold islands. The migration of gold on the surface of particles and wires has been noted by several researches and is particularly important in silicon nanowire growth with gold catalysts [157]. Several studies have examined the effect of size on thermodynamic properties, such as vapor pressure and melting temperature [87, 158], and demonstrate that as the particle size decreases the atoms on the surface are more loosely bound, leading to a decrease in melting point and an increase in vapor pressure at a given temperature.

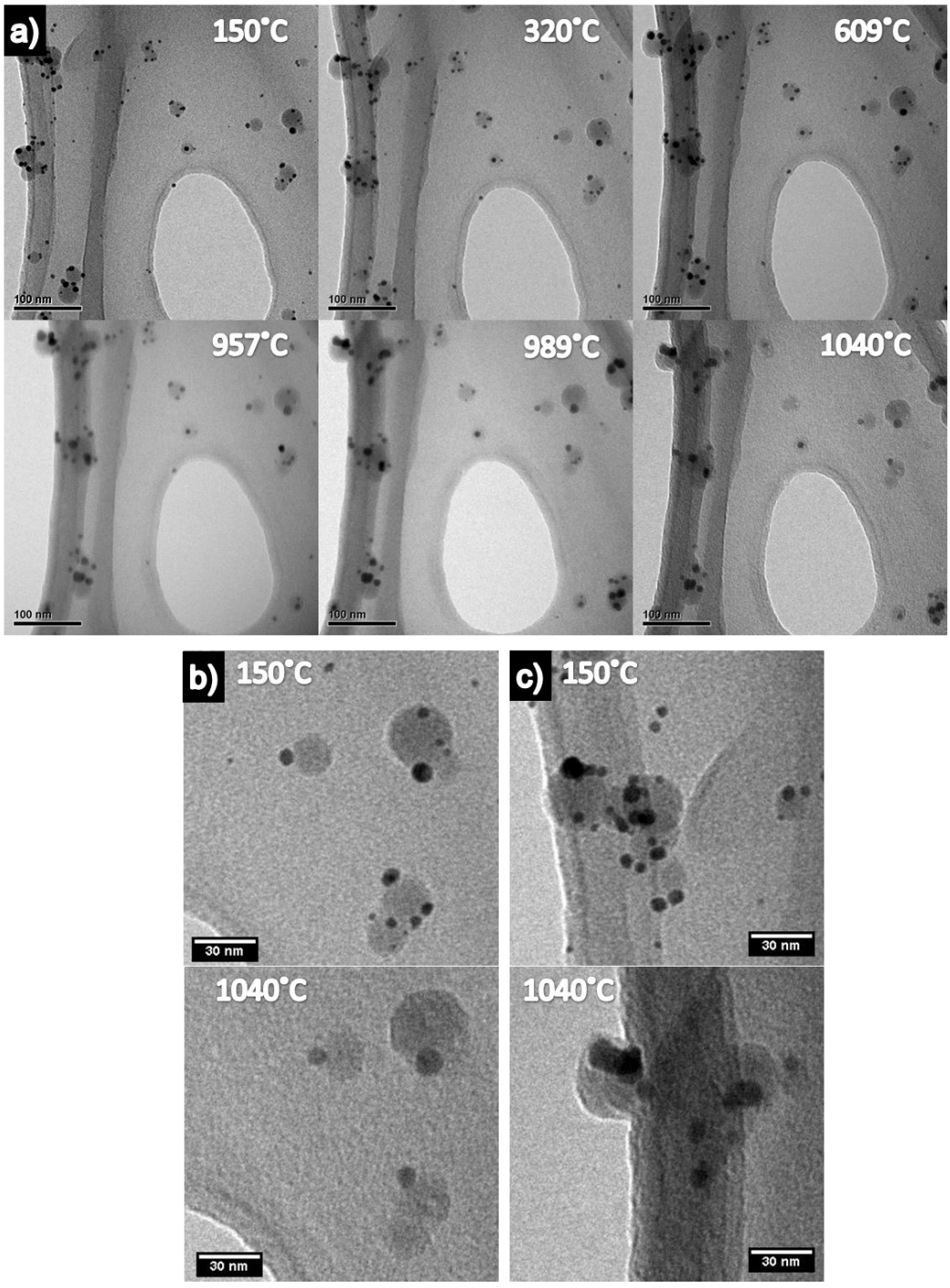

Figure 5.9: TEM images of gold-decorated silica nanoparticles at increasing temperatures. The figure includes (a) low-resolution images, (b) example of gold evaporation and (c) example of gold coalescence.

5.3 Gold Decoration by Tube Furnace Counter Flow

In addition to particle decoration with gold by passing particles through an evaporation furnace, gas-phase particles were also tested to determine whether a counter flow coating arrangement could be used. The development of methods that allow for decoration without heating of the aerosol is necessary if particle cores are sensitive to high temperature regions, such as γ-Fe_2O_3 particles that can undergo a phase transformation to α-Fe_2O_3 if heated. Initial attempts were made to produce gold-decorated silica and iron oxide particles by a counter-flow arrangement. An example of the experimental setup for iron oxide nanoparticles is shown in Figure 5.10. In the experiment, silica nanoparticles produced by thermal decomposition of TEOS as discussed previously or iron oxide particles produced by plasma synthesis were injected into a mixing region where gold was sublimated into a hot-nitrogen cross flow. The core-particle aerosol and gas-phase gold are mixed in a counter-flow arrangement. Parameters that are important in the decoration of nanoparticles with gold in a counter-flow arrangement include, the position of the aerosol inlet relative to the high-temperature zone, the flow rate of the nitrogen gas, the flow rate of the core aerosol and temperature of the furnace.

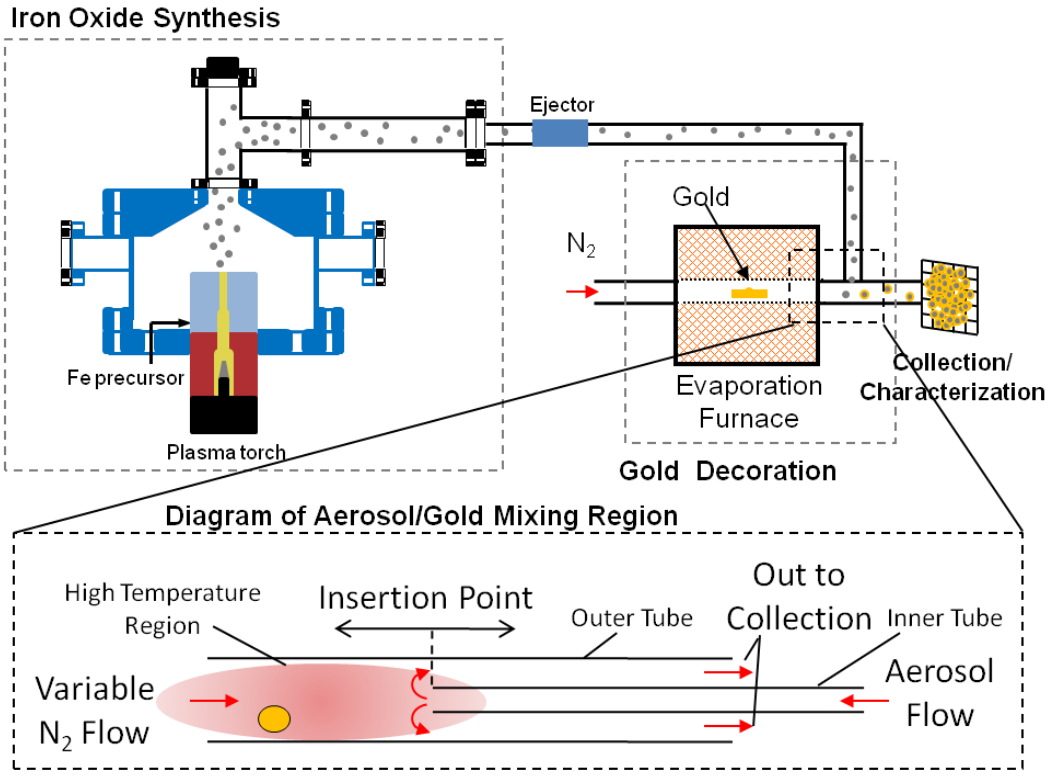

Figure 5.10: Gold decoration schematic in which iron oxide nanoparticles particles are mixed with gas-phase gold in a counter-flow mixing region.

A variety of experiments were conducted that used silica as the core particles for gold-surface decoration in the counter-flow arrangement. Results of these studies indicated that particles that were injected into the high-temperature region resulted in a significant reduction in the overall concentration of particles. Inspection of the apparatus after the experiment indicated that large quantities of particles were deposited on the outside walls of the center tube (the aerosol flow tube in Figure 5.10). These results indicate that thermophoresis likely drove particles from the hot walls of the outer tube to the outer walls of the inner aerosol tube, which was cooled by the injection of the room-temperature aerosol. Numerous experiments were conducted varying the gold carrier gas flow, injection position and tube furnace temperatures. In all cases the total concentration of particles that

remained after entering the counter-flow was lower than what was required for adequate sampling to infer coating thicknesses from TDMA.

Further experiments were conducted by using plasma-synthesized iron oxide nanoparticles that were injected into counter-flow region in order to produce gold decoration. A polydisperse distribution of iron oxide nanoparticles was injected ~10 cm into the hot zone of the furnace, which was maintained at 1400°C. The aerosol flow rate was 1.5 slm and the nitrogen carrier gas for the gold was 1.4 slm. Particles were monitored by DMPS measurement at the exit of the furnace and particles were collected onto a TEM grid with an electrostatic precipitator. As shown in Figure 5.11, the experiment resulted in gold-decorated iron oxide particles similar to the silica decoration discussed in section 5.2.2. The bright- and dark-field STEM images indicated that gold was present both on and off the iron oxide particle surface. These results were corroborated by DMPS measurements which showed a slight increase in total particle concentration when carrier gas was passed over the gold evaporation slug, thus entraining the gold vapor. EDX analysis confirmed that the high-contrast regions seen within the STEM images consisted of gold and the low-contrast regions were primarily composed of iron and oxygen. Results from the counter-flow studies indicate that it is possible to produce gold decoration on the surface of particles, but the production was found to be highly variable and resulted in significant particle losses. The gold decoration methods discussed in section 5.2.2 resulted in more consistent decoration with higher particle concentrations.

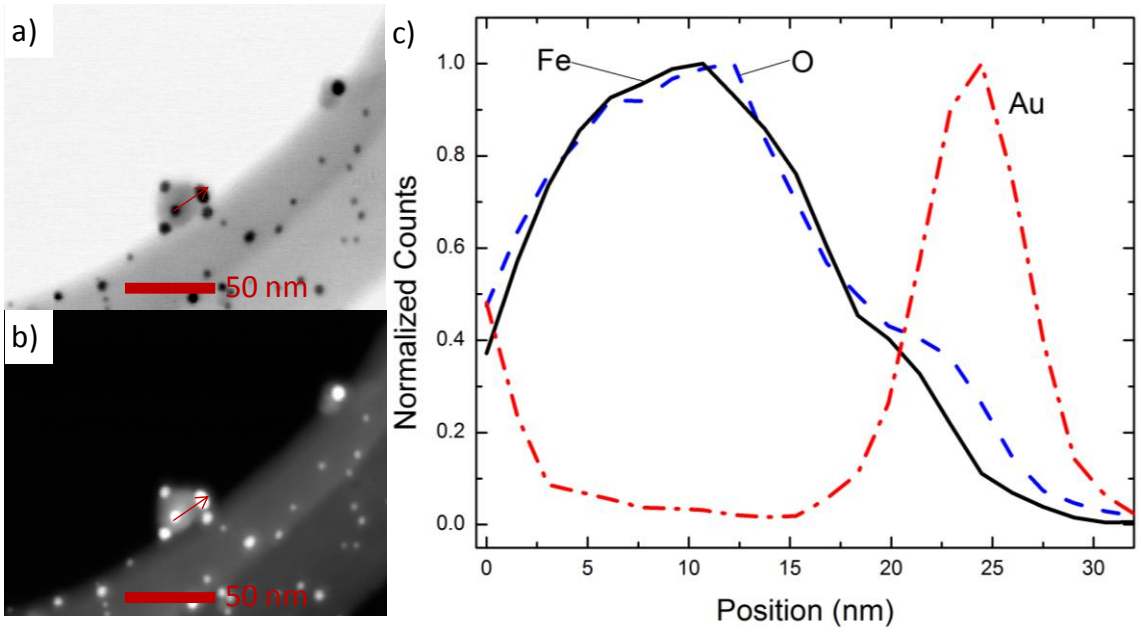

Figure 5.11: (a) Bright- and (b) dark-field STEM images with (c) an accompanying EDX elemental line scan of gold-decorated iron oxide nanoparticles.

5.4 Photo-CVD Decoration of Nanoparticles with Gold

As the previous sections have shown, thermal evaporation techniques for depositing gold on the surface of particles lead to surface decoration rather than thin films. In order for thin films to be achieved by an aerosol process, gold must be delivered to the surface in the gas phase, *i.e.* it cannot nucleate in the gas phase then deposit on the surface; and the particle surface must be cool to prevent migration of the gold into islands on the surface once it deposits. One available method that satisfies both of these conditions is the photo-CVD coating of particles. The challenge in creating nanoparticle gold coatings via photo-CVD is in finding a gold precursor that has a high enough vapor pressure so that it can be delivered into the photo-CVD chamber. A review of the literature reveals two types of gold organometallic precursors with sufficiently high vapor pressures, dimethyl gold diketonates [13, 159-162]and alkyl gold trialkylphosphines [28]. As the trialkylphosphines are hazardous, our efforts focused on the dimethyl gold

diketonates. Of the diketonates, dimethyl-gold-hexafluoroacetylacetonate [$Me_2Au(hfac)$ or DMA(hfac)] has been shown to be dissociated with similar wavelengths of light produced by the xenon excimer lamp [159], to effectively coat silica [159], to have good adhesion properties [161] and to coat micro-sized features [163]. Replies from several chemical supply companies indicated that in order purchase $Me_2Au(hfac)$ would require purchasing a large amount of the precursor, >5 g, which was prohibitively expensive. Therefore an attempt was made to synthesize $Me_2Au(hfac)$ in the lab following the synthesis steps outlined by Wexler *et al.* [160]. While the resulting liquid was not verified to ensure that $Me_2Au(hfac)$ was produced (the synthesis yielded less than 100 mg so we conserved the solution), the resulting precursor had a deep purple hue, which is indicative of gold. The precursor was stored in packed dry ice to prevent evaporation until use.

The experimental setup resembled a combination of the photo-CVD setup discussed in Chapter 2 with the silica particle synthesis discussed previously in this chapter. As shown in Figure 5.12, the silica nanoparticles were produced by the thermal decomposition of TEOS. The silica nanoparticles were size selected and injected into the photo-CVD chamber along with the $Me_2Au(hfac)$ precursor. The $Me_2Au(hfac)$ was kept in dry ice and room temperature nitrogen was bubbled through. The vapor pressure of $Me_2Au(hfac)$ is given by the relation $\log_{10} P_{vap} = A + B/T$, where the pressure, P_{vap}, has units of Pascal, T has units of Kelvin and the constants have values of A=13.9 and B=-3559 K [164]. The resulting flow rates of $Me_2Au(hfac)$ for differing nitrogen carrier gas flows and various temperatures are shown in Figure 5.13. The $Me_2Au(hfac)$ photo-CVD process is hypothesized to proceed in a similar manner as TEOS where radiation activates the gas-phase precursor which then attaches to the particle surface, resulting in a coating.

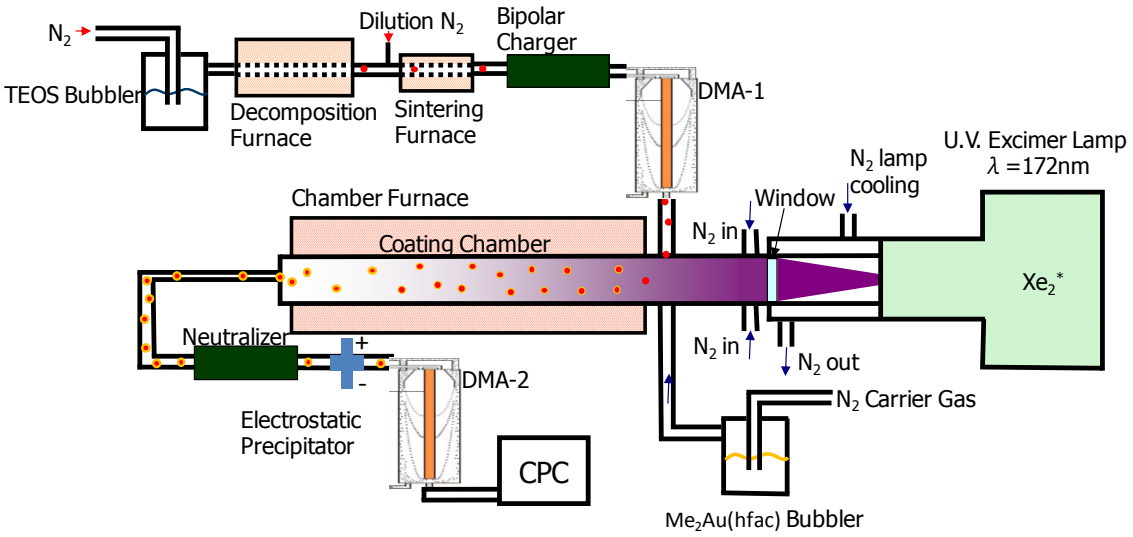

Figure 5.12: Photo-CVD coating schematic for the production of gold on the surface of silica nanoparticles.

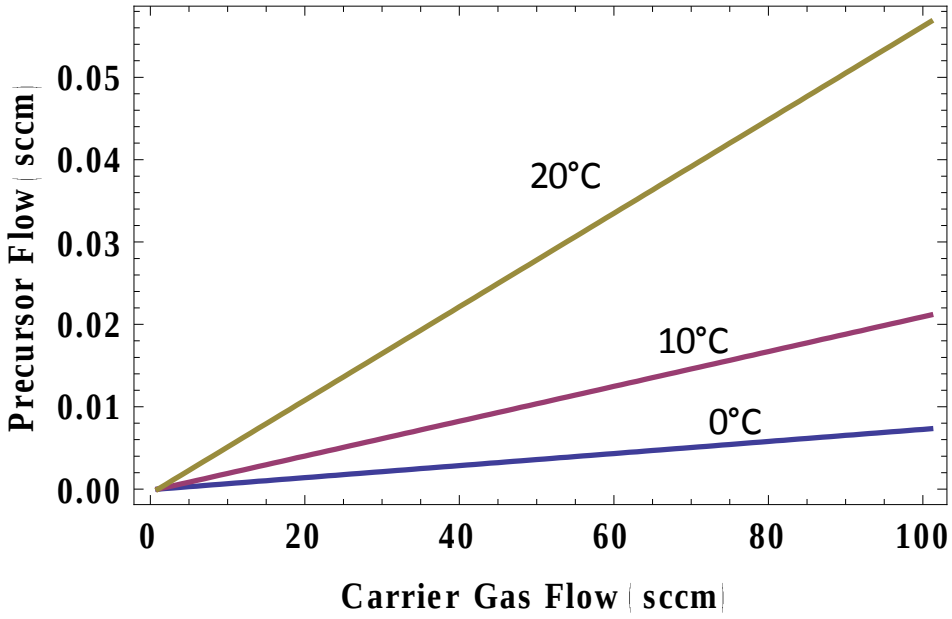

Figure 5.13: Gold precursor, $Me_2Au(hfac)$, flow rate versus carrier gas flow rates for differing temperatures [164].

Initial studies were conducted using TDMA in which size-selected 30-nm silica particles where injected into the photo-CVD chamber along with $Me_2Au(hfac)$.

The photo-CVD chamber was unheated and remained at ambient temperature. The silica particles were produced with the same conditions discussed in section 5.2.2, but the second tube furnace could only reach 900°C, as a higher temperature furnace was not available for these experiments. The nitrogen purge flow within the chamber was 3.3 slm and the aerosol flow of the silica particles out of DMA-1 was 1 slm. Particular attention was paid to the smaller particle sizes within the TDMA spectrum to monitor for $Me_2Au(hfac)$ homogenous nucleation. An initial nitrogen carrier gas flow rate through the precursor was set to 25 sccm which corresponds to 0.002 sccm of $Me_2Au(hfac)$ at 0°C (the actual temperature of the gas within the bubbler was not known as it was delivered at room temperature and the bubbler was encased in dry ice) [164]. As shown in Figure 5.14, a bi-modal distribution was measured upon exiting the photo-CVD chamber. The smaller mode had a peak size, in terms of counts, at ~10 nm, which is likely an indication of homogenous nucleation of the gold precursor. The larger mode, representative of the silica particles, shifted to larger sizes when compared to the bare silica particles, indicating that bare silica particles were undergoing growth within the photo-CVD chamber.

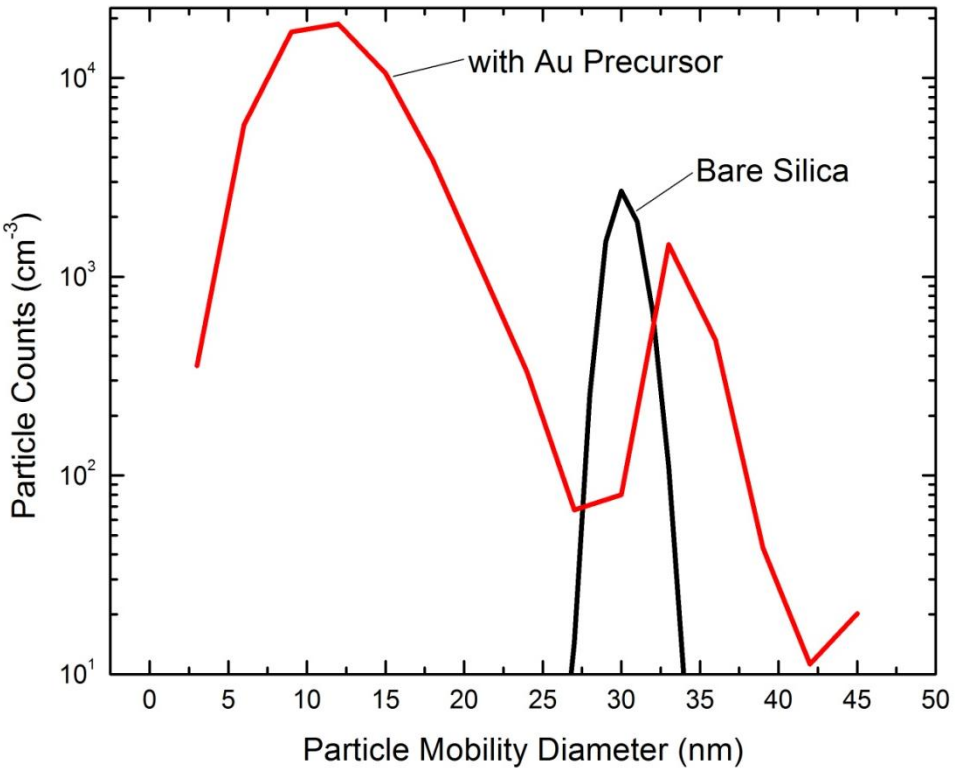

Figure 5.14: TDMA measured particle counts versus particle mobility diameter for the photo-CVD coating of silica particles with gold using $Me_2Au(hfac)$ with a nitrogen carrier gas flow rate of 25 sccm.

Particles from the experiment depicted in Figure 5.14 were collected onto TEM grids by electrostatic precipitation. The particles were imaged using STEM and the results are shown in Figure 5.15. The bright- and dark-field images show a high density of gold particles (high-contrast particles) collected on the lacey carbon grid. EDX analysis of the high-contrast particles confirmed that the particles were composed of gold, with background signals of carbon and copper from the TEM grid. The presence of gold on the TEM grid indicates that gold was delivered into the photo-CVD system by a gas-phase precursor that was effectively dissociated with the excimer lamp. A survey of the TEM grid found no lower-contrast particles that would have indicated the presence of silica. It is possible that the grid contained a much lower concentration of silica particles as there were many more gold

nucleated particles (the ordinate axis in Figure 5.14 has a log scale and is not divided by the transfer function which is smaller for small particle sizes) and that smaller particles are more easily collected by electrostatic precipitation. It is also possible that the gold present on the particle surface of the silica provided a high contrast enhancement that made it undistinguishable from the other gold particles.

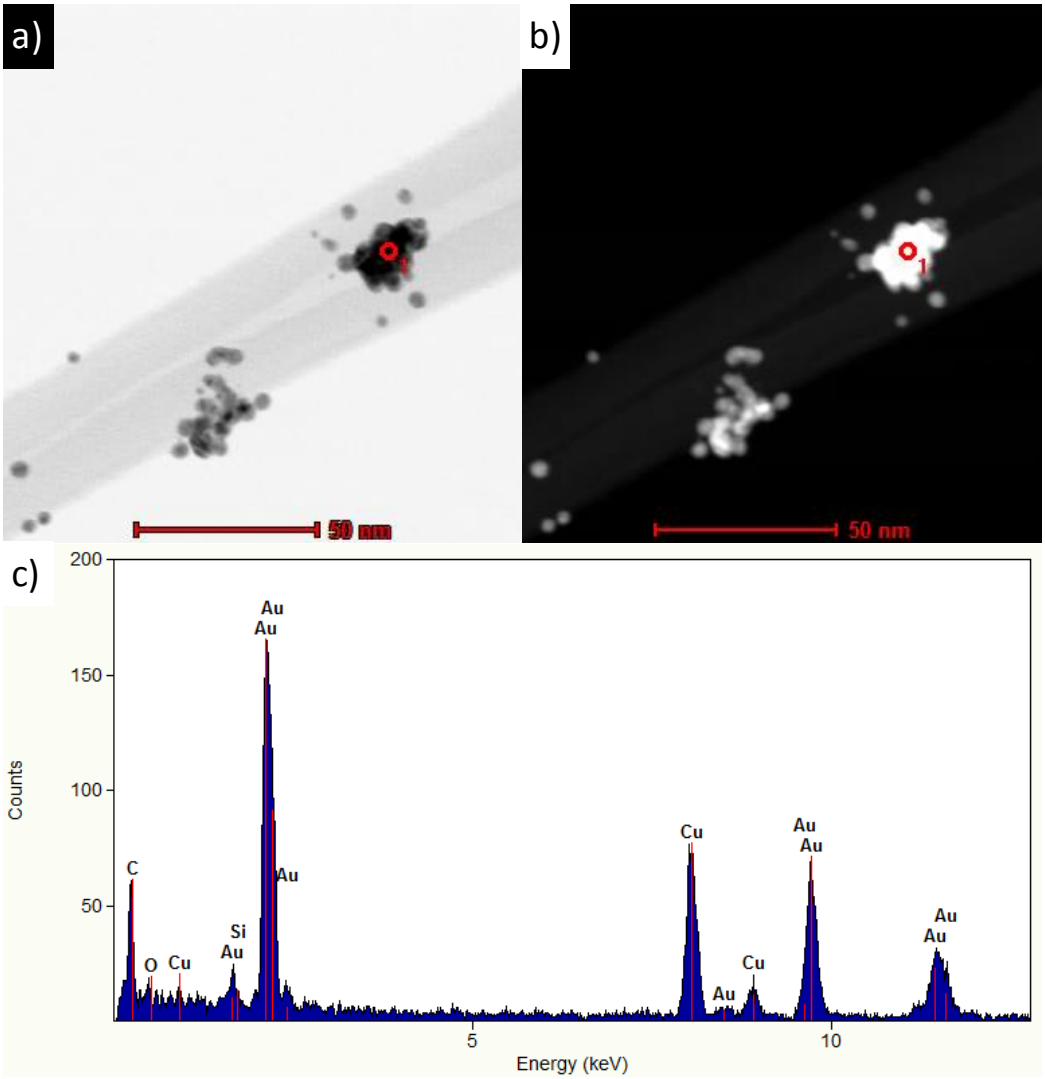

Figure 5.15: (a) Bright- and (b) dark-field STEM images with (c) an accompanying EDX single point measurement of gold particles synthesized by the photo-CVD using $Me_2Au(hfac)$ as a gold precursor.

A second study was conducted in which the nitrogen flow rate through the gold precursor was decreased below the accuracy limit of the nitrogen rotameter by inspection of the rate of bubbles within the precursor. While this method does not allow for the flow rate of the carrier gas through the precursor to be determined, it was done merely as a test to investigate whether particle growth could occur without the presence of homogenously nucleated gold particles. As shown in Figure 5.16, several runs (two runs shown) were conducted in which no $Me_2Au(hfac)$ homogeneous nucleation was detected. It is possible that nucleation occurred but was below the detection limit of the CPC. The resulting particle diameter shift of the silica particles during these runs were measured as ~3 nm. STEM analysis of particles collected for these runs, Figure 5.17a and b, showed that gold did appear on the silica particle surfaces as indicated by the higher-contrast spots on the larger, lower-contrast particles. Like the previous results the gold appeared as small islands rather than thin films for the given conditions. EDX analysis of the particles, Figure 5.17c, shows that a small gold signal was detected on the surface of the silica particles. Due to the low concentration of silica particles it was not possible to increase the flow rate of the purge gas, which would have allowed for higher flow rates of $Me_2Au(hfac)$ without nucleation, but would have lowered the concentration of silica particles below 10^3 cm^{-3}, which is required for accurate measurement by the TDMA system.

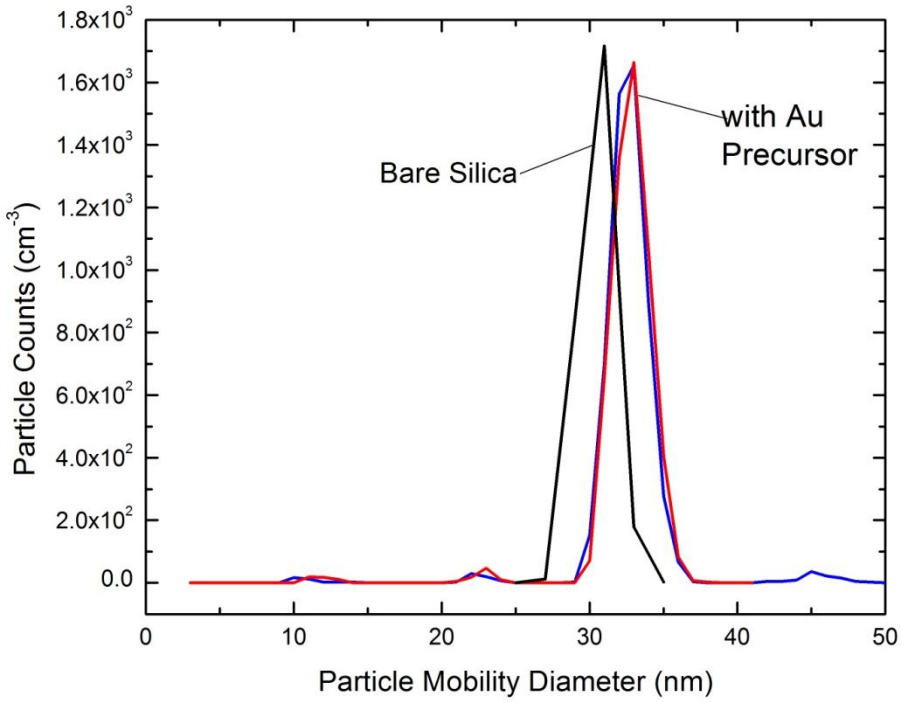

Figure 5.16: TDMA measured particle counts versus particle mobility diameter for the photo-CVD coating of silica particles with gold using $Me_2Au(hfac)$ with a nitrogen carrier gas flow rate of <<25 sccm.

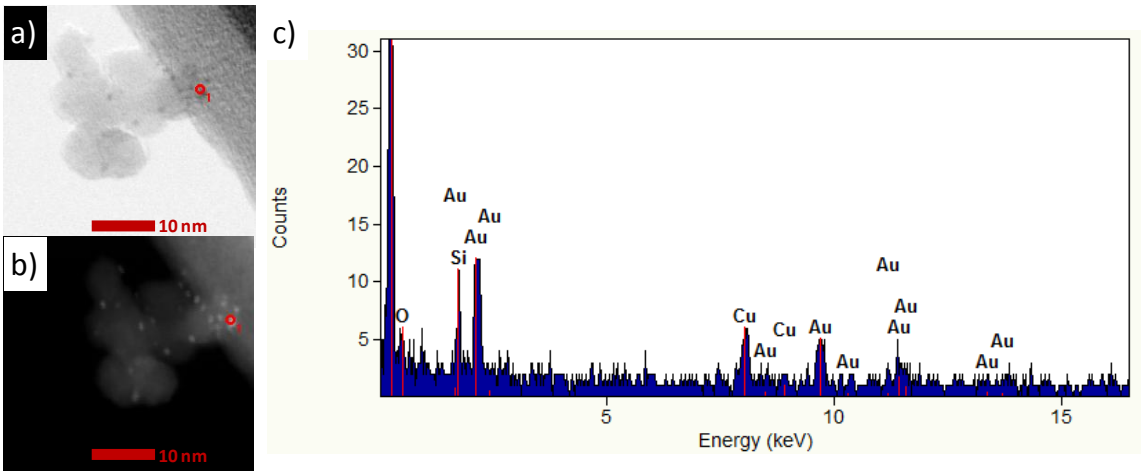

Figure 5.17: (a) Bright- and (b) dark-field STEM images with (c) an accompanying EDX elemental line scan of gold-decorated silica particles synthesized by photo-CVD of $Me_2Au(hfac)$.

5.5 Tri-Material Nanoparticles

All of the results discussed previously within this chapter and in previous chapters have focused on the production of single-material and bi-material nanoparticles. As discussed in Chapter 1, nanoparticles composed of three materials are of interest for imaging and thermal treatment of tumors. A few studies were conducted that attempted to combined multiple coating steps with a synthesis step to produce tri-material nanoparticles. The production of tri-material nanoparticles can be achieved by combining the methods discussed in previous chapters, as shown by the simplified schematic in Figure 5.18. Critical to the success of such coating is controlling factors such as agglomeration, particle loss, differing system pressures and unreacted precursors. Residence times for the entire production process range from 10-40 s and are critical in controlling the various processes.

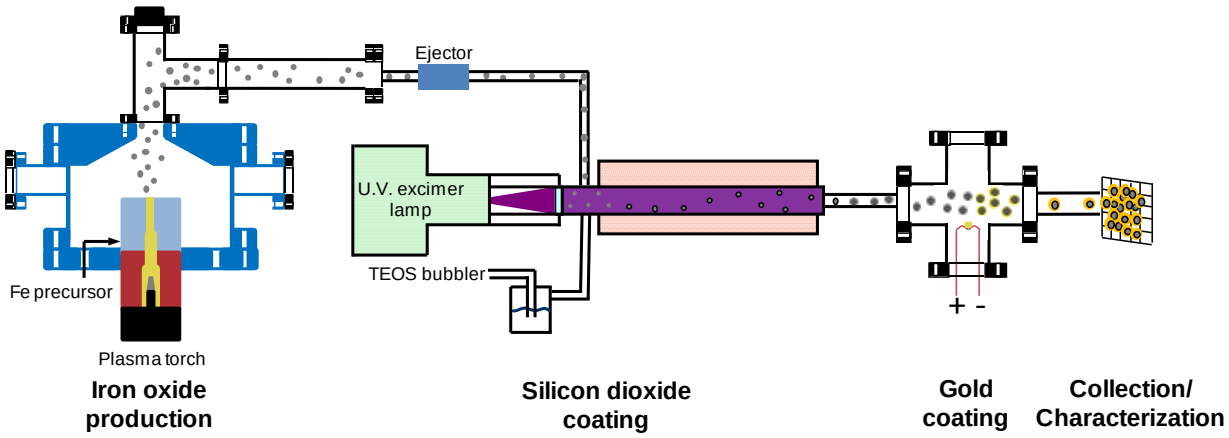

Figure 5.18: Tri-material nanoparticle synthesis schematic consisting of iron oxide nanoparticle plasma production, silica coating by photo-CVD and gold decoration by hot-wire evaporator.

An experiment was conducted in which iron oxide nanoparticles were synthesized in the DC plasma using typical conditions discussed in Chapter 2. An iron oxide aerosol flow of 1 slm was ejected from the plasma and injected into the photo-CVD chamber along with TEOS at ~0.7 sccm. The photo-CVD chamber was

maintained at 400°C and a nitrogen purge flow of 6.2 slm was used. No oxygen was explicitly added to the chamber as it was present in the aerosol from the plasma chamber. The resulting particles were then passed out of the photo-CVD chamber into the hot-wire evaporator, where they were mixed with gold particles. The resulting aerosol was then passed out of the evaporator and either directly into the DMPS or collected onto TEM grids within the electrostatic precipitator. The resulting DMPS measurements are shown in Figure 5.19. The mode of the bare iron oxide nanoparticle distribution is near ~12 nm. As the bare iron oxide nanoparticles were coated with silica, the distribution as measured by the DMPS shows no significant shift. The addition of gold to the aerosol as it passes through the evaporator causes the distribution becomes bi-modal with a smaller mode <10 nm that represents the gold nanoparticles and a larger mode which has shifted to slightly larger sizes (~15 nm) when compared to the bare iron oxide nanoparticles. As the power dissipated across the hot wire was increased both the nucleation mode and the core particle mode shifted to larger sizes.

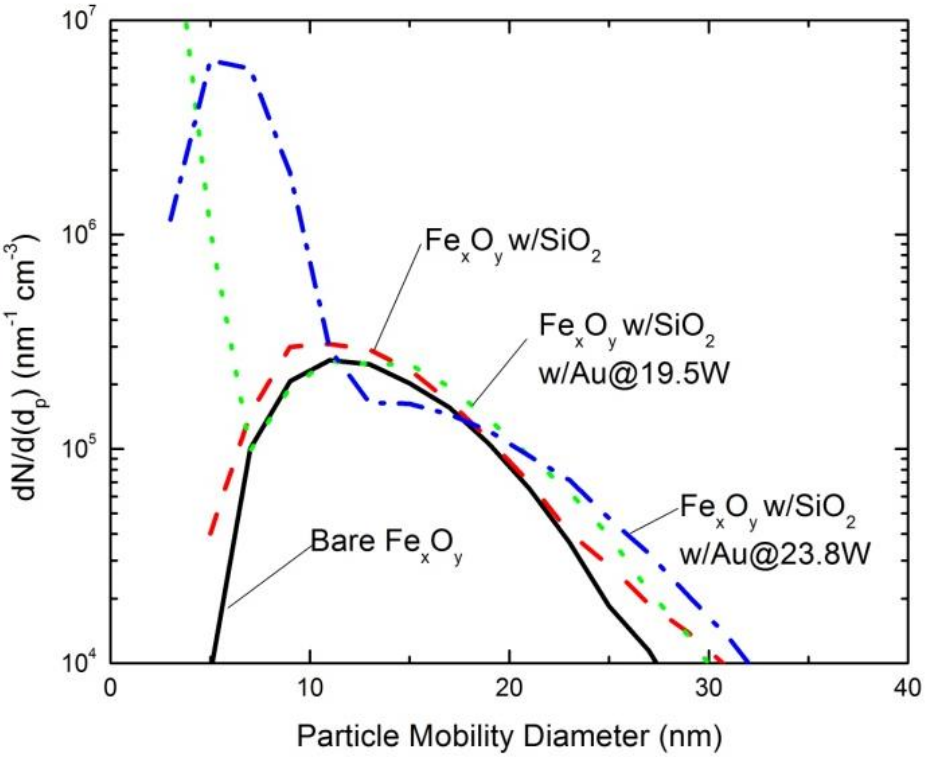

Figure 5.19: DMPS measured particle mobility distributions for bare iron oxide nanoparticles, silica-coated iron oxide nanoparticles and gold-decorated, silica-coated iron oxide nanoparticles.

Particles were collected and imaged within the TEM for the same conditions that were used to produce the Fe_xO_y w/SiO_2 and Fe_xO_y w/SiO_2 w/Au@23.8W in Figure 5.19. As shown in Figure 5.20a and b, the iron oxide nanoparticles coated with silica often were found to have a hexagonal structure which is common for α-Fe_2O_3 due to the hexagonal crystal structure of the material. Both uniform and uneven silica coatings were found on different particles. The non-uniform coatings were likely a result of TEOS homogenous nucleation as discussed in Chapter 2. As shown in Figure 5.20, the gold decoration resulted in small spots of higher contrast particles on the surface of the silica. By varying the focus of the TEM it was apparent that when the core crystal structure of the iron oxide was in focus the surface gold particles were not (and vice versa), which indicated that the materials were located

different depths. The presence of gold on the particle surface corresponds to the runs in which the upper mode shifted to larger sizes and a lower mode was measured by the DMPS, as shown in Figure 5.19. Further EDX analysis is needed to confirm that the small high-contrast particles on the surface of the larger particles are gold.

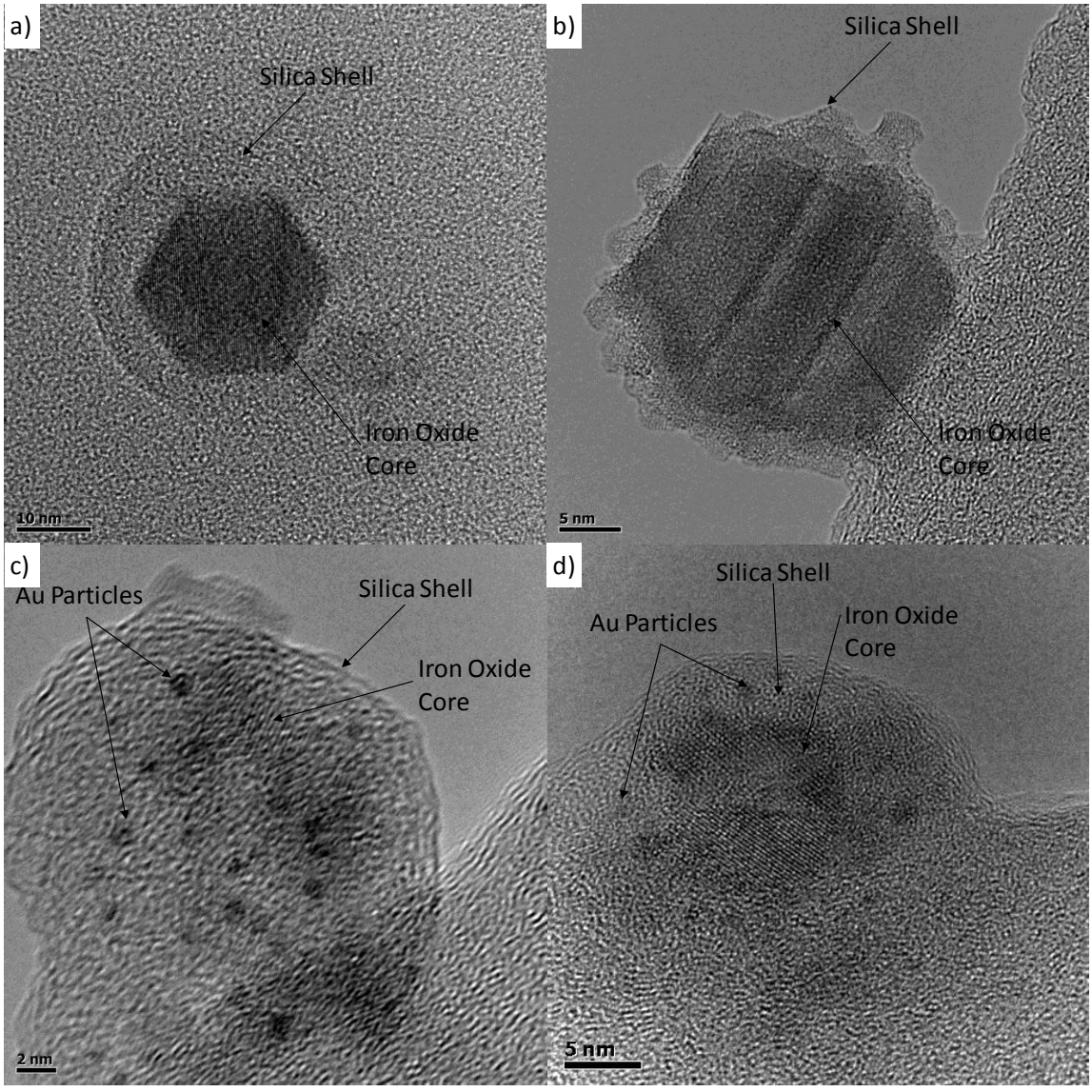

Figure 5.20: High-resolution TEM images of silica coated iron oxide nanoparticles (a & b) without and (c & d) with gold surface decoration.

5.6 SUMMARY

Chapter 5 demonstrates the gold decoration of silica and iron oxide nanoparticles by gas-phase methods. By evaporating solid gold by two different processes it was shown that gold can be delivered to the particle surface by two distinct mechanisms. When the entire aerosol (silica nanoparticles and surrounding gas) was heated in the presence of gold, gold vapor entered the aerosol stream and condensed on the particle surface upon cooling. Due to the surface energies of gold and silica, the gold atoms were able to self-orient on the hot silica nanoparticles to minimize their surface energy and "balled up" on the particle surface. Using a second method, hot-wire evaporation, the aerosol remained cool which caused the nucleation of gold particles upon leaving the hot-wire surface. Therefore when the gold reached the silica particle surface by agglomeration it again formed decoration of the surface, but through a different mechanism than when the entire aerosol was heated. Increased gold density was achieved by adding residence time to the system to allow the gold particles produced from the hot-wire evaporator to be scavenged by the silica particles. In both cases, the particles had similar absorbance spectra with peak intensities at wavelengths from 500-550 nm. It was shown that the gold decoration remained stable at temperatures below 900°C, above which the gold decoration began to evaporate as well as form larger islands on the silica surface.

The results of the photo-CVD coating with $Me_2Au(hfac)$ indicate that gold vapor can be delivered to the photo-CVD chamber and can be effectively dissociated with the VUV excimer lamp. Results also indicate that decorated silica particles can be produced without significant homogenous nucleation of $Me_2Au(hfac)$. Much of the parameter space has yet to be explored within the system. The relatively low production rates of silica nanoparticles limited an increase in purge flow rate that could have been used to suppress $Me_2Au(hfac)$ homogenous nucleation. A coalescence furnace with a higher upper temperature limit is now in place and allows for higher production rates of silica particles. Also by replacing the rotameter used to control the carrier gas through the $Me_2Au(hfac)$ bubbler with a low-flow

mass flow rate controller, lower flow rates of $Me_2Au(hfac)$ could be accurately and reproducibly delivered to the system. The results presented here do not preclude that particles could be coated with uniform films by a photo-CVD method, and therefore more work is necessary.

Studies investigating the production of tri-layer nanoparticles have shown that tri-layer particles are achievable by combining multiple synthesis and coating systems. The results indicate that while DMPS monitoring cannot measure small changes in particle diameter (unlike TDMA), the DMPS system can monitor the coating process and can determine whether the total particle concentration in the system is increased by homogenously nucleated particles from coating precursors. Further work is needed to find parameter ranges where gold-decorated, silica-coated iron oxide nanoparticles can be repeatedly produced at high concentrations.

Chapter 6 – Summary and Future Directions

6.1 SUMMARY

This study has demonstrated that a series of decoupled gas-phase synthesis and coating methods can produce core-shell nanoparticles and surface-decorated nanoparticles with a variety of different materials. Gas-phase methods have inherent advantages over liquid phase synthesis techniques, as they do not require the use of solvents and are continuous processes with production times on the order of seconds, rather than hours or days. Another advantage of gas-phase synthesis techniques is the availability of aerosol monitoring devices, such as DMAs, as well as other chemical analysis techniques, such as infrared spectroscopy, to give real-time feedback on the effects of variations in system parameters. Gas-phase production of individually coated nanoparticles is limited by the availability of gaseous precursors for the production of CVD coatings and by the agglomeration rate of particles in the gas phase. This study focused on the coating of a variety of particle surfaces by two different methods, photoinduced chemical vapor deposition (photo-CVD) coating using TEOS as a silica precursor and thermal evaporation techniques for the surface decoration of particles with gold.

This study's examination of the photo-CVD coating process showed for the first time that inorganic silica coatings could be readily produced on nanoparticles with a variety of core chemistries, including sodium chloride, yttrium aluminum oxide, silver and iron oxide. The only core chemistries that were found to be unsuitable for use in photo-CVD coating were those, such as polystyrene latex (PSL), in which the particles were broken apart by the vacuum ultraviolet (VUV) photons from the excimer lamp. The systematic variation of key system parameters of the photo-CVD system, including precursor flow rate, bulk gas flow rate, particle size and radiation intensity, lead to a greater understanding of coating phenomena

within the photo-CVD chamber. Reproducible and tunable coating thicknesses on different core-particle chemistries were demonstrated by varying system parameters such as precursor and nitrogen flow rates. Analysis of the coatings indicated that they were composed of silica with few hydrocarbon inclusions.

Chemical kinetic modeling of the photo-CVD process was conducted to give a better understanding of the coating mechanism. A model was developed within CHEMKIN-PRO, which was the first known attempt to include photochemical reactions within a chemical mechanism to simulate the growth of CVD coatings on nanoparticle surfaces. In order to include photochemical reactions within the CHEMKIN-PRO environment, auxiliary subroutines were written to determine the rates of the photochemical reactions, which were then combined with other reactions within the mechanism. The photochemical model was verified by comparing results of the simulation to analytically derived solutions for a simplified reaction mechanism. The results of the entire silica coating mechanism were tested for a variety of precursor, oxygen and nitrogen flow rates for conditions that were comparable to the experimental studies in Chapter 2. Using input parameters and assumptions that matched experimental conditions resulted in modeled results similar to the experimental results, where coating thickness had a near linear increase with higher precursor flow rates and decreased with increased nitrogen flow rate. The modeled growth always indicated thinner coatings than were measured experimentally but were within the same order of magnitude.

Gold nanoparticle synthesis and surface decoration was accomplished by adapting a known method of aerosol production, hot-wire synthesis, with a new wire geometry that allowed for the creation of gold particles. Previous studies had found that gold wires melted, thus breaking the electrical circuit, before significant quantities of particles could be produced. In this study, a gold-coated platinum wire was used as the evaporation source, which allowed for temperatures in excess of the gold melting temperature (~1065°C) to be reached without melting the entire wire.

The gold-particle size distributions from the hot-wire generator were measured for varying system parameters such as applied power and flow rate. Results indicated that the production of particles in a nozzle with a 3-mm throat diameter resulted in small particle sizes with the less agglomeration than similar experiments conducted with larger diameters. Chemical analysis of the particles indicated that they were composed of gold without platinum contamination from the wire core. Computational fluid dynamics modeling and analytical calculations showed that for a given flow rate, variation in the generator tube size could result in a shift from forced flow to buoyancy driven flow, which affected the morphology and distribution of the particles.

Using the gold hot-wire evaporator discussed in Chapter 4 and an inert-gas condensation method, particles were decorated with gold. A comparison of the two methods indicated that while the resulting morphology of the coatings was similar, the gold decoration occurred by different routes. In the hot-wire generator, the aerosol remained relatively cool, which resulted in the nucleation of gold within the gas phase before it reached the surface of the core nanoparticles. In the inert-gas condensation method the entire aerosol was heated such that the gold likely condensed on the surface of the particles, but "balled up" due to differences in surface tensions between gold and silica. Coating density was found to depend on residence time for the hot-wire generated decoration. Both methods produced particles with similar absorption spectra. Initial studies indicated that photo-CVD gold coatings might be achievable using a gold organometallic precursor, $Me_2Au(hfac)$. Finally an initial attempt was made to produce tri-component nanoparticles with an iron oxide core, silica shell and gold surface decoration. TEM results showed promising results for the tri-layer particles although further work remains. The tri-component nanoparticles as well as other core-shell nanoparticles produced in this study are shown in the summary image in Figure 6.1.

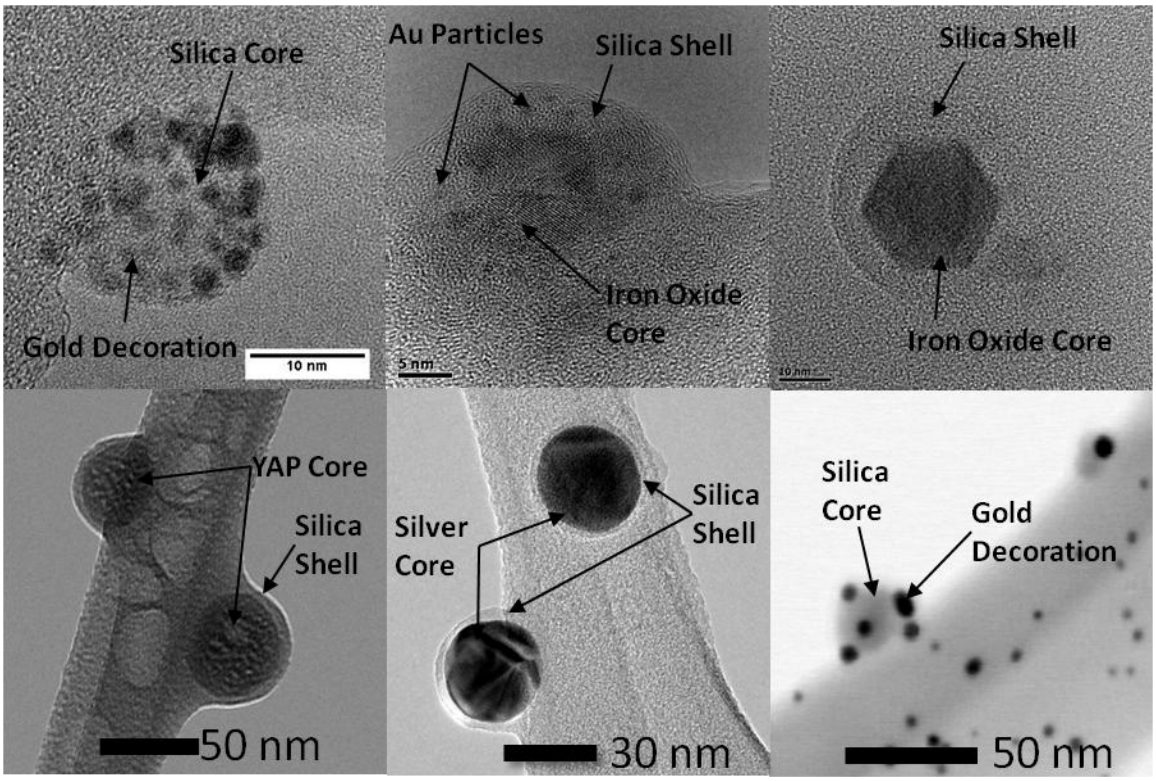

Figure 6.1: Summary image of different core-shell nanoparticles produced in this study.

6.2 Future Directions

Future work in the production of bi- and tri-component nanoparticles depends heavily on the degree to which different synthesis and coating modules can be incorporated with one another. Important challenges remain in this area. Currently flow rates within the plasma system are ~35 slm whereas the maximum flow rate ever used within the photo-CVD system that resulted in coated particles is ~10 slm. Additionally the difference in operating pressures between the two systems remains a challenge to monitor the coating process. Ultimately if the majority of plasma synthesized nanoparticles are to be coated, the operating pressure of the photo-CVD chamber will likely need to be lowered to match that of the plasma (~300 Torr). While there is no physical reason why particles cannot be

coated at the lower pressures (in fact there is evidence to believe that coatings may be enhanced) the monitoring of the process becomes problematic because the TDMA system (in particular the CPC) requires atmospheric pressure to operate. Some information can be gathered by using an ejector after the coating chamber to monitor the presence of a second mode within the DMPS-measured particle size distribution which can indicate homogeneous nucleation of the precursor. Ultimately, factors affecting results such as coating thickness will have to be determined in an iterative process by successive TEM studies. Another important challenge in combining the two systems is the presence of reacting species left after the nanoparticles have been synthesized. In particular, this study has shown that the coating process is sensitive to oxygen concentration within the system. While DMAs effectively remove the particles from the aerosol gas, if particles are injected directly into the photo-CVD chamber from the plasma, differences in coatings and homogeneous precursor nucleation may occur. Finally, while the coating chamber is maintained at relatively low temperatures, the possibility exists for phase transformation of the particle core during the coating process. Future work should examine the magnetic properties of the iron oxide nanoparticles before and after coating.

It is believed that the photo-CVD coating method is very robust and that a variety of inorganic coatings, beyond silica, can be achieved provided gas-phase precursors exist. In particular the photo-CVD method has advantages over other gas-phase coating methods, such as flame synthesis, because it can conceivably produce non-oxide coatings which are hard to achieve in flames. Coatings can be envisioned consisting of metals such as copper [165] and platinum [166] which have organometallic precursors available. Advancing these coating technologies could prove useful in the production of materials for renewable fuel synthesis [167] and fuel cell catalysts [143]. The ultimate success of these coatings is dependent

upon the discovery of parameter windows where coatings can be produced without homogenous nucleation of the precursor.

The kinetic mechanism that was developed to describe the photo-CVD system could be improved upon by additional experimental validation and an improved treatment of radiation flux within the system. This study presented the results of analyses where either the radiation flux was held constant or decayed as a diffuse source, which represents the maximum and minimum radiation flux profiles likely within the system. Neither flux profile is affected by the number of absorbing species within the photo-CVD chamber. Further development of the mechanism could be achieved by incorporating a routine that tracked the number of photons absorbed within each differential element due to photochemical reactions and then used the reduced number of photons to determine the interactions within the next differential element. The incorporation of such a mechanism would then make the axial distribution of radiation flux a function of the number of absorbing species within the gas, which better represents the physical reality of the system. Further verification of the chemical mechanism could be studied by measuring the gas-phase products of the photo-CVD reaction downstream by FTIR. By tracking the signal intensity of the O-C bond in TEOS, it could be verified whether the removal of ethyl groups from TEOS is the dominant gas-phase reaction for the photo-CVD system as proposed in the mechanism.

For gold decoration by thermal methods, increased gold density on the nanoparticle surface may be achieved by increasing the collisional frequency between the silica and gold particles. Differential charging of the core particles and smaller gold particles could be achieved by applying a bias voltage between the hot-wire generator and the surrounding system, which would increase the fraction of charged gold particles produced by the wire. The particles could then be passed into an agglomeration chamber where Po-210 strips were present which serve to neutralize the large particles (which would be required as the silica particles

scavenge charged gold particles) at much faster rates than the smaller gold particles. The enhanced agglomeration rates of charged and neutral particles [168] would decrease the residence time needed for agglomeration and perhaps result in higher density coatings without the need for additional size selection. Further advancements of the gold-decoration system as well as other systems could be achieved if impactors were used before collection to act as band-pass filters to eliminate unwanted particles based on the Stokes number of the particles. Such a device would be particularly useful in systems where unwanted homogenously nucleated particles were present.

Ultimately, for engineered nanoparticles to be applied to biological systems they must be transferred from the gas phase to the liquid phase without significant particle agglomeration. Attempts at collecting particles onto filters and then dispersing them into solutions have been problematic due to agglomeration once the particles are collected on the filter and breakup of the filter during sonication leading to unwanted contamination. A better approach would be to collect the particles directly from the gas flow by impaction. Because of the small particle sizes, the particle Stokes numbers are not large enough to impact into a solution. The deformation of the solution surface limits the distance and velocity of the impinging aerosol jet from the impactor. As shown in Figure 6.2, two methods are possible for collecting low-Stokes particles into solution. The schematic shown in Figure 6.2a depicts how particles can be grown to micron size by condensing water on the particle surface. The increased particle Stokes number then allows for the particles to be impinged into the solution. As shown in Figure 6.2b, an alternate approach exists where the Stokes number remains low, but the particles and solution are oppositely charged so that as they pass near the solution surface they are attracted to the solution by electrostatic forces. Ongoing work is being conducted in both of these areas by fellow researchers and synergy could be found through collaboration

to develop a particle collection design that meets the particular needs of the system in terms of particle size, flow rates and desired solvent [169-171].

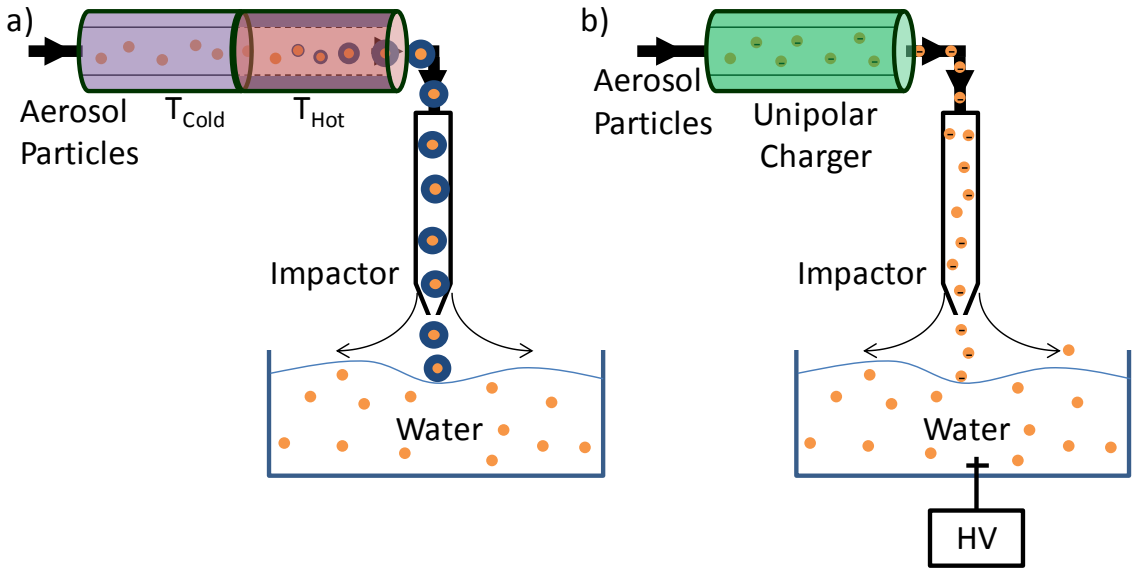

Figure 6.2: Particle into liquid collection schematics where (a) particles are grown to micron size droplets by condensing water on the particle surface before being impacted into the solution and (b) where particles are charged then passed near a fluid with an electrode causing electrostatic precipitation of the particles into the solution.

References

[1] U. Kortshagen, Nonthermal plasma synthesis of semiconductor nanocrystals. *Journal of Physics D: Applied Physics* **2009**, *42*, 113001.

[2] A. P. Alivisatos, Perspectives on the Physical Chemistry of Semiconductor Nanocrystals. *Journal of Physical Chemistry* **1996**, *100*, 13226.

[3] K. S. Leschkies, R. Divakar, J. Basu, E. Enache-Pommer, J. E. Boercker, C. B. Carter, U. R. Kortshagen, D. J. Norris, E. S. Aydil, Photosensitization of ZnO Nanowires with CdSe Quantum Dots for Photovoltaic Devices. *Nano Letters* **2007**, *7*, 1793.

[4] A. K. Gupta, M. Gupta, Synthesis and surface engineering of iron oxide nanoparticles for biomedical applications. *Biomaterials* **2005**, *26*, 3995.

[5] Z. Qu, M. Cheng, X. Dong, X. Bao, CO selective oxidation in H_2-rich gas over Ag nanoparticles--effect of oxygen treatment temperature on the activity of silver particles mechanically mixed with SiO_2. *Catalysis Today* **2004**, *93-95*, 247.

[6] D. O. Klenov, G. N. Kryukova, L. M. Plyasova, Localization of copper atoms in the structure of the ZnO catalyst for methanol synthesis. *Journal of Material Chemistry* **1998**, *8*, 1665.

[7] A. G. Nasibulin, P. P. Ahonen, O. Richard, E. I. Kauppinen, I. S. Altman, Copper and Copper Oxide Nanoparticle Formation by Chemical Vapor Nucleation From Copper (II) Acetylacetonate. *Journal of Nanoparticle Research* **2001**, *3*, 383.

[8] Q. A. Pankhurst, J. Connolly, S. K. Jones, J. Dobson, Applications of magnetic nanoparticles in biomedicine. *Journal of Physics D: Applied Physics* **2003**, *36*, R167.

[9] J. H. Son, H. Y. Park, D. P. Kang, D. S. Bae, Synthesis and characterization of Ag/Pd doped SiO_2 nanoparticles by a reverse micelle and sol-gel processing. *Colloids and Surfaces A: Physicochemical and Engineering Aspects* **2008**, *313-314*, 105.

[10] G. S. Pappas, P. Liatsi, I. A. Kartsonakis, I. Danilidis, G. Kordas, Synthesis and characterization of new SiO_2-CaO hollow nanospheres by sol-gel method:

Bioactivity of the new system. *Journal of Non-Crystalline Solids* **2008**, *354*, 755.

[11] A. J. Ruys, Y.-W. Mai, The nanoparticle-coating process: a potential sol-gel route to homogeneous nanocomposites. *Materials Science and Engineering A* **1999**, *265*, 202.

[12] F. Caruso, Nanoengineering of Particle Surfaces. *Advanced Materials* **2001**, *13*, 11.

[13] S. Jain, G. P. Fotou, T. T. Kodas, A Theoretical Study on Gas-Phase Coating of Aerosol Particles. *Journal of Colloid and Interface Science* **1997**, *185*, 26.

[14] Q. H. Powell, G. P. Fotou, T. T. Kodas, B. M. Anderson, Synthesis of Alumina- and Alumina/Silica-Coated Titania Particles in an Aerosol Flow Reactor. *Chemistry of Materials* **1997**, *9*, 685.

[15] B. S. Lee, D. J. Kang, S. G. Kim, Properties of binary TiO_2-SiO_2 composite particles with various structures prepared by vapor phase hydrolysis. *Journal of Materials Science* **2003**, *38*, 3545.

[16] L. Zhang, M. B. Ranade, J. W. Gentry, Formation of organic coating on ultrafine silver particles using a gas-phase process. *Journal of Aerosol Science* **2004**, *35*, 457.

[17] J. Bai, J.-P. Wang, High-magnetic-moment core-shell-type FeCo--Au/Ag nanoparticles. *Applied Physics Letters* **2005**, *87*, 152502.

[18] T. Enz, M. Winterer, B. Stahl, S. Bhattacharya, G. Miehe, K. Foster, C. Fasel, H. Hahn, Structure and magnetic properties of iron nanoparticles stabilized in carbon. *Journal of Applied Physics* **2006**, *99*, 044306.

[19] A. M. Nienow, J. T. Roberts, Chemical Vapor Deposition of Zirconium Oxide on Aerosolized Silicon Nanoparticles. *Chemistry of Materials* **2006**, *18*, 5571.

[20] P. Biswas, C. Y. Wu, M. Zachariah, B. McMillin, Characterization of iron oxide-silica nanocomposites in flames: Part II. Comparison of a discrete-sectional model predictions to experimental data. *J Mater Res* **1997**, *12*, 714.

[21] B. McMillin, P. Biswas, M. Zachariah, In situ characterization of vapor phase growth of iron oxide-silica nanocomposites: Part I. 2-D planar laser-induced fluorescence and Mie imaging. *Journal of Material Research* **1996**, *11*, 1552.

[22] F. Yu, J. N. Wang, Z. M. Sheng, L. F. Su, Synthesis of carbon-encapsulated magnetic nanoparticles by spray pyrolysis of iron carbonyl and ethanol. *Carbon* **2005**, *43*, 3018.

[23] D. Vollath, D. V. Szabó, Coated Nanoparticles: A New Way to Improved Nanocomposites. *Journal of Nanoparticle Research* **1999**, *1*, 235.

[24] M. Schallehn, M. Winterer, T. E. Weirich, U. Keiderling, H. Hahn, In-Situ Preparation of Polymer-Coated Alumina Nanopowders by Chemical Vapor Synthesis. *Chemical Vapor Deposition* **2003**, *9*, 40.

[25] K. S. Kim, D. J. Kim, Q. Qiu Zhao, Numerical analysis on particle coating by the pulsed plasma process. *Chemical Engineering Science* **2006**, *61*, 3278.

[26] B. Zhang, Y. C. Liao, S. Girshick, J. Roberts, Growth of coatings on nanoparticles by photoinduced chemical vapor deposition. *Journal of Nanoparticle Research* **2008**, *10*, 173.

[27] Y. He, B. Zhang, S. L. Girshick, J. T. Roberts, Photo-Assisted Chemical Vapor Deposition of Organic Coatings on Aluminum Nanoparticles Produced by a Thermal Plasma Reactor. *Journal of Applied Physics* **In Preparation**.

[28] J. L. Davidson, P. John, P. G. Roberts, M. G. Jubber, J. I. B. Wilson, Laser Photochemical Deposition of Gold from Trialkylphosphine Alkylgold(I) Complexes. *Chemistry of Materials* **1994**, *6*, 1712.

[29] J. Bai, J. P. Wang, High-magnetic-moment core-shell-type FeCo--Au/Ag nanoparticles. *Applied Physics Letters* **2005**, *87*, 152502.

[30] Y. H. Xu, J. P. Wang, FeCo--Au core-shell nanocrystals. *Applied Physics Letters* **2007**, *91*, 233107.

[31] I. Brigger, C. Dubernet, P. Couvreur, Nanoparticles in cancer therapy and diagnosis. *Advanced Drug Delivery Reviews* **2002**, *54*, 631.

[32] R. Hergt, R. Hiergeist, I. Hilger, W. A. Kaiser, Y. Lapatnikov, S. Margel, U. Richter, Maghemite nanoparticles with very high AC-losses for application in RF-magnetic hyperthermia. *Journal of Magnetism and Magnetic Materials* **2004**, *270*, 345.

[33] G. F. Paciotti, L. Myer, D. Weinreich, D. Goia, N. Pavel, R. E. Mclaughlin, L. Tamarkin, Colloidal gold: A novel nanoparticle vector for tumor directed drug delivery. *Drug Delivery* **2004**, *11*, 2004.

[34] N. B. Shah, J. Dong, J. C. Bischof, Cellular uptake and nanoscale localization of gold nanoparticles in cancer using label free Confocal Raman Microscopy. *Molecular Pharmaceutics* **2010**, null.

[35] S. Eustis, M. A. El-Sayed, Why gold nanoparticles are more precious than pretty gold: Noble metal surface plasmon resonance and its enhancement of the radiative and nonradiative properties of nanocrystals of different shapes. *Chemical Society Reviews* **2006**, *35*, 209.

[36] S. J. Oldenburg, J. B. Jackson, S. L. Westcott, N. J. Halas, Infrared extinction properties of gold nanoshells. *Applied Physics Letters* **1999**, *75*, 2897.

[37] S. Chah, J. H. Fendler, J. Yi, Nanostructured Gold Hollow Microspheres Prepared on Dissolvable Ceramic Hollow Sphere Templates. *Journal of Colloid and Interface Science* **2002**, *250*, 142.

[38] M. P. Melancon, W. Lu, C. Li, Gold-Based magneto/Optical Nanostructures: Challenges for *In Vivo* Applications in Cancer Diagnostics and Therapy. *MRS Bulletin* **2009**, *34*.

[39] W. A. Hoppel, Determination of the aerosol size distribution from the mobility distribution of the charged fraction of aerosols. *Journal of Aerosol Science* **1978**, *9*, 41.

[40] E. O. Knutson, K. T. Whitby, Aerosol classification by electric mobility: apparatus, theory, and applications. *Journal of Aerosol Science* **1975**, *6*, 443.

[41] G. S. Hewitt, The charging of small particles for electrostatic precipitation. *Transactions of the American Institute of Electrical Engineers* **1957**, *76*.

[42] P. H. McMurry, A review of atmospheric aerosol measurements. *Atmospheric Environment* **2000**, *34*, 1959.

[43] B. Y. H. Liu, D. Y. H. Pui, A submicron aerosol standard and the primary, absolute calibration of the condensation nuclei counter. *Journal of Colloid and Interface Science* **1974**, *47*, 155.

[44] M. D. Allen, O. G. Raabe, Re-evaluation of millikan's oil drop data for the motion of small particles in air. *Journal of Aerosol Science* **1982**, *13*, 537.

[45] TSI Incorporated, Series 2080 Electrostatic Classifies: Operation and Service Manual. **2006**. http://www.tsi.com/documents/1933792g-3080.pdf.

[46] Y. Kousaka, K. Okuyama, M. Adachi, Determination of particle size distribution of ultrafine aerosols using a differential mobility analyzer. *Aerosol Scienece and Technology* **1985**, *4*.

[47] D. J. Rader, P. H. McMurry, Application of the tandem differential mobility analyzer to studies of droplet growth or evaporation. *Journal of Aerosol Science* **1986**, *17*, 771.

[48] A. Wiedensohler, An approximation of the bipolar charge distribution for particles in the submicron size range. *Journal of Aerosol Science* **1988**, *19*, 387.

[49] W. Li, L. Li, D. R. Chen, Technical Note: A New Deconvolution Scheme for the Retrieval of True DMA Transfer Function from Tandem DMA Data. *Aerosol Science and Technology* **2006**, *40*, 1052

[50] H. Bubbert, H. Jennet, *Surface and thin film analysis: principles, instrumentation, applications*, Weinheim: Wiley-VCH, **2002**.

[51] U. Kogelschatz, B. Eliasson, H. Esrom, Industrial applications of excimer ultraviolet sources. *Materials & Design* **1991**, *12*, 251.

[52] P. Bergonzo, I. W. Boyd, Rapid photo-deposition of silicon dioxide films using 172 nm VUV light. *Electronics Letters* **1994**, *30*, 606.

[53] P. Bergonzo, U. Kogelschatz, I. W. Boyd, Direct photo-deposition of silicon dioxide films using a xenon excimer lamp. *Applied Surface Science* **1993**, *69*, 393.

[54] N. Takezoe, A. Yokotani, K. Kurosawa, W. Sasaki, T. Igarashi, H. Matsuno, SiO_2 thin film preparation using dielectric barrier discharge-driven excimer lamps. *Applied Surface Science* **1999**, *138-139*, 340.

[55] K. Kurosawa, N. Takezoe, H. Yanagida, J. Miyano, Y. Motoyama, K. Toshikawa, Y. Kawasaki, A. Yokotani, Silica film preparation by chemical vapor deposition using vacuum ultraviolet excimer lamps. *Applied Surface Science* **2000**, *168*, 37.

[56] Y. Motoyama, K. Kurosawa, A. Yokotani, Electrical properties of SiO_2 films deposited by photon-assisted CVD with vacuum-ultraviolet excimer lamp. *Electronics and Communications in Japan (Part II: Electronics)* **2005**, *88*, 36.

[57] S. Okuzaki, K. Okude, T. Ohishi, Photoluminescence behavior of SiO_2 prepared by sol-gel processing. *Journal of Non-Crystalline Solids* **2000**, *265*, 61.

[58] P. Mulvaney, L. M. Liz-Marzan, M. Giersig, T. Ung, Silica encapsulation of quantum dots and metal clusters. *Journal of Material Chemistry* **2000**, *10*, 1259.

[59] L. M. Liz-Marzan, P. Mulvaney, Au@SiO_2 colloids: Effect of temperature on the surface plasmon absorption. *New Journal of Chemistry* **1998**, *22*, 1285.

[60] J. B. Shi, C. W. Lee, J. W. Guo, M. J. Cheng, C. Wu, C. J. Chen, Y. C. Chen, Y. T. Lin, C. C. Chang, Optical and magnetic properties of elliptical hematite (α-Fe2O3) nanoparticles coated with uniform continuous layers of silica of different thickness. *Materials Letters* **2007**, *61*, 5268.

[61] A. Ulman, Formation and Structure of Self-Assembled Monolayers. *Chem. Rev.* **2996**, *96*, 1533.

[62] W. Chang Ee, K. Yew Cheong, Effects of annealing temperature on ultra-low dielectric constant SiO_2 thin films derived from sol-gel spin-on-coating. *Physica B: Condensed Matter* **2008**, *403*, 611.

[63] I. Matsubara, M. Paranthaman, S. W. Allison, M. R. Cates, D. L. Beshears, D. E. Holcomb, Preparation of Cr-doped $Y_3Al_5O_{12}$ phosphors by heterogeneous precipitation methods and their luminescent properties. *Materials Research Bulletin* **2000**, *35*, 217.

[64] M. Zarzecka, M. M. Bucko, J. Brzezinska-Miecznik, K. Haberko, YAG powder synthesis by the modified citrate process. *Journal of the European Ceramic Society* **2007**, *27*, 593.

[65] H. Liu, Q. Chen, L. Song, R. Ye, J. Lu, H. Li, Ag-doped antibacterial porous materials with slow release of silver ions. *Journal of Non-Crystalline Solids* **2008**, *354*, 1314.

[66] J. B. Jackson, N. J. Halas, Silver Nanoshells: Variations in Morphologies and Optical Properties. *The Journal of Physical Chemistry B* **2001**, *105*, 2743.

[67] F. X. Liu, Y. Xiao, Y.-S. Li, Silica-supported silver nano-particles for surface-enhanced Raman spectroscopy. *Journal of Raman Spectroscopy* **2001**, *32*, 73.

[68] Y. H. Xu, J. Bai, J. P. Wang, High-magnetic-moment multifunctional nanoparticles for nanomedicine applications. *Journal of Magnetism and Magnetic Materials* **2007**, *311*, 131.

[69] NIST, Silicic acid (H_4SiO_4), tetraethyl ester. **2008**. http://webbook.nist.gov/cgi/cbook.cgi?ID=C78104&Units=SI&Mask=4#Thermo-Phase.

[70] Z. C. Holman, U. R. Kortshagen, A flexible method for depositing dense nanocrystal thin films: impaction of germanium nanocrystals. *Nanotechnology* **2010**, *21*, 335302.

[71] H. F. Johnstone, R. B. Feild, M. C. Tassler, Gas Absorption and Aerosol Collection in a Venturi Atomizer. *Industrial & Engineering Chemistry* **1954**, *46*, 1601.

[72] TSI Incorporated, Model 3076 - Constant Output Atomizer. **2005**. www.tsi.com.

[73] J. Kim, G. Mulholland, S. Kukuck, D. Pui, Slip Correction Measurements of Certified PSL Nanoparticles Using a Nanometer Differential Mobility Analyzer (Nano-DMA) for Knudsen Number From 0.5 to 83. *Journal of Research of the National Institute of Standards and Technology* **2005**, *110*, 31.

[74] P. Kinney, D. Pui, G. Mulholland, N. Bryner, Use of the Electrostatic Classification Method to Size 0.1 μm SRM Particles - A Feasibility Study. *Journal of Research of the National Institute of Standards and Technology* **1991**, *96*, 147.

[75] B. Liu, J. Sun, *United States Patent*, **1995**.

[76] Sigma Aldrich, Mineral Adsorbents, Filter Agents and Drying Agents - Molecular Sieves. **2008**. http://www.sigmaaldrich.com/Brands/Aldrich/Tech Bulletins/AL 143/Molecular Sieves.html.

[77] G. Bengtsson, P. Jönsson, J. Larsson, S. Svanberg, Time-resolved spectroscopic studies of the $7p^2P$ states of neutral silver following VUV excitation. *Zeitschrift für Physik D Atoms, Molecules and Clusters* **1991**, *22*, 437.

[78] B. K. Ku, A. D. Maynard, Generation and investigation of airborne silver nanoparticles with specific size and morphology by homogeneous nucleation, coagulation and sintering. *Journal of Aerosol Science* **2006**, *37*, 452.

[79] H. G. Scheibel, J. Porstendörfer, Generation of monodisperse Ag- and NaCl-aerosols with particle diameters between 2 and 300 nm. *Journal of Aerosol Science* **1983**, *14*, 113.

[80] S. K. Friedlander, *Smoke, Dust, and Haze: Fundamentals of Aerosol Dynamics*, Oxford University Press, New York **2000**.

[81] A. Yokotani, K. Amari, Y. Maezono, K. Toshikawa, K. Kurosawa, Analysis of the Photochemical Reaction on the Surface for Room Temperature Deposition of SiO2 Thin Films by Photo-CVD using Vacuum Ultraviolet Light. *Japanese Journal of Applied Physics* **2005**, *44*, 1019.

[82] M. E. Coltrin, P. Ho, H. K. Moffat, R. J. Buss, Chemical kinetics in chemical vapor deposition: growth of silicon dioxide from tetraethoxysilane (TEOS). *Thin Solid Films* **2000**, *365*, 251.

[83] Y. Motoyama, J. Miyano, K. Toshikawa, Y. Yagi, H. Yanagida, K. Kurosawa, A. Yokotani, Study of SiO_2 -films deposited by adding N_2O or O_2 to TEOS in photo-chemical vapor deposition at room temperature. *Journal of Physics IV France* **2001**, *11*, 1131.

[84] J. J. Mock, M. Barbic, D. R. Smith, D. A. Schultz, S. Schultz, Shape effects in plasmon resonance of individual colloidal silver nanoparticles. *The Journal of Chemical Physics* **2002**, *116*, 6755.

[85] R. C. Weast, Ed. *CRC Handbook of Chemistry and Physics*, CRC Press, Inc., Boca Raton, FL **1984**.

[86] J. M. Zuo, J. C. Mabon, Web-based Electron Microscopy Application Software: Web-EMAPS. *Microscopy and Microanalysis* **2004**, *10*.

[87] K. Dick, T. Dhanasekaran, Z. Zhang, D. Meisel, Size-Dependent Melting of Silica-Encapsulated Gold Nanoparticles. *Journal of the American Chemical Society* **2002**, *124*, 2312.

[88] Z. Qiao, G. Jianping, G. James, H. Yongxing, S. Yugang, Y. Yadong, Tailored Synthesis of Superparamagnetic Gold Nanoshells with Tunable Optical Properties. *Advanced Materials* **2010**, *22*, 1905.

[89] J. Luo, L. Wang, D. Mott, P. N. Njoki, Y. Lin, T. He, Z. Xu, B. N. Wanjana, I.-I. S. Lim, C.-J. Zhong, Core/Shell Nanoparticles as Electrocatalysts for Fuel Cell Reactions. *Advanced Materials* **2008**, *20*, 4342.

[90] D. K. Kim, Y. Zhang, W. Voit, K. V. Rao, M. Muhammed, Synthesis and characterization of surfactant-coated superparamagnetic monodispersed iron oxide nanoparticles. *Journal of Magnetism and Magnetic Materials* **2001**, *225*, 30.

[91] A. Teleki, M. Suter, P. R. Kidambi, O. Ergeneman, F. Krumeich, B. J. Nelson, S. E. Pratsinis, Hermetically Coated Superparamagnetic Fe_2O_3 Particles with SiO_2 Nanofilms. *Chemistry of Materials* **2009**, *21*, 2094.

[92] L. M. Liz-Marzan, M. Giersig, P. Mulvaney, Synthesis of Nanosized Gold-Silica Core-Shell Particles. *Langmuir* **1996**, *12*, 4329.

[93] R. Sardar, T. B. Heap, J. S. Shumaker-Parry, Versatile Solid Phase Synthesis of Gold Nanoparticle Dimers Using an Asymmetric Functionalization Approach. *Journal of the American Chemical Society* **2007**, *129*, 5356.

[94] A. M. Boies, J. T. Roberts, S. L. Girshick, B. Zhang, T. Nakamura, A. Mochizuki, SiO_2 coating of silver nanoparticles by photoinduced chemical vapor deposition. *Nanotechnology* **2009**, 295604.

[95] C. Radloff, N. J. Halas, Enhanced thermal stability of silica-encapsulated metal nanoshells. *Applied Physics Letters* **2001**, *79*, 674.

[96] A. Schroedter, H. Weller, R. Eritja, W. E. Ford, J. M. Wessels, Biofunctionalization of Silica-Coated CdTe and Gold Nanocrystals. *Nano Letters* **2002**, *2*, 1363.

[97] S. Romet, M. F. Couturier, T. K. Whidden, Modeling of Silicon Dioxide Chemical Vapor Deposition from Tetraethoxysilane and Ozone. *Journal of The Electrochemical Society* **2001**, *148*, G82.

[98] O. Sanogo, M. R. Zachariah, Kinetic Studies of the Reaction of Tetraethoxysilane with Oxygen Atoms. *Journal of The Electrochemical Society* **1997**, *144*, 2919.

[99] J. E. Crowell, L. L. Tedder, H. C. Cho, F. M. Cascarano, M. A. Logan, Model studies of dielectric thin film growth: Chemical vapor deposition of SiO_2. *Journal of Vacuum Science & Technology A: Vacuum, Surfaces, and Films* **1990**, *8*, 1864.

[100] M. D. Allendorf, C. F. Melius, P. Ho, M. R. Zachariah, Theoretical Study of the Thermochemistry of Molecules in the Si-O-H System. *The Journal of Physical Chemistry* **1995**, *99*, 15285.

[101] J. C. S. Chu, R. Soller, M. C. Lin, C. F. Melius, Thermal Decomposition of Tetramethyl Orthosilicate in the Gas Phase: An Experimental and Theoretical Study of the Initiation Process. *The Journal of Physical Chemistry* **1995**, *99*, 663.

[102] S. R. Kalidindi, S. B. Desu, Analytical Model for the Low Pressure Chemical Vapor Deposition of SiO_2 from Tetraethoxysilane. *Journal of The Electrochemical Society* **1990**, *137*, 624.

[103] R. J. Kee, F. M. Rupley, J. A. Miller, M. E. Coltrin, J. F. Grcar, E. Meeks, H. K. Moffat, A. E. Lutz, G. Dixon-Lewis, M. D. Smooke, J. Warnatz, G. H. Evans, R. S. Larson, R. E. Mitchell, L. R. Petzold, W. C. Reynolds, M. Caracotsios, W. E. Stewart, P. Glarborg, C. Wang, C. L. McLellan, O. Adigun, W. G. Houf, C. P. Chou, S. F. Miller, P. Ho, P. D. Young, D. J. Young, D. W. Hodgson, M. V. Petrova, K. V. Puduppakkam, Reaction Design: Theory Manual. CHEMKIN-PRO Release 15101, San Diego, CA **2010**, 360.

[104] S. E. Pratsinis, Simultaneous nucleation, condensation, and coagulation in aerosol reactors. *Journal of Colloid and Interface Science* **1988**, *124*, 416.

[105] J. Appel, H. Bockhorn, M. Frenklach, Kinetic modeling of soot formation with detailed chemistry and physics: laminar premixed flames of C_2 hydrocarbons. *Combustion and Flame* **2000**, *121*, 122.

[106] M. Frenklach, S. J. Harris, Aerosol dynamics modeling using the method of moments. *Journal of Colloid and Interface Science* **1987**, *118*, 252.

[107] NASA Glenn Research Center, Wind-US Version 2.0. *Available at: http://www.grc.nasa.gov* **2010**.

[108] R. P. Wayne, *Principles and Applications of Photochemistry*, Oxford University Press, New York **1988**.

[109] R. J. Kee, F. M. Rupley, J. A. Miller, M. E. Coltrin, J. F. Grcar, E. Meeks, H. K. Moffat, A. E. Lutz, G. Dixon-Lewis, M. D. Smooke, J. Warnatz, G. H. Evans, R. S. Larson, R. E. Mitchell, L. R. Petzold, W. C. Reynolds, M. Caracotsios, W. E. Stewart, P. Glarborg, C. Wang, C. L. McLellan, O. Adigun, W. G. Houf, C. P. Chou, S. F. Miller, P. Ho, P. D. Young, D. J. Young, D. W. Hodgson, M. V. Petrova, K. V. Puduppakkam, Reaction Design: Applications Programming Interface Manual. CHEMKIN-PRO Release 15101, San Diego, CA **2010**, 228.

[110] R. J. Kee, F. M. Rupley, J. A. Miller, M. E. Coltrin, J. F. Grcar, E. Meeks, H. K. Moffat, A. E. Lutz, G. Dixon-Lewis, M. D. Smooke, J. Warnatz, G. H. Evans, R. S. Larson, R. E. Mitchell, L. R. Petzold, W. C. Reynolds, M. Caracotsios, W. E. Stewart, P. Glarborg, C. Wang, C. L. McLellan, O. Adigun, W. G. Houf, C. P. Chou, S. F. Miller, P. Ho, P. D. Young, D. J. Young, D. W. Hodgson, M. V. Petrova, K. V. Puduppakkam, Reaction Design: Input Manual. CHEMKIN-PRO Release 15101, San Diego, CA **2010**, 322.

[111] H. Keller-Rudek, G. K. Moortgat, MPI-Mainz-UV-Vis Spectral Atlas of Gaseous Molecules. Max-Planck-Gesellschaft, **2010**.

[112] F. Antonii, *Panacea Aurea-Auro Potabile*, Bibliopolio Frobeniano, Hamburg, Germany **1618**.

[113] M. C. Daniel, D. Astruc, Gold Nanoparticles: Assembly, Supramolecular Chemistry, Quantum-Size-Related Properties, and Applications toward Biology, Catalysis, and Nanotechnology. *Chemical Reviews* **2003**, *104*, 293.

[114] H. Wohltjen, A. W. Snow, Colloidal Metal-Insulator-Metal Ensemble Chemiresistor Sensor. *Analytical Chemistry* **1998**, *70*, 2856.

[115] A. H. Lu, G. H. Lu, A. M. Kessinger, C. A. Foss, Dichroic Thin Layer Films Prepared from Alkanethiol-Coated Gold Nanoparticles. *The Journal of Physical Chemistry B* **1997**, *101*, 9139.

[116] M. Turner, V. B. Golovko, O. P. H. Vaughan, P. Abdulkin, A. Berenguer-Murcia, M. S. Tikhov, B. F. G. Johnson, R. M. Lambert, Selective oxidation with dioxygen by gold nanoparticle catalysts derived from 55-atom clusters. *Nature* **2008**, *454*, 981.

[117] R. J. Tseng, J. Huang, J. Ouyang, R. B. Kaner, Yang, Polyaniline Nanofiber/Gold Nanoparticle Nonvolatile Memory. *Nano Letters* **2005**, *5*, 1077.

[118] H. Daniel, L. Frank, M. Steven, R. David, S. Vivek, Plastic-Compatible Low Resistance Printable Gold Nanoparticle Conductors for Flexible Electronics. *Journal of The Electrochemical Society* **2003**, *150*, G412.

[119] I. H. El-Sayed, X. Huang, M. A. El-Sayed, Selective laser photo-thermal therapy of epithelial carcinoma using anti-EGFR antibody conjugated gold nanoparticles. *Cancer Letters* **2006**, *239*, 129.

[120] S. Keren, C. Zavaleta, Z. Cheng, A. de la Zerda, O. Gheysens, S. S. Gambhir, Noninvasive molecular imaging of small living subjects using Raman

spectroscopy. *Proceedings of the National Academy of Sciences* **2008**, *105*, 5844.

[121] R. N. Pedro, T. Thekke-Adiyat, R. Goel, M. Shenoi, J. Slaton, S. Schmechel, J. Bischof, J. K. Anderson, Use of Tumor Necrosis Factor-alpha-coated Gold Nanoparticles to Enhance Radiofrequency Ablation in a Translational Model of Renal Tumors. *Urology* **2010**, *76*, 494.

[122] R. Goel, D. Swanlund, J. Coad, G. F. Paciotti, J. C. Bischof, TNF-alpha-based accentuation in cryoinjury--dose, delivery, and response. *Molecular Cancer Therapeutics* **2007**, *6*.

[123] M. Brust, C. J. Kiely, Some recent advances in nanostructure preparation from gold and silver particles: a short topical review. *Colloids and Surfaces A: Physicochemical and Engineering Aspects* **2002**, *202*, 175.

[124] M. Brust, M. Walker, D. Bethell, D. J. Schiffrin, R. Whyman, Synthesis of thiol-derivatised gold nanoparticles in a two-phase Liquid–Liquid system *Journal of the Chemical Society, Chemical Communications* **1994**.

[125] M. Giersig, P. Mulvaney, Preparation of ordered colloid monolayers by electrophoretic deposition. *Langmuir* **1993**, *9*, 3408.

[126] T. Yonezawa, T. Kunitake, Practical preparation of anionic mercapto ligand-stabilized gold nanoparticles and their immobilization. *Colloids and Surfaces A: Physicochemical and Engineering Aspects* **1999**, *149*, 193.

[127] M. H. Magnusson, K. Deppert, J.-O. Malm, J.-O. Bovin, L. Samuelson, Gold Nanoparticles: Production, Reshaping, and Thermal Charging. *Journal of Nanoparticle Research* **1999**, *1*, 243.

[128] U. Müller, A. Schmidt-Ott, H. Burtscher, First measurement of gas adsorption to free ultrafine particles: O_2 on Ag. *Physical Review Letters* **1987**, *58*, 1684.

[129] M. E. Messing, K. Hillerich, J. Johansson, K. Deppert, K. A. Dick, The use of gold for fabrication of nanowire structures. *Gold bulletin* **2009**, *42*.

[130] M. E. Messing, R. Westerström, B. O. Meuller, S. Blomberg, J. Gustafson, J. N. Andersen, E. Lundgren, R. van Rijn, O. Balmes, H. Bluhm, K. Deppert, Generation of Pd Model Catalyst Nanoparticles by Spark Discharge. *The Journal of Physical Chemistry C* **2010**, *114*, 9257.

[131] N. Tabrizi, Q. Xu, N. van der Pers, U. Lafont, A. Schmidt-Ott, Synthesis of mixed metallic nanoparticles by spark discharge. *Journal of Nanoparticle Research* **2009**, *11*, 1209.

[132] J. H. Byeon, J. H. Park, J. Hwang, Spark generation of monometallic and bimetallic aerosol nanoparticles. *Journal of Aerosol Science* **2008**, *39*, 888.

[133] C. Peineke, M. B. Attoui, A. Schmidt-Ott, Using a glowing wire generator for production of charged, uniformly sized nanoparticles at high concentrations. *Journal of Aerosol Science* **2006**, *37*, 1651.

[134] H. Burtscher, A. Schmidt-Ott, H. C. Siegmann, Photoelectron yield of small silver and gold particles suspended in gas up to a photon energy of 10 eV. *Zeitschrift für Physik B Condensed Matter* **1984**, *56*, 197.

[135] NIST, Web Book: Gold and Platinum Antoine Equations. Vol. 2010, **2008**. http://webbook.nist.gov/cgi/cbook.cgi?Spec=C7631869&Index=3&Type=IR&Large=on.

[136] S. Vemury, S. E. Pratsinis, Self-preserving size distributions of agglomerates. *Journal of Aerosol Science* **1995**, *26*, 175.

[137] C. D. Wagner, A. V. Naumkin, A. Kraut-Vass, J. W. Allison, C. J. Powell, J. John R. Rumble, NIST X-ray Photoelectron Spectroscopy Database **2010**. http://srdata.nist.gov/xps/Default.aspx.

[138] C. Peineke, A. Schmidt-Ott, Explanation of charged nanoparticle production from hot surfaces. *Journal of Aerosol Science* **2008**, *39*, 244.

[139] H. Zhang, *Ion sources*, Springer, Beijing; New York: Science Press **1999**.

[140] B. E. Launder, D. B. Spalding, *Lectures in Mathematical Models of Turbulence*, Academic Press, London, England **1972**.

[141] A. F. Mills, *Heat Transfer*, Prentice-Hall, Inc., Upper Saddle River, New Jersey **1999**.

[142] Y. Sun, Y. Xia, Increased Sensitivity of Surface Plasmon Resonance of Gold Nanoshells Compared to That of Gold Solid Colloids in Response to Environmental Changes. *Analytical Chemistry* **2002**, *74*, 5297.

[143] C. J. Zhong, J. Luo, B. Fang, B. N. Wanjala, P. N. Njoki, R. Loukrakpam, J. Yin, Nanostructured catalysts in fuel cells. *Nanotechnology* **2010**, *21*, 062001.

[144] M. Haruta, Gold as a Novel Catalyst in the 21st Century: Preparation, Working Mechanism and Applications. *Gold bulletin* **2004**, *37*, 1.

[145] D. Cameron, R. Holliday, D. Thompson, Gold's future role in fuel cell systems. *Journal of Power Sources* **2003**, *118*, 298.

[146] M. D. Hughes, Y.-J. Xu, P. Jenkins, P. McMorn, P. Landon, D. I. Enache, A. F. Carley, G. A. Attard, G. J. Hutchings, F. King, E. H. Stitt, P. Johnston, K. Griffin, C. J. Kiely, Tunable gold catalysts for selective hydrocarbon oxidation under mild conditions. *Nature* **2005**, *437*, 1132.

[147] C. J. Jia, Y. Liu, H. Bongard, F. Schüth, Very Low Temperature CO Oxidation over Colloidally Deposited Gold Nanoparticles on $Mg(OH)_2$ and MgO. *Journal of the American Chemical Society* **2010**, *132*, 1520.

[148] I. H. El-Sayed, X. Huang, M. A. El-Sayed, Surface Plasmon Resonance Scattering and Absorption of anti-EGFR Antibody Conjugated Gold Nanoparticles in Cancer Diagnostics: Applications in Oral Cancer. *Nano Letters* **2005**, *5*, 829.

[149] A. Gaiduk, M. Yorulmaz, P. V. Ruijgrok, M. Orrit, Room-Temperature Detection of a Single Molecule's Absorption by Photothermal Contrast. *Science* **2010**, *330*, 353.

[150] S. J. Oldenburg, R. D. Averitt, S. L. Westcott, N. J. Halas, Nanoengineering of optical resonances. *Chemical Physics Letters* **1998**, *288*, 243.

[151] H. D. Jang, Generation of Silica Nanoparticles from Tetraethylorthosilicate (TEOS) Vapor in a Diffusion Flame. *Aerosol Science & Technology* **1999**, *30*, 477.

[152] B. Zhang, Thermal plasma synthesis and photoinduced coating of aluminum nanoparticles. Vol. Doctor of Philosophy, University of Minnesota, Minneapolis **2008**, 127.

[153] M. L. Ostraat, J. W. D. Blauwe, M. L. Green, L. D. Bell, H. A. Atwater, R. C. Flagan, Ultraclean Two-Stage Aerosol Reactor for Production of Oxide-Passivated Silicon Nanoparticles for Novel Memory Devices. *Journal of The Electrochemical Society* **2001**, *148*, G265.

[154] S. Roberto, M. Maria L, C. Dominique, E. Nicolas, Wettability and Work of Adhesion of Nonreactive Liquid Metals on Silica. *Journal of the American Ceramic Society* **1988**, *71*, 742.

[155] A. M. Boies, P. Lei, S. Calder, W. G. Shin, S. L. Girshick, Hot-Wire Synthesis of Gold Nanoparticles. *Aerosol Science & Technology* **In Press**.

[156] V. Salgueirio-Maceira, M. A. Correa-Duarte, M. Farle, A. Lpez-Quintela, K. Sieradzki, R. Diaz, Bifunctional Gold-Coated Magnetic Silica Spheres. *Chemistry of Materials* **2006**, *18*, 2701.

[157] J. B. Hannon, S. Kodambaka, F. M. Ross, R. M. Tromp, The influence of the surface migration of gold on the growth of silicon nanowires. *Nature* **2006**, *440*, 69.

[158] H. H. Farrell, C. D. V. Siclen, "Binding energy, vapor pressure, and melting point of semiconductor nanoparticles", **2007**.

[159] J. A. Dagata, E. Villa, M. C. Lin, UV Desorption and Photochemistry of Dimethylgold Hexafuoroacetylacetonate Absorbed on a Quatz Substrate. *Applied Physics B* **1990**, *51*, 443.

[160] D. Wexler, J. I. Zink, L. W. Tutt, S. R. Lunt, Laser-assisted deposition of pure gold from (hexafluoroacetylacetonate)dimethylgold(III) and gas-phase luminescence identification of photofragments. *The Journal of Physical Chemistry* **1993**, *97*, 13563.

[161] Y. Morishige, S. Kishida, Thick gold-film deposition by high-repetition visible pulsed-laser chemical vapor deposition. *Applied Physics A: Materials Science & Processing* **1994**, *59*, 395.

[162] T. T. Kodas, T. H. Baum, P. B. Comita, Kinetics of laser-induced chemical vapor deposition of gold. *Journal of Applied Physics* **1987**, *62*.

[163] M. Hoshino, K. Kasai, J. Komeno, Surface Morphology and Line Fill Properties of Gold Grown by Organometallic Chemical Vapor Deposition. *Japanese Journal of Applied Physics* **1992**, *31*, 4403.

[164] T. Ohta, F. Cicoira, P. Doppelt, L. Beitone, P. Hoffmann, Static Vapor Pressure Measurement of Low Volatility Precursors for Molecular Vapor Deposition Below Ambient Temperature. *Chemical Vapor Deposition* **2001**, *7*, 33.

[165] M. C. Artaud-Gillet, S. Duchemin, R. Odedra, G. Orsal, N. Rega, S. Rushworth, S. Siebentritt, Evaluation of copper organometallic sources for $CuGaSe_2$ photovoltaic applications. *Journal of Crystal Growth* **2003**, *248*, 163.

[166] A. Z. Rubezhov, Platinum Group Organometallics Coatings for Electronics and Related Uses. *Platinum Metals Review* **1992**, *36*, 26.

[167] L.-C. Wang, Y.-M. Liu, M. Chen, Y. Cao, H.-Y. He, G.-S. Wu, W.-L. Dai, K.-N. Fan, Production of hydrogen by steam reforming of methanol over Cu/ZnO catalysts prepared via a practical soft reactive grinding route based on dry oxalate-precursor synthesis. *Journal of Catalysis* **2007**, *246*, 193.

[168] D. D. Huang, J. H. Seinfeld, K. Okuyama, Image potential between a charged particle and an uncharged particle in aerosol coagulation--enhancement in all size regimes and interplay with van der Waals forces. *Journal of Colloid and Interface Science* **1991**, *141*, 191.

[169] R. J. Weber, D. Orsini, Y. Daun, Y. N. Lee, P. J. Klotz, F. Brechtel, A Particle-into-Liquid Collector for Rapid Measurement of Aerosol Bulk Chemical Composition. *Aerosol Science & Technology* **2001**, *35*, 718.

[170] Y. Zhuang, Y. Jin Kim, T. Gyu Lee, P. Biswas, Experimental and theoretical studies of ultra-fine particle behavior in electrostatic precipitators. *Journal of Electrostatics* **2000**, *48*, 245.

[171] S. V. Hering, M. R. Stolzenburg, A Method for Particle Size Amplification by Water Condensation in a Laminar, Thermally Diffusive Flow. *American Association for Aerosol Research* **2005**, *39*, 428.

Appendix A

A.1 CKUPROG ROUTINE

```
SUBROUTINE CKUPROG (LOUT, NII, I, ITYP, T, C, ICKWRK, RCKWRK,
1                    RPROG, IFLAG)
!DEC$ IF DEFINED (DLL_EXPORT)
!DEC$ ATTRIBUTES DLLEXPORT :: CKUPROG
!DEC$ ENDIF
C
C  START PROLOGUE
C
C  SUBROUTINE CKUPROG  (LOUT, NII, I, ITYP, T, C, ICKWRK, RCKWRK,
C                       RPROG, IFLAG)
C  Template for user-modify of default reaction rates-of-
C  progress.
C  CAUTIONS!!!
C  (1)
C  CKUPROG should only modify RPROG and possibly the error flag
C  (IFLAG);
C  use local variables and arrays for any other work;
C  some local arrays have been provided as an example.
C  (2)
C  CKUPROG should NOT call any other CHEMKIN routine that returns
C  reaction rates-of-progress (CKQYP, CKQXP, CKQYR, CKKFKR),
C  to avoid any recursion.
C
C  INPUT
C  LOUT      - if positive, the unit number of an open output fil
C  NII       - Integer scalar; the total number of reactions.
C  I         - Integer scalar; the current reaction index.
C  ITYP      - Integer scalar; an optional type parameter which
C              may have been provided in the mechanism,
C              otherwise, zero.
C  T(*)      - Real array, temperature(s).
C              cgs units, K
C  C(*)      - Real array, concentrations of the species;
C              the length of this array is KK, the total species
C              count.
C              cgs units, mole/cm**3
C  ICKWRK(*) - Integer workspace array; dimension at least
C              LENICK.
C  RCKWRK(*) - Real workspace array; dimension at least LENRCK.
C  RPROG     - Real scalar, the default rate of progress of
C              reaction I;
```

```
C              cgs units, moles/(cm**3*sec)
C
C  OUTPUT
C  RPROG     - User-provided reaction rate of progress for
C              reaction I. rate-of-progress of reaction I.
C  IFLAG     - Integer scalar, provides reverse communication to
C              the calling routine about the user-rate modify.
C  END PROLOGUE
      IMPLICIT DOUBLE PRECISION (A-H, O-Z), INTEGER (I-N)
      INCLUDE 'user_routines_interface.inc'
      DIMENSION ICKWRK(*), RCKWRK(*), C(*), T(*)
      DOUBLE PRECISION PHOTO1, PHOTO2, X1, X2, VEL, SIGMA
      DOUBLE PRECISION RPROG1, RPROG2, NCONC, AVGN, PHI
      DOUBLE PRECISION XDIF
C
C     Example: create array space to facilitate calculations;
C     KMAX is an upper limit for species data,
C     IMAX is an upper limit for reaction data.
      PARAMETER (LIPAR=1000, LRPAR=1000, KMAX=100, IMAX=500)
      DIMENSION IPAR(LIPAR), RPAR(LRPAR), WT(KMAX)
C
C     Example: find additional mechanism parameters
      CALL CKINDX (ICKWRK, RCKWRK, MM, KK, II, NFIT)
C
C     Example: set error flag if inconsistent data
      IF (NII .NE. II) THEN
         IFLAG = 1
         RETURN
      ENDIF
C
C Example: partition local work array to store molecular weights
      NWT = 1
      IF (KK .LE. LRPAR) CALL CKWT (ICKWRK, RCKWRK, RPAR(NWT))
C
C     Example: store molecular weights in local array
      IF (KK .LE. KMAX)  CALL CKWT (ICKWRK, RCKWRK, WT)
C
C     Local copy of Q(I)
       RTEMP = RPROG
C
C     Copy the default value for this reaction into RPROG
C       RPROG = RTEMP
C
C    AMB Code to read in the x location
C
C    Read in position, units mm
```

```
        OPEN(UNIT = 13, file = "./XCORD.DAT")
        READ (13,*) X
        CLOSE(13)
C
CCCC AMB define the reaction which varies according to the power
C    law (consistant with a difuse light source).
        SIGMA = 6E-19
        PHOTO1 = 3.14E16
        AVGN = 6.022E23
        PHI = 1.0
C    Calculate the number of photons according to the power law
        PHOTOX=PHOTO1*(10**2)/((10+X)**2)
        OPEN(202, FORM="FORMATTED", ACCESS="APPEND",
FILE="./PHOTOX")
        WRITE(202,*) PHOTOX
        CLOSE(202)
C
C    Calculate the rate of progress for Rxn 1 the photodecomp of
C    O2
C   !!Check gas output file to make sure O2 decomp is Rxn #1 and
C   O2 is species #16!!
      IF (I .EQ. 1) THEN
       RPROG = PHI*C(16)*SIGMA*PHOTOX
       OPEN(301, FORM="FORMATTED", ACCESS="APPEND",
FILE="./RPROGO2")
       WRITE(301,*) RPROG
       CLOSE(301)
      END IF
C
C    Calculate the rate of progress for Rxn 2 the photodecomp of
TEOS
C   !!Check gas output file to make sure TEOS decomp is Rxn #2
and TEOS is species #1!!
      IF (I .EQ. 2) THEN
       RPROG = PHI*C(1)*SIGMA*PHOTOX
       OPEN(302, FORM="FORMATTED", ACCESS="APPEND",
FILE="./RPROGTEOS")
       WRITE(302,*) RPROG
       CLOSE(302)
      END IF
C
C
CCalculate the rate of progress for Rxn 2 the photodecomp of TEOS
C!!Check gas output file to make sure TEOS decomp is Rxn #2 and
C!!TEOS is species #1!!
      IF (I .EQ. 3) THEN
```

```
       RPROG = PHI*C(2)*SIGMA*PHOTOX
       OPEN(303, FORM="FORMATTED", ACCESS="APPEND",
FILE="./PRGSUBTEOS")
       WRITE(303,*) RPROG
       CLOSE(303)
      END IF
C
       RETURN
       END
```

A.2 PLGEOM ROUTINE

```
SUBROUTINE PLGEOM (X, LOUT, A, DADX, AI, AE, DIAM)
!DEC$ IF DEFINED (DLLEXPORT)
!DEC$ ATTRIBUTES DLLEXPORT :: PLGEOM
!DEC$ ENDIF
C
      IMPLICIT DOUBLE PRECISION (A-H, O-Z), INTEGER (I-N)
      EXTERNAL CKUFIRST
      SAVE IFIRST
      DATA IFIRST/0/
C
C     acknowledge that PLGEOM has been applied
      IF (IFIRST .EQ. 0) CALL CKUFIRST (IFIRST, LOUT, 'PLGEOM')
C
C         CROSS-SECTIONAL (FLOW) AREA (CM**2)
C
      A = 9.008D0
C
C             DERIVATIVE OF CROSS-SECTIONAL AREA WITH RESPECT TO
LENGTH (CM)
C
      DADX = 0.D0
C
C         DEPOSITION AREA PER UNIT LENGTH (CM)
C
      AI = 10.6395D0
CC      IF (X .LE. 0.1D0) AI = 2073.9D0
C
C         EXTERNAL SURFACE AREA PER UNIT LENGTH (CM)
C
      AE = 11.6395D0
C
C         HYDRAULIC DIAMETER (CM)
C
      DIAM = 4.D0*A/AI
```

```
C
C   AMB code to output the x location to a file, append each time
       OPEN(140,        FORM="FORMATTED",        ACCESS="APPEND",
FILE="./XCORDALL")
       WRITE(140,*) X
       CLOSE(140)
C
C AMB code to output the x location to a file, replaced each time
      OPEN(13,         FORM="FORMATTED",         STATUS="REPLACE",
FILE="./XCORD.DAT")
      WRITE(13,*) x
      CLOSE(13)
C
C     end of SUBROUTINE PLGEOM
      RETURN
      END
```

A.3 GAS-PHASE REACTIONS

```
!!!!!!!!!!!!!!!!!!!!!!!!!!!!!!!!!!!!!!!!!!!!!!!!!!!!!!!!!!!!!!!!!!!!!!!
!                                                                      !
!   TEOS deposition GAS CHEMKIN input file w oxygen reaction:          !
!                                                                      !
!                                                                      !
!   Ref 1: M. E. Coltrin, P. Ho, H. K. Moffat, and R. J. Buss          !
!              Thin Solid Films, vol. 365, 251-263 (2000).             !
!   Ref 2: S. Romet, M. F. Couturier, T. K. Whidden                    !
!          Journal of Electrochemical Society, vol. 148, (2001).       !
!                                                                      !
!!!!!!!!!!!!!!!!!!!!!!!!!!!!!!!!!!!!!!!!!!!!!!!!!!!!!!!!!!!!!!!!!!!!!!!
ELEMENTS
   Si O H C N
END
!
!
!
SPECIES
   Si(OC2H5)4
   Si(OH)(OC2H5)3
   Si(OH)2(OC2H5)2
   O(Si(OC2H5)3)2
   C2H5OH
   C2H4
   CH3CHO
   CH3CO
```

```
   CH3
   CH3O
   CH2O
   CO2
   CO
   H2O
   N2
   O2
   O
   O3
   OH
   H
   HCO
   CH2O
   Oligomer
   Oligo(OH)
   Oligo(OH)2
END
!
!
REACTIONS
!
!Added by AMB
!
!This is the radiation reaction. HV is not included since it has
no mass.
!These reactions are carried out in the CKUPROG routine
!
        O2 => 2O                              2.04E-2   0.0     0.0
        USRPROG
!
        Si(OC2H5)4 => Si(OH)(OC2H5)3 + C2H4 2.04E-1   0.0     0.0
        DUP
        USRPROG
!
        Si(OH)(OC2H5)3 => Si(OH)2(OC2H5)2 + C2H4
                                              2.04E-1   0.0     0.0
        USRPROG
!
!
!Coltrin Reactions
!1
   Si(OC2H5)4 = Si(OH)(OC2H5)3 + C2H4
                                              4.9E13    0.0   61460.
   DUP
!2
```

```
   Si(OC2H5)4 + H2O = Si(OH)(OC2H5)3 + C2H5OH
                                                1.0E11   0.0   25000.
!
!  Condensation reactions
!3
   Si(OH)(OC2H5)3 + Si(OC2H5)4 = O(Si(OC2H5)3)2 + C2H5OH
                                                1.0E11   0.0   30000.
!4 This is the same as Romet Rxn 24
!   2Si(OH)(OC2H5)3 = O(Si(OC2H5)3)2 + H2O
                                                1.0E11   0.0   30000.
!
!AMB Oxygen Reactions from Romet et al 2001
!5
   Si(OC2H5)4 + O = Si(OH)(OC2H5)3 + CH3CHO
                                                2.04E13  0.0   10800.
!6
   Si(OC2H5)4 + O3 = Si(OH)(OC2H5)3 + CH3CHO + O2
                                                8.64E8   0.0   29100.
!7
   Si(OH)(OC2H5)3 + O = Si(OH)2(OC2H5)2 + CH3CHO
                                                2.04E13  0.0   10800.
!8
   Si(OH)(OC2H5)3 + O3 = Si(OH)2(OC2H5)2 + CH3CHO + O2
                                                8.64E8   0.0   29100.
!9
   CH3CHO + O = CH3CO + OH
                                                1.10E13  0.0    9610.
!10
   CH3CHO + OH = CH3CO + H2O
                                                1.00E13  0.0       0.
!11
   CH3CO + O = CH3 + CO2
                                                9.60E12  0.0       0.
!12
   CH3CO + OH = CH3 + CO + OH
                                                3.00E13  0.0       0.
!13
   CH3 + O = CH2O + H
                                                8.00E13  0.0       0.
!14
   CH3 + OH = CH3O + H
                                                5.74E12  -0.2  58300.
!15
   CH2O + O = HCO + OH
                                                1.82E13  0.0   12900.
!16
```

```
   CH2O + OH = HCO + H2O
                                          3.43E9   1.2    1880.
!17
   HCO + HCO = CH2O + CO
                                          1.82E13  0.0       0.
!18
   CH3O + O = CH2O + OH
                                          6.00E12  0.0       0.
!19
   CH3O + OH = CH2O + H2O
                                          1.80E13  0.0       0.
!20
   HCO + O = CO + OH
                                          3.00E13  0.0       0.
!21
   HCO + OH = CO + H2O
                                          3.00e13  0.0       0.
!22
   HCO + O = CO2 + H
                                          1.00e13  0.0       0.
!23
   O3 + CO = CO2 + O2
                                          6.02e02  0.0       0.
!24 This is the same as Coltrin Rxn 4
   2Si(OH)(OC2H5)3 = Oligomer + H2O
                                          1.00E10  0.0       0.
!25
   Oligomer + O = Oligo(OH) + CH3CHO
                                          1.00E10  0.0       0.
!26
   Oligomer + O3 = Oligo(OH) + CH3CHO + O2
                                          8.64E8   0.0   29100.
!27
!   Oligo(OH) + Si(OH)(OC2H5)3 = Oligomer + H2O
                                          1.00E10  0.0       0.
!28
!   2Oligo(OH) = Oligomer + H2O
                                          1.00E10  0.0       0.
!29
!   Oligo(OH) + O = Oligo(OH)2 + CH3CHO
                                          2.04E13  0.0   10800.
!30
!   Oligo(OH) + O3 = Oligo(OH)2 + CH3CHO + O2
                                          8.64E8   0.0   29100.
!31
!   Si(OH)(OC2H5)3 + Oligo(OH)2 = Oligo(OH) + H2O
```

```
                                                1.00E10  0.0       0.
!32
!   Oligo(OH) + Oligo(OH)2 = Oligo(OH) + H2O
                                                1.00E10  0.0       0.
!33
   Si(OH)(OC2H5)3 + Si(OH)2(OC2H5)2 = Oligo(OH) + H2O
                                                1.00E10  0.0       0.
!34
!   Si(OH)2(OC2H5)2 + Oligo(OH)2 = Oligo(OH) + H2O
                                                1.00E10  0.0       0.
!35
   2Si(OH)2(OC2H5)2 = Oligo(OH)2 + H2O
                                                1.00E10  0.0       0.
!36
!   Si(OH)2(OC2H5)2 + Oligo(OH)2 = Oligo(OH)2 + H2O
                                                1.00E10  0.0       0.
!37
!   Oligo(OH)2 + Oligo(OH)2 = Oligo(OH)2 + H2O
                                                1.00E10  0.0       0.
!
!
END
```

A.4 SURFACE REACTIONS

```
!!!!!!!!!!!!!!!!!!!!!!!!!!!!!!!!!!!!!!!!!!!!!!!!!!!!!!!!!!!!!!!!!!!!!!!
!            TEOS deposition SURFACE CHEMKIN input file:        !
!                                                               !
!     Ref 1: M. E. Coltrin, P. Ho, H. K. Moffat, and R. J. Buss !
!            Thin Solid Films, vol. 365, 251-263 (2000).        !
!     Ref 2: S. Romet, M. F. Couturier, T. K. Whidden
!             Journal of Electrochemical Society, 148 (2), 2001.!
!!!!!!!!!!!!!!!!!!!!!!!!!!!!!!!!!!!!!!!!!!!!!!!!!!!!!!!!!!!!!!!!!!!!!!!
!
!AMB Addition of nanoparticles called silicaNP
!
MATERIAL silicaNP
DISPERSED
END
!
!
!
!
!  Surface site density is given in moles/cm**2.  This number is
!  actually fairly controversial.  If the bulk density is used as
```

```
!  the basis, then a theoretical value of 1.3E-9 moles/cm**2
!  (i.e. 7.9 nm**-2) is arrived at.  However, some of the Si
!  groups on the surface are sterically blocked by O atoms from
!  having OH groups attached.  Moreover, adsorption studies
!  confirm lower OH concentrations.  The (111) face of octahedral
!  cristobalite can be used as the basis. Then 4.55 nm**-2 is
!  obtained. This is the number that will be used.
!
!  "E" stands for an ethoxy group -"(OC2H5)"
!  "G" stands for a glass bond.  It is assigned a stoichiometric
!  coefficient for oxygen of 1/2.  The rule is to round down the
!  number of oxygen atoms in a molecule, i.e. G3 is assigned a
!  stoichiometric coefficient of 1 for oxygen.
!
SITE/SiO2/        SDEN/0.750E-9/
   SiG3(OH)      ! Hf = -191.89
   SiG3E         ! Hf = -191.41
   SiG(OH)2E     ! Hf = -241.73
   SiG(OH)E2     ! Hf = -241.25
   SiGE3         ! Hf = -240.77
END
!
!  bulk phase: vitreous SiO2
!
!  Number after the name is the density of the phase in gm/cm**3
!
BULK/Glass/
    SiO2(D)/2.19/        ! Hf =

END
!Surface Species
THERMO ALL
!
  300.     600.     10000.
SiG3(OH) 121591O   2Si  1H   1     I    300.00   3000.00 1000.00
0.66466584E+01 0.33231564E-02-0.29541198E-06-0.31399386E-09
0.69825405E-13
-0.98982922E+05-0.33869411E+02 0.26748490E+01 0.12014943E-01-
0.13939117E-05
-0.83051193E-08 0.44394740E-11-0.97866992E+05-0.13004364E+02
!
SiG3E    121591C   2H   5O   2Si  1I    300.00   3000.00 1000.00
 0.12659941E+02 0.11178698E-01-0.96102099E-06-0.11064012E-08
0.24469427E-12
-0.10153567E+06-0.64059296E+02 0.34100885E+01 0.28247360E-01-
0.56295153E-06
```

```
-0.16109125E-07 0.70305402E-11-0.98559328E+05-0.14126812E+02
!
SiG(OH)2E  62692C   2H   7O   3Si  1I    300.00   3000.00 1000.00
 0.13577039E+02 0.14641373E-01-0.11149998E-05-0.14189627E-08
0.30468458E-12
-0.12723145E+06-0.61076580E+02 0.57280946E+01 0.27964467E-01
0.50749497E-06
-0.13237452E-07 0.50265321E-11-0.12457464E+06-0.18233299E+02
!
SiG(OH)E2 62692C   4H  11O   3Si  1I    300.00   3000.00 1000.00
 0.19473230E+02 0.22570338E-01-0.17838936E-05-0.22180249E-08
0.48075975E-12
-0.12976159E+06-0.90081039E+02 0.66617913E+01 0.43213133E-01
0.17241006E-05
-0.19916659E-07 0.68400398E-11-0.12528808E+06-0.19669796E+02
!
SiGE3 62692C   6H  15O   3Si  1I    300.00   3000.00 1000.00
 0.25609777E+02 0.30346680E-01-0.24455890E-05-0.30030116E-08
0.65423480E-12
-0.13233747E+06-0.11858306E+03 0.72320976E+01 0.60353167E-01
0.21851304E-05
-0.28773197E-07 0.10164894E-10-0.12596620E+06-0.17743988E+02
!
!
! from Babushkin et al., "Thermodynamics of Silicates"
!
SiO2(D) 72391Si  1O   2          S    298.00   2000.00 1000.00
 0.48925619E+01 0.41191629E-02-0.94570083E-07-0.80073115E-09
0.25433412E-12
-0.11005530E+06-0.23469570E+02 0.22325585E+01 0.12478522E-01-
0.28715690E-05
-0.96847970E-08 0.62160411E-11-0.10962063E+06-0.10594849E+02
!
! Fictitious phase whose growth rate should always be zero.
!
O(D) 121591O   1               S    300.00   3000.00 1000.00
 0.23625109E+01 0.57858101E-03-0.82644831E-07-0.58489401E-10
0.15022128E-13
-0.49901734E+05-0.13022270E+02 0.31750876E+00 0.54401071E-02-
0.10133198E-05
-0.46017092E-08 0.26723929E-11-0.49372941E+05-0.24420185E+01
!
END
!
!!!!!!!!!!!!!!!!!!!!!!!!!!!!!!!!!!!!!!!!!!!!!!!!!!!!!!!!!!!!!!!!
!
```

```
REACTIONS
!                                                    A   T**B   E_A
!
======================
!
! Nucleation reaction. Needed to run chemkin but not for study.
! AMB
100 Si(OC2H5)4 => 100 SiO2(D) + 400 C2H4 + 200 H2O
                                                   1.E-20   0.   0.
NUCL
!
!!!  Initial sticking coefficient reaction for TEOS !!!!!!!!!!!!
!
!
!      Main TEOS reaction.
!   (S1)
Si(OC2H5)4 + SiG3(OH) => SiO2(D) + SiGE3 + C2H5OH
                                                 8.75E3   0.   43830.
STICK
!
!!! Beta Elimination reactions involving ethoxy groups !!!!!!!!!!
!
!
! (notes - all reactions are assigned equal activation energies.
!  Pre-exponential factors are proportional to the number of
!  ethoxy groups.)
!    (S2)
SiG3E     => SiG3(OH) + C2H4
                                                 1.7E+12  0.   47000.
DUP
!    (S3)
SiG(OH)E2 => SiG(OH)2E + C2H4
                                                 3.4E+12  0.   47000.
DUP
!    (S4)
SiGE3     => SiG(OH)E2 + C2H4
                                                 5.1E+12  0.   47000.
DUP
!
!!! Intra-adsorbate ethanol elimination !!!!!!!!!!!!!!!!!!!!!!!!
!
!    (S5)
SiG(OH)2E => SiG3(OH) + C2H5OH
                                                 2.0e+12  0.   44000.
DUP
!    (S6)
```

```
SiG(OH)E2 => SiG3E + C2H5OH
                                                2.0e+12  0.   44000.
DUP
!
!
!!! Intramolecular Elimination of water !!!!!!!!!!!!!!!!!!!!!!!!
!
!     (S7)
SiG(OH)2E => SiG3E+H2O
                                                2.0e+12  0.   44000.
DUP
!
!
!!!! Insertion reactions of gas-phase products !!!!!!!!!!!!!!!!!
!     (S8)
Si(OH)(OC2H5)3 + SiG3(OH) => SiO2(D) + SiGE3 + H2O
                                                20.0     0.  12000.
STICK
!
!AMB Oxygen Reactions from Romet et al 2001
!The constants need to be sufficiently large such that any
!further increase does not change results.
!
!Equations 39-38 are not needed because there is no O3
!
!38
!SiG(OC2H5)3 + 18O3 => SiO2(D) + 6CO2 + 8H2O + 18O2
                                                        1.0e+12 0. 0.
!39
!Si(OH)2(OC2H5)2 + 12O3 => SiO2(D) + 4CO2 + 6H2O + 12O2
                                                        1.0e+12 0. 0.
!
!Note Equations 40-41 modified to match Coltrin's notation.
!
!40
SiGE3 + 18O => SiG3(OH) + 6CO2 + 7H2O
                                                        1.0e+17 0. 0.
!41
SiG(OH)E2 + 12O => SiG3(OH) + 4CO2 + 5H2O
                                                        1.0e+17 0. 0.
!
!
!Photon-Surface Reactions Added by AMB!!!!!!!!!!!!!!!!!!!!!!!!!
!    (S2)
SiG3E     => SiG3(OH) + C2H4
                                                17.37    0.       0.
```

```
DUP
!    (S3)
SiG(OH)E2 => SiG(OH)2E + C2H4
                                                17.37    0.       0.
DUP
!    (S4)
SiGE3     => SiG(OH)E2 + C2H4
                                                17.37    0.       0.
DUP
!    (S5)
SiG(OH)2E => SiG3(OH) + C2H5OH
                                                17.37    0.       0.
DUP
!    (S6)
SiG(OH)E2 => SiG3E + C2H5OH
                                                17.37    0.       0.
DUP
!     (S7)
SiG(OH)2E => SiG3E+H2O
                                                17.37    0.       0.
DUP
!
!!!!!!!!!!!!!!!!!!!!!!!!!!!!!!!!!!!!!!!!!!!!!!!!!!!!!!!!!!!!!!!!!!!!!!!!!!
END
!
MATERIAL  WALL
! no chemistry
END
END
```